Measurement of Z-boson production cross sections at $\sqrt{s} = 13$ TeV and $t\bar{t}$ to Z-boson cross-section ratios with the ATLAS detector at the LHC

Dissertation

zur Erlangung des Doktorgrades
an der Fakultät für Mathematik, Informatik und Naturwissenschaften
Fachbereich Physik
der Universität Hamburg

vorgelegt von

Nataliia Zakharchuk

aus Ivano-Frankivsk, Ukraine

Hamburg
2018

Gutachter der Dissertation:	PD Dr. Alexandre Glazov Prof. Dr. Peter Schleper
Zusammensetzung der Prüfungskommission:	PD Dr. Alexandre Glazov Prof. Dr. Dieter Horns PD Dr. Krisztian Peters Prof. Dr. Peter Schleper Prof. Dr. Sven-Olaf Moch
Vorsitzender der Prüfungskommission:	Prof. Dr. Sven-Olaf Moch
Datum der Disputation:	13. Februar 2018
Vorsitzender Fach-Promotionsausschusses PHYSIK:	Prof. Dr. Wolfgang Hansen
Leiter des Fachbereichs PHYSIK:	Prof. Dr. Michael Potthoff
Dekan der Fakultät MIN:	Prof. Dr. Heinrich Graener

Abstract

The measurement of Z-boson production cross sections in pp collisions at centre-of-mass energy of $\sqrt{s} = 13$ TeV is presented. Results are based on data corresponding to an integrated luminosity of $3.16\,\text{fb}^{-1}$ recorded with the ATLAS detector in 2015 at the LHC operating with the 25 ns bunch spacing configuration. The selection criteria of the measurement are optimized to be consistent with the new measurement of the $t\bar{t}$ production cross section to maximize elimination of the experimental and theoretical systematic uncertainties for the ratio of the top-quark pair to Z-boson cross sections. Single ratios at the centre-of-mass energy of 13 TeV and double ratios at different centre-of-mass energies, including published ATLAS results for Z-boson and $t\bar{t}$ production at $\sqrt{s} = 7$ TeV and 8 TeV, are reported. The results are compared to the predictions of perturbative quantum chromodynamics calculations at next-to-next-to-leading order using various sets of parton distribution functions (PDFs) and including electroweak corrections. The comparison is performed using the open-source xFitter package. The measured cross sections are used to estimate the impact on the uncertainties of the current PDF set. Moreover, they are used to extract the top-quark mass using the PDF profiling method.

The latest scheduled upgrade, High-Luminosity LHC, foresees an increase of an instantaneous luminosity at the LHC up to $5 \times 10^{34}\,\text{cm}^{-2}\text{s}^{-1}$. The ATLAS tracker will need to be completely replaced with a new all-silicon tracker due to the higher radiation dose and track density. Highly modular structures will be used for the strip system, so-called staves for the barrel region and petals for the end-caps region. A small-scaled strip prototype for the petal, called petalet, consists of silicon sensors, powering and readout components placed into a low mass carbon-based core. Double-sided petalets with different sensor designs and with two different readout and powering electronics layouts are evaluated. The electrical performance of the prototypes and single modules are reported as well as a description of the assembly procedure and tools. The outcomes of the production of the petalets are summarized and the best layout is chosen as a baseline for the future production of the petal.

Zusammenfassung

Die Messung von Produktionswirkungsquerschnitten für Z-Bosonen in pp-Kollisionen bei einer Schwerpunktsenergie von $\sqrt{s} = 13$ TeV wird vorgestellt. Die Ergebnisse basieren auf Daten, die einer integrierten Luminosität von $3.16\,\text{fb}^{-1}$ entsprechen und im Laufe des Jahres 2015 am LHC bei einem Paketabstand von 25 ns aufgezeichnet wurden. Die Selektionskriterien in dieser Messung sind dahingehend optimiert, konsistent mit der neuen Messung der $t\bar{t}$-Produktionswirkungsquerschnitte zu sein und experimentelle und theoretische Unsicherheiten auf das Verhältnis von Wirkungsquerschnitten für die Produktion von Top-Quark-Paaren und Z-Bosonen so weit wie möglich zu eliminieren. Es werden einfache Verhältnisse bei einer Schwerpunktsenergie von 13 TeV und doppelte Verhältnisse bei verschiedenen Energien, unter anderem publizierte ATLAS-Resultate für Z-Boson- und $t\bar{t}$-Produktion bei $\sqrt{s} = 7$ TeV and 8 TeV, berichtet. Die Ergebnisse werden mit Vorhersagen von perturbativen QCD-Rechnungen auf NNLO mit verschiedenen PDFs sowie elektroschwachen Korrekturen verglichen. Der Vergleich wird mit dem quelloffenen Paket xFitter durchgeführt. Die gemessenen Wirkungsquerschnitte werden benutzt um den Einfluss auf die Unsicherheiten von aktuellen PDFs abzuschätzen. Außerdem werden sie benutzt, um die Masse des Top-Quarks mittels der PDF-Profiling-Methode zu bestimmen. Der aktuell geplante Upgrade des LHC, der High-Luminosity LHC, sieht eine Steigerung der instantanen Luminosität auf $5 \times 10^{34}\,\text{cm}^{-2}\text{s}^{-1}$ vor. Aufgrund der höheren Strahlungsbelastung und der steigenden Spurdichte wird der ATLAS Spurdetektor vollständig durch einen neuen, komplett aus Silizium gefertigten Spurdetektor ersetzt werden müssen. Für das Streifensystem werden hochgradig modulare Strukturen, sogenannte Staves in der Barrel-Region und Petals in den Endkappen, benutzt werden. Ein Prototyp für das Petal im kleineren Maßstab, ein sogenanntes Petalet, besteht aus Siliziumsensoren, der Stromversorgung und der Ausleseelektronik, die auf einem leichten Karbon-basierten Kern angebracht sind. Doppelseitige Petalets mit unterschiedlichen Sensordesigns und zwei unterschiedlichen Anordnungen der Auslese- und Stromversorgungssysteme werden evaluiert. Das elektrische Verhalten der Prototypen sowie einzelner Module wird berichtet sowie eine Beschreibung der Montageprozedur und der Werkzeuge gegeben. Die Ergebnisse der Produktion der Petalets werden zusammengefasst und das beste Design wird als Referenz für die zukünftige Petal-Produktion ausgewählt.

Contents

CHAPTER 1

Introduction

The experimental and theoretical aspects of particle physics explore the properties of elementary particles and their interactions. All known particles discovered at particle accelerators are successfully explained within the theoretical framework, called the Standard Model (SM). As stated in the SM, the fundamental building blocks of matter are particles called quarks and leptons and they interact by exchange of gauge bosons. Many free parameters, including quark masses, are not predicted by theory and need to be extracted from the experimental results. In addition, the SM does not explain all physical phenomena and has open questions. The various extensions to the Standard Model and precise values of parameters can be examined with high energies and precision measurements. Any deviation from the SM predictions can hint at new physics.

The largest recent accelerator, the Large Hadron Collider (LHC), located at the European Organization for Nuclear Research (CERN) began operation in 2008 and collided first beams at a centre-of-mass energy of 7 TeV in the proton–proton collisions on 30 March 2010. A huge amount of data from four interaction points has now been collected, offering valuable input for physics analyses. The latest achieved centre-of-mass energy, $\sqrt{s} = 13$ TeV, has extended the kinematic region that can be probed, and the volume of data. The data analyzed in this thesis were collected by the ATLAS (A Toroidal LHC Apparatus) detector during 2015 year. It is a general purpose detector, which detects and stores huge numbers of collision events and allows the reconstruction of electrons, muons, photons, and hadrons with high precision.

The LHC plans to cover a broad physics program with maximum achievable energy and instantaneous luminosity. Towards this programme, a series of upgrades for the detectors is planned. The Phase-II upgrade of the ATLAS will take place in a preparation for the High-Luminosity Large Hadron Collider project. In this upgrade phase, the current ATLAS Inner Detector will be replaced with a new silicon tracker. Small versions of basic mechanical constituents for the forward strip region, called petalets, were assembled at DESY, the University of Freiburg and the Institute for Corpuscular Physics (IFIC) in Valencia. Two different readout and powering schemes are considered in order to study electrical performance and understand the suitability, benefits and drawbacks of the two different designs for a production of full-sized structures. Details of the assembly, testing and evaluation of several petalets are presented in this thesis.

The main topic of this thesis is measurements of Z bosons produced by the Drell–Yan mechanism. This process is well known and plays an important role in studying of the partonic structure of hadrons. The measurement of its total cross section provides a unique opportunity to test the Standard Model predictions at the new higher operating centre-of-mass energy of 13 TeV at the LHC. This process benefits from clear experimental signature, large cross sections and small background and, therefore, can be

measured with high precision. Recent precise measurements [1–8] were performed by CMS [9] and ATLAS [10] collaborations and reached the sub-percent level of precision.

The measured cross sections are compared to the theoretical calculations performed at next-to-next-to-leading-order (NNLO) accuracy in quantum chromodynamics (QCD) plus next-to-leading order (NLO) electroweak (EW) accuracy [11–18]. More precise comparison can be achieved by a calculation of ratios between various processes and at different centre-of-mass energies in which some experimental and theoretical uncertainties can be cancelled. Three scenarios can be investigated [19]:

- the experimental uncertainty is smaller than the theoretical uncertainty: the data versus theory comparison can be used to improve the PDF determination;
- the theoretical uncertainty is of similarly small size to the experimental uncertainty: the measurements can be sensitive to physics beyond the SM;
- systematic errors are small and no contribution found from physics beyond the SM: the cross section ratios can be used for luminosity measurement and cross calibration.

The ratios of $t\bar{t}$ to Z-boson fiducial and total cross sections at given centre-of-mass energy as well the double ratio of $t\bar{t}$ to Z-boson total cross sections between different centre-of-mass energies are evaluated and publised in Reference [20]. The dominant uncertainty, luminosity uncertainty, in the double ratio can be completely eliminated. The previously published ATLAS measurements of the $t\bar{t}$ and Z-boson production cross section at the centre-of-mass energy of $\sqrt{s}$ = 7 TeV and 8 TeV [2, 3, 21] and new accurate measurement of the $t\bar{t}$-pair production cross-section [22] at the centre-of-mass energy of $\sqrt{s}$ = 13 TeV are used for the calculation of ratios. The top-quark pair and Z-boson production at various $\sqrt{s}$ values probes different Bjorken-x regions and their ratio is sensitive to the gluon-to-quark parton distribution function ratio [23].

Quantitative comparisons between the measurements and predictions based on different parton distributions sets are performed in order to estimate constraints on a number of Standard Model parameters such as the parton distribution functions and the top-quark mass.

This dissertation is organized as follows: Chapter 2 gives a brief overview of the Standard Model of particle physics and the process of hadron–hadron collisions. The Z-boson and top-quark production at the LHC are also discussed. Chapter 3 reviews the Large Hadron Collider accelerator complex with a main focus on the ATLAS detector and its subsystems, tracking, calorimeter, muon and trigger, that are relevant for this study. A description of the ATLAS software used in the analysis and the outline of future ATLAS upgrades is presented as well. In Chapter 4 the structure and details on an assembly of petalet are described. The electrical characterization and results of the sensors and petalets are examined. The final comparison of results obtained from different petalets is discussed. Chapter 5 addresses all details on the measurement of Z-boson cross sections in electron and muon channels. A method for a cross-section extraction, data and Monte Carlo samples used for this analysis are specified. The corrections applied to the Monte Carlo samples to improve the agreement between data and simulation are described. An analysis framework, the reconstruction of the physics objects used in the analysis and Z-boson selection procedure is given. A determination of background processes and methods are described. The sources of the uncertainty and their propagation to the final result are explained. The comparison between data and Monte Carlo simulations for relevant kinematic distributions are presented. A combination of the cross sections and their comparison with the theoretical predictions using different parton distribution functions are demonstrated. The ratios of $t\bar{t}$ to Z-boson production cross sections are reported in Chapter 6. An impact of the measured cross sections on the recent parton distribution function and an extraction of the top-quark mass are interpreted in Chapter 7. All results are summarized in Chapter 8.

CHAPTER 2

Theoretical overview

2.1 The Standard Model of particle physics

2.1.1 Fundamental particles and interactions

The Standard Model (SM) of particle physics [24] is a theoretical model established in the 1970s. It is formulated as a quantum field theory which describes fundamental constituents of matter, the elementary particles, and interactions between them. So far, the SM predictions have been successfully tested and confirmed by different high energy experiments over a wide range of energies and showed good agreement between theory and experimental results.

The SM classifies the fundamental particles according to their spin into two classes:

- fermions: half-integer spin (following Fermi–Dirac statistics)
- bosons: integer spin (following Bose–Einstein statistics)

The fermions are the building blocks of matter and can interact with one another by the exchange of bosons via the electromagnetic, weak, strong and gravitational[1] interactions. The electromagnetic interactions are described by quantum electrodynamics (QED), the weak interaction is responsible for radioactive decays and the strong interactions are described by quantum chromodynamics (QCD). The QED and weak interactions were combined into so-called electroweak theory (EW) by Glashow, Weinberg and Salam.

The fermions are categorized into two types of particles, six leptons and six quarks, which are subdivided into three generations (see Table 2.1). Each generation is classified according to the mass of fermions. The first generation includes light and stable particles while the last one includes heavy and unstable particles. All three leptons (electron, muon and tau) have charge of $-1e$[2], while all neutrinos are electrically neutral. The electron (e^-) has the least mass and is followed by the muon (μ^-), approximately 200 times heavier than electron. The muon is followed by the tau lepton (τ^-), which is the heaviest of all leptons. Each lepton has a corresponding antiparticle with the same mass but opposite charge.

The quarks are point-like particles which were proposed by Gell-Mann and Zweig in their quark model in 1964 [25, 26]. There are six types of quarks: down (d), strange (s) and bottom (b) with the charge of $-1/3e$ and up (u), charm (c) and top (t) with the charge of $+2/3e$. One key feature of the quarks is that they carry a strong charge, so-called color. There are three colors, 'red' (r), 'green' (g), and 'blue'

[1] Gravitational interaction is not yet included into the SM

[2] e is elementary electric charge, $e = 1.6021766208 \times 10^{-19}$ C

(b), and their anti-colors. The quarks can not be observed in free states due to confinement. They can be found in colorless bound states, *hadrons*. Hadrons can be classified into two groups: mesons with integer spin (a pair of quark and anti-quark) and baryons with half-integer spin (composed of three quarks). The most stable hadrons are proton and neutron. The proton is made of three valence quarks uud, gluons and 'sea' quarks (virtual $q\bar{q}$). Subsequently, the neutron is made of three valence quarks udd. The sea quarks are virtual pairs of quark and antiquark produced in the interactions of gluons with quarks. The valence quarks give the quantum numbers of the hadrons (the electric charge). The gluons, valence- and sea-quarks are commonly referred to as *partons*.

FERMIONS								
Generation	**Leptons (spin = 1/2)**				**Quarks (spin = 1/2)**			
	Particle	Symbol	Charge	Mass [MeV]	Particle	Symbol	Charge	Mass [MeV]
1^{st}	electron	e^-	-1	0.5109	down	d	$-\frac{1}{3}$	4.7
	e neutrino	ν_e	0	$< 2 \times 10^{-6}$	up	u	$+\frac{2}{3}$	2.2
2^{nd}	muon	μ^-	-1	105.66	strange	s	$-\frac{1}{3}$	96
	μ neutrino	ν_μ	0	$< 2 \times 10^{-6}$	charm	c	$+\frac{2}{3}$	1.28×10^3
3^{rd}	tau	τ^-	-1	1776.86	bottom	b	$-\frac{1}{3}$	4.18×10^3
	τ neutrino	ν_τ	0	$< 2 \times 10^{-6}$	top	t	$+\frac{2}{3}$	173.1×10^3

Table 2.1: The characteristic fundamental particles of the Standard Model. The mass, electrical charge and spin of particles are taken from the PDG 2016 [27].

Bosons are divided into two groups: gauge bosons and scalar bosons (see Table 2.2). The gauge bosons have the spin of 1 and mediate the interactions between quarks and leptons. The electromagnetic interaction is mediated by the exchange of virtual photons, the weak charged-current interactions by the charged W^+ and W^- bosons, and weak neutral-current interactions by Z bosons. The strong force is carried by eight different massless and electrically neutral gluons. Above all, the charged leptons interact electromagnetically and weakly, while the neutral leptons only weakly. In contrast, the quarks interact via all three interactions: strong, weak and electromagnetic.

The Higgs boson is the scalar boson, which has no intrinsic spin and plays an essential role in the SM by explaining the origin of mass of all particles. The Higgs boson generates the masses of the weak gauge bosons and fermions through Higgs mechanism, which causes a spontaneous electroweak symmetry breaking (EWSB) [28, 29]. The Higgs boson was only last missing part of the SM and its discovery was announced in 2012.

2.1.2 Lagrangian and gauge invariance

The mathematical framework that combines quantum mechanics and special relativity is a quantum field theory (QFT), which describes and analyze the physics of elementary particles. In a QFT, the fermions are described by fermion fields ψ (spinor) and bosons (with the spin of 1) are described by vector fields A_μ. The dynamics of the fundamental fields are determined by the Lagrangian density $\mathcal{L}$ (or simply Lagrangian).

The mathematical basis of the Standard Model relies on principles of symmetry. The symmetries refer to an invariance of the Lagrangian and require the existence of a principle of least action, $\delta S = 0$, from

FORCES	**GAUGE BOSONS**			
Name	Particle	Symbol	Charge	Mass [GeV]
Strong	gluon	g	0	–
Electromagnetism	photon	γ	0	–
Weak	Z boson	Z	0	91.19
	W boson	$W^{\pm}$	± 1	80.39
	SCALAR BOSONS			
	Higgs boson	h	0	125.09

Table 2.2: The characteristic of bosons of the Standard Model. The masses for particles are taken from the PDG 2016 [27].

which the equations of motion can be derived. The action is defined as the time integrated Lagrangian density:

$$S(\phi(x)) = \int \mathrm{d}^4 x \mathcal{L}(\phi(x), \partial_\mu \phi(x)), \tag{2.1}$$

and the principle of least action produces the Euler–Lagrange equation, the equation of motion:

$$\partial_\mu \left(\frac{\partial \mathcal{L}}{\partial(\partial_\mu \phi)} \right) - \frac{\partial \mathcal{L}}{\partial \phi} = 0. \tag{2.2}$$

Each symmetry of the group defines the fundamental interactions by requiring local gauge invariance under particular group and has a relation to conservation laws (Noether's theorem). There are global symmetries, which do not depend on a position in space and time and give rise to conserved currents and charges as described by Noether's theorem, and the local symmetries, which depend on a position in space and time. The SM is specified by the gauge symmetry group which is a combination of the $SU(3)_C \otimes SU(2)_L \otimes U(1)_Y$, where

- $U(1)$: one-dimensional abelian group which consist of 1×1 unitary[3] matrices. Local $U(1)$ symmetry describes the electromagnetic interactions. The field can be transformed under local gauge transformations, $U(x)$ as

  $$\psi(x)' = U(x)\psi(x) = e^{i\alpha(x)}\psi(x)$$

  The $U(1)$ group corresponds to a single generator, the massless photon, and describes a weak hypercharge Y symmetry;

- $SU(n)$: special non-abelian unitary group of $n \times n$ matrices with the property of $\det U = 1$. The group elements are generated by n generators and there are $n^2 - 1$ generators (for $n > 1$). The field can be transformed under local gauge transformations as

  $$\psi(x)' = U(x)\psi(x) = e^{it_a \alpha^a(x)}\psi(x),$$

  where t_a is the generator of $SU(n)$.

  – $SU(2)$: two-dimensional special unitary group, which describes the weak interactions and

[3] $U^\dagger = U^{-1}$

isospin symmetries. This group has three generators of gauge symmetry, $\frac{1}{2}\sigma_a$, which are represented as Pauli spin matrices, σ_a.

– $SU(3)$: three-dimensional special unitary group, which describes the strong interactions. The symmetry has eight generators, which are associated with eight types of gluons and represented as the Gell–Mann matrices, $\frac{1}{2}\lambda_a$. The conserved charge associated to this symmetry is known as 'color charge', C.

The result of a separate symmetry group generates the three fundamental forces (strong, electromagnetic and weak).

Quantum Electrodynamics. The Lagrangian describing a free Dirac fermion is:

$$\mathcal{L} = \overline{\psi}(i\gamma^\mu\partial_\mu - m)\psi, \tag{2.3}$$

where ψ are four dimensional vectors (Dirac spinor), $\overline{\psi}$ is the Dirac adjoint ($\overline{\psi} = \psi^\dagger\gamma^0$), γ^μ are the Dirac matrices. This Lagrangian is not invariant under local transformation of the $U(1)$ group and generate an extra term through the derivative. The local gauge invariance can be achieved by replacing the derivative ∂_μ by the covariant derivative D_μ:

$$D_\mu \equiv \partial_\mu + ieA_\mu, \tag{2.4}$$

where e is the electric charge and A_μ is new massless vector field, identified as the photon field, and introduced as:

$$A_\mu(x) \to A_\mu(x) - \partial_\mu\alpha(x) \tag{2.5}$$

Using Equation 2.4 instead of ∂_μ in Equation 2.3 and by adding missing kinetic energy term for the photon field one can obtain the QED Lagrangian:

$$\mathcal{L}_{\text{QED}} = \overline{\psi}(i\gamma^\mu\partial_\mu - m)\psi + e\overline{\psi}\gamma^\mu A_\mu\psi - \frac{1}{4}F_{\mu\nu}F^{\mu\nu}, \tag{2.6}$$

where second term corresponds to the QED interaction of the fermion field with the vector field and third term describes the electromagnetic field $F_{\mu\nu}$ defined as $F_{\mu\nu} = \partial_\mu A_\nu - \partial_\nu A_\mu$.

Quantum Chromodynamics. The QCD Lagrangian has similar structure to the QED Lagrangian

$$\mathcal{L} = \sum_f \overline{\psi}^f(i\gamma^\mu\partial_\mu - m^f)\psi^f, \tag{2.7}$$

where the sum is over all six quark flavours f and ψ^f is the three fermion spin-1/2 fields. The Lagrangian should be invariant under $SU(3)$ transformations and accordingly the covariant derivative is introduced as

$$D_\mu \equiv \partial_\mu + ig\frac{\lambda_a}{2}G^a_\mu, \tag{2.8}$$

where G^a_μ is gluon fields (3×3 matrix) with a running over all eight kinds of gluons and g stands for the gauge coupling constant. Adding the kinetic energy term for each gluon as $-\frac{1}{4}G^a_{\mu\nu}G^{\mu\nu}_a$, one can obtain final QCD Lagrangian:

$$\mathcal{L}_{\text{QCD}} = \sum_f \left(\overline{\psi}^f(i\gamma^\mu\partial_\mu - m^f)\psi^f - g\overline{\psi}^f\gamma^\mu G^a_\mu\frac{\lambda_a}{2}\psi^f\right) - \frac{1}{2}G^a_{\mu\nu}G^{\mu\nu}_a. \tag{2.9}$$

Electroweak theory. In the quantum field theory of weak interactions, the Lagrangian is required to be invariant under transformation of $SU(2)_L$ group. In this theory, quarks and leptons have a different chirality. They are divided into the left-handed, L, (appear in doublets) and the right-handed, R (appear in singlets). The left-handed fermions only participate in the charged-current interactions and the right-handed in the neutral-current interactions, respectively. They can be defined using projection operators:

$$\psi_{R,L} = \frac{1}{2}(1 \pm \gamma^5)\psi. \tag{2.10}$$

The weak interactions together with the electromagnetic interactions are based on the symmetry group $SU(2)_L \otimes U(1)$. Similar to QED and QCD, the free Lagrangian is [30]:

$$\mathcal{L} = \sum_{j=1}^{3} \overline{\psi}_j \gamma^\mu \partial_\mu \psi^j, \tag{2.11}$$

where the mass term is not included because it would mix the left- and right-handed fields.

The required local gauge invariance can only be satisfied by introducing four different gauge bosons, W_μ^k with $k = 1, 2, 3$ and B_μ. The corresponding covariant derivative defined as

$$D_\mu \equiv \partial_\mu + i\frac{g}{2} W_\mu^k \tau_a + i\frac{g'}{2} B_\mu Y, \tag{2.12}$$

where g and g' are the coupling constants of the two interactions, τ_a are the corresponding generators of $SU(2)$ and Y is the weak hypercharge. The invariant Lagrangian for the electroweak interactions, that describes the EM and weak interactions in a unified manner, is the following:

$$\mathcal{L}_{\mathrm{EW}} = \sum_{j=1}^{3} \overline{\psi}_j \gamma^\mu D_\mu \psi^j - \frac{1}{4} W_{\mu\nu}^a W_a^{\mu\nu} - \frac{1}{4} B_{\mu\nu} B^{\mu\nu}. \tag{2.13}$$

The photon and Z boson are orthogonal linear combinations of the fields B and W_μ^3 related via the weak mixing angle θ_W :

$$\begin{aligned} A^\mu &= B^\mu \cos\theta_W + W_3^\mu \sin\theta_W \\ Z^\mu &= -B^\mu \sin\theta_W + W_3^\mu \cos\theta_W, \end{aligned} \tag{2.14}$$

where where A_μ and Z_μ are photon and the Z boson. The $W_\mu^\pm$ can be obtained via a linear combination of W_μ^1 and W_μ^2:

$$W_\mu^\pm = \frac{1}{\sqrt{2}}(W_\mu^1 \mp W_\mu^2). \tag{2.15}$$

The fermions and bosons have to be massless to preserve the electroweak gauge symmetry. However, the experimental results demonstrate that measured masses for them are found to be non-zero. Therefore, the electroweak gauge symmetry has to be broken involving the mechanism of *spontaneous symmetry breaking*, the Higgs mechanism. To generate the mass for the W and Z bosons a complex scalar field is introduced as:

$$\phi = \begin{pmatrix} \phi^0 \\ \phi^+ \end{pmatrix} \tag{2.16}$$

and described by the Lagrangian density

$$\mathcal{L}_{Higgs} = (\partial_\mu \phi)^\dagger (\partial^\mu \phi) - V(\phi) \tag{2.17}$$

with the potential defined as

$$V(\phi) = \mu^2 \phi^\dagger \phi + \lambda (\phi^\dagger \phi)^2. \tag{2.18}$$

In the ground state, the vacuum, the potential has a minimum. For $\lambda > 0$ and $\mu^2 > 0$, the potential is in the form of symmetric parabola and the scalar field has a minimum at $\phi = 0$. For $\lambda > 0$ and $\mu^2 < 0$, the potential will have an infinite set of degenerate minima satisfying the condition $\phi^\dagger \phi = \frac{v^2}{2} = -\frac{\mu^2}{2\lambda}$, where v denotes a vacuum expectation value. The choice of vacuum state breaks the symmetry of the Lagrangian and is called spontaneous symmetry breaking. The local gauge symmetry of the $SU(2)_L \otimes U(1)_Y$ gets spontaneously broken into the $U(1)$ symmetry of QED, while the $U(1)$ and $SU(3)$ symmetries remain unbroken. If ϕ is expanded around non-zero vacuum expectation value, it is found to have the following form:

$$\phi = \frac{1}{\sqrt{2}} \begin{pmatrix} 0 \\ v + h \end{pmatrix}. \tag{2.19}$$

The field h is the Higgs boson with the mass $M_H = \frac{\mu}{\sqrt{2}}$. The non-zero v of the Higgs fields leads to the mass terms for three bosonic fields. After symmetry breaking, the photon and gluons remains massless, while the W and Z acquire masses. The boson masses are following:

$$\begin{aligned} M_W &= \frac{1}{2} v g \\ M_Z &= \frac{1}{2} v \sqrt{g^2 + g'^2}. \end{aligned} \tag{2.20}$$

Mass terms for the fermions can be generated by the Higgs mechanism via Yukawa coupling between fermions and the Higgs field.

2.2 Proton–proton collisions

2.2.1 Structure of the proton

In high-energy hadron collider, Large Hadron Collider (LHC), the collisions involve complex composite particles, protons, which consist of three valence quarks, gluons and quark–antiquark pairs. Therefore, in contrast to electron collisions (point-like collisions), hadron collisions are complicated, since the protons do not interact as whole objects, but only the partons inside them. When two protons collide, the partons, with carrying a momentum fractions of the proton, scatter in the hard scattering process. A collision between two partons, with large momentum transfer, gives the hard process of interest.

The structure of the proton can described by parton distribution functions (PDFs). The PDFs quantify the probability (density) of finding a parton (quark or gluon) in the proton carrying a fraction x of its momentum at an energy scale Q^2. The PDFs can not be calculated perturbatively and, therefore, they are extracted from global fits to various data from different experimental measurements. The knowledge of proton PDFs comes from the Deep Inelastic Scattering (DIS) HERA, fixed target, Tevatron and LHC data. PDFs depend on the energy scale, therefore, they are parametrised at a starting scale of order $Q_0^2 = 1$ GeV^2 as:

$$x f(x, Q_0^2) = A x^B (1 - x)^C P(x, D). \tag{2.21}$$

where the normalisation parameters A are constrained by the quark number sum-rules and momentum sum-rule and B and C are free fit parameters. $P(x, D)$ are polynomials in x. The PDF evolution to any other scale $Q^2 > Q_0^2$ can be determined by the Dokshitzer–Gribov–Lipatov–Altarelli–Parisi (DGLAP) evolution equations [31–33]:

$$\frac{\partial f(x,\mu_F^2)}{\partial \log \mu_F^2} = \frac{\alpha_S(\mu_R^2)}{2\pi} \sum_{b=q,\hat{q},g} \int_x^1 \frac{\mathrm{d}z}{z} P_{ab}(\frac{x}{z}, \mu_F^2) f_b(z, \mu_F^2), \tag{2.22}$$

where $P_{ab}(\frac{x}{z}, \mu_F^2)$ are the evolution kernels or splitting functions, which represent the probability for the parton b to emit parton a carrying a fraction $\frac{x}{z}$ of the momentum of the parton b. $\alpha_S(\mu_R^2)$ is a running strong coupling constant, which depends on the renormalization scale, μ_R. If $\mu_R^2 \simeq Q^2$ then α_S is indicative of the effective strength of the strong interaction. The α_S value at a given energy scale can be determined from experiments. The one-loop running α_S is given by the formula:

$$\alpha_S(\mu_R^2) = \frac{12\pi}{(33 - 2n_f) \ln \frac{\mu_R^2}{\Lambda_{QCD}^2}}, \tag{2.23}$$

where Λ_{QCD}^2 is the QCD scale parameter (~200 MeV) and n_f is the number of flavors (6 in the Standard Model). The measurements of α_S as a function of the energy scale are shown in Figure 2.1.

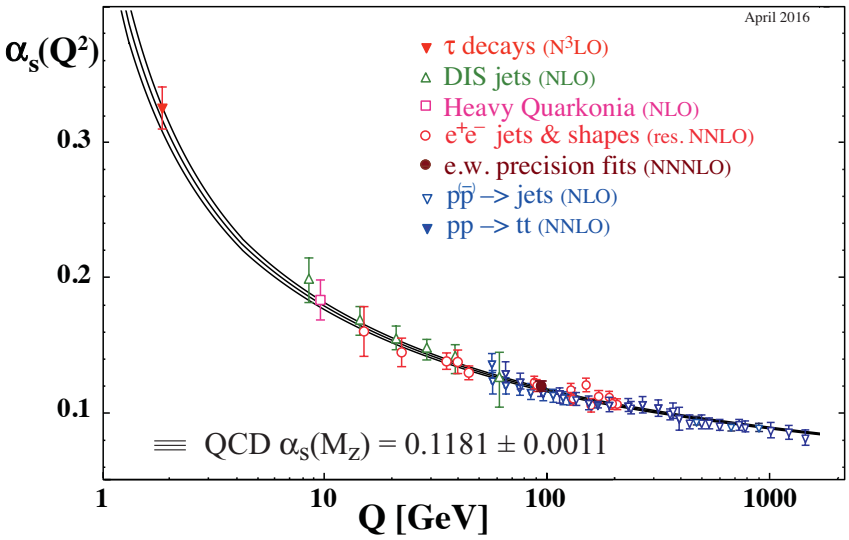

Figure 2.1: Measurements of α_S as a function of the energy scale Q. The respective order of pertubative QCD used in the extraction of α_S is indicated in brackets. Taken from [27].

The splitting functions depend on the type of the parton splitting. They can be expanded in powers of the running coupling α_S as:

$$P_{ab}(z, \alpha_S) = P_{ab}(z)^0 + \frac{\alpha_S}{2\pi} P_{ab}(z)^1 + ... \tag{2.24}$$

The splitting functions have four different forms: P_{qq} – a quark radiates a quark, P_{qg} – a gluon radiates a quark (antiquark), P_{gq} – a quark radiates a gluon, P_{gg} – a gluon radiates a gluon. They are calculated up

to NLO and NNLO [34–36]. The evolution equations can not describe the x-dependence of the parton distributions at a given Q^2. The x-dependence needs to be determined from fits to experimental data.

Various PDF fitting collaborations work on the PDFs using different fitting methods and experimental data. Some of the latest PDF releases include CT14 [37], NNPDF3.0 [38], MMHT14 [39], ATLAS-epWZ12 [40], HERAPDF2.0 [41], and ABM12 [42]. The CT14 PDFs, for the different types of quarks and antiquarks and gluons as a function of x fraction for $Q = 2$ GeV and $Q = 100$ GeV are shown in Figure 2.2. This PDF on top of HERA and Tevatron data includes data sets from the ATLAS, CMS and LHCb experiments: vector boson (W, Z) production cross sections and asymmetries from $\sqrt{s} = 7$ TeV data (impose constraints on the light quark and antiquark PDFs at $x \geq 0.01$) and inclusive jet cross sections (help to constrain the gluon PDF). The distributions from Figure 2.2 show that valence quarks tend to carry a much higher fraction of proton momentum, and gluon and sea-quark distributions increase at higher energy scales (right).

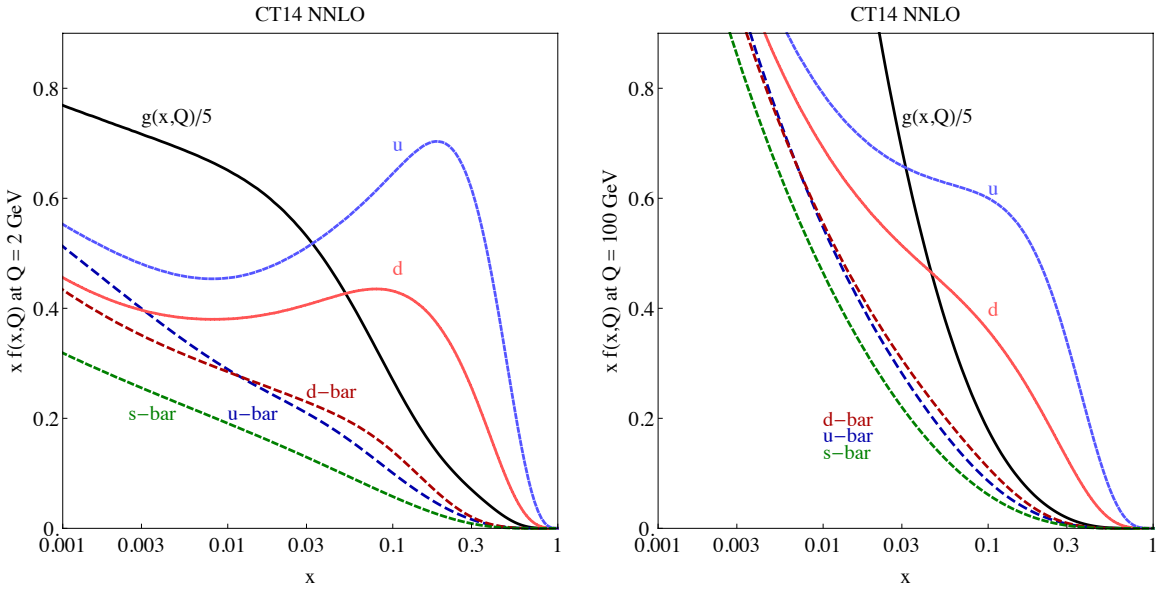

Figure 2.2: The CT14 NNLO parton distribution functions at $Q = 2$ GeV and $Q = 100$ GeV. Taken from [37].

The determined PDFs are used in the calculation of cross-section predictions. Hence, a good knowledge of the PDFs is essential to make predictions for the Standard Model and beyond the Standard Model processes. Nowadays, the predicted cross sections have sizeable PDF uncertainties which influence on the determination of fundamental parameters. They can be reduced by adding new precise data to the QCD fits covering different x ranges. Moreover, the concept of calculating the ratios and double ratios of cross sections allows an elimination of several experimental and theoretical uncertainties. The precision ratio measurements can provide discrimination power among proton PDFs (see Chapter 6).

2.2.2 Partonic cross section

The processes that appear in collisions of hadrons involve both hard- and soft-scattering processes. The hard QCD processes correspond to large momentum transfers Q^2 of interacting partons and can be calculated perturbatively, while the soft-scattering processes correspond to low Q^2. The hard-scattering cross section can be factorized into the long- and short-distance parts using the QCD factorization theorem [43]. The long-distance part is a non-perturbative part which corresponds to PDFs, while the

short-distance, hard scatter part, can be calculated using perturbative QCD. The total proton–proton cross section for a specific hard process, where two partons scatter in a hard collision producing a final state X, can be calculated as follows:

$$\sigma(AB \to X) = \sum_{a,b} \int \mathrm{d}x_a \mathrm{d}x_b f_{a/A}(x_a, \mu_\mathrm{F}^2) f_{b/B}(x_b, \mu_\mathrm{F}^2) \hat{\sigma}_{ab\to X}, \tag{2.25}$$

where the sum is over all partons that contribute to the process (a runs over the partons of proton A, and b runs over the partons of proton B). $f_{a/A}$ and $f_{b/B}$ are parton distribution functions (PDFs) for the partons a, b, in the proton A, B. $\hat{\sigma}_{ab\to X}$ is the partonic cross section for interactions of two partons, which can be calculated perturbatively in QCD in powers of the strong coupling α_S. The μ_F is the factorization scale, which separates the long- and short-distance regimes. The partonic cross section can be expressed as a power series expansion of the α_S coupling constant:

$$\hat{\sigma}_{ab\to X} = \underbrace{\hat{\sigma}_0}_{\text{LO}} + \underbrace{\alpha_S(\mu_\mathrm{R}^2)\hat{\sigma}_1}_{\text{NLO}} + \underbrace{\alpha_S^2(\mu_\mathrm{R}^2)\hat{\sigma}_2}_{\text{NNLO}}, \tag{2.26}$$

where LO is leading order, NLO is next-to-leading order and NNLO is next-to-next-to-leading order calculations. The μ_R^2 is s the renormalization scale of the running coupling.

2.3 Z-boson physics

The first observation of the Z bosons occurred at UA1 and UA2 experiments in 1983 [44, 45]. The Z boson is an electrically neutral vector boson with an extremely short life time ($\sim 10^{-25}$ sec). The production of Z bosons in high energy collisions at the LHC is dominated by the Drell–Yan mechanism, in which quark and antiquark from the incoming protons annihilate into a pair of leptons, muons or electrons for this analysis (see Figure 2.3):

$$q\bar{q} \to Z/\gamma^* \to l^+l^-$$

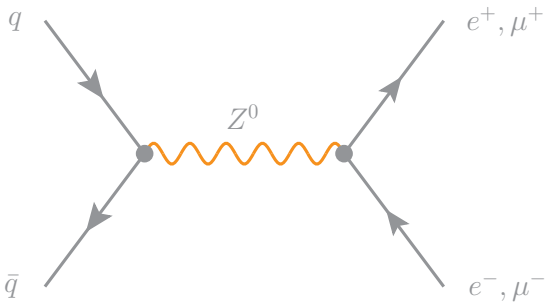

Figure 2.3: The Drell–Yan process: quark–antiquark annihilation into a dilepton final state.

Both valence-sea and sea-sea quark interactions contribute to the process. The dominant contribution comes from $d\bar{d}$ and $u\bar{u}$ quarks. The branching ratios of Z-boson decay channels are given in Table 2.3. The branching fractions for lepton decay modes are similar for all three final states which means that interactions between leptons and Z bosons are the same for all leptons. This feature is referred to a *lepton universality*.

Decay mode	Br [%]
$Z \to e^+e^-$	3.363 ± 0.004
$Z \to \mu^+\mu^-$	3.366 ± 0.007
$Z \to \tau^+\tau^-$	3.370 ± 0.008
$Z \to \nu\bar{\nu}$ (invisible)	20.00 ± 0.06
$Z \to q\bar{q}$ (hadrons)	69.91 ± 0.06

Table 2.3: Branching fractions of the Z boson. Values taken from [27].

The total energy in the centre-of-mass frame of two colliding protons with four-momenta P_1 and P_2 (neglecting proton mass) can be determined by

$$s = (P_1 + P_2)^2 \approx 2P_1P_2 \tag{2.27}$$

The square of the total energy in the center of mass frame of the two partons with momenta p_1 and p_2 is defined as

$$\begin{aligned} \hat{s} = (p_1 + p_2)^2 = (x_1P_1 + x_2P_2)^2 &\approx 2x_1x_2P_1P_2 \\ &= x_1x_2s = M_Z^2 \end{aligned} \tag{2.28}$$

The centre-of-mass energy necessary for a production of Z boson is $\sqrt{s} = M_Z$. Taking the four vectors as $p_{1,2} = x_{1,2}\frac{\sqrt{s}}{2}(1, 0, 0, \pm 1)$, the rapidity of the vector boson can be defined as

$$y = \frac{1}{2}\ln\frac{E + p_z}{E - p_z} = \frac{1}{2}\ln\frac{x_1}{x_2} \tag{2.29}$$

Accordingly, using Equations 2.28 and 3.1, the fraction of parton momentum, rapidity and mass of boson can be related as following

$$x_{1,2} = \frac{M}{\sqrt{s}}e^{\pm y} \tag{2.30}$$

Thus different invariant masses and different rapidity y of Z bosons probe different regions of the parton x. The kinematic phase space in $x - Q^2$ demonstrating the allowed region for parton kinematics at LHC and other experiments is shown in Figure 2.4. The x and Q^2 ranges covered by the LHC is wider due to increased centre-of-mass energy.

The cross section for Drell–Yan process at leading order can be obtained from the fundamental QED $e^+e^- \to \mu^+\mu^-$ cross section, with the addition of appropriate color and charge factors:

$$\hat{\sigma}(q\bar{q} \to ll) = \frac{4\pi\alpha^2}{3\hat{s}}\frac{1}{N_C}Q_q^2, \tag{2.31}$$

where Q_q is the quark/antiquark charge, $\hat{s}$ is the squared center of mass energy of the incoming partons and $1/N_C$ is a factor of colors, where $N_C = 3$. Of the nine possible colour combinations, the annihilation process can only occur for three.

Theoretical predictions for the Z-boson cross sections are calculated up to next-to-next-to leading order (NNLO) with the program FEWZ [47–50] using the CT14nnlo parton density function parameterisation. A comparison between the predictions and experimental data provides a precision test of perturbative

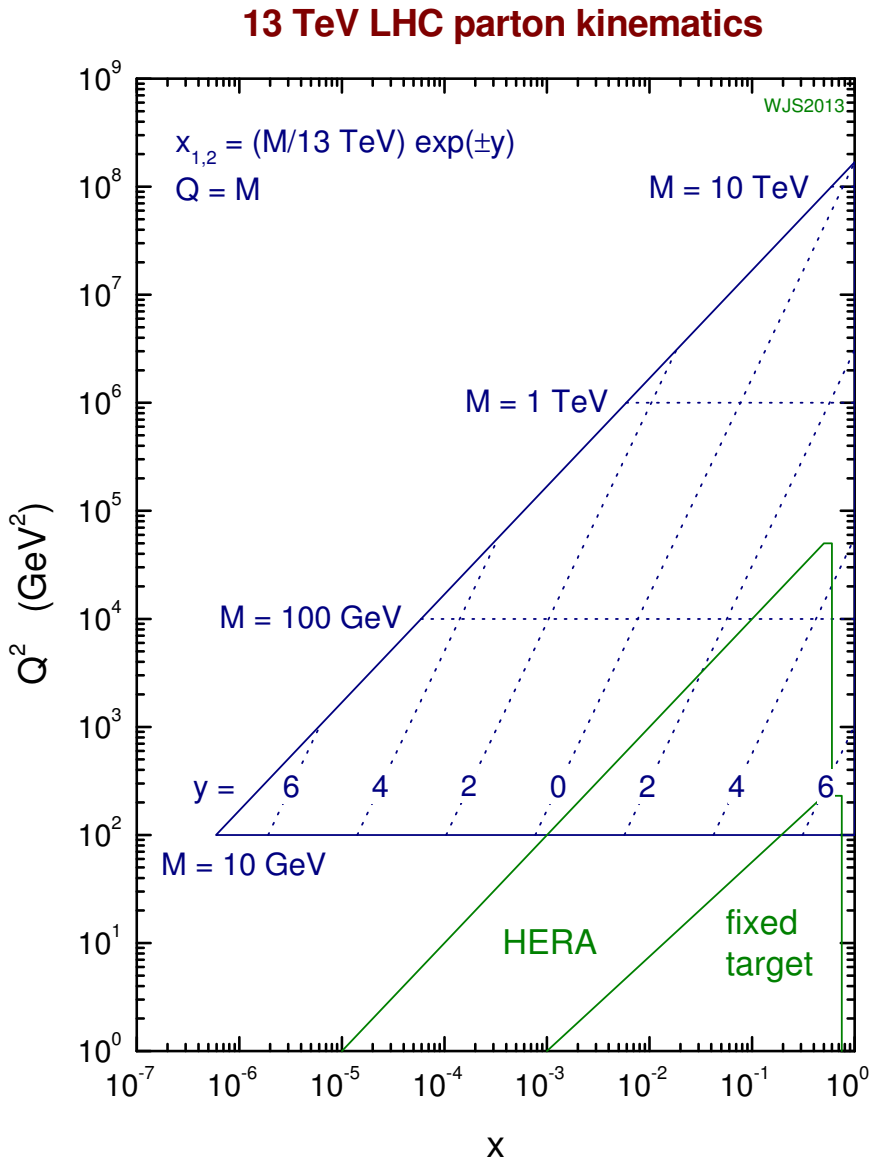

Figure 2.4: Illustration of kinematic plane in bins of Bjorken x and Q^2 showing coverage of the LHC and fixed-target and HERA experiments. Taken from [46].

QCD and is presented in Figure 2.5. It illustrates good agreement between results and the dependence of the Z-boson production with the centre-of-mass energy. The study of Z-boson production at $\sqrt{s}$ = 13 TeV benefits from the higher center-of-mass energy and from improved statistical and systematic uncertainties and offers a unique opportunity to test models of parton dynamics at the LHC.

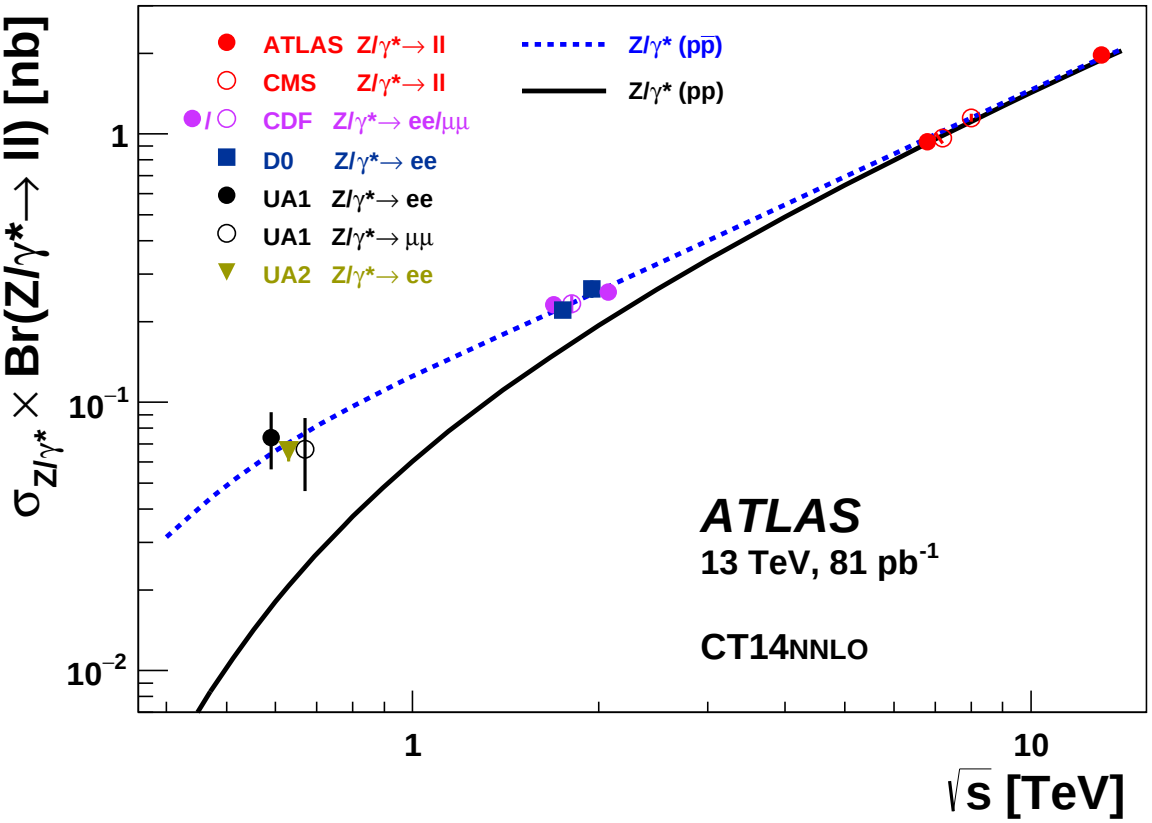

Figure 2.5: The LHC measurements of the Z-boson production cross section as a function of the centre-of-mass energy compared to the NNLO calculation. The ATLAS results are shown for the combined electron–muon channels. The predictions and previous measurements are shown for both proton–proton and proton–antiproton colliders. All data points are displayed with their total uncertainty. The calculations were performed with the program FEWZ using the CT14nnlo parton density function parameterisation. The theoretical uncertainties on the cross-section predictions are not shown.

2.4 Top-quark physics

2.4.1 Top-quark production

The top quark is the heaviest elementary particle predicted by the Standard Model and discovered almost 20 years ago at proton–antiproton $p\bar{p}$ colider, Tevatron, at Fermilab [51, 52]. Due to its huge mass (m_t = 173.34 GeV [53]) high-energy collisions are needed for its production, at least twice the top mass (minimal energy $\hat{s} > 4m_t^2$). The high centre-of-mass energies at the LHC, $\sqrt{s}$ = 7 TeV, 8 TeV and 13 TeV, have allowed the ATLAS and CMS experiments to record datasets with about a million top-quark events.

The typical parton momentum fraction needed for a creation of top-quark pairs at $\sqrt{s} = 13$ TeV is[4]:

$$x \sim \frac{2m_t}{\sqrt{s}} \approx 0.025,$$

which is smaller than corresponding values at the Tevatron (0.2) at the centre-of-mass energy $\sqrt{s} = 1.96$ TeV. The top quarks can be produced in pairs via strong interaction or as the single top quark via electroweak interactions. At the LHC at $\sqrt{s} = 13$ TeV the top-quark pairs originate mainly in two processes:

- gluon–gluon fusion: $pp \to gg \to t\bar{t}$ (90%)
- quark–antiquark annihilation: $pp \to q\bar{q} \to t\bar{t}$ (10%),

whereas at the Tevatron it is opposite situation (15% and 85%). The corresponding Feynman diagrams for leading order (LO) are shown in Figure 2.6. Figure 2.2 shows that for low-x values (typical for the LHC) the dominant contribution comes from gluons, while at high-x values (typical for the Tevatron) valence quarks make the dominant contribution. The top quark has extremely short lifetime, $\tau_t \simeq 1/\Gamma_t \approx$

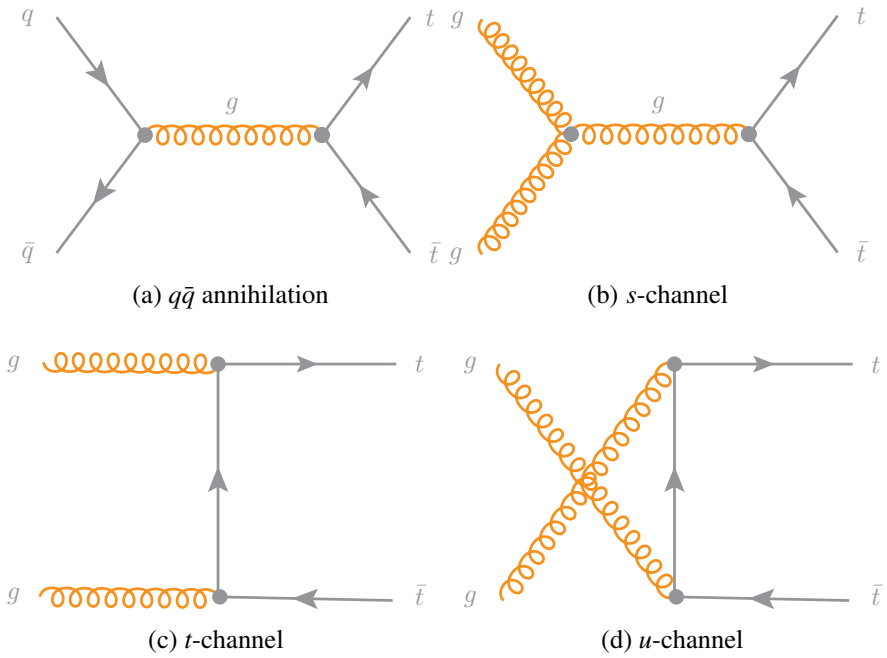

(a) $q\bar{q}$ annihilation (b) s-channel

(c) t-channel (d) u-channel

Figure 2.6: Feynman diagrams for $t\bar{t}$ production via strong interaction at leading order (LO). (a) quark–antiquark annihilation and (b), (c), (d) gluon–gluon fusion.

5×10^{-25} s, which is shorter than hadronization scale of QCD by about one order of magnitude. Thus the top quark decays before the formation of hadronic bound states, top mesons or top baryons, which give a possibility to study the properties of a 'bare' quark. The top quarks mainly decay into a W boson and bottom quark (95.7%), since matrix elements of CKM are $V_{tb} >> V_{ts} > V_{td}$. Subsequently, events containing the $t\bar{t}$ pairs are subdivided into three classes according to the decays of W boson [27]:

[4] with a assumption that $x_1 = x_2$

- **all-hadronic** (45.7%): both W-bosons decay into quark–antiquark pairs

$$W^+ \to q_i' + \bar{q}_j, W^- \to q_i + \bar{q}_j',$$

  where q_i = u-type quark and $\bar{q}_j$ = down-type quark

- **semileptonic** (lepton+jet) (43.8%): one W-boson decays to quarks, another one into two leptons, $l = e, \mu, \tau$

$$W^+ \to q_i' + \bar{q}_j, W^- \to l^- + \bar{\nu}_l$$

- **dileptonic** (10.5%): both W-bosons decay into two leptons, $l = e, \mu, \tau$

$$W^+ \to l^+ + \nu_l, W^- \to l^- + \bar{\nu}_l,$$

are shown in Figure 2.7 and an overview of different possible final states of the $t\bar{t}$ production is presented in Figure 2.8.

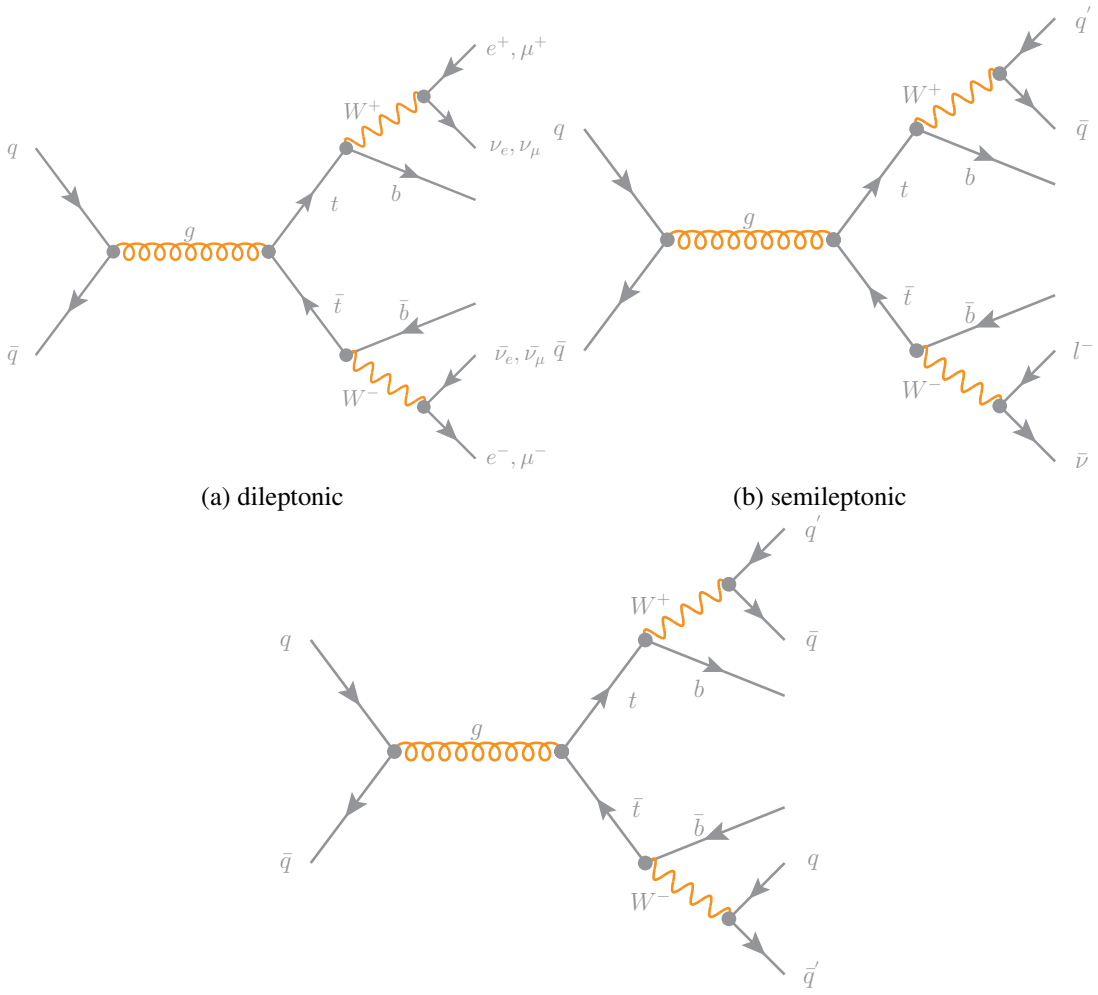

(a) dileptonic

(b) semileptonic

(c) hadronic

Figure 2.7: Overview of $t\bar{t}$ decay channels.

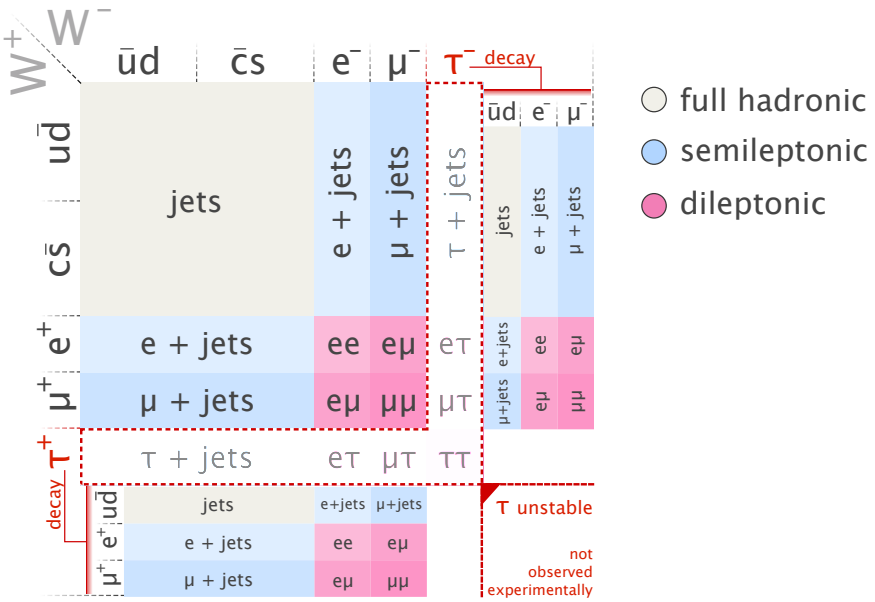

Figure 2.8: All possible final states of the decay of a top-quark pair. Taken from [54].

Theoretical predictions for the $t\bar{t}$ cross sections are discussed in Subsection 2.5.2. A comparison of the predictions with experimental data provides a precision test of perturbative QCD. The available experimental and theoretical results for the inclusive $t\bar{t}$ cross section measurements from the LHC and Tevatron are presented in Figure 2.9. It illustrates the dependence of the $t\bar{t}$ production on the centre-of-mass energy, indicating that the $t\bar{t}$ production cross sections obtained at the LHC are more than 20 times higher then at the Tevatron. Overall the comparison shows good agreement between results.

The latest detailed overview about top-quark production can be found in [27, 56]. In this work, the $t\bar{t}$ production cross sections measured in dileptonic decay channel are considered and the corresponding Feyman diagram is shown in Figure 2.7(a).

2.4.2 Top-quark mass

The top-quark mass is a fundamental parameter of the Standard Model (SM) and plays a significant role in high-energy physics. The top-quark mass can not be measured directly given the fact that the top quark does not exist as a free particle. Its value is used in the theoretical predictions and influences the results for many observables either directly or via radiative corrections. The top mass can constrain the masses of the W and Higgs boson based on its contribution to the total radiative correction. It is essential to measure top-quark mass precisely in order to test the consistency of the SM and to constrain any new physics as it provides information for global fits of electroweak parameters [57]. Precision measurement of the top-quark mass takes a central role in the question of the stability of the electroweak vacuum because top-quark radiative corrections tend to drive the Higgs-boson self-coupling (λ) towards negative values, potentially leading to an unstable vacuum [27].

The mass is not predicted by theory and must be inferred from experimental measurements using various techniques and different decays channels by experiments at the LHC and Tevatron. The value of the top-quark mass can be determined using two different approaches: *direct* or *indirect*.

The direct approach uses the determination of the top-quark mass from the reconstruction of the final

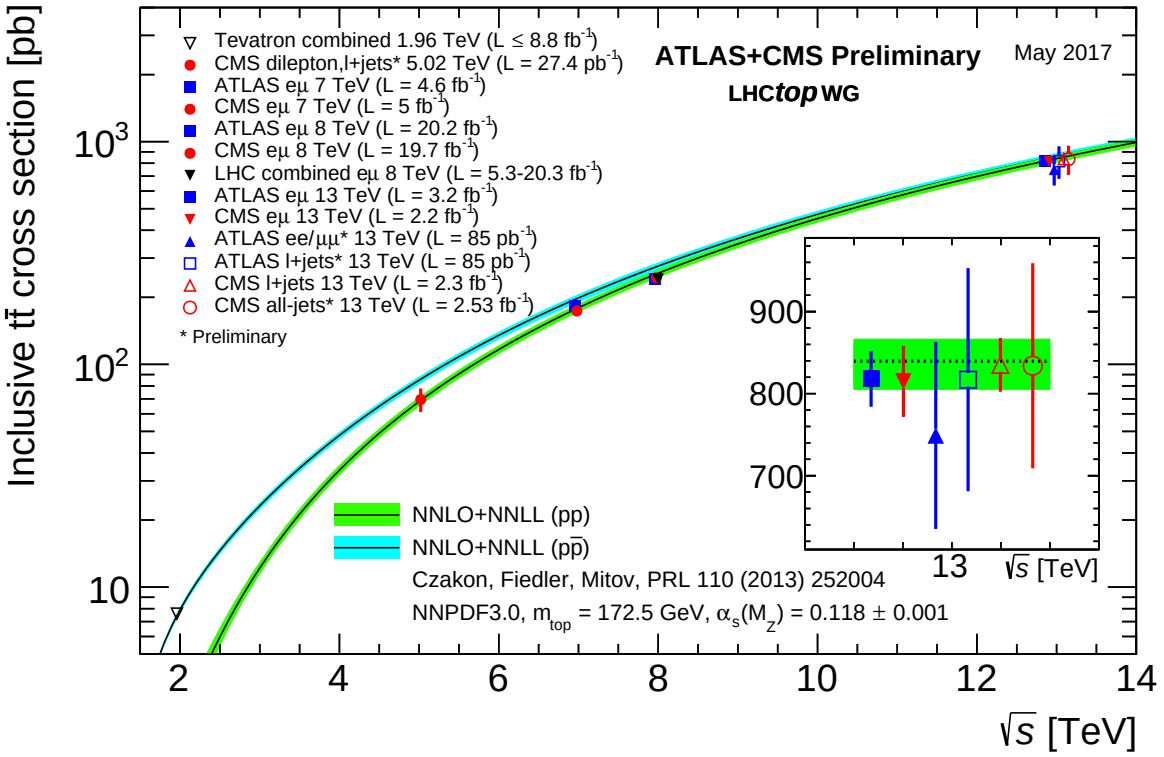

Figure 2.9: The LHC and Tevatron measurements of the top-pair production cross section as a function of the centre-of-mass energy compared to the NNLO+NNLL QCD calculation (Top++2.0). The theory band represents uncertainties due to renormalisation and factorisation scale, parton density functions and the strong coupling. The measurements and the theory calculation are quoted at m_t = 172.5 GeV. Taken from [55].

states in decays of the top-quark pair and gives most precise results. Usually this technique is based on the template method, comparing Monte Carlo templates for different assumed values of m_t with the invariant mass distributions measured in data [58, 59]. Thus, the extracted value from the direct measurement corresponds to the top-quark mass scheme used in the Monte Carlo simulation and is referred to as Monte Carlo top mass, m_t^{MC}. This mass can not be used directly in the theoretical calculation since it is not a renormalized field theory mass.

The indirect approach relies on the determination of the top-quark mass from measured inclusive $t\bar{t}$ pair production cross sections. The top-quark mass can be extracted by comparing dependence of calculated predictions to measured cross sections as the function of top-quark mass. Different concepts of the mass can be defined by a corresponding renormalization scheme used in the fixed-order perturbative calculations in the QCD and referred as pole mass (m_t^{pole}) or $\overline{\mathrm{MS}}$ running mass ($m_t^{\overline{\mathrm{MS}}}$), depending on the scheme. The calculations beyond the leading order contain loops which can yield ultraviolet (UV) divergences in the top self-energy Feynman diagrams due to infinite momentum in the loops. These UV divergences and additional finite contributions of the self-energy can be absorbed into the mass by applying the renormalization procedure. The different top mass schemes are defined by different choices for finite contributions.

Pole mass The m^{pole} is so-called large distance (energy is of order m) mass which is defined in the on-shell (OS) renormalizaiton scheme. The m^{pole} is defined through a position of the pole in the quark propagator in perturbation theory:

$$G(\not{p}) = \frac{i}{\not{p} - m - \sum(\not{p})} \tag{2.32}$$

In this scheme all UV divergences and finite contribution are absorbed. The m_t^{pole} can be related to the m_t^{MC} with an uncertainty of around 1 GeV [60, 61]. The pole mass depends strongly on the perturbative order and has an ambiguity of the order of Λ_{QCD} referred to as the infrared renormalon problem [62].

$\overline{\text{MS}}$ mass The $\overline{\text{MS}}$ is so-called short distance (high-energy) mass which is calculated in the modified minimal subtraction ($\overline{\text{MS}}$) scheme [63, 64] and which depends on the renormalization scale μ_R ($\mu_R \gg \Lambda_{QCD}$). In this scheme only divergent part is removed. This definition of the mass doest not suffer from the non-perturbative ambiguities and is more stable at high orders.

The relation between the pole mass m_t^{pole} and the $m(\mu_{\text{R}})$, running mass $m_t^{\overline{\text{MS}}}$, at one-loop order in a perturbative expansion in α_S is given by [65]:

$$m^{\text{pole}} = m(\mu_{\text{R}})\Big(1 + \alpha_S(\mu_{\text{R}})d^{(1)} + \dots\Big),$$
$$d^{(1)} = \frac{4}{3} + ln\frac{\mu_{\text{R}}^2}{m(\mu_{\text{R}})^2},$$

where coefficients d^i are known to four-loop order in QCD [66].

Recent most precise direct measurements are from the ATLAS and CMS combination results with the relative uncertainties 0.41% and 0.28% (see Figure 2.10 (top)), respectively.

The top-quark mass obtained from the combination of the measurements from the CDF [67] and D0 [52] experiments, operating at the Tevatron, with the relative precision of 0.34% [68] is:

$$m_t = 174.34 \pm 0.37(\text{stat}) \pm 0.52(\text{syst})\ \text{GeV} \equiv 174.34 \pm 0.64\ \text{GeV}$$

The world average value, which includes the measurements of the ATLAS, CMS, CDF and D0 Collaborations available in March 2014 is [53]:

$$m_t = 173.34 \pm 0.27(\text{stat}) \pm 0.71(\text{syst})\ \text{GeV} \equiv 173.34 \pm 0.76\ \text{GeV}$$

The world average value is in a good agreement with the results obtained at the LHC as can be seen in Figure 2.10 (top). A summary of the input measurements from Tevatron and its combination is shown in Figure 2.10 (bottom).

The latest indirect measurements from ATLAS, which used 7 TeV and 8 TeV data sets, were derived for each centre-of-mass energy [21] and were the following:

$$m_{\text{t}}^{\text{pole}} = 171.4 \pm 2.6\ \text{GeV}(\sqrt{s} = 7\ \text{TeV}) \text{ and}$$
$$m_{\text{t}}^{\text{pole}} = 174.1 \pm 2.6\ \text{GeV}(\sqrt{s} = 8\ \text{TeV})$$

and from the combined $\sqrt{s} = 7$ TeV and $\sqrt{s} = 8$ TeV data sets with slightly smaller uncertainty:

$$m_{\text{t}}^{\text{pole}} = 172.9^{+2.5}_{-2.6}\ \text{GeV}. \tag{2.33}$$

The extracted values are consistent with the average of the top-quark mass measurements obtained

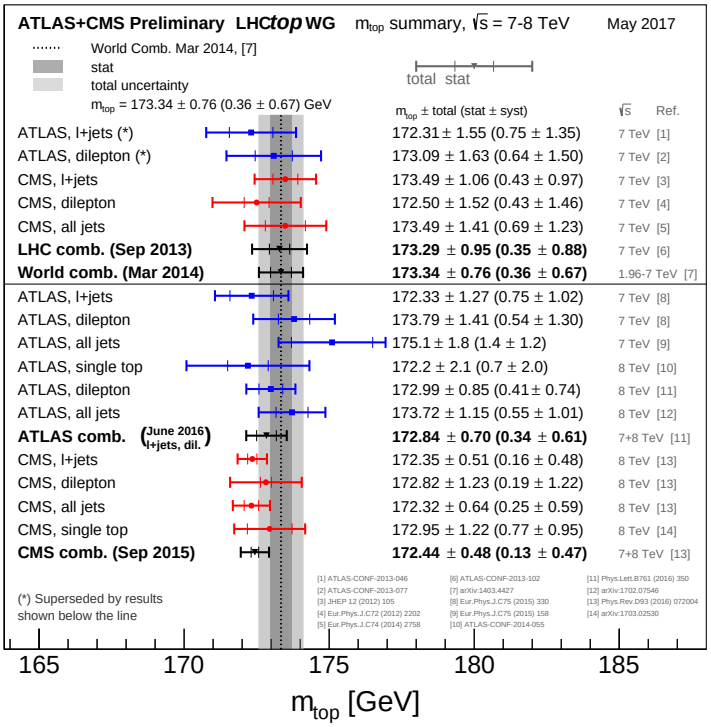

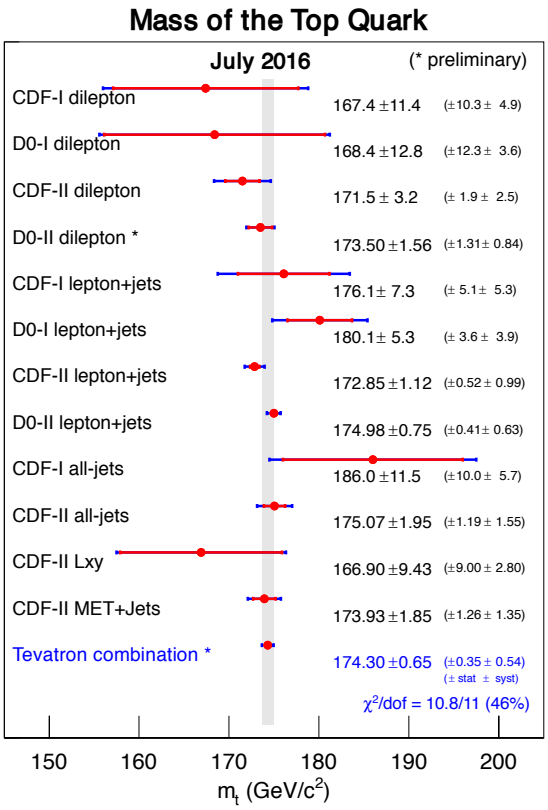

Figure 2.10: Top: Summary of the ATLAS and CMS direct top-quark mass measurements. The results are compared with the LHC and Tevatron+LHC top-quark mass combinations. For each measurement, the statistical and systematics uncertainties are reported separately. Taken from [55]. Bottom: Summary of the input measurements and resulting Tevatron average mass of the top quark. The red lines correspond to the statistical uncertainty while the blue lines show the total uncertainty. Taken from [69].

from the direct reconstruction and are shown in Figure 2.10. As can be seen, the values of the top-quark mass extracted from the cross sections suffer from the size of uncertainty, which is mostly due to the limited accuracy of predictions.

2.5 Theoretical predictions

2.5.1 Z-boson predictions

The fiducial and total production cross sections for Z bosons decaying into lepton pairs ($Z \to e^+e^-$ and $Z \to \mu^+\mu^-$) were calculated using a parton-level Monte Carlo program, DYNNLO 1.5 [11, 12], and a fast theory calculation tool, DYTURBO. The DYNNLO 1.5 program allows the computation of the cross sections for vector-boson production in pp and $p\bar{p}$ collisions at next-to-next-to-leading order (NNLO) in the strong coupling α_s. Electroweak (EW) corrections were calculated with FEWZ 3.1 (Fully Exclusive W and Z production) [13, 48–50] at next-to-leading order (NLO) in the G_μ EW scheme [70], where the input parameters are G_F, M_Z, M_W. The following set of Standard Model input parameters were taken from PDG14 [71] and are given in Table 2.4. The following components of the EW corrections were taken into an account: virtual QED and weak corrections, intial-state radiation (ISR), and interference between ISR and final-state radiation FSR [72].

Fermi coupling constant, G_F	1.1663787×10^{-5} GeV^{-2}
Z-boson mass, M_Z	91.1876 GeV
Decay width, Γ_Z	2.4949 GeV
W-boson mass, M_Z	80.385 GeV
Decay width, Γ_W	2.0906 GeV
Matrix elements of CKM	
$\lvert V_{ud}\rvert$	0.97427
$\lvert V_{cd}\rvert$	0.2252
$\lvert V_{us}\rvert$	0.2253
$\lvert V_{cs}\rvert$	0.97344
$\lvert V_{ub}\rvert$	0.00351
$\lvert V_{cb}\rvert$	0.0412

Table 2.4: Set of the Standard Model input parameters used in the theoretical calculations of the Drell–Yan production cross sections.

The predictions were calculated using the following PDF sets: CT14 [37], NNPDF3.0 [38], MMHT14 [39], ATLAS-epWZ12 [40], HERAPDF2.0 [41], and ABM12 [42]. The dynamic scale m_{ll} was used as the nominal renormalization, μ_R, and factorization, μ_F, scale. The CT14 PDF set was chosen as the baseline set.

The fiducial cross sections were calculated for all three centre-of-mass energy $\sqrt{s}$ = 13 TeV, 8 TeV and 7 TeV in the following common fiducial phase space:

- lepton transverse momentum: $p_{\mathrm{T}}^{l} > 25$ GeV
- lepton pseudorapidity: $|\eta^{l}| < 2.5$
- dilepton invariant mass: $66 < m_{ll} < 116$ GeV
- Born level leptons: leptons from the Z-boson decay before any photon radiation

$\sqrt{s}$ [TeV]	**7**	**8**	**13**
Fiducial [pb]	-1.37 ± 0.13	-1.74 ± 0.15	-2.45 ± 0.24
Total [pb]	-2.06 ± 0.08	-2.52 ± 0.09	-4.76 ± 0.18

Table 2.5: The size of the NLO EW corrections δ_{EW}^{Z} (in pb) at 7 TeV, 8 TeV and 13 TeV except QED FSR and real weak emissions, given for the 13 TeV fiducial phase space and for the total phase space.

	CT14	NNPDF3.0	MMHT14	ATLAS-epWZ12	HERAPDF2.0	ABM12
α_S	0.1180	0.1180	0.1180	0.1176	0.1180	0.1132

Table 2.6: The central value of strong coupling constant, α_S, for different PDF sets.

and are given for the baseline set in Table 2.7. The total cross sections were calculated in the dilepton invariant mass window of Z boson for all three centre-of-mass energies and are given in Table 2.7.

The electroweak corrections, which were applied to the central value of the cross sections are shown in Table 2.5.

The systematics uncertainties were considered from the following sources:

- PDF: these uncertainties are evaluated from the variations of the NNLO PDFs. The uncertainties are calculated using separate sums of negative and positive eigenvector variations. The PDF uncertainty of CT14 was rescaled from 90% CL to 68% CL.

- Scales: these uncertainties are defined by the envelope of the variations in which the scales are changed by factors of two subject to the constraint $0.5 \leq \mu_R/\mu_F \leq 2$.

- α_S: the uncertainty due to α_S is estimated following the prescription given with the CT14nnlo PDF [37], varying α_S by one sigma, ± 0.001, to correspond to 68% CL. It is implemented by using the PDFs: CT14nnlo_as_0117 and CT14nnlo_as_0119. The central α_S values for different PDF sets are given in Table 2.6.

- Intrinsic theory uncertainties: these uncertainties are related to the limitations in the NNLO calculations and are estimated from the comparison between different programs DYNNLO 1.5 and Fewz 3.1. For the total cross section predictions this difference was found to be less than 0.2% and hence negligible. For the fiducial cross-section prediction the difference was estimated to be 0.7%, due to involving leptons with symmetric p_{T} requirements. The study was performed by calculating the fiducial cross sections at fixed p_{T} of one lepton at 25 GeV and varied p_{T} of the second lepton. When the p_{T} requirements were asymmetric, the difference between DYNNLO and Fewz was at the level of 0.1%. When the p_{T} requirements were symmetric, Fewz predicted higher cross sections by 0.6%.

In general, prediction uncertainties are dominated by the limited knowledge of the proton PDFs. The estimated uncertainties for the CT14 PDF set together with PDF uncertainties for different PDF sets, NNPDF3.0, MMHT14, ATLAS-epWZ12, HERAPDF2.0, and ABM12, are presented in Table A.1 of Appendix A.1.

	σ^{fid}			σ^{tot}		
$\sqrt{s}$ [TeV]	**7**	**8**	**13**	**7**	**8**	**13**
Central value, [pb]	432	486	744	954	1 110	1 886
Uncertainties [%]						
PDF	$^{+2.5}_{-3.0}$	$^{+2.5}_{-3.1}$	$^{+2.7}_{-3.4}$	$^{+2.2}_{-2.5}$	$^{+2.2}_{-2.5}$	$^{+2.4}_{-2.7}$
α_s	$^{+1.0}_{-0.7}$	$^{+1.0}_{-0.8}$	$^{+0.9}_{-1.1}$	$^{+0.8}_{-0.9}$	$^{+0.8}_{-0.8}$	$^{+1.0}_{-0.9}$
Scale	$^{+0.7}_{-0.3}$	$^{+0.5}_{-0.5}$	$^{+0.5}_{-0.8}$	$^{+0.5}_{-0.9}$	$^{+0.6}_{-0.9}$	$^{+0.7}_{-1.1}$
Intrinsic	$^{+0.7}_{-0.7}$	$^{+0.7}_{-0.7}$	$^{+0.7}_{-0.7}$	–	–	–
Total	$^{+2.9}_{-3.2}$	$^{+2.8}_{-3.3}$	$^{+3.0}_{-3.7}$	$^{+2.4}_{-2.8}$	$^{+2.4}_{-2.8}$	$^{+2.7}_{-3.0}$

Table 2.7: Theoretical predictions for total and fiducial Z-boson cross sections at $\sqrt{s}$ = 7 TeV, 8 TeV and 13 TeV using CT14 PDF. The systematics uncertainties are given in %. The statistical uncertainties are small and are not given in the table.

2.5.2 $t\bar{t}$ predictions

Theoretical predictions of the $t\bar{t}$ cross sections were calculated at next-to-next-to leading order (NNLO) in QCD including resummation of next-to-next-to-leading logarithmic (NNLL) soft gluon terms with Top++v2.0 program [73]. The calculations were verified with the Hathor v1.5 [74] (The HAdronic Top and Heavy quarks crOss section calculatoR) program, which compute the exact NNLO $t\bar{t}$ cross sections. The cross section for top-quark pair production is measured with high precision provided by the perturbative QCD corrections at next-to-leading order (NLO). Initially radiative NLO corrections were calculated some time ago taking into account unpolarized top-quark production [75, 76] and later including information about top-quark spin [77]. The analytical results were presented in [78]. Large logarithmic corrections due to soft gluon emission were investigated and resummed at the NLL accuracy [79] and recently improved to include also the NNLL corrections [80, 81].

Predictions of fiducial $t\bar{t}$ cross sections were not available at the NNLO accuracy at the moment of analysis.

The systematic theoretical uncertainties are performed in a similar way as for the Z-boson calculations in the following way:

- PDF: these uncertainties are evaluated from the variations of the NNLO PDFs by using separate sums of negative and positive eigenvector variations.
- Scales: the renormalization scale, μ_R, and factorization scale, μ_F, were set to $\mu_R = \mu_F = m_t$ for the central value. The uncertainties were evaluated by the envelope of variations for the values of μ_R and μ_F by a factor of two subject to the constraint: $0.5 \leq \mu_R/\mu_F \leq 2$.
- α_S: the uncertainty due to the α_S depends on the PDF set, but for the more modern PDFs generally implies varying of the central value of α_S by ± 0.001.
- Top-quark mass, m_t: the calculated cross sections have a dependence on the value of m_t. Therefore, the variation of the baseline value of 172.5 GeV by ± 1 GeV was assigned as systematic uncertainty.

The predictions determined with the CT14 PDF set and their corresponding uncertainties are given in Table 2.8. The determined predictions for all other PDFs, mentioned above, are presented in Reference [82].

	σ^{tot}		
$\sqrt{s}$ [TeV]	**7**	**8**	**13**
Central value, [pb]	182	259	842
Uncertainties [%]			
PDF	$^{+4.4}_{-3.7}$	$^{+3.9}_{-3.4}$	$^{+2.6}_{-2.7}$
α_s	$^{+2.2}_{-2.1}$	$^{+2.1}_{-2.1}$	$^{+1.9}_{-1.8}$
Scale	$^{+2.6}_{-3.5}$	$^{+2.6}_{-3.5}$	$^{+2.4}_{-3.6}$
m_t	$^{+3.1}_{-3.0}$	$^{+3.0}_{-2.9}$	$^{+2.8}_{-2.7}$
Total	$^{+6.0}_{-6.0}$	$^{+6.0}_{-6.0}$	$^{+5.0}_{-6.0}$

Table 2.8: Theoretical predictions for total $t\bar{t}$ cross sections at $\sqrt{s}$ = 7 TeV, 8 TeV and 13 TeV using CT14 PDF. The systematics uncertainties are given in %. The statistical uncertainties are small and are not given in the table.

As in case of Z-boson predictions, the dominated systematic uncertainty is due to choice of PDF and also due to the QCD scale.

2.5.3 Ratio predictions

The fiducial and total Z-boson and total $t\bar{t}$ cross sections were used to build single and double cross-section ratios (see Section 6):

- Single ratio at the same $\sqrt{s}$: $R^{\text{tot/fid(tot)}}_{t\bar{t}/Z}$ (i TeV) = $\sigma^{\text{tot}}_{t\bar{t}(i)}/\sigma^{\text{fid(tot)}}_{Z(i)}$
- Double ratio at different $\sqrt{s}$: $R^{\text{tot/fid(tot)}}_{t\bar{t}/Z}(i,j) = \left[\sigma^{\text{tot}}_{t\bar{t}(i)}/\sigma^{\text{fid}}_{Z(i)}\right]/\left[\sigma^{\text{tot}}_{t\bar{t}(j)}/\sigma^{\text{fid}}_{Z(j)}\right]$,

where i, j = 7 TeV, 8 TeV and 13 TeV.

The systematic uncertainties in ratios were treated as follows:

- PDF: this uncertainty was considered as correlated, eigenvector by eigenvector, between predictions
- Scale: this uncertainty was considered as uncorrelated between processes but correlated, variation by variation, at the different $\sqrt{s}$ values for a given process.
- α_S: this uncertainty was considered as correlated between predictions

Predicted single and double ratios are given in Table 2.9.

	$R^{\text{tot/fid}}_{t\bar{t}/Z}(i\text{ TeV})$			$R^{\text{tot/tot}}_{t\bar{t}/Z}(i\text{ TeV})$	$R^{\text{tot/fid}}_{t\bar{t}/Z}(i/j)$		
i or i/j	13	8	7	13	13/7	13/8	8/7
Central value	1.132	0.533	0.421	0.446	2.691	2.124	1.267
Uncertainties [%]							
PDF	$^{+6}_{-5}$	$^{+7}_{-5}$	$^{+7}_{-5}$	$^{+5}_{-5}$	$^{+1.5}_{-2.0}$	$^{+1.1}_{-1.6}$	$^{+0.4}_{-0.5}$
α_S	$^{+0.9}_{-0.8}$	$^{+1.1}_{-1.3}$	$^{+1.1}_{-1.5}$	$^{+0.9}_{-0.9}$	$^{-0.22}_{+0.70}$	$^{-0.22}_{+0.50}$	$^{-0.00}_{+0.20}$
Scale	$^{+2.6}_{-3.6}$	$^{+2.6}_{-3.5}$	$^{+2.7}_{-3.6}$	$^{+2.7}_{-3.7}$	$^{+0.62}_{-0.27}$	$^{+0.32}_{-0.20}$	$^{+0.31}_{-0.07}$
Intrinsic Z	$^{+0.7}_{-0.7}$	$^{+0.7}_{-0.7}$	$^{+0.7}_{-0.7}$	–	$^{+0.00}_{-0.00}$	$^{+0.00}_{-0.00}$	$^{+0.00}_{-0.00}$
m_t	$^{+2.8}_{-2.7}$	$^{+3.0}_{-2.9}$	$^{+3.1}_{-3.0}$	$^{+2.8}_{-2.7}$	$^{+0.29}_{-0.29}$	$^{+0.22}_{-0.22}$	$^{+0.07}_{-0.07}$
Total	$^{+7}_{-7}$	$^{+8}_{-7}$	$^{+8}_{-7}$	$^{+7}_{-7}$	$^{+1.8}_{-2.1}$	$^{+1.3}_{-1.6}$	$^{+0.5}_{-0.5}$

Table 2.9: Predictions of the cross-section ratios $R^{\text{tot/fid}}_{t\bar{t}/Z}$, $R^{\text{tot/tot}}_{t\bar{t}/Z}(i\text{ TeV})$ and $R^{\text{tot/fid}}_{t\bar{t}/Z}(i/j)$ at the different $\sqrt{s}$ values where $i, j = 13, 8, 7$ using the CT14 PDF. The uncertainties, given in %, correspond to variations of CT14 eigenvector set at 68% CL, α_S, scale, intrinsic Z-boson prediction, and top-quark mass. The statistical uncertainties in the predictions are small and are not given in the table.

CHAPTER 3

ATLAS experiment at the LHC

The Large Hadron Collider (LHC) [83] is a particle accelerator located at the European Center for Nuclear Research (CERN) between Geneva airport, in Switzerland, and the Jura mountain range, in France. It is designed to collide two types of beam, proton and heavy-ion beams, at the highest energies and luminosities in order to explore building blocks of matter.

The measurements performed in this dissertation used the data from proton collisions recorded by the ATLAS detector. It is one of the two multi-purpose particle detectors located around one of the collision points at the LHC accelerator complex, designed to test the Standard Model predictions and search for physics beyond the Standard Model.

A short overview of LHC performance is described in Section 3.1, followed by the ATLAS detector description, including its main relevant constituent components, in Section 3.2. Section 3.3 provides information about luminosity measurement. A summary of future ATLAS detector upgrades is provided in Section 3.5.

3.1 The LHC accelerator

The LHC is built in the tunnel of the former linear electron-positron (LEP) accelerator and began its operation in late 2009. The LHC machine accelerates and collides beams of particles in opposite directions though two beam pipes in the underground tunnel, which is 26.7 km in a circumference and situated from 100 m to 75 m below the surface. The beam collisions occur at four different locations along the accelerator ring, called interaction points (IP), where the LHC experiments have massive particle detectors: A Toroidal LHC ApparatuS (ATLAS), A Large Ion Collider Experiment (ALICE), a Compact Muon Solenoid (CMS) and a Large Hadron Collider beauty (LHCb) (see Figure 3.1). ATLAS and CMS are multi-purpose high-luminosity experiments, which are located on opposite sides of the ring (interaction points 1 and 5), and are designed to cover a broad physics program. Two other experiments, the ALICE and LHCb, are designed to work with low luminosities. The purpose of the ALICE experiment is to study Pb–Pb collisions and the quark–gluon plasma. The LHCb experiment is focused on interactions that involve b-physics.

For proton–proton collisions, protons are extracted from a tank of hydrogen gas, where they are stripped of their electrons using a strong electric field. They need to be pre-accelerated before entering the main LHC ring and are therefore transferred to the accelerator chain. The accelerator chain starts with a linear accelerator, Linac2, where the protons are pre-accelerated to energy of 50 MeV. Next, they are injected to the PS Booster (PSB) and accelerated to energy of 1.4 GeV. Following the Proton Synchrotron (PS), the protons are accelerated to the energy of 25 GeV. Finally, they are sent to the Super

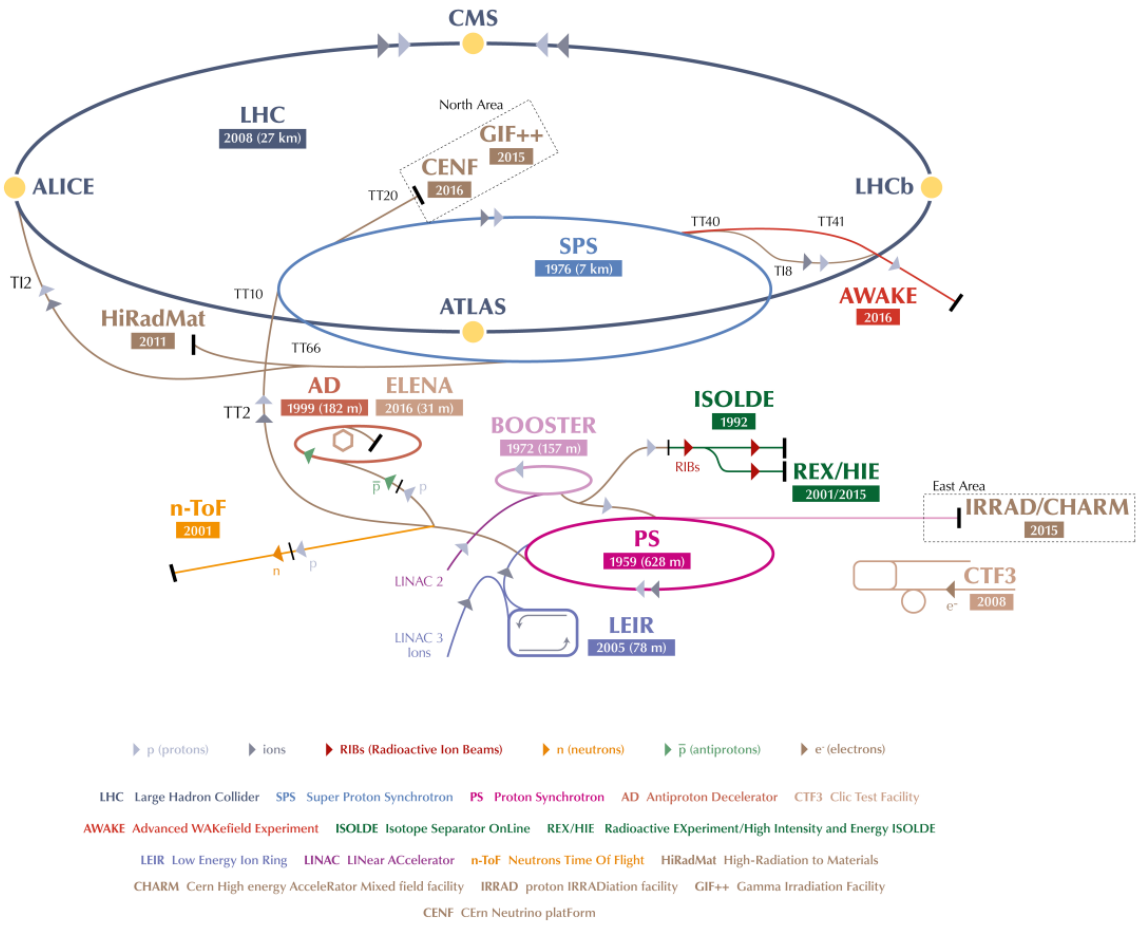

Figure 3.1: Schematic of the CERN accelerator complex for the LHC proton–proton collisions along with the four main experiments and its preaccelerators. Taken from [84].

Proton Synchrotron (SPS) and filled into the LHC (in clockwise and counter clockwise directions) with an energy of 450 GeV per proton. In general, the preparation phase lasts 4–5 hours and is followed by 15–20 hours of collisions. The protons are circulated in bunches, each containing around 100 billion protons, with a spacing between them of 25 ns (corresponds to 7.5 m). During period of data-taking in 2015 the number of bunches (intensity of the beams) was up to 2244. The LHC set a new record with the maximum possible number of bunches 2556 on 28 June 2017.

The proton bunches are directed and focused around the circle using magnets. The LHC uses superconducting magnets made of niobium and titanium. The main dipole magnets, which produce a high magnetic field of 8.33 T in order to bend the trajectory of the protons are followed by quadrupole magnets, which are used to focus the beams. There are 1232 dipoles (each is nearly 15 m long and weighs around 35 t) and 392 quadrupole (each 3 m long) magnets. All magnets are cooled down with liquid nitrogen and helium to temperature of 1.9 K, to maintain their superconductivity.

The LHC delivered over $\mathcal{L} \simeq 5\,\text{fb}^{-1}$ of data with luminosities peaking at $\mathcal{L} \simeq 3 \times 10^{33}\,\text{cm}^{-1}\text{s}^{-1}$ at a centre-of-mass energy of 7 TeV in 2011. In 2012, the LHC operated at a centre-of-mass energy of 8 TeV and delivered $23\,\text{fb}^{-1}$ to the ATLAS. After a successful data-taking period known as ‘Run 1’ during

2009–2012, the LHC started proton–proton collisions at a new record centre-of-mass energy of 13 TeV in spring 2015, initiating new data-taking period, called 'Run 2'. During 2015, the ATLAS recorded an integrated luminosity of 3.2 fb^{-1}, and during 2016 around 33 fb^{-1}.

Additionally, heavy ion collisions usually occur at the end of each year for one month. The beams of fully stripped lead ions ($^{208}Pb^{82+}$) were collided with a centre-of-mass energy per nucleon pair ($\sqrt{s_{NN}}$) of 2.76 TeV in Run 1 with a collected integrated luminosity of 0.1 nb^{-1}, and with a centre-of-mass energy of 5.02 TeV in 2015, with the corresponding integrated luminosity of 0.24 nb^{-1}.

3.2 ATLAS detector

The ATLAS detector is the largest particle detector at the LHC and consists of several layers of different sub-detector systems, which identify particles and measure their momentum and energy. It has a cylindrical shape and is 44 m in length, 25 m in diameter and weighs 7000 t [10]. Its main components are an inner detector tracking system outside the beam pipe, an electromagnetic and hadronic calorimeters and the muon spectrometer system as the outermost shell. A schematic view of the ATLAS detector is shown in Figure 3.2.

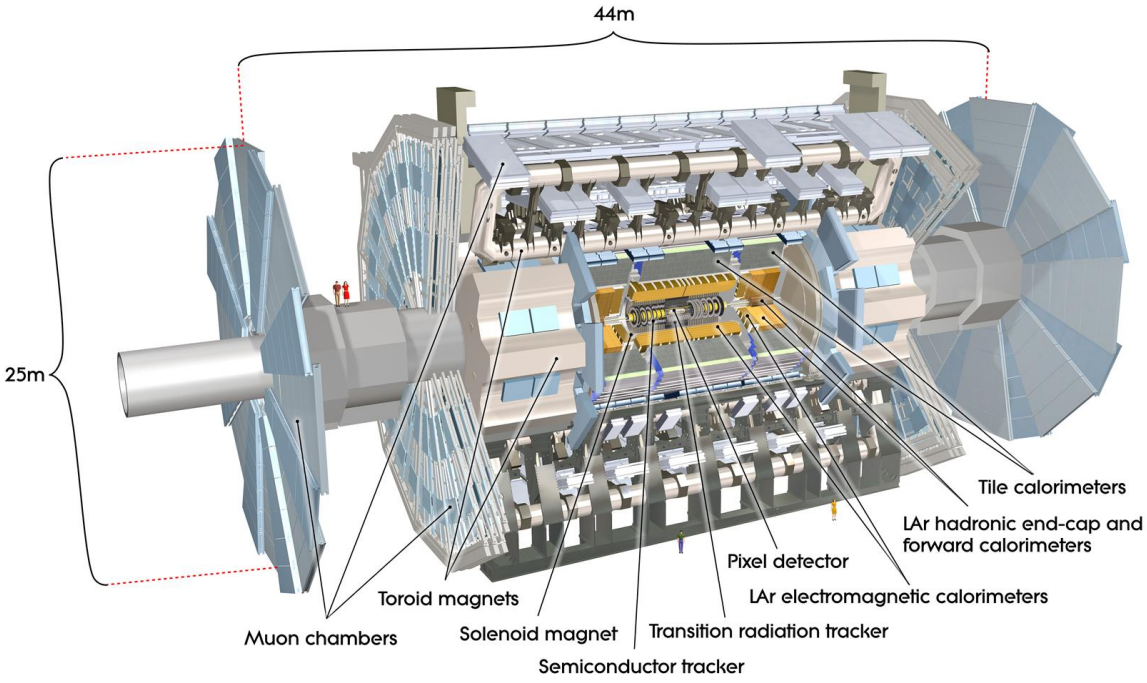

Figure 3.2: Scheme of the ATLAS detector. Taken from [85].

The inner detector is designed to measure the charge and transverse momentum of charged particles. The calorimeter system measures the energy deposited by electrons, photons and hadrons, and identifies them. The goal of the muon system is to determine the muons by measuring their charge and momentum. An illustration of particle passage through the ATLAS detector is shown in Figure 3.3. The ATLAS magnet system consists of four superconducting magnets: a thin solenoid magnet supplying magnetic field of 2 T and long barrel and two end-cap toroid magnets providing magnetic field of 0.5 T and 1 T

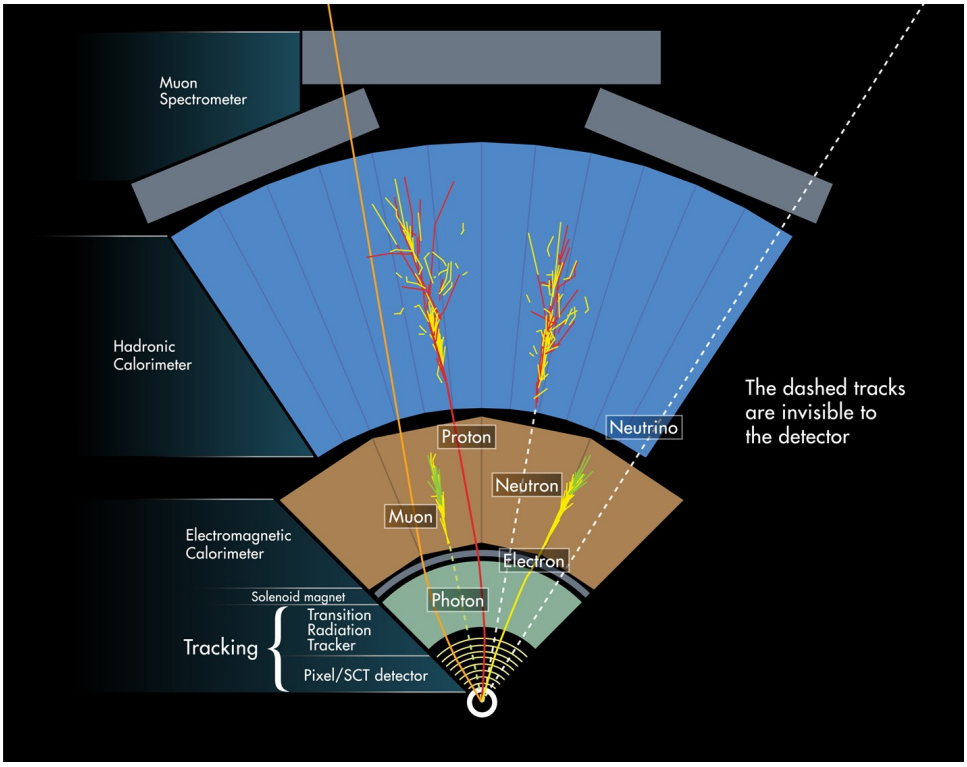

Figure 3.3: An illustration of ATLAS detector in $x - y$ plane and the passage of different particle types traversing the various layers of the detector. Toroidal magnets located at higher radii are not visible in this picture. Taken from [85].

respectively. The magnetic field bends the tracks of charged particles and provides an opportunity to measure the momentum of particle by the curvature of its track.

In order to record the collisions, the event rate has to be reduced from 40 MHz to 1 kHz. A three-level trigger system achieved this in Run 1, and a two-level trigger system in Run 2.

3.2.1 Coordinate system and kinematics

The ATLAS detector uses a right handed coordinate system with its origin at the interaction point. The z-axis is defined along the beam direction and the $x - y$ plane is perpendicular to beam. The $x - y$ plane is called the transverse plane (and uses cylindrical coordinates (r, ϕ)). The x-direction points toward the center of the LHC ring, and y-direction points upward from the origin. The radial axis r is a distance from beam line. The positive z defines the A-side of the detector and negative z defines the C-side. The azimuthal angle ϕ is measured around the beam axis in the $x - y$ plane, and the polar angle θ is the angle from the positive z-axis.

One of the significant quantities in the high energy physics is rapidity of a particle, y, which is defined as:

$$y = \frac{1}{2} \ln \left(\frac{E + p_z}{E - p_z} \right), \tag{3.1}$$

where E denotes the energy of the particle and p_z is the longitudinal momentum. Under the approximation

that the particle is highly relativistic ($pc >> mc^2$), Equation 3.1 can be rewritten:

$$\eta = -\ln\left(\tan\left(\frac{\theta}{2}\right)\right),$$

where η is called pseudorapidity. This quantity does not depend on the energy of particle, only on the polar angle of the particle's trajectory.

Besides, the transverse momentum p_T of the particle, measured in the $x-y$ plane, is defined as:

$$p_T = \sqrt{p_x^2 + p_y^2}.$$

The pseudorapidity is used for angular separation between particles in $\eta - \phi$ space as ΔR and is defined as follows:

$$\Delta R = \sqrt{\Delta\eta^2 + \Delta\phi^2}.$$

3.2.2 Tracking system

The ATLAS tracking system, the Inner Detector (ID) [86], is the innermost part of the ATLAS detector and is located closest to the interaction point. It is designed to provide a measurement of track trajectories and vertices as well as their momentum and charge with high resolution. Charged particle tracks with transverse momentum above 0.5 GeV, which is measured from the curvature of tracks, are reconstructed in the ID within the pseudorapidity range $|\eta| = 2.5$. The charge of the particle tracks is measured from the curvature of their paths in opposite directions (positive and negative particle curves in the same magnetic field). The reconstructed tracks are extrapolated to common points of origin, identifying interaction vertices.

The ID consists of three different sub-detectors placed around the beam which are immersed in a magnetic field: the Pixel Detector, the Semiconductor Tracker (SCT) and the Transition Radiation Tracker (TRT). A geometrical layout of the ID is shown in Figure 3.5. They are fine-granularity detectors, which are required to handle with the large track density around the vertex region in order to provide precise vertex and momentum resolution. Each track is expected to be reconstructed with hits by charged ionizing particles: 3 hits in the Pixel Detector, 8 hits in the SCT and 36 hits in the TRT on average.

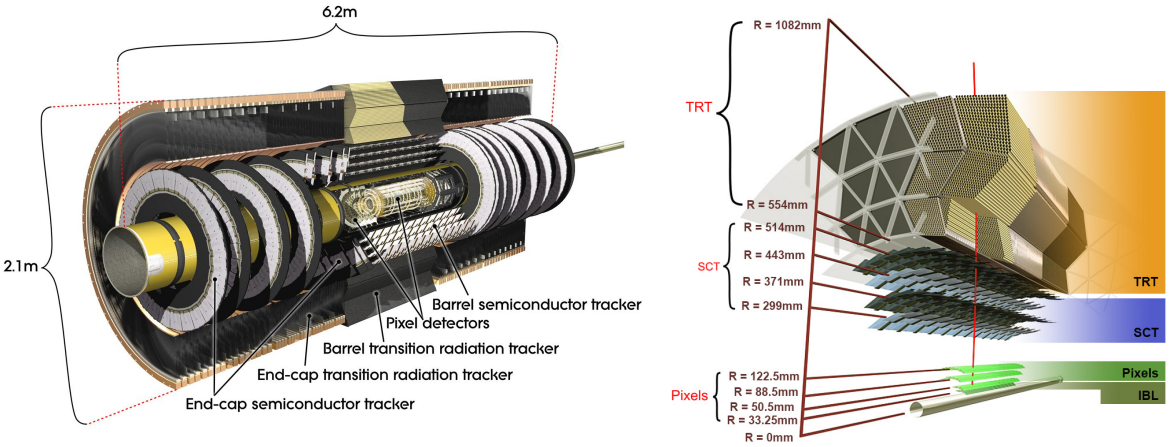

Figure 3.4: Left: a schematics view of the ATLAS inner detector. Right: a cross-section of the ATLAS inner detector showing the layers and radii. Taken from [87].

The tracks can be parametrized by five parameters, which are estimated from the reconstruction:

- d_0: a transverse impact parameter, which defines a distance of closest approach of the track to the primary vertex point in $r - \phi$ plane
- z_0: a longitudinal impact parameter, the defines a value of z of the point on the track that determines d_0
- ϕ: an azimuthal angle at the point of closest approach, the angle with the x-axis in the $x - y$ plane
- θ: a polar angle of the track, the angle with the z-axis in the $r - z$ plane
- q / p: a charge signed curvature ($q \neq 0$)

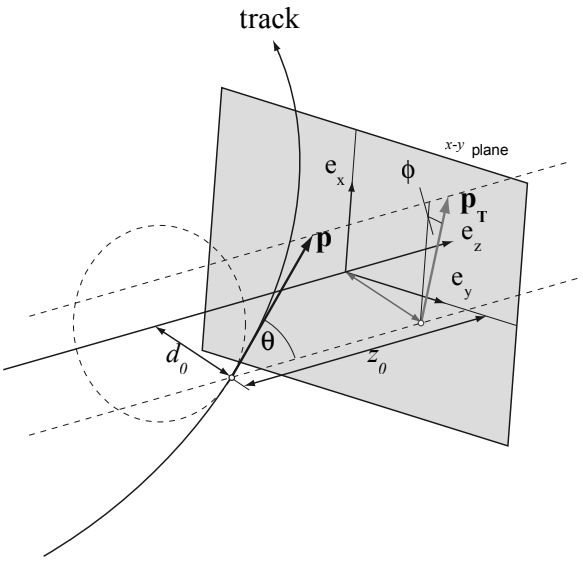

Figure 3.5: An illustration of the track parametrization. Taken from [88].

3.2.2.1 Pixel detector

The ATLAS pixel detector is a silicon-based detector that consists of three cylindrical layers in the central region (barrel) and three disks on each side. The barrel layers are placed at radii of 51 mm, 89 mm and 123 mm and the discs stand ±495 mm, ±580 mm and ±650 mm from the collision point orthogonal to the z-axis.

A fourth Insertable B-layer (IBL) [89], was installed between a new beam pipe and the inner pixel layer in May 2014 during the shut-down to recover the loss of sensitivity due to radiation damage. This layer provides additional tracking information close to the interaction point. It is designed to improve the tracking robustness and precision of the reconstruction of tracks, primary and secondary vertices. The secondary vertices are essential for detection of short-lived particles, such as B hadrons and τ quarks.

The minimal size of pixels is $50 \times 400\ \mu\text{m}^2$ in $R - \phi \times z$. Each pixel module consists of a 250 μm thick n^+-in-n silicon sensor. In total, there are 1744 identical pixel sensors, where each includes 16 readout chips, supplying the pixel detector with 80 millions readout channels and covering a total area of 1.7 m^2. The precision of the pixel detector is 14 μm in the in-plane transverse direction ($r - \phi$) and 115 μm in the in-plane longitudinal direction (z for barrel and R for end-cap).

3.2.2.2 Semiconductor Tracker

The SCT is the middle layer of the ID and consist of four barrel layers and nine end-cap discs per each side. The barrel layers are placed at various radii from 29 mm to 514 mm, while the end-cap discs are fixed on distance from 854 mm to 2720 mm.

The SCT is silicon strip detector and covers the region $|\eta| < 2.5$. It consists of 15912 p-in-n strip sensors which are mounted into 4088 two-sided modules. Each sensor is 285 ± 15 μm thick with 40 milliradian stereo angle between strips allowing to measure $r - \phi$ and z coordinates. The strips have a constant pitch of 80 μm.

The spatial resolution of the SCT is 17 μm in the in-plane transverse direction and 580 μm in the in-plane longitudinal direction. The SCT has around 6.3 million readout channels and the total covered area of silicon is 61 m^2.

3.2.2.3 Transition Radiation Tracker

The TRT is the outermost layer of the tracking system which covers the region $|\eta| < 2.0$. It comprises many layers of narrow straw tubes with a diameter of 4 mm and length of 1.44 m, each of them is filled with a gas mixture of Xe + CO_2 + O_2 in the proportions 70%, 27%, 3% and contains a 30 μm diameter gold-plated W-Re wire. The Xe is chosen to provide transition radiation absorption, and CO_2 + O_2 to increase electron drift velocities and good ageing resistance [90].

The barrel is composed of 50000 straws interleaved with fibres (73 layers), while in the end-cap are 250000 straws interleaved with foils (160 planes). The barrel is divided into three rings, each with 32 modules and the end-cap part consist of two sets of independent wheels.

When a charged particle travels through TRT, it ionizes the gas and the resulting free electrons move towards the wire. There they are amplified and read out. The TRT detector can provide additional information on the particle type. The space between the tubes is filled with a mesh of polypropylene foil. The separation between the light electrons and hadrons can be provided by measuring the transition radiation photons in xenon, which absorbs X-rays. Transition radiation is emitted when a highly relativistic particle (Lorentz factor $\gamma = E \,/\, m > 10^3$) traverses the boundary between materials with different dielectric properties. The lighter particles radiate significantly more energy at certain energy. The TRT has lower resolution than the silicon detectors. The accuracy of the determination of the transverse momentum is 130 μm in the $r - \phi$ plane. The total number of readout channels in the TRT is around 350000 and the total covered area is around 12 m^3.

3.2.3 Calorimeter system

The ATLAS calorimeter system surrounds the ID and is designed to stop both charged and neutral particles and measure their energy deposits. It is divided into electromagnetic and hadronic calorimeters which cover the pseudorapidity range up to 4.9 and is shown in Figure 3.6. The purpose of the electromagnetic part is to measure precisely the energy of electrons and photons and to identify them, while the hadronic part is for the identification and energy measurement of hadrons, jets and missing transverse energy.

A standard parameterization of the energy resolution of the calorimeter by adding up all contributions in quadrature yields to following equation:

$$\frac{\sigma}{E} = \frac{a}{\sqrt{E}} \oplus \frac{b}{E} \oplus c \tag{3.2}$$

where a is a stochastic variable that represents the statistical fluctuation of the measured signal (determined

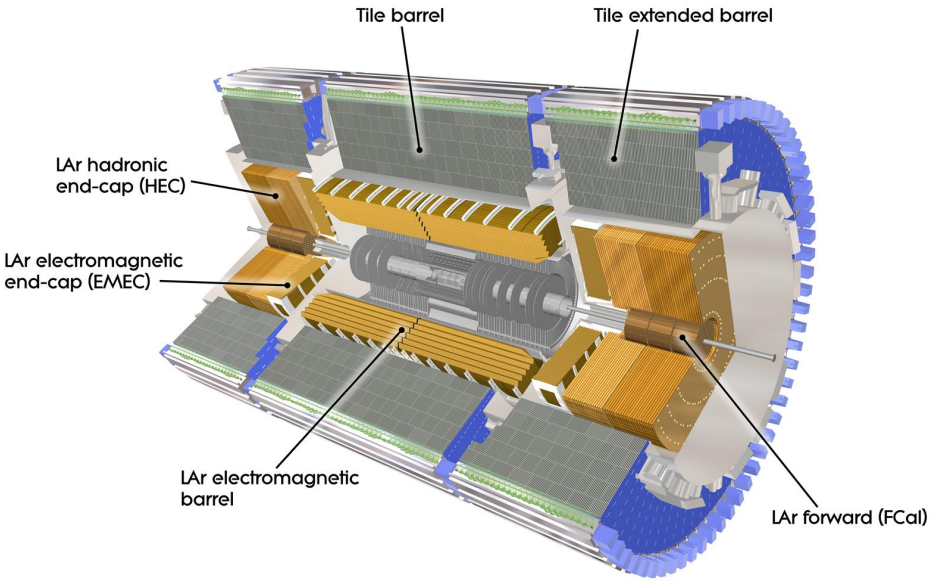

Figure 3.6: An illustration of the ATLAS calorimeter system. Taken from [91].

by material and geometry of the calorimeter), b is a noise variable, and c is a constant.

3.2.3.1 Electromagnetic calorimeter

The ATLAS electromagnetic (EM) calorimeter has an accordion shape, for both the barrel (EMB) and the end-cap (EMEC) parts, providing full coverage in ϕ (without cracks). It covers the pseudorapidity range $|\eta| < 1.475$ in EMB region and the range $1.375 < |\eta| < 3.2$ in the EMEC region. The EMB consists of two half-barrels housed in the same cryostat closed by two wheels of EMEC, one per side. The EM calorimeter uses lead (short radiation length $X_0 = 0.56$ cm) as an absorber medium for incident particles, and liquid argon (LAr) ($X_0 = 0.56$ cm) as an active medium to produce an output signal proportional to the input energy. The readout electrodes are placed between the absorber plates, to which two stainless-steel sheets are glued to provide stiffness. The electrodes are made of three conductive copper layers (to perform readout of signal) separated by insulating polyimide sheets (at high-voltage potential).

The EM calorimeter is segmented into three radial sections, with different $\eta - \phi$ granularities, to best combine the physics reach of the detector with requirements related to the design of the detector electronics [88]. The second layer collects the largest amount of the energy and has fine segmentation (0.025×0.025), while the last one only tail of energy and, therefore, is less segmented in η. The different layers in the barrel region are shown in Figure 3.8. For instance, the first layer is highly segmented in η (0.0031×0.0982) to distinguish single photon events from double photons which come from π^0 decays. In total, the LAr detector comprises more than 182000 cells.

When electrons or photons traverse the EM calorimeter, they lose their energy by bremsstrahlung and electron–positron pair production. They then produce further electrons and positrons creating a cascade of secondary particles (electromagnetic showers), which are stopped by ionization in the LAr medium. The signal from the electrodes is amplified on front-end boards, shaped and saved.

The energy resolution of the electromagnetic calorimeter is around $10\%/\sqrt{E}$ GeV in the stochastic

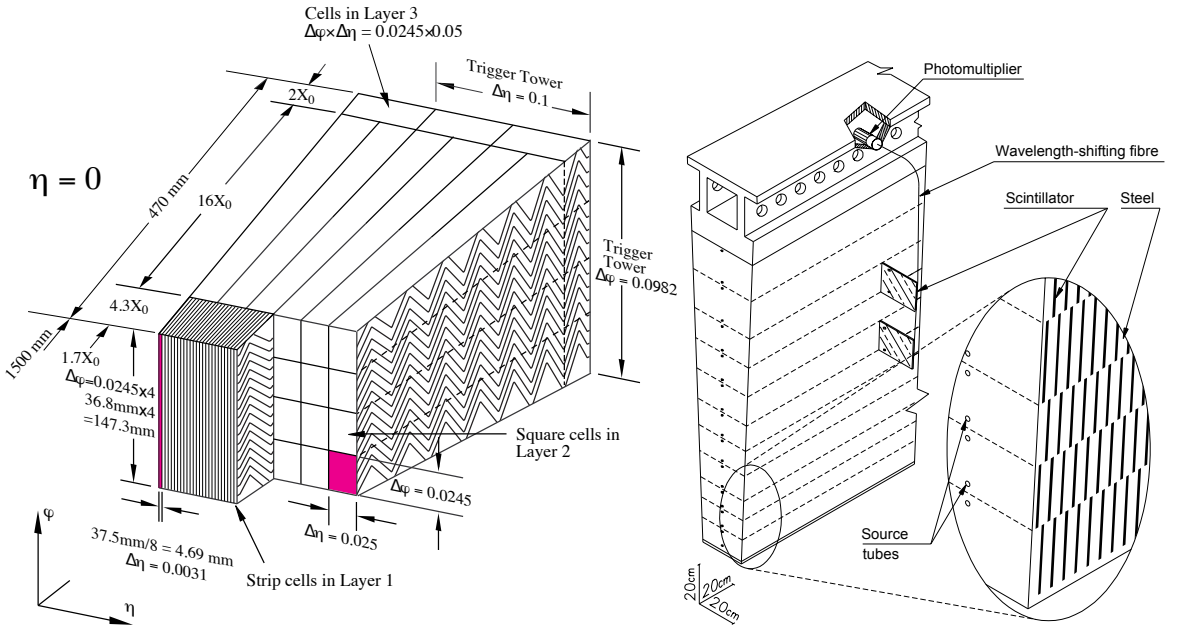

Figure 3.7: An illustration of barrel module for the electromagnetic calorimeter showing the different layers. The granularity in η and ϕ of the cells is also shown. Right: an illustration of the tile calorimeter module geometry showing the layout of the steel absorbing plates and scintillating tiles. Taken from [10].

term and 0.17% in the constant term. The stochastic term contributes mostly at low energy and depends on η, with larger η it is expected to worsen as the amount of material in front of the calorimeter increases. The noise term is about $350 \times \cosh \eta$ MeV in the barrel, and is dominated by the pile-up noise. At higher energies, the sampling term and the noise term become less important and the relative energy resolution tends asymptotically to the constant term [92].

3.2.3.2 Hadronic calorimeter

The hadronic calorimeters are the tile calorimeter (TileCal) in the central region ($|\eta| < 1.7$), the liquid-argon end-cap (HEC) ($1.5 \leq |\eta| < 3.2$) and the liquid-argon forward calorimeter (FCal) ($3.1 \leq |\eta| < 4.9$) in the forward region [86].

The TileCal is divided into three cylindrical sections: one central ($|\eta| < 0.8$) and two extended parts ($0.8 < |\eta| < 1.7$), which are composed of 64 modules. The TileCal is a sampling calorimeter which uses scintillating tiles as an active material and steel as an absorber. The scintillating tiles are placed in a plane perpendicular to the colliding beams and are read out by wavelength shifting fibres, which deliver the light to photo-multipliers (PMTs). A particle traversing through the steel plates induces a shower of secondary particles, which in turn produces photons in the scintillator tiles that are then converted into an electric signal and read out by photo-multipliers. The modular structure of the TileCal is shown in Figure 3.8.

The HEC and FCal use liquid argon as an active material and copper as an absorber, while FCal uses in some parts tungsten (W) instead of copper, for increased resistance to a radiation damage. The HEC consist of two wheels per end-cap (HEC front, HEC back) and each wheel is built from 32 modules. The HEC uses copper plates as a passive material interleaved with liquid-argon gaps.

The FCal consists of three modules in each end-cap: the first module (FCal1) is used for the electromagnetic measurements and is made of copper and the other two (FCal2, FCal3) are used for hadronic

measurements and are made of tungsten. The FCal modules consist of a metal matrix of radiation-hard empty copper tubes, acting as the cathode, with tungsten/copper rods, acting as the anode, placed inside. The rod is at a positive potential and the tube at ground. The gaps between them are filled with liquid argon. A helically-wound insulating fiber defines the size of the gaps and the position of the rod. The hadrons traverse the tubes and interact with nuclei in the absorber producing showers of hadrons (with energies lower than the primary). An ionization of the liquid-argon stops them, and the resulting electrons drift to the rod inducing the electrical signal. The granularity of the FCal in $\Delta\eta \times \Delta\phi$ is 0.2×0.2, while for the HEC the granularity is 0.1×0.1 for $1.5 < |\eta| < 2.5$ and 0.2×0.2 for $2.5 < |\eta| < 3.2$. The relative energy

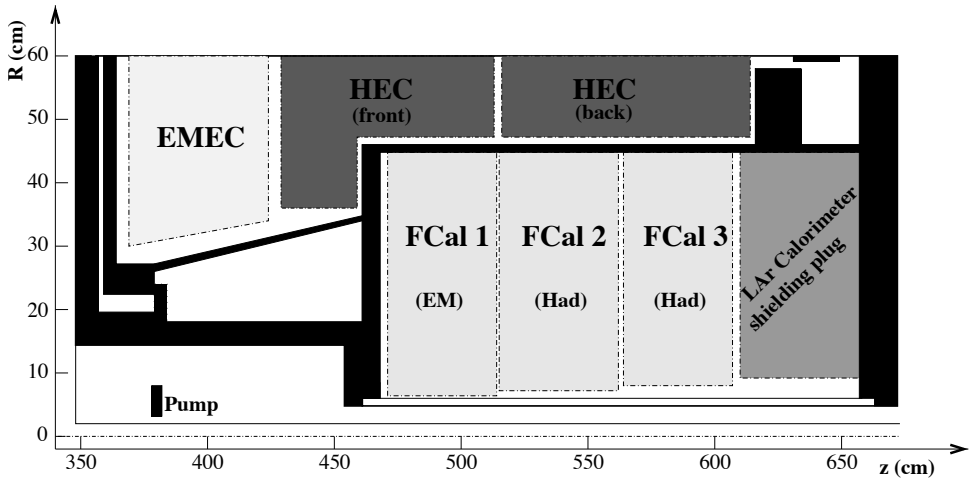

Figure 3.8: An illustration of the FCal modules located in the end-cap cryostat. Taken from [10].

resolution of the TileCal and HEC is $50\%/\sqrt{E}$ GeV for the stochastic term and 3% for the constant term, while for the FCal, it is $100\%/\sqrt{E}$ GeV and 10%, respectively.

3.2.4 Muon system

Muons deposit only a small amount of their energy in the calorimeter system and must be identified by the muon spectrometer (MS). The MS is the outermost sub-detector of the ATLAS and is designed to detect muons and to measure their momentum, relying on the magnetic deflection of the muon tracks. The MS operates in a toroidal magnetic field created by eight coils of superconducting barrel toroid magnet in the pseudorapidity range $|\eta| < 1.4$ and two smaller end-cap toroid magnets in pseudorapidity range $1.6 < |\eta| < 2.7$. The strength of the generated field ranges between 0.5 T and 1 T. The magnetic deflection is provided by a combination of the barrel and end-cap fields in the transition region ($1.4 < |\eta| < 1.6$) with reduced bending power. The design goal of the MS is to measure the momentum of 1 TeV muons with an accuracy of 10%.

Three barrel layers are positioned at radii of 5 m, 7.5 m and 10 m from the beam-axis and the end-caps are placed at distances of $|z|$ = 7.4 m, 14 m and 21.5 m, providing the coverage ranges up to $|\eta| < 2.7$. In the center of the detector ($|\eta|$ =0), a large gap in the chamber coverage exists to allow for services to solenoid magnet, the calorimeter and inner detector. This can affect the efficiency of the reconstruction performance. The ATLAS MS consists of four muon chambers: Monitored Drift Tubes (MDTs) ($|\eta| < 2.7$) and Cathode Strip Chambers (CSCs) ($|\eta| > 2.0$) for precision tracking, and Resistive Plate Chambers (RPCs) ($|\eta| < 1.05$) and Thin Gap Chambers (TGCs) ($1.05 < |\eta| < 2.4$) for triggering in the barrel and end-cap, respectively. All of the MS subsystems are gas ionization drift chambers. The cross-sections of the overall layout of the muon system of the ATLAS is presented is Figure 3.9.

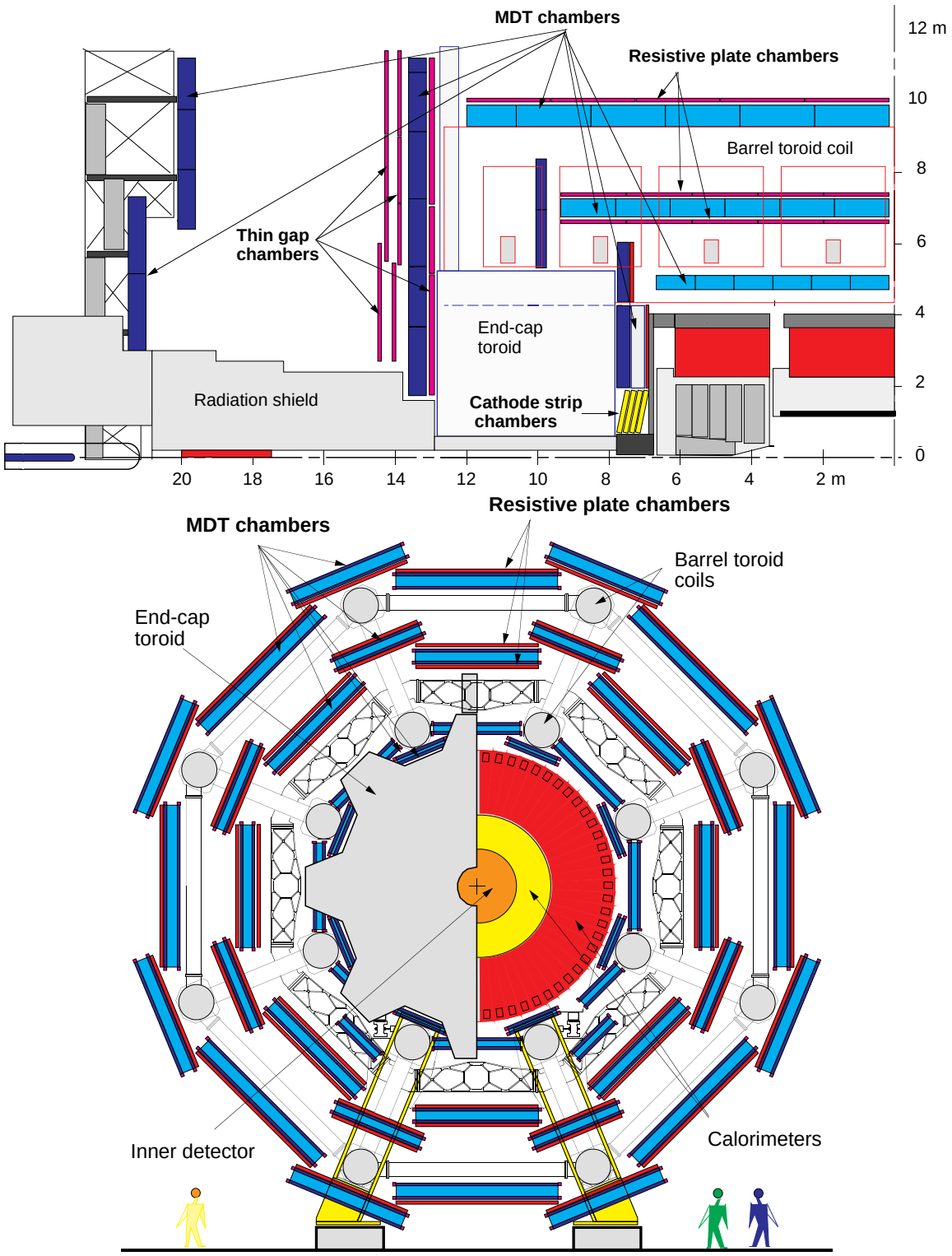

Figure 3.9: Top: a view of one quadrant of the ATLAS muon system. Bottom: transverse view of the muon spectrometer. Taken from [93].

The MDT consists of two multi-layer aluminium tubes that are filled with a gas mixture of Ar + CO_2 in the proportions 97%, 3% and have a tungsten-rhenium wire positioned at the centres of each tube. Each multi-layer consists of four (innermost layers) or three (outer layers) tube layers, with a gap between them. The muons traverse the chamber and leave trails of electrically charged particles which ionize the gas. The resulting electrons are collected by wire. Before Run 2, two new small-diameter Muon Drift Tube (sMDT) chambers were installed inside the feet of the detector, where the MDT chambers do not fit, and chambers in the transition region between the barrel and end-caps ($1.0 < |\eta| < 1.4$) were added to improve the momentum resolution in the barrel. The first layer of the MDT has a coverage of $|\eta| < 2.0$, and at higher pseudorapidity it is supplemented by the CSC to cope with the higher hit rate (> 200 Hz/cm^2) and background. The CSCs are multi-wire proportional chambers filled with the gas mixture of Ar + CO_2 + CF_4 in the proportions 30%, 50%, 20% and with a segmented cathode readout (one cathode with the strips perpendicular to the wires and the other with the strips parallel to the wires). The wires are oriented in the radial direction. Each chamber provides both an η and a ϕ measurement. In the CSC the precision coordinate is obtained by measuring the charge induced on the segmented cathode by the avalanche formed on the anode wire. The CSC consists of two disks with eight chambers each.

The RPCs provide muon triggers and a measurement of the position for muons passing through the barrel. It consists of three concentric cylindrical layers. The chamber consists of two parallel electrode-plates separated by 2 mm and filled with a gas mixture of $C_2H_2F_4$ + Iso + i-C_4H_{10} + SF_6 in the proportions 94.7%, 5%, 0.3% without wires. The $C_2H_2F_4$ is characterized by high density, relatively low operating voltage, low cost and easy availability. The signal is read out via capacitive coupling to metallic strips, which are mounted on the outer side of plates.

The TGCs provide muon triggers and a measurement of the azimuthal coordinate to complement the measurements from the MDT. They have higher spatial resolution then the RPCs. They are a multi-wire proportional chambers with a highly quenching gas mixture of CO_2 and n-C_5H_{12}. They consist of two cathode plates and anode wires placed in between the plates. A voltage of 3.1 kV is applied across the wires. The anode-wire pitch is larger than the cathode-anode pitch. The TGCs consist of seven layers of chambers in the middle station of the end-cap, and two layers of chambers in the inner station. The middle station chambers provide information for Level-1 trigger.

3.2.5 Trigger system and data acquisition

In proton–proton collisions at the LHC an enormous amount of events is produced, which can not be directly stored. These events need to be pre-selected (triggered) during online data taking in order to select interesting events for the physics analysis. The ATLAS trigger system reduces an event rate of 40 MHz to an average recording rate of 1 kHz.

The ATLAS trigger system for Run 2 was redesigned from three to two levels of event selection with increased trigger rates: a hardware Level-1 (L1) and a software-based high-level trigger (HLT). The Trigger and Data Acquisition (TDAQ) system is shown in Figure 3.10. The L1 uses information from the muon trigger chambers and the calorimeters. Therefore, the L1 system consists of the L1 calorimeter trigger system (L1Calo), the L1 muon trigger system (L1Muon), the new L1 topological trigger modules (L1Topo) and the Central Trigger Processors (CTP). The rates of the triggers are controlled via prescale factors, which are configured for a set of fixed values of instantaneous luminosity. The prescale factors define which fraction of events will be accepted by trigger (if this factor is equal 20 then 1 of 20 events will be accepted).

Initially, front-end (FE) electronics read out and process signals received from the detector's sensors and keep it in pipeline memories. Then, the L1 trigger receives this output from the detectors and makes a decision whether to accept the event or discard it in less than 2.5 μs. It reduces the event rate from

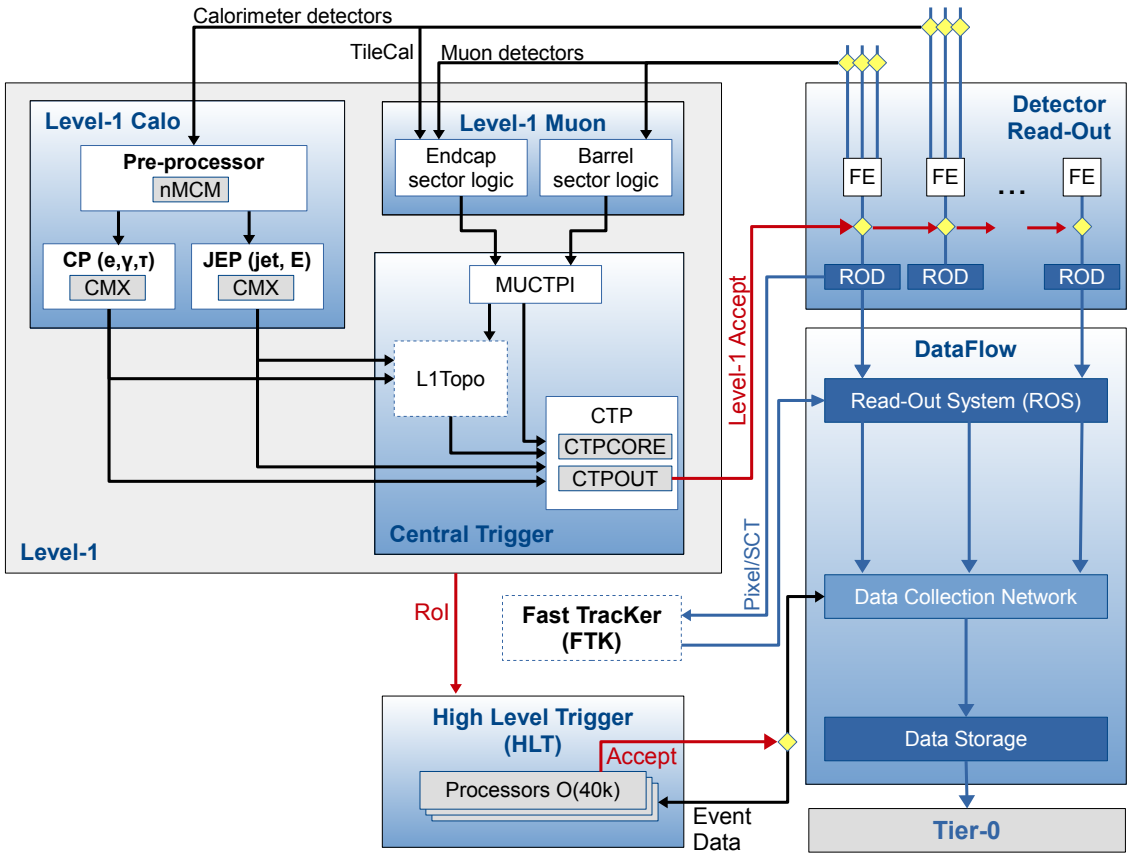

Figure 3.10: Schematic overview of the Run 2 configuration of the trigger and data acquisition system. Taken from [94].

40 MHz to 100 kHz and determines Regions-of-Interest (ROIs) with detailed trigger information (a geometrical region in $\eta \times \phi$ with information about a type of object and passed threshold). If the event is accepted, then the sub-detector will transfer data from its front-end pipelines to a Read-Out Driver (ROD). The ROD collects and formats the data and transfer to Read-Out System (ROS).

The L1Calo triggers on high-E_{T} objects (electrons, photons, jets, taus) and events with large total transverse and missing energy. The L1Muon triggers on muons for each of the predefined p_{T} thresholds. The L1Topo combines information from L1Calo and/or L1Muon into topological variables, which are based on geometric properties of the event, and form input for the CTP. The CTP receives the inputs from the L1Calo, L1Muon and L1Topo and makes final accept decision. It supports up to 512 items in trigger menus, where each item defines the objects to be triggered on with specific combination of requirements on the input data [86]. For instance, the item in trigger menu L1_MU20 will require that at least one muon has passed the a threshold of 20 GeV.

The output from the L1 in form of ROIs is passed to the HLT. The HLT was created by merging the Level-2, Event Builder and Event Filter farms used in Run 1. It runs on a computing cluster accessing data from the ROIs, applying offline-like algorithms using the full-event information. The final output from the HLT is around 1 kHz. After the events are accepted by the HLT, they are transferred to local storage at the experimental site and exported to the Tier-0 facility at CERN's computing centre for offline

reconstruction [94].

3.3 Luminosity measurement

Luminosity is an important characteristic of the LHC performance. Two types of luminosity are defined: the delivered and recorded luminosity. The delivered luminosity is the luminosity evaluated before any trigger decision, which the accelerator delivered to certain experiment. The recorded luminosity is actual recorded on disk data, after corrections for a dead-time and operational problems in sub-detectors filtered by a data acquisition system. Precise measurement of the luminosity is an essential task, since the uncertainty in the delivered luminosity influences the precision of the physical cross section determination. Moreover, it is an important ingredient for searches for physics beyond Standard Model by normalizing the background calculations. Also, luminosity measurements help to monitor beam conditions during the run.

A parameter that shows a number of physics events produced in the collisions per second is called 'instantaneous' luminosity, $\mathcal{L}(t)$, and is usually expressed in units of $\mathrm{cm}^{-2}\mathrm{s}^{-1}$. It is a proportionality factor between the rate of any process, $R_{pp\to X}$, and its cross section, $\sigma_{pp\to X}$:

$$R \equiv \frac{N_{pp\to X}(t)}{\mathrm{d}t} = \mathcal{L} \cdot \sigma_{pp\to X} \tag{3.3}$$

and, therefore, the luminosity is defined regardless of the process and can be measured if the cross section is known.

The integrated luminosity, L, determines the total number of produced events associated with certain process over the lifetime of a machine and is defined by integrating the instantaneous luminosity with respect to time as follows:

$$L = \int_0^t \mathcal{L}\mathrm{d}t = \frac{N_{pp\to X}}{\sigma_{pp\to X}} \tag{3.4}$$

The integrated luminosity is used to obtain the measured cross sections and usually is expressed in inverse barns ($\mathrm{b} = 10^{-24}\mathrm{cm}^2$).

Furthermore, the luminosity can be determined from the properties of colliding beams. If two beam bunches, with N_1 and N_2 particles each, collide with a revolution frequency, f_r, the bunch luminosity can be expressed through an overlap integral over the particle density profiles of the two beams, ρ_1 and ρ_2 , as follows [95]:

$$L_b = f_r N_1 N_2 \int \rho_1(x,y)\rho_1(x,y)\mathrm{d}x\mathrm{d}y, \tag{3.5}$$

where $f_r = c\,/\,r$ is equal to 11245 Hz for the LHC ring. This equation is valid if the crossing angle between beams is equal to zero. Under an assumption of uncorrelated horizontal and vertical components of the density profiles, the bunch density profiles can be factorised into independent horizontal and vertical component distributions, $\rho_1(x,y) = \rho_1(x)\rho_2(y)$, and by solving the integral analytically Equation 3.5 can be written as:

$$L_b = f_r \frac{N_1 N_2}{2\pi \sum_x \sum_y}, \tag{3.6}$$

where $\sum_x$ and $\sum_y$ are convolved beam widths of the Gaussian transverse beam profiles in the horizontal and vertical directions. They can be extracted by measuring counting rate which is proportional to the luminosity (see Equation 3.3) as a function of a beam separation in x and y directions during specific

calibration runs, so-called van der Meer (vdM) scans [96]. In a vdM scan, two beams are first centred on each other and then they are displaced in discrete steps of known distances (until the event counting rate approaches zero) at the same time recording the relative change of the rate.

The instantaneous and integrated luminosity can be measured by counting the event rate of a physical process with a well known sizeable cross section using Equation 3.3. For instance, the process of a Z boson decaying to leptons, which has a clean signal and is theoretically well understood, can be used. Alternatively, in case of very small cross sections, the luminosity can be measured from the beam parameters. Dedicated ATLAS luminosity detectors with the associated algorithms can be used to measure visible rate per each colliding-bunch pair, μ_{vis}, taking into account the efficiency of the detector. To define the absolute luminosity, the rate of the collisions can be expressed through the average number of collisions per bunch as follows:

$$L_b = \frac{\mu_{vis} f_r}{\sigma_{vis}} \tag{3.7}$$

The value of σ_{vis} is initially unknown and can be calibrated with Equation 3.5. This is the default method for the measurement of the luminosity in the ATLAS. The vdM method allows the determination of σ_{vis} without a priori knowledge about cross section or detector efficiencies. By comparing the known luminosity delivered in the vdM scan to the visible interaction rate μ_{vis}, the visible cross section can be determined from Equations 3.7 and 3.6. The measurement of μ_{vis} and a value of σ_{vis} are extracted for each algorithm and each detector.

Systematic uncertainties on the luminosity measurement are estimated in part by comparing the luminosity measurements from all algorithms and all detectors. The uncertainty in the integrated luminosity is 2.1% and is derived following a methodology similar to that are detailed in Reference [95], from a calibration of the luminosity scale using $x - y$ beam-separation scans performed in August 2015. The largest error in luminosity uncertainty for 2015 data set comes from the error in the determination of σ_{vis}.

3.4 ATLAS software

3.4.1 The ATHENA framework

Athena [97] is the ATLAS common software framework. It is derived from the Gaudi framework [98] primarily developed by the LHCb experiment. Hence, the Gaudi project is the kernel of Athena with ATLAS-specific enhancements including the event data model and the event generator framework. The principal purpose of the software is to generate, simulate, digitize and reconstruct the proton–proton events collected by the ATLAS detector and to produce objects that can be easily accessed by the analysers in order to produce physics results. It uses an object-oriented programming language, C++, for the software and a common scripting language, Python, for the configuration files, called JobOptions files, where the user can set all necessary options for the analysis. It was developed following main design principles as a clear distinction between data and algorithms and between persistent data and transient data.

The framework is organized in a hierarchical way and contains various common analysis algorithms, tools and services (see Figure 3.11), which are implemented by the ATLAS software developers. They perform a dedicated task and are organized in a specified order via AthSequencer. This works with an input dataset providing basic event processing and produces output data. The input files enter into the Athena via a selector (EventSelector) which selects the events that the application will process. Each algorithm contains three main methods called in the following order: initialize (the algorithms

are initialized by application manager once before reading event data), execute (called once per event for each algorithm object in the order in which they were declared to the application manager) and finalize (called at the end of the job). All algorithms have access to the event information and the detector description via the StoreGate service. The output of the algorithm is written to a transient event store, from where the next algorithm can take the output and process it further. All components within the application are controlled by the Application Manager which is common to all applications.

Tools are similar to the algorithms working on the input data and producing outputs but can be executed multiple times per event by the algorithm. An example tool is the GoodRunsListSelectionTool, where performs the selection according to the good runs. Every tool has at least one corresponding interface class in the ATHENA.

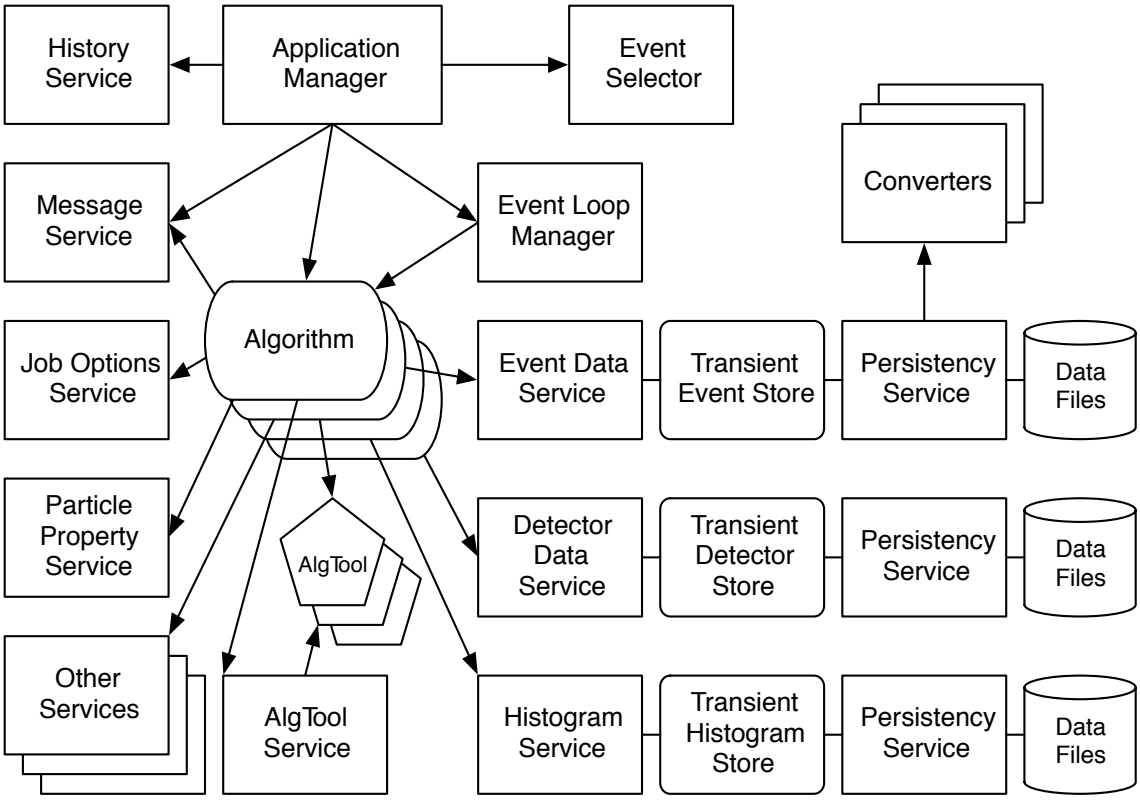

Figure 3.11: A diagram of the ATHENA framework and servise architecture. Taken from [97].

The services are globally available software components providing specific framework task which is required by the algorithms. They can be run multiple times within a single event. Typical services are JobOptionSvc (configuration of tools), MessageSvc (message service), StoreGateSvc (stores results of algorithm) and etc. The JobOptionSvc service allows configuring the properties of algorithms or tools. Progress or on errors that occur during the execution of the algorithm are reported via the IMessageSvc. The StoreGateSvc manages the data objects in transient form and steers their transient/persistent conversion.

3.5 ATLAS upgrade

The current second LHC data-taking period, so-called LHC Run 2, is planned to be completed by the end of 2018 with an expected luminosity nominal value of $L \simeq 100\,fb^{-1}$. Afterwards, the LHC project is aiming to increase both the collision energy and luminosity. Towards this direction, the LHC devised a twenty-year timetable. Directly after Run 2, a two-year shutdown is planned before the next data-taking period, Run 3, which will start with the higher collision energy up to 14 TeV and increased instantaneous luminosity by a factor of two of nominal value, which will correspond to 55–80 interactions per crossing. Following Run 3, another shutdown period will start before the High-Luminosity Large Hadron Collider (HL-LHC) phase [99]. The aim of the HL-LHC is to record the highest integrated luminosity in order to boost discoveries after 2025. The idea is to record dataset corresponding to a integrated luminosity ten times greater, $L \simeq 3\,000\,fb^{-1}$, than the initial design value, $L \simeq 300\,fb^{-1}$. The new conditions will bring the new challenges for the current detectors.

The current ATLAS detector is not designed for the high particle flux, large numbers of interactions per beam crossing and high trigger rates that will result from the HL-LHC. The new requirements such as higher granularity, wider area coverage, faster readout electronics, and much greater power delivery to the front-end systems will require new detectors in the innermost region of the experiment. Therefore, the ATLAS detector described in the previous sections need of a series of upgrades. A new tracking detector, significant changes in the calorimeter and muon systems, as well as improved triggers and data acquisition system will be required. In order to implement all needed changes, two stages of upgrades are planned in the future for the LHC collider and are shown in Figure 3.12. The first stage, long shutdown 2 (LS2), called Phase-I , is scheduled from 2019 to 2020 and the long shutdown 3 (LS3), called Phase-II , is planned to start in 2024 with a duration of two to three years. The baseline plan for the Phase-I upgrade of the ATLAS experiment is described in the Letter of Intent [100] and for the Phase-II upgrade in Reference [101].

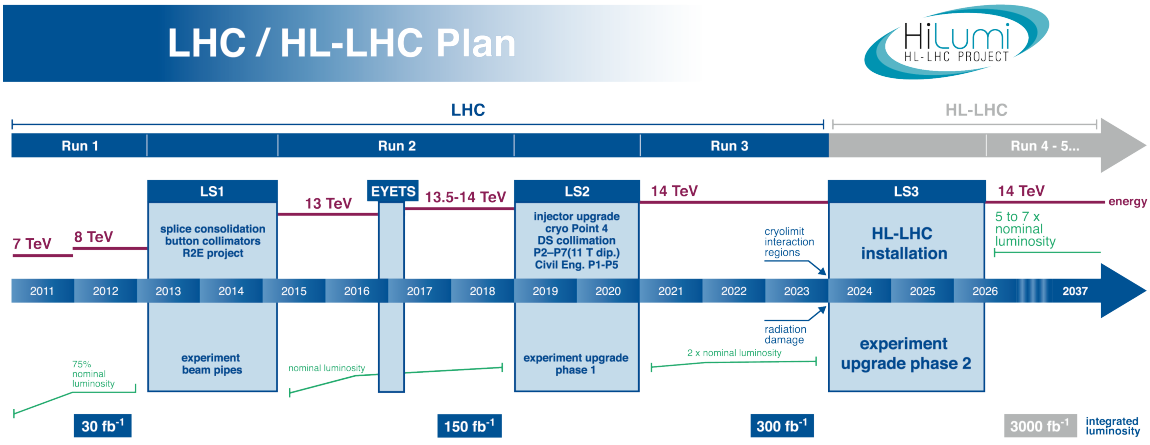

Figure 3.12: The schedule for the LHC operation. Taken from [99].

A summary of the improvements and changes that are foreseen for the future upgrades are outlined:

Phase-I This period will include significant changes for the proton injectors, collimators, installation of the new muon end-cap system, New Small Wheels (NSW), and several updates for the Liquid Argon (LAr) Calorimeter trigger, trigger systems and DAQ, specifically:

- the integration of a new 160 MeV H^- Linac4 into the injector complex with a replacement of the present 50 MeV proton Linac2, upgrade for the energy of the PS Booster;
- the first station of the end-cap muon system, Small Wheel (SW), will be replaced with the NSW, which will include significantly improved Level-1 muon trigger in the forward region. The NSW will employ a new type of small-strip, Thin Gap Chambers (sTGC) and Micromegas detectors for better muon tracking performance in the high rate environment. More details are described in the technical design report [102];
- the impementation of the better trigger algorithms to L1Calo trigger system. The new Super-Cell readout geometry will be implemented to increase the granularity accessible at the L1 level and will allow to read out separately from each LAr Calorimeter layer. More details are described in the technical design report [103].
- new Fast Tracker (FTK) will be added to provide fast hardware tracking instead of Level-2 software farm;
- the TDAQ and HLT processing farm will require an adaptation to the changes.

Phase-II In this period, one of the main requirements will be to replace the current Inner Detector. The trigger and calorimeter systems will experience upgrades as well. The detailed program is described in the scoping document [104] and foresees the following:

- the current Inner Detector will be replaced with a new all-silicon Inner Tracker (ITk) consisting of ~8 m^2 pixel and ~192 m^2 strip detectors [105]. The current pixel and gaseous straw-tube based TRT and SCT will be replaced with the all-silicon tracker;
- the new trigger system is required. The split Level-0/Level-1 hardware trigger scheme with L0 level rate of 1 MHz is foreseen;
- a new read-out architecture for the calorimeter electronics and muon spectrometer;
- upgrades for the TDAQ towards the new trigger rates.

CHAPTER 4

Electrical test of end-cap prototype of the Inner Tracker

This part of the dissertation work is devoted to the ATLAS Inner Tracker (ITk) upgrade for the High-Luminosity Large Hadron Collider project. One of the main requirements is to replace the current inner detector with the new, all-silicon tracker. A small-scale prototype for an end-cap region was built to study some features of the complex wedge-shaped structures. It consists of silicon strip sensors and electronic readout components that are hosted on a carbon-based core. Single- and double-sided prototypes were assembled at Deutsches Elektronen-Synchrotron (DESY). The details regarding the structure and the assembly of the prototype are described in Section 4.2. Prototypes with two different readout architectures, the so-called common and split readout schemes, were assembled and evaluated at DESY, the University of Freiburg and the Institute for Corpuscular Physics (IFIC) in Valencia. The characterisation and main differences are outlined in Section 4.2.2. In order to evaluate and choose the best alternative for production of real structures, a set of electrical tests was performed for the split version at DESY and Freiburg and the common version at IFIC. The main results were compared and considered to support a decision about the electronics layout for the end-cap of the ATLAS ITk strip detector taking into account all essential aspects and summarised in Section 4.3.

4.1 ATLAS Inner Tracker upgrade for High Luminosity LHC

The ATLAS inner tracker will consist of an all-silicon tracker for the Phase-II upgrade. The main pixel layout design, called ITK inclined, is considered for the ITk detector upgrade and is shown in Figure 4.1. According to this layout, silicon pixel modules at the inner radii providing tracking coverage up to $|\eta| = 4$ are surrounded by silicon strip modules at larger radii. The barrel part consists of five pixel layers (with an inclination of the sensors in the forward part of the barrel) and four strip layers (two short strips and two long strips with a length of 24.1 mm and 48.2 mm, respectively) [105]. The end-cap regions will be composed of four-pixel rings and six strip double-sided disks per end-cap side.

The strip tracker is the element of interest in this study and is described in detail. The basic mechanical constituents for the new tracker in the central and forward region are called *stave* and *petal*, respectively. The stave is a rectangle-shaped and the petal a trapezoid-shaped structure. These structures have similar mechanical construction and consist of a low mass carbon-based core which supports all modules and hosts all electrical services and cooling components. The carbon-based core is designed to be as light as possible, maintaining high rigidity at the same time. A carbon honeycomb together with titanium cooling pipes is embedded between two carbon fiber layers. On top of this structure, a bus tape is co-cured to

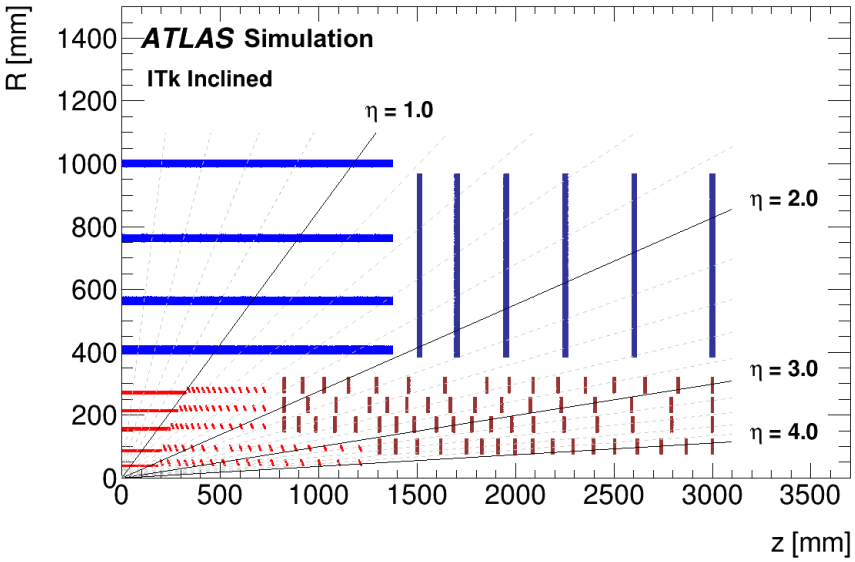

Figure 4.1: The baseline layout design of the ATLAS inner tracker for HL-LHC upgrade indicating the coverage of the pixel detector (in red) and strip detector (in blue). A horizontal axis is the axis along the beam line and a vertical axis is a radius measured from the interaction point. Taken from [105].

carbon fiber skins in order to route the power and data between the modules and End-Of-Stave (EoS)/ End-of-Petal (EoP) board located at one end. The data from the petal and stave is collected by EoS/EoP, which interfaces with the off-detector electronics. On the top surface of the core, the modules are glued. The module is a structure which combines silicon sensors with readout hybrids. The hybrids are low-mass printed circuit board (PCB's) glued on top of the sensor and host the readout chips (ASIC's) which are wire-bonded to the sensor strips. The layout of the internal structure of a core is shown in Figure 4.2.

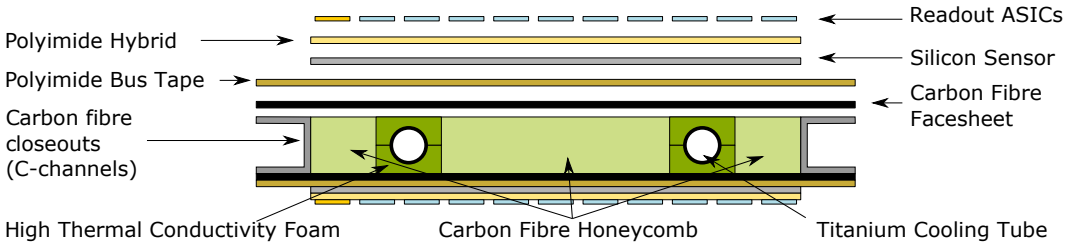

Figure 4.2: The layout of the internal structure of a core. Taken from [105].

For the petal, different types of modules are needed for the various rings while for the stave they are identical within a stave. All nine modules of the petal are organized in six segments, so-called rings (R0–R5), which are arranged around the beam axis (see Figure 4.3(b)). The three inner rings (R0–R2) have one module each with one or two hybrids and the outer three rings (R3–R5) have two modules with one hybrid placed over the two modules. In each ring, the sensors have different geometries to cover a wedge-shaped surface. The innermost ring has a fine strip pitch (close to 75 μm) and very short strips. In the outer rings, the petal splits into two-sensor columns which are manufactured on 6-inch silicon wafer. The strip pitch is chosen to be as close as possible to that in the barrel and to maintain reasonable wire bonding angles for bonding reliability. The straight edges of the sensors are parallel to the strips to avoid truncated strips, while the curved inner and outer edges of the sensors serve for uniform length of the

strip within the module rows.

One end-cap disk is composed of 32 double-sided petals and 576 modules. One petal will hold 18 modules, and the whole end-cap will consist of 3456 modules [105]. The structure and geometry of one end-cap and one petal, a constituent element of the disk, is shown in Figure 4.3.

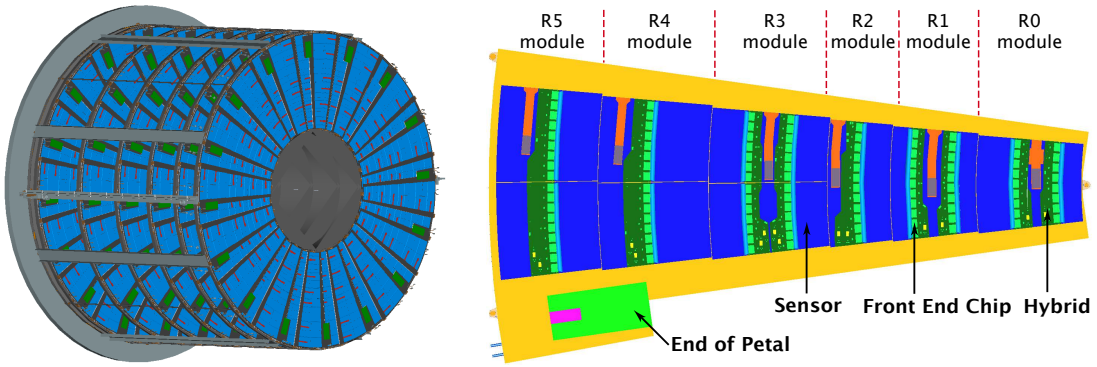

(a) (b)

Figure 4.3: (a) The sketch of design for one end-cap side for new ITk. (b) Single-sided petal, constituent element of the disk for the new ITk. Taken from [105].

In general, the design for the new ITk is optimized to simplify the production and aims to be low-cost by using industry-proven technologies and similarity in the module designs.

To evaluate various options and solutions for the different features of the inner and outer regions of the petal, small-scaled prototypes called *petalets* have been built, based on the first and fifth rings (R0 and R4), with three modules on each side. One of the goals was to study an electrical performance for different powering and readout options and to understand the issues, benefits and suitability of the two different designs. An overview of this concept with the corresponding dimensions is shown in the schematic representation in Figure 4.4. A concept of the stave with the similar structure was evaluated, prototyped and described in Reference [106].

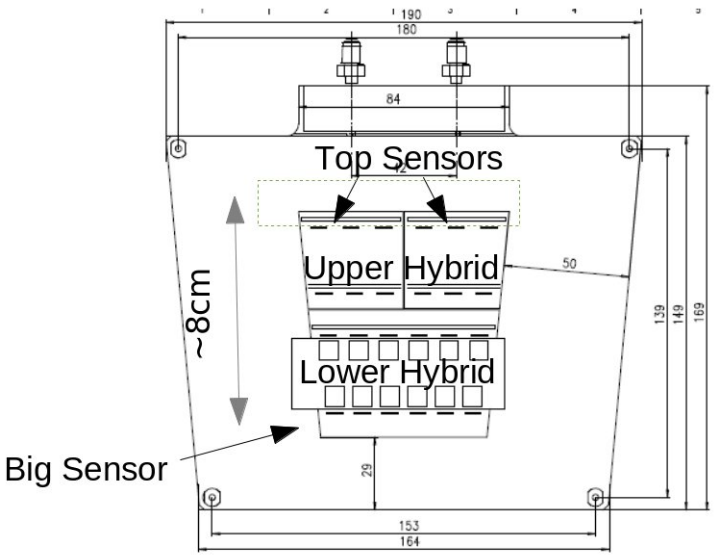

Figure 4.4: Schematics representation of the petalet indicating corresponding dimensions. Taken from [107].

4.2 Petalet description

4.2.1 Prototype components

Core and bus tape. One of the main building components for the assembly of a petalet is the core, which provides support, cooling, power and data lines to the modules while keeping materials at low level. Nine petalet cores were produced at DESY using specially designed tools and distributed to other institutes. The core weights around 77 g. The materials were chosen to provide good thermal and mechanical performance. The facings, which cover the core from both sides, are made of a 3-layers layup of carbon fiber reinforced polymer (CFRP), co-cured[1] together. The cooling titanium tubes, which have a diameter of 2.275 mm, were made in a U-shape and embedded in the core, providing cooling to the whole petalet volume. They are wrapped around highly thermally conductive carbon foam, which has low density and weight and comes from Allcomp Inc. [108]. The foam increases the effective dissipation of heat in the vicinity of the cooling pipes. The end of the tubes and the stainless steel fittings for the connection with the cooling are vacuum-brazed together. The rest of the area is composed of the honeycomb which is glued between back and front sides of facings. The open area on the edges is closed with C-shaped closeout elements. The final thickness of the core is 5.4 mm. A photograph of the internal structure of cores is shown in Figure 4.5.

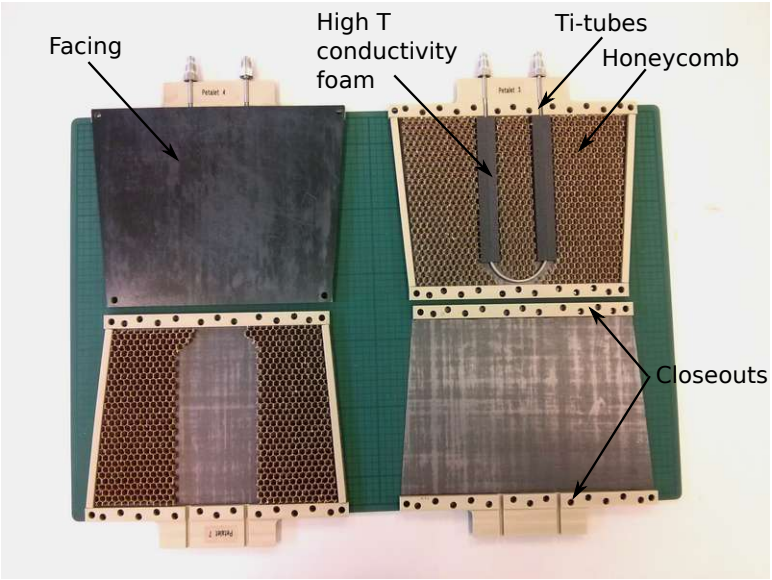

Figure 4.5: An illustration of the structure of the petalet cores showing all internal components.

The bus tape is a multi-layer flexible circuit which includes layers of copper traces under an aluminium shield and several kapton layers. It connects each hybrid with the EoP providing digital data return, distributes the signal and power to the hybrid including high-voltage (HV) and low-voltage (LV) traces. It is co-cured on top of the facings of the core covering the entire area. The HV supply for the sensors is provided by independent HV lines per sensor. The LV lines provide a voltage of 10–12 V for the operation of the DC–DC converters. The bus tape plays a significant role in the evaluation of the two readout options, and therefore two different designs were considered and manufactured at 'Elgoline' [109]. They are shown in Figure 4.6.

[1] This refers to the process in which preimpregnated fibers are laid up together under heat and pressure in an autoclave ('chamber') over a period of time.

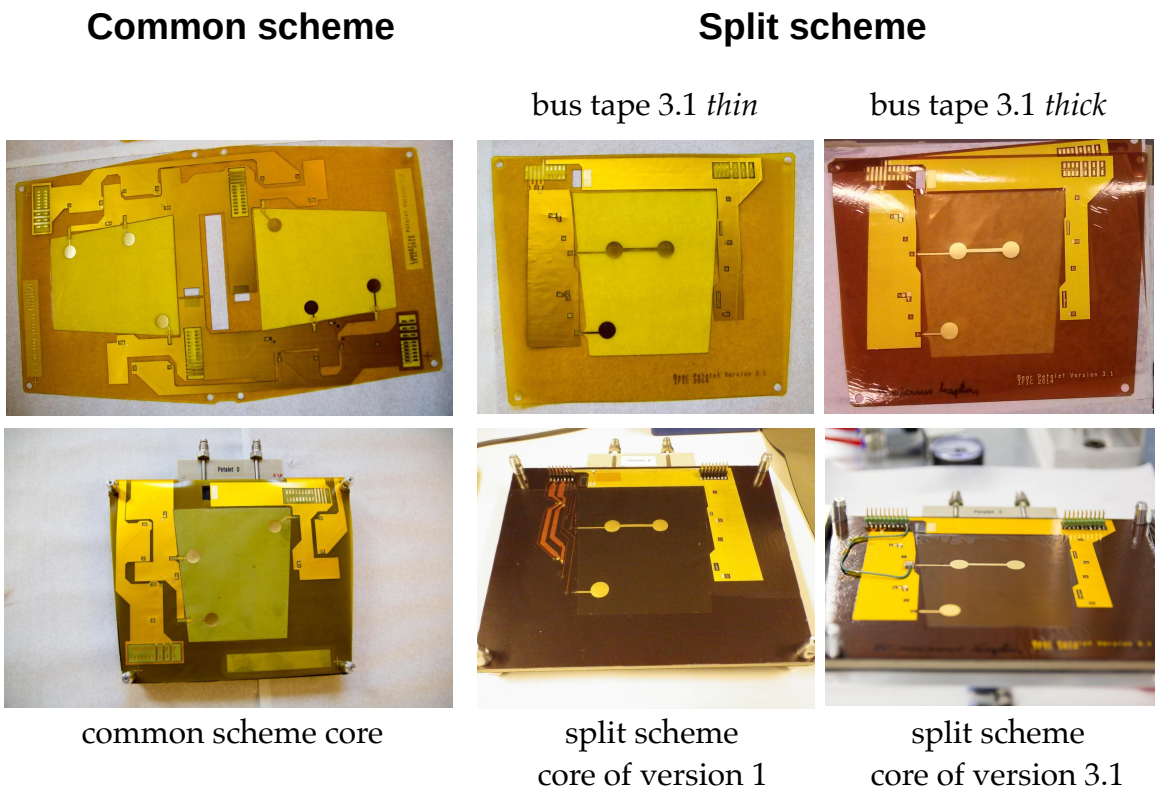

Figure 4.6: Two main designs of bus tape, for common (left top) and split (right top) readout versions and corresponding assembled cores (bottom).

Modules. The petalet module is based on silicon strip sensors and consists of three sensors per side. One big sensor ('Big Sensor') with the innermost radius (R0 ring) is located on the bottom part and two smaller ('Top Sensors') with two split modules in two columns (R3 ring) are on the upper part.

The sensors, n-type implants on a p-type bulk, were manufactured using a float zone (FZ) technology in 4-inch wafers in the clean room at the Centro Nacional de Microelectronica (IMB-CNM), Barcelona, Spain. The wafer mask layouts were designed with the standard sensors, one for the Big Sensor and other for the two Top Sensors. Each of the sensors has two strip rows and was designed with a built-in stereo angle of 20 mrad to have a total stereo angle of 40 mrad between the front and back sensors. It provides two-dimensional hit information. Each strip has a p-stop implant for proper interstrip insulation. The Big and Top Sensors have a varying strip pitch and length. The Big Sensor has the longer strips and smaller strip pitch. Table 4.1 shows the size of strip pitch and length for the different sensors of the petalet.

	Top-Left Sensor	Top-Right Sensor	Big Sensor
Pitch (μm)	95.4–103.7	95.7–103.4	86.9–96.3
Length (μm)	17895–18012	17890–17941	23919–24081

Table 4.1: The size of the strip pitch and length for the Top and Big Sensors of the petalet [110].

An additional set of wafers were designed as 'embedded sensors'. The embedded sensors have a double metal layer to implement embedded fan-in structures, so-called embedded pitch adapters, which match with the bond pads of the readout chips to avoid large bond angles. Five different embedded

fan-ins were designed to find the best option. More details can be found in Reference [110].

The readout hybrids are glued on top of the sensors , one or two per sensor depending on the petalet design. The hybrid is a low mass flexible four-layer copper polyimide construction hosting the readout electronics, necessary components for readout and power circuitry. The prototype of the readout chip for the petalet project was an ATLAS Binary Chip Next (ABCN) produced in 250 nm (ABCN-25) CMOS technology [111]. One hybrid holds two rows of chips, six per row, and each chip reads out 128 channels, which are wire bonded to the sensors. Hence, one hybrid reads out 1 536 channels. The chip has a binary readout and only provides hit information if the deposited charge was above the threshold. The new ABCN, in 130 nm CMOS technology, with 256 channels per chip will be used for the final petal design.

Powering and electronics elements. One of the main elements of the petalet is a low noise and a low mass DC–DC converter. It distributes and converts the input voltage from around 10 V to the supply voltage of 2.5 V required for the front-end chips. Then the front-end chip converts the voltage down to the level which is necessary to internal voltage regulators. The key feature of the DC–DC converter is that it uses a shielded inductor in order to reduce the emitted electromagnetic field. A Buffer Control Chip (BCC) was fabricated in 250 nm CMOS technology and it is located on a daughter Printed Circuit Board (PCB) next to the hybrid. The hybrid and BCC boards are connected via wires bonds. The BCC addresses and reads out hybrids, performs digital control of input and output signals, multiplexes incoming data and handles triggers, timing and command (TTC) signals.

4.2.2 Readout versions of petalet

During the petalet project, two different readout designs were developed in order to determine the optimal design towards the petal building. Both versions of common and split layouts, so-called *Lamb and Flag* and *Bear*, were studied at IFIC and DESY.

A principal difference between two versions is that the Lamb and Flag petalet has the data, power, trigger, timming and control (TTC) lines on the same side of the module. As a consequence, the DC–DC converters and BCC boards are placed on the same side as well. Each sensor has its own hybrid with the readout electronics delivering in total three modules per petalet side and six modules for the full petalet, respectively. Two smaller hybrids are needed to cover the upper sensors and one standard hybrid for the bottom sensor. Wrapped-around bus tape, fitted through the cooling pipes over the top edge of the core, is required to connect the bottom left (right) upper modules from the front side with the left (right) upper modules from the back-side of the petalet and visa versa. The Bear petalet routes the data, TTC on one side and control signals and power on the opposite side of the modules. Therefore, the DC–DC converters and BCC boards are glued on opposite side of the modules. One hybrid is required to cover two Top sensors, left and right, and one for Big sensor. As a result, one side of the petalet consists of two modules, and the full petalet is compoused of four modules, respectively. The Bear petalet layout requires two mirrored bus tapes which are glued separately on each side of the core. The illustration of the two different petalet layouts according to the different readout designs is shown in Figure 4.7. The prototyping of hybrids and modules for the petalet project is discussed in more detail in Reference [112].

4.2.3 Mounting of modules on the core

Two single-sided petalets with the standard and embedded sensors and one double-sided petalet with the standard sensors have been prototyped at DESY. Custom precise tools were developed and manufactured for this purpose.

Before the assembly of the petalets, it is necessary to check and prepare all basic components: the modules, cores, DC–DC converters and BCC boards. The core with co-cured bus tape is required to have

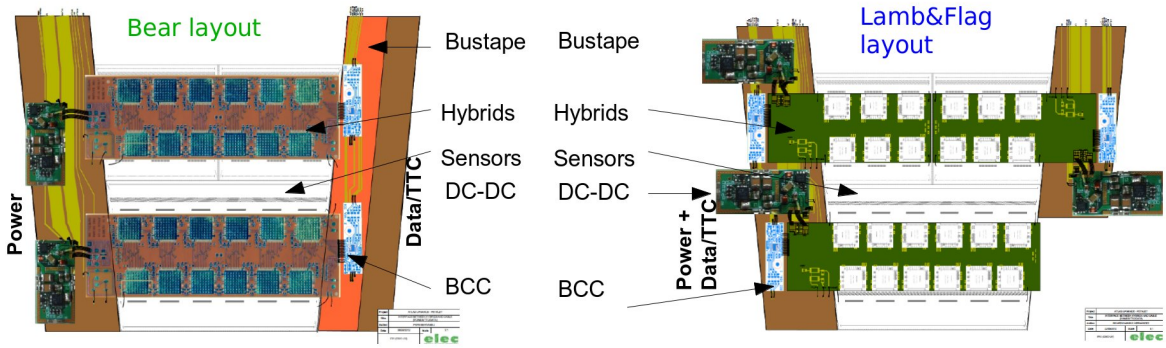

Figure 4.7: The illustration of two different petalet layouts. On the left side is the Bear and on the right side the Lamb and Flag layouts. Taken from [107].

two SAMTEC connectors with 12 and 16 pins, for data and power lines, soldered onto the core. All connections should be probed. The modules were assembled at DESY Zeuthen and transported to DESY Hamburg. Accordingly, a visual quality assurance for the sensors and wire-bonds should be performed at the beginning. Then, before gluing modules onto the core, the modules are tested on a test frame to ensure that they function properly, showing low noise without abnormal behaviour. The results are compared to results obtained at DESY-Zeuthen before shipment. Details of the module testing on the test frame are described in Section 4.3.

The core is placed into the custom precision frame after it is fully prepared (the bus tapes and connectors are on the core). Then, a two-layer frisket foil is used as a stencil for the glue spreading over the surface of the foil. The stencil is designed to maximize glue spreading and thermal contact between the petalet core and strip modules. To achieve that, the corresponding pattern is sketched on the foil, cut and carefully glued onto the bus tape (see Figure 4.9(a), 4.9(b)). Then, thermally conductive and electrically insulating glue SE4445 from Dow Corning Inc. [113] is mixed in the Thinky ARE-250 mixer and distributed throughout the stencil (see Figure 4.9(c)). Afterwards, the foil can be removed and electrically conductive silver-epoxy can be used in small drops to make high-voltage contacts. On top of the glue, fishing lines of 140 µm in diameter (for the lower and upper part) are placed to control glue thickness during mounting of the modules to the core (see Figure 4.9(d)).

The modules are aligned on an alignment tool to the right position in x-, y-, z-axis with a microscope and computer using fiducials on the silicon as a reference and mounting tools. When the alignment is finished, a control bridge and check-up tool are placed on the pins to inspect the position of each chip and ensure that all wires are protected from damage in the next step. Then, the module can be picked up using a vacuum-holding pickup tool with twelve vacuum cups. This tool substitutes for the check-up tool and descends slowly using micromanipulators until it touches the module. Using vacuum, the module can be picked up and placed on the core with the prepared glue. The modules should be left weighted down and under the vacuum for 6–12 hours. Following that, the DC–DC converters and BCC boards are glued onto the core with the thermally conductive glue. At the final stage, the petalet can be sent to the wire-bonding lab to make corresponding wire connections between the core pads, DC–DC converters and BCC boards. Three fully assembled petalets from the modules, DC–DC converters and BCC's and the core are shown in Figure 4.10.

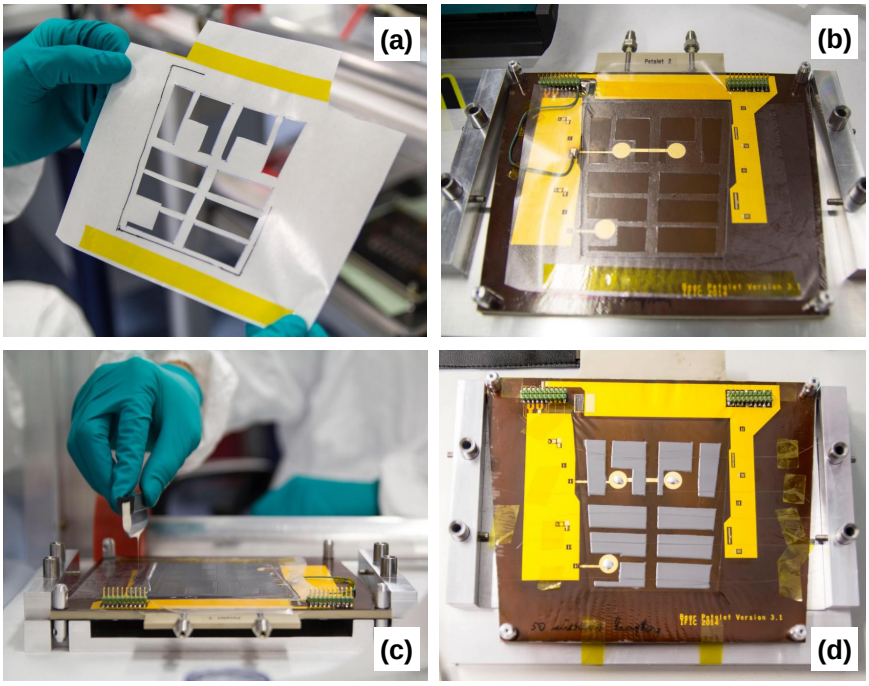

Figure 4.8: The preparation of glue for the module mounting with the corresponding steps: (a) a frisket foil; (b) the glued stencil on the bus tape; (c) the spread of glue; (d) the prepared glue and the fishing lines on top of glue.

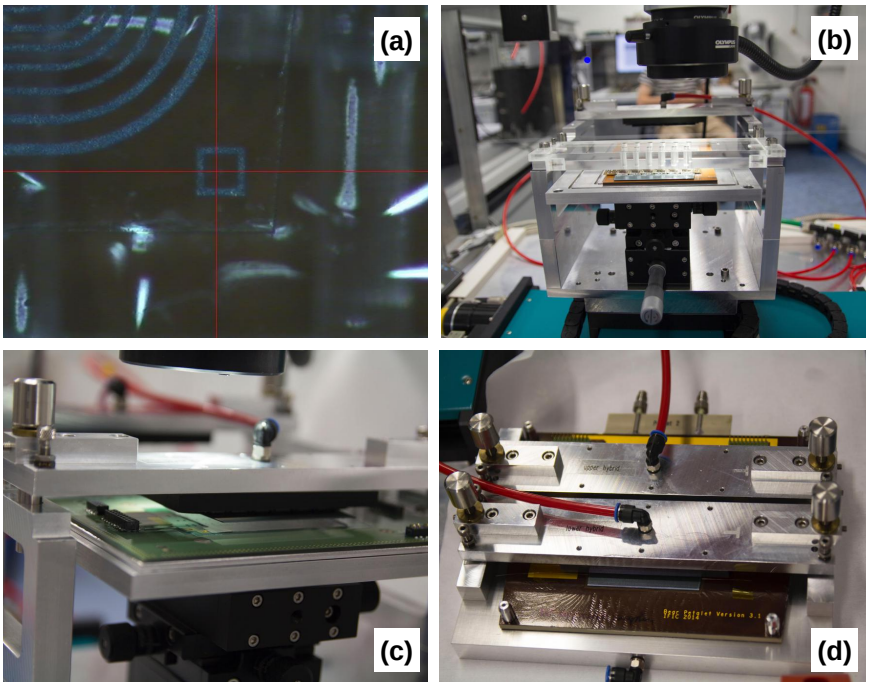

Figure 4.9: The module alignment and mounting tools: (a) the fiducial on the silicon; (b) the check-up tool; (c) the pick up of the module; (d) placement of the modules onto the core.

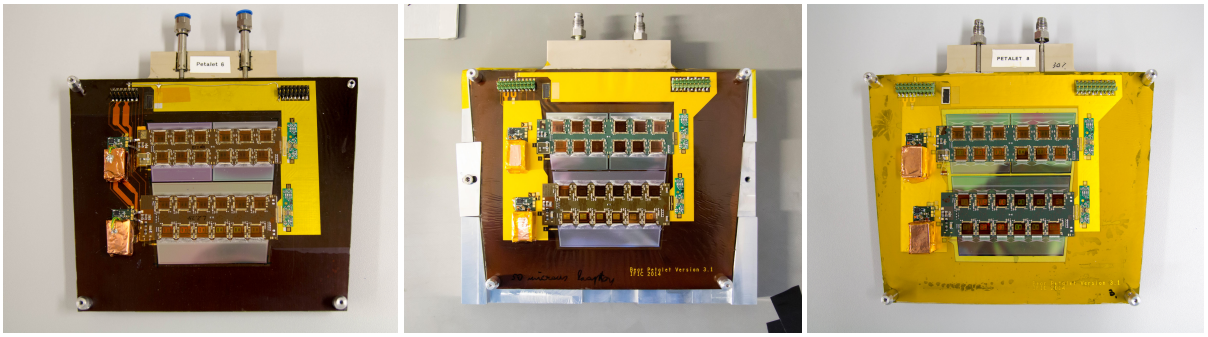

(a) (b) (c)

Figure 4.10: The picture of fully assembled petalets at DESY. (a) the single-sided petalet with the standard sensors, (b) the double-sided petalet (back side) with the standard sensors and shielded bus tape, (c) the single-sided petalet with the embedded sensors.

4.3 Electrical performance

The general concept of semiconductor detector operation relies on ionization due to incident particles. Charged particles traverse through a silicon layer and deposit energy generating electron-hole pairs. The created charges are separated by applying a electric field and drift towards the oppositely charged electrode. The charge carrier movement causes a current signal, which is typically small, but measurable. The produced signal has to be acquired and integrated through a common routine: charge sensitive amplifier, pulse shaper and digitizer. It is delivered by using the front-end electronics (ABCN-25). Since the module operates in a binary readout mode, final signal output is presented as a positive (one) or negative (zero) value without saving detailed information about the magnitude, depending on whether it passes threshold in a discriminator of the ABCN-25 chip. The scheme of the signal processing is shown in Figure 4.11.

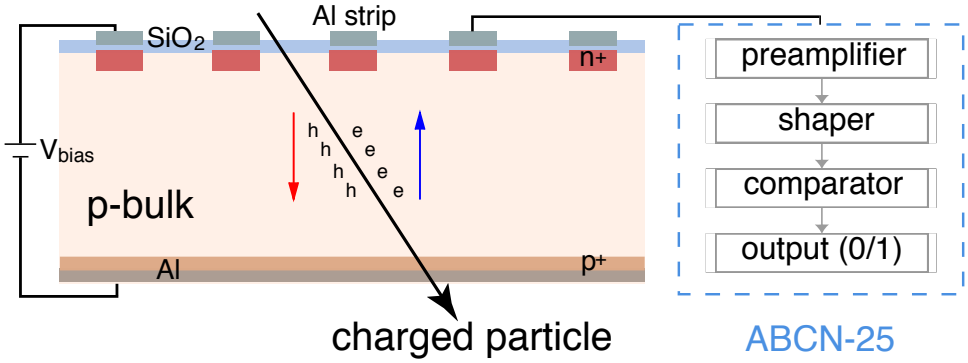

Figure 4.11: Sketch illustrating a basic working principle of semiconductor detectors.

The signal, whose amplitude depends on the sensor thickness, is affected by random fluctuations. These fluctuations are referred to as noise. It can originate from different sources depending on operating conditions, detector layout, processing techniques and on the manufacturing process. The most important source is electronic noise which is compoused of thermal noise, shot noise and low frequency noise. Besides, the front-end amplifier electronic noise is described by a combination of voltage and current fluctuation sources such as sensor bias current, shunt and series resistances. A detailed description of noise sources is presented in Reference [114]. One of the most important characteristics for the

production of new detectors, which is necessary to control in designing signal processing circuitry, is low noise operation of the front-end amplifiers. In order to know to what extent the signal is influenced by noise, the ratio of signal to noise (S/N) is measured. A sufficiently high ratio needs to be achieved in order to avoid presence of the noise. As a baseline, a minimum S/N greater than ten is necessary for unequivocal recognition of the signal. The noise of the front-end signal processing channel is usually expressed as equivalent noise charge (ENC). The ENC is defined as the number of electrons that would be necessary in order to yield a signal-to-noise ratio of one and can be measured by injecting a known signal into circuitry through the threshold tests which are described in the next sections.

4.3.1 Experimental setup and tests

In order to perform the standardized tests for the modules and petalets and to characterize them, a testing facility was set in the clean room at DESY. It was equipped with the necessary materials and devices to run the tests and conduct minor repairs and adjustments. The experimental setup for the petalet project was used to measure electrical performance and is shown in Figure 4.12. The object under test is placed in an aluminium box (see Figure 4.12(a)), in order to shield the sensor surface from the light and damages and to provide a Faraday enclosure. The box has special openings to connect the object to the outside world. Two cooling tubes from a chiller which uses water-based coolant C20 (see Figure 4.12(f)), are attached to the box in order to supply cold liquid to the object. The flow of nitrogen is regulated with a nitrogen system (see Figure 4.12(e)) and delivered into the box to remove the humidity from the box and reduce the possibility of surface current. The power supplies (see Figure 4.12(b), 4.12(c)), Keithley 2410 as a high-voltage source for the sensor and TTI Q355TP for the supplying of a readout board and providing low voltage for the hybrids, are connected to the box.

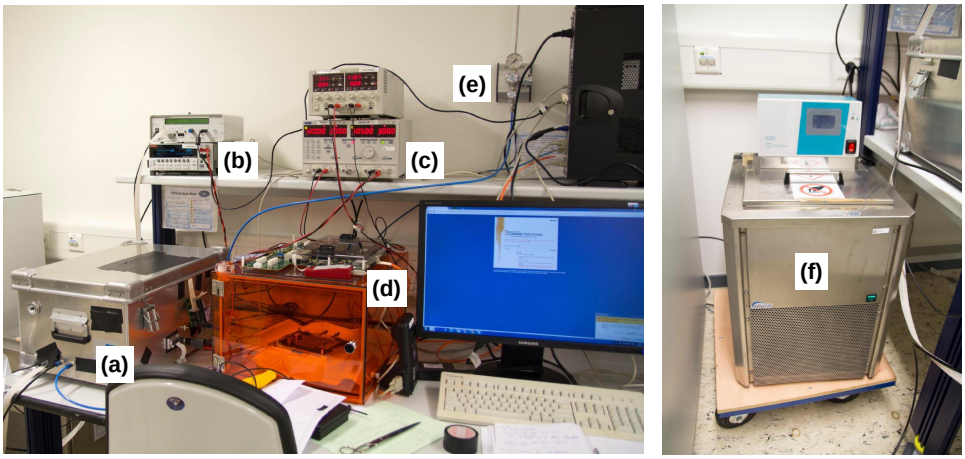

Figure 4.12: The experimental setup for the modules and petalet testing.

The petalet or module control and analysis require a data acquisition system. This consists of a developed software package called SCTDAQ [115] and binary High-Speed-Input/Output (HSIO) board (see Figure 4.12(d)). The SCTDAQ software was used for the system tests of the current SCT and subsequently, modified for petalet geometry requirements: to configure and control the front-end electronics. It includes a set of ROOT [116] macros which analyses the raw data and allows the use of a graphical user interface. The HSIO board is used for data processing and the hybrids connection with a computer via the interface board and generic board with a programmable Virtex-4 field-programmable gate array (FPGA) chip. The HSIO is connected to the petalet by means of the second, suffer board called

EoP, with an SAMTEC ribbon cable.

For the binary readout system, one of the best methods to acquire the desired information about the input noise and a gain for each channel is called *threshold scan*. This consists of charge injection calibration, which is produced by charge injection circuitry which includes calibration capacitors of the chip, into every channel over a possible range of the discriminator threshold settings. This procedure is repeated for typical number of times. In an ideal case, the scan will show a sharp-edge step function with no hits if the injected charge is below the threshold and with all the hits if the injected charge is above the threshold. Due to the presence of the electronic noise the step function is smeared out and has an appearance of S-curve and shown in Figure 4.13(a). Then each threshold scan, S-curve, is fitted with a complementary error function. A mean value of the fit function gives the threshold voltage for which the occupancy is about 50% and defined as the V_{t50} point. The output noise of the channel is interpreted as a width of the function. The complementary error function is defined as:

$$f(V_{thr}, \mu, \sigma) = \frac{1}{2}\Big(1 + erf\Big(\frac{\mu - V_{thr}}{\sqrt{2}\sigma}\Big)\Big), \tag{4.1}$$

where V_{thr} is the certain threshold voltage, μ is the mean signal height and σ is the width.

The V_{t50} points yielded for three different input charges are used to determine the gain and extrapolated offset (indicates an output at the zero charge injection) of each chip. The gain is obtained from the linear fit to the data points and shown in Figure 4.13(b). Afterwards, the input noise is calculated through dividing the output noise by the calculated gain as follows:

$$\text{Noise}_{\text{input}}[ENC] = \frac{\text{Noise}_{\text{output}}[\mu V] \cdot 6250}{\text{Gain}[\mu V/fC]}, \tag{4.2}$$

where 6250 is the conversion between fC.

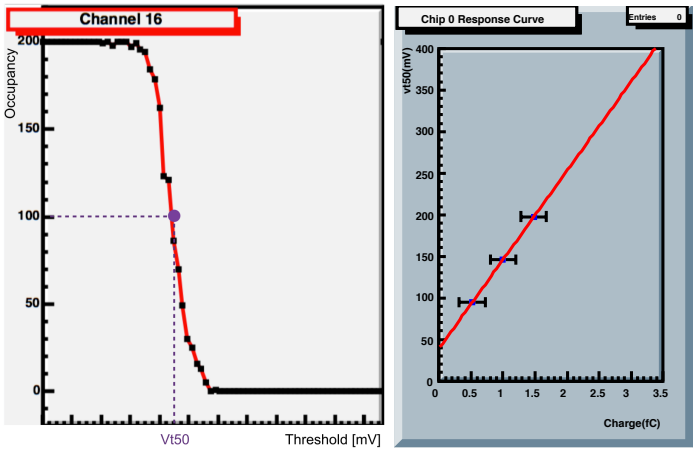

(a) (b)

Figure 4.13: (a) Result of the threshold scan showing the number of hits versus the threshold value for one channel from one chip measured by the SCTDAQ. (b) The V_{t50} value as a function of the injected charge measured by the SCTDAQ.

The set of tests and calibrations were defined to estimate the electrical performance of the modules and petalets. All tests are based on the threshold scans, strobe delay and trim values for different input charges. Once the strobe delay, idelay and trim settings are defined they are unchanged for all tests. The sequence of those tests was defined as follows [117]:

- **Capture and configuration of BCC ID.** This captures important ABCN-25 specific actions that determine proper communication with the hybrids and ensures that the data can be read out from them. It allows the reading BCC IDs and the BCC configuration register of each hybrid. In a case that no IDs or configurations are written to the burst panel, it indicates the problems with BCC (not working BCC, missing wire bonds, etc.) and further test will be not allowed.

- **Idelay scan.** The idelay scan is needed to optimize the delay time for the HSIO. It compensates the delay between the clock sent out and sent out back by the HSIO to the readout chip. This delay is mainly influenced by the length of the flat ribbon cable between the buffer board and the HSIO interface. Once the value for each module is defined and saved to the configuration file, it is used for further tests.

- **Strobe delay scan.** The strobe delay calibration is one of the necessary calibrations before other tests and allows to adjust the best charge injection timing. The strobe delay is the time between injecting charge into a channel of the chip, ABCN-25, and a discriminator's clock to read it out. It is important to set a timing for a synchronization of the calibration signal with a discriminator's clock. When the timing is too short, the discriminator will fire too early and no hits will be read out. And if it is too long, the discriminator will fire too late with no signal arriving. Figure 4.14 shows the hit occupancy as a function of the strobe delay for each strip channels. The rising edge and falling edge of the region with maximum occupancy are used to find an optimal value of the strobe delay. It is calculated from the fits for each chip taking the value which is 25% of the distance between the rising edge and the falling edge with respect to the rising edge. The average value of the hit efficiency from every channel of each chip versus the strobe delay and the resulting width of the working strobe delay range is shown in the second row in Figure 4.14.

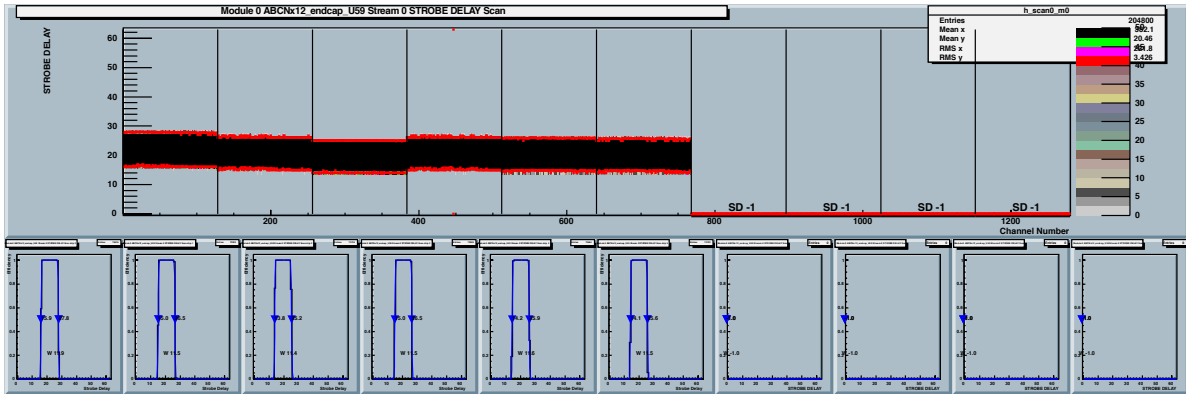

Figure 4.14: The strobe delay for all channels of the ABCN-25 chip on the upper part and the average hit efficiency of all channels of each individual chip versus the strobe delay and fit on the bottom part.

- **Three point gain.** One of the important tests that is a part of the threshold scan performance, described before, at three different injected charges is a three point gain test. Two three-point gain scans were used, which correspond to an injected charge of 1 fC (with corresponding charges of 0.5 fC, 1.0 fC and 1.5 fC) and 2 fC (with corresponding charges of 1.5 fC, 2.0 fC and 2.5 fC). The output of the test is presented for all six readout chips (768 channels). The results of the test which are obtained with full characterization of each channel, the V_{t50} point, gain, extrapolated offset and output noise values, is shown in Figure 4.15.

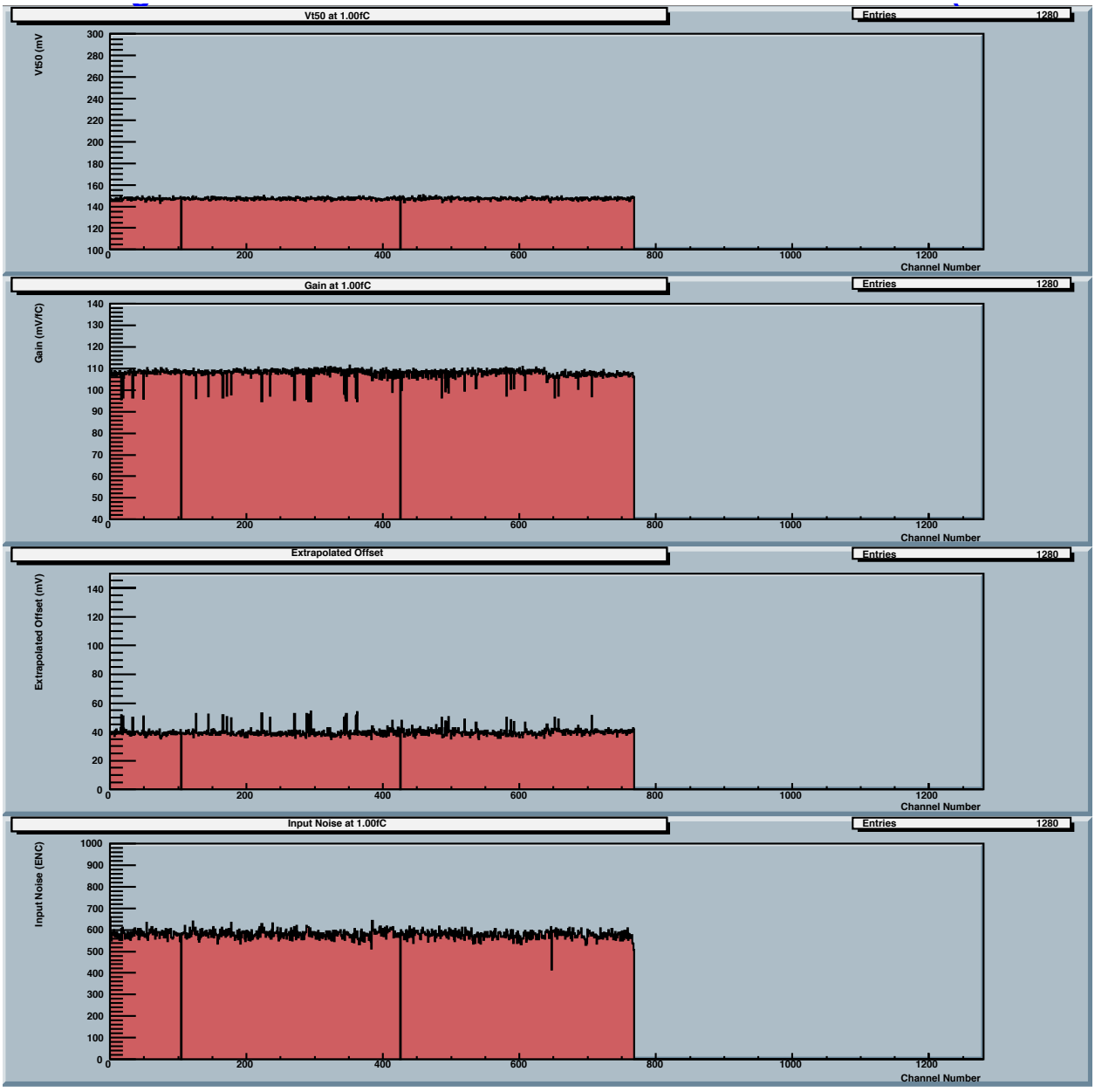

Figure 4.15: The results of three point gain test showing the V_{t50}, gain, extrapolated offset and output noise values for each channel for one module and for one stream of the petalet.

- **Trim range.** Trim settings are important to minimize differences in a response of individual channels. The test selects the optimal trim range settings to have as low as a possible variation of the offset of signals for a maximum number of channels and can be applied to each channel. Each channel has internal TrimDAC (digital-to-analog converters) to control the comparator offset. For this purpose, the threshold scan is started for all possible TrimDAC settings in order to determine the best value for each channel. The test results are more accurate for the entire hybrid as the characteristic of each individual channel is taken into account.

- **Response curve.** The response curve test is based on the three point gain but with an extension to ten different charge injections and with more statistics per the injection point. This test gives a more precise measurement of the gain and offset.

4.3.2 Single-sided Petalet

The first assembled single-sided petalet, so-called petalet-01, is displayed in Figure 4.10. The details on the structure were given in Section 4.2.

Before measuring the electrical performance of the modules on the test frames or mounted onto the core, an important current-voltage characteristic, I–V curve, should be measured to assess the sensor quality. It provides the information on an amount of the leakage current and on the depletion voltage by showing possible combinations of the current and voltage. Furthermore, it indicates the maximum feasible HV which can be applied to the sensors in order to avoid breakdown and minimize the leakage current which can negatively affect the sensor performance by increasing the noise contribution.

To examine the I–V characteristic of the sensors mounted onto the core of the petalet-01, HV was applied in a step of 10 V and the leakage current was monitored and measured in parallel. It was repeated at three different temperatures, 5 °C, 10 °C and 15 °C, with low voltage powered on and off. The low voltage introduces the additional heat which translates on the amount of leakage current. The I–V curve for the upper and lower module of petalet-01 is presented in Figure 4.16. The values of the current from the I–V curve reflect the dependence of the leakage current from the temperature. Especially, in the case of powering with low voltage the sensors get hotter, and the current values become approximately three times higher. It can be seen in the thermal picture of the whole petalet after the testing in Figure 4.18. Furthermore, the HV, which corresponds to the plateau region and the condition for the safe operation of the module for further tests, is defined to be not higher than –150 V.

In order to evaluate the petalet, the set of tests described in the previous section was performed. The main results were obtained from the three point gain tests (after correct settings of the strobe delay, idelay and trimming), concentrating on the input noise. The comparison of the input noise between the lower and upper modules including both streams (each of the streams from the hybrid consist of six front-end chips, reading a full strip row each) at the single-sided petalet-01 is shown in Figure 4.17. The noise tests were performed at the injected charge of 1 fC with the different sensor bias voltage: –70 V, –100 V, –120 V and –150 V. The chiller temperate was set to 5 °C during the test. The obtained values, measured in electrons, are calculated as the average values per chips. The results indicate that the input noise stops to decrease with the depletion of the sensor and that the lower module has higher input noise in comparison to the upper module. The average noise per module was 858 e^- for the lower and 598 e^- for the upper module. Those results are comparable with the values from the test of modules on the test frame, which showed the average input noise of 736 e^- and 564 e^- per module, respectively. The higher noise for the lower module originates from the sensor characteristics. The upper and bottom sensors have been designed with the different size of strip pitch and different length of the strip, and as a consequence, different interstrip capacitances and resistances are expected. The interstrip capacitance strongly depends

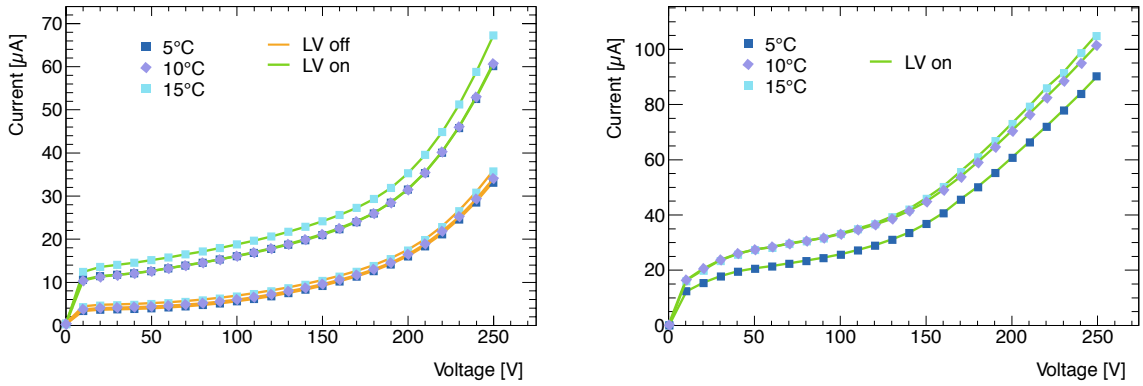

Figure 4.16: The I–V curves characteristic of the modules mounted to the core for the petalet-01. The I–V measurements are shown for three different chiller temperatures for the lower (left) and upper (right) modules and with low voltage powered on and off (only lower module). The sign of the voltage is not considered on the plot.

on the ratio of the strip width to the pitch and is the main factor contributing to the noise and should be kept as small as possible. In the case of the same width for the upper and lower module, the larger strip pitch (upper sensors) will translate to the smaller interstrip capacitance and smaller noise and vice versa. The longer strips of the lower module (see Table 4.1) will imply a higher interstrip capacitance as well, therefore, the higher input noise.

The acquired noise measurements depend on the particular setup optimization level as an grounding and shielding. Therefore the DC–DC converters were optimized with the copper foil shielding which was connected to the LV ground of the petalet. In addition, the noise also depends on the hybrid temperature, increasing by 1.5 electrons per degree Celsius. The overall infrared recording of the heat output from the petalet-01 shows that the hottest part of petalet is DC–DC converters with the temperature above 46 °C and the hybrids with the temperature in the range from 34 to 41 °C. The infrared monitoring is also a helpful tool which allows to identify the problematic parts of the petalet in the case of the readout or power failure.

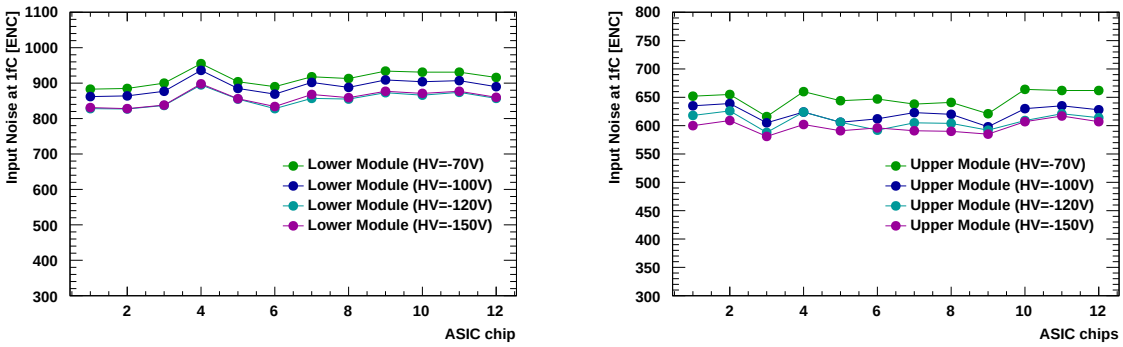

Figure 4.17: The averaged input noise values per each chip obtained for the different sensor bias voltage at the chiller temperature of 5 °C for the petalet-01, including the values for the lower and upper modules.

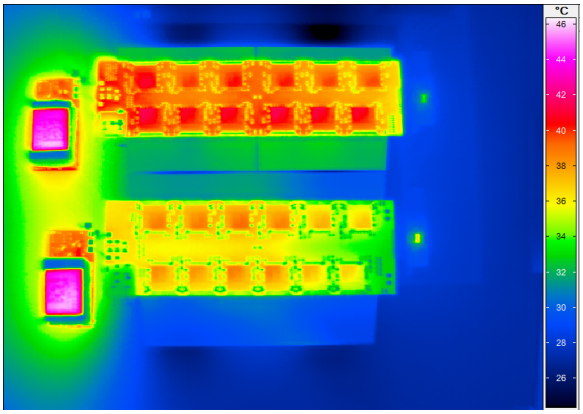

Figure 4.18: The infrared recording of heat output from the petalet-01 during the measurement.

4.3.3 Double-sided Petalet

The second assembled petalet, so-called petalet-02, is double-sided and one of the sides is shown in Figure 4.10. The main difference in comparison with the petalet-01 is the shielded bus tape on the power lines and below the DC–DC converters, apart from having modules on both sides.

Modules on the test frame

The first tests were done to evaluate the performance of the modules following the standard principle of the testing. First of all, before the gluing of modules onto the core, they were tested on the test frame to have the reference noise for the modules which correspond to the front and back side of the petalet-02.

Front side. The three point gain test was performed at the injected charge of 1 fC with applying bias voltage of –70 V to the upper (59 BCC) and lower (60 BCC) modules. The chiller temperature setting was 10 °C. The results of the test, which consist of values of input noise averaged per chip for the lower and upper modules including both streams (Stream 0 and Stream 1), are given in Figure 4.19. The upper module specifies the lower input noise and finer consistency between two streams in comparison with the lower one which has the higher noise and some variation of the noise between the first chips in both streams.

Back side. The same test was done for the upper (61 BCC) and lower (62 BCC) modules on the back side of the petalet-02 but with different sensor bias voltages, –70 V, –100 V and –130 V, and the chiller temperature was set to 5 °C for the tests. The input noise averaged per each chip is shown in Figure 4.20(a) and demonstrates similar amount of the noise. The modules are depleted starting from –100 V bias voltage except the upper module. The dependence of the input noise from the applied HV is shown in Figure 4.20(b) as well. An additional evaluation of the chips exhibiting higher noise was performed comparing the results measured before shipping to DESY Hamburg and after. It demonstrates a small impact of the transportation for few chips in Figure 4.21, which is unexpected. Nonetheless, it is a small effect and new transportation boxes are currently being designed and one needs to look at this with more modules.

Modules glued onto the core

The I–V characteristics were measured for the modules glued onto the core of the front side of the petalet-02 and the results are shown in Figure 4.22. The current was measured for two cases: HV steps

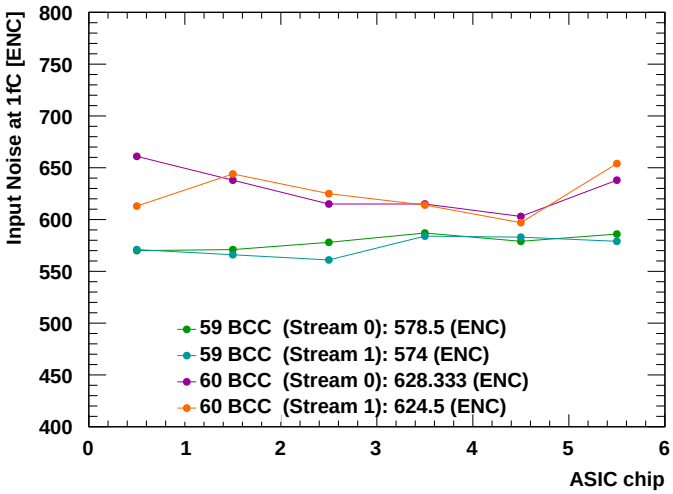

Figure 4.19: The averaged input noise values per each chip obtained for upper (59 BCC) and lower (60 BCC) modules on the front side of the petalet-02 at biasing voltage of –70 V before gluing onto the core. The measured values are presented for each stream.

of 2 V (LV off) and 5 V (LV on). The I–V curve indicates that the applied HV can be beyond –100 V for further tests. The upper module stays hotter than the lower one as expected, and as it was seen in the case of the petalet-01.

In order to compare both single-sided petalets, the same set of tests were performed for the front side of the petalet-02 for different sensor bias voltages, –70 V, –100 V, –120 V and –150 V, as it was done for the petalet-01. The average input noise per chip is shown for both modules in Figure 4.23. The higher noise for the left upper sensor disappeared with the increased HV and became flatter. The average input noise for both petalets is similar for the upper modules while the lower module of the petalet-02 shows the lower noise by around 170 e^-. The final comparison between two single-sided petalets is shown in Table 4.2. In general, the petalet-02 shows the lower input noise then the petalet-01, which had the fully depleted sensors. The lower noise can be explained by improved grounding and shielding on the petalet-02: LV ground and LV shield, data return and data shield, and data shield and CF facing were connected. In addition, the petalet-01 had lower quality sensors, grade B, in comparison to the petalet-02 which can be translated to the difference in the noise results as well.

	Upper Module		Lower Module	
HV [V]	(petalet-01) ENC	(petalet-02) ENC	(petalet-01) ENC	(petalet-02) ENC
–70	647	631	913	817
–100	621	598	891	746
–120	606	588	854	711
–150	598	577	858	685

Table 4.2: The comparison of two single-sided petalets at the same test conditions. The input noise is given for the upper and lower modules at different bias voltages.

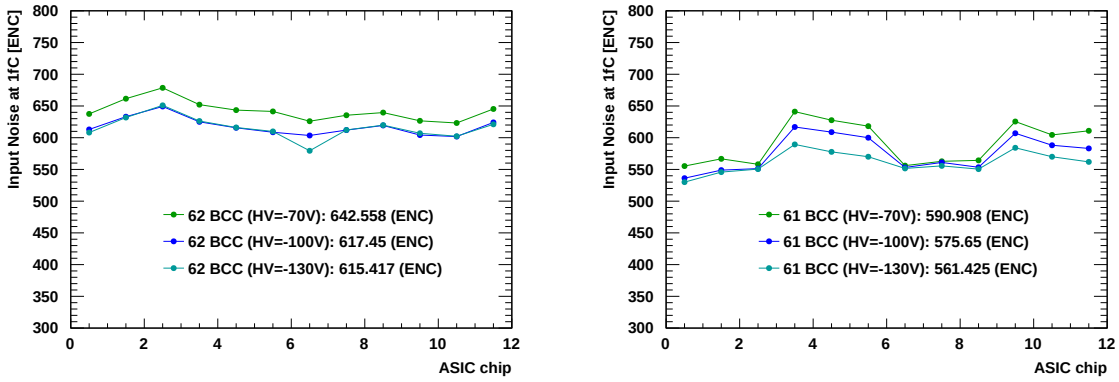

(a)

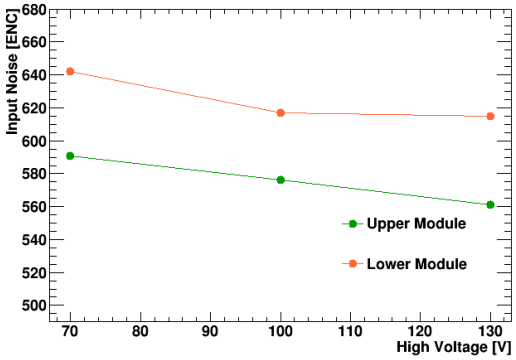

(b)

Figure 4.20: (a) The averaged input noise values per each chip obtained for the upper (61 BCC) and lower (62 BCC) modules on back side of the petalet-02 at the different biasing voltage before gluing onto the core. (b) The dependence of the input noise from applied high voltage.

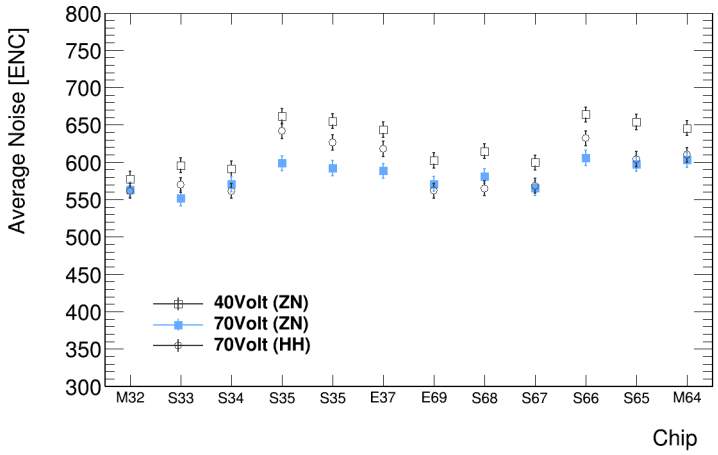

Figure 4.21: Comparison of averaged input noise values per each chip for upper module obtained at DESY-Zeuthen (ZN) before shiping and at DESY Hamburg (HH) after shipping. Taken from [105].

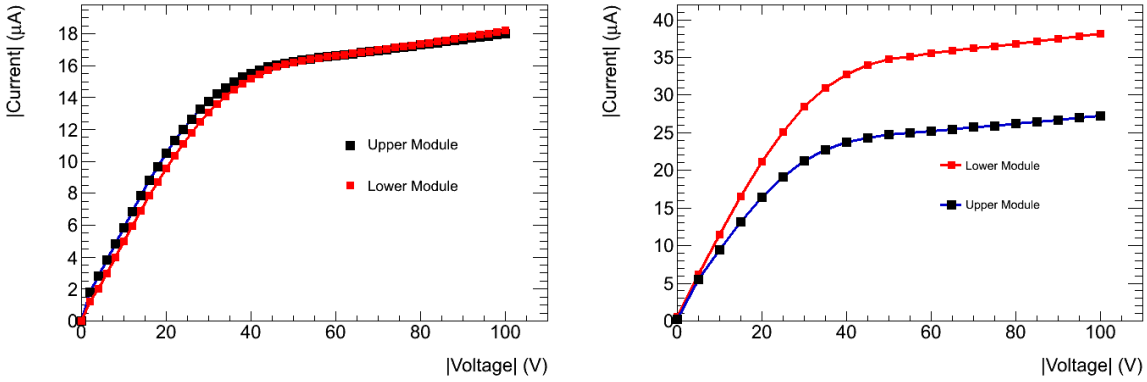

Figure 4.22: The I–V curve characteristic of the modules assembled to the core for the front side of the petalet-02. The I–V measurements are shown for the lower (left) and upper (right) modules and with the low voltage powered on and off.

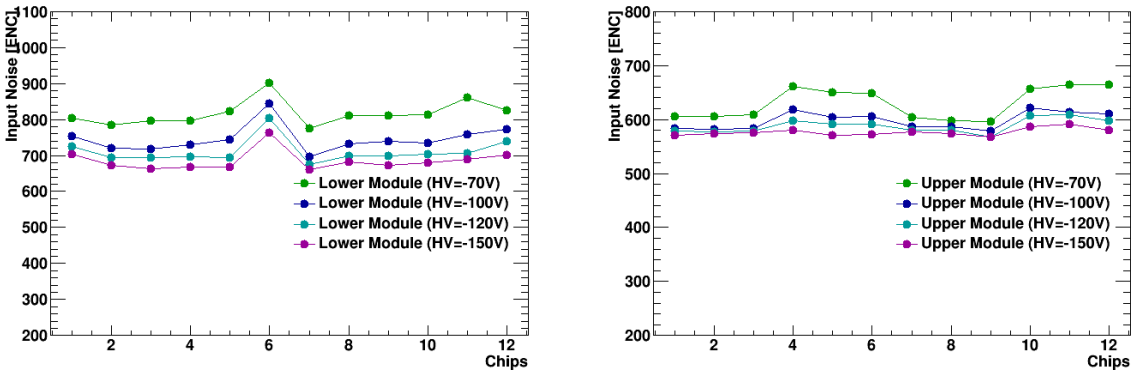

Figure 4.23: The averaged input noise values per chip obtained for the different sensor bias voltage from the petalet-02, including the values for the lower and upper modules.

The final results for the double-sided petalet with simultaneously and independently running both sides were obtained with fully depleted sensors at –150 V bias voltage and by holding the chiller temperature around 0 °C. The results are shown for both sides simultaneously and synchronously read out and with each side independently operated (turning off one of the sides) in Figure 4.24(a), and demonstrate the averaged input noise per each chip obtained from the three point gain test for both cases. It indicates an almost negligible increase in noise concerning each side tested simultaneously, related to the increased temperature due to the higher power dissipation.

The measurements were repeated ten times following the standard test sequence and showed an extremely stable behaviour after the trimming (see Figure 4.24(b)).

4.3.4 Comparison between two readout versions

A variety of tests have been done for six petalets in different institutions. Two double-sided (DS) petalets with the split readout scheme and with the standard and embedded sensors were evaluated in the University of Freiburg; one DS petalet with the common readout scheme has been evaluated in IFIC, Valencia; three petalets with the split readout scheme were evaluated at DESY: two, DS and single-sided

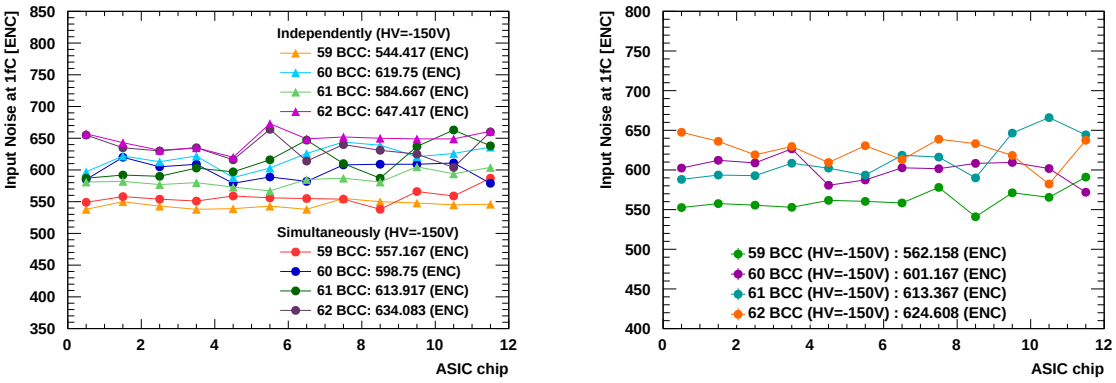

(a) (b)

Figure 4.24: The averaged input noise values per each chip obtained for the full double-sided petalet-02 which consist of four modules. (a) The measurements are presented for the simultaneous and independent readout of both sides. (b) The measurements are presented for ten times performed three point gain test on four modules running simultaneously. The errors bars are tiny and are not visible on the plot.

(SS), with standard sensors and one SS with the embedded sensors. The outcome from the production of all petalets, including the cores, bus tapes and modules on the core assembly, and the electrical tests was summarized on the ITk strips petalet review.

The comparison of the input noise and key features between all petalets are summarised in Table 4.3. All values of the input noise were obtained for fully depleted sensors at the lowest temperature of the operation. All modules were run simultaneously, except the embedded petalet at DESY, due to issues related to the misconfiguration of the BCC ASICs that were not solved at the time of summarizing all the results. The comparison between two readout versions shows that the split versions of petalets run with lower input noise. The petalets with the lower quality sensors, grade B, indicate the higher noise values compared to the values obtained for higher quality sensors, grade A. In general, the results demonstrate that the petalets with the embedded sensors had the higher noise compared to the standard ones as it is expected, and the results are lower then the expected values created by minimum ionizing particle (MIP), which is about 22000 electrons. The signal to noise ratio is for greater than ten for the double-sided petalets with the standard sensors of grade A for injected charge of 1 fC.

The general problems and issues observed during the testing of the petalets and modules were the following:

- BCC configuration and defective BCC's
- broken wires
- complications related to simultaneous readout of both sides
- replacement and shielding of DC–DC converters
- broken traces on the bus tape

In addition to comparison of the input noise between two readout versions, the main features of the cores, bus tapes and mounting modules onto the core were reviewed in the framework of a future production of the petal.

	DESY (DS)	DESY (SS)	DESY (SS)	Uni Freiburg (DS)	Uni Freiburg (DS)	IFIC (DS)
Type of sensors	standard	standard	embedded	standard	embedded	standard
Grade of sensors	A	B	A	A/B	A/B	A
T [°C]	0	15	5	–20	–20	–15
HV [V]	–150	–150	–140/–130	–200	–100/–250	–150
Input noise per petalet [ENC]	601	674	728	597	727	618

Table 4.3: The averaged input noise values together with the main conditions of the test and characterisation of sensors for double-sided (DS) and single-sided (SS) petalets evaluated in the different institutions.

The gluing procedure for the bus tapes onto the core is similar for the split and common readout versions. The small difficulties appeared in the gluing of the common readout version due to the wrapped-around design: the bus tape is glued from the top because it has to be fitted through the cooling pipes first. It can cause more mechanical complications for the bus tape co-curing with face sheets for the real petal. Moreover, the coefficient of thermal expansion (CTE) mismatches can appear on a larger object like the bus tape for the common readout layout.

The module mounting onto the core for both versions of the petalet requires equal number of assembly steps. The split hybrid, where each hybrid has its own sensor, was easier for the module assembly and mounting, but would require more mounting steps. The module placement accuracy strongly depends on the module assembling accuracy, therefore small realignments were needed. From the module mounting experience, higher accuracy is expected if the pick-up of the module with the vacuum tools occurs from the sensors as opposed to pick them up from the ASICs.

Finally, two approaches, single-sided and double-sided electrical topologies depending if data and power lines are at the same side of the petal, were considered with important electrical and mechanical differences towards the petal manufacture. The single-sided electrical topology can deliver the advantage in a smaller amount of DC–DC converters, separation of power and data lines on the bus tapes and provided HV isolation by the bus tape. Also, this topology will require the bus tapes covering entire petal surface with two flavors, one per side (left and right). The double-sided electrical topology foresees the data and power lines on the same lateral side and, therefore, double-sided bus tape, folded on the top, and a bridge that connects one side to EoP. One of the advantages of this topology is that only one flavor of bus tape and a smaller version of it (since not all petal area will be covered) is required.

The short summary of advantages and disadvantages for building split or common readout scheme towards the petal is given in Table 4.4.

In general, the split readout version allows the production and development of the hybrids and bus tapes in a more direct manner with the barrel staves, while the common readout version will require an additional solution with the single EoP. The review panel, taking into account all features presented during the review, recommended the selection of the split readout scheme with split hybrids as the baseline for development of petals in the 130 nm program.

Electrical performance			
Split scheme		Common scheme	
advantages	*drawbacks*	*advantages*	*drawbacks*
• separated power and data lines • HV isolation by bus tape • less DC–DC converters	• two flavours of bus tapes	• one flavour of bus tape	• bridge required on one side to connect to EoP • two ears of EoP • more DC–DC converters
Mechanical assembly			
Split scheme		Common scheme	
advantages	*drawbacks*	*advantages*	*drawbacks*
• equal module assembly steps • identical hybrids per side	• more steps for module mounting • precise alignment for upper hybrid	• split and independent hybrids with its own sensors • easier to handle	• left/right hybrid design • difficulties with interconnections
Bus tape design			
Split scheme		Common scheme	
advantages	*drawbacks*	*advantages*	*drawbacks*
• one per side of petal • easy to glue	• covers all petal surface	• one covers both side of petal • less material	• wrapped-around design • co-curing with face sheets • CTE mismatches

Table 4.4: The short summary of advantages and disadvantages for the split and common readout scheme towards the petal building

CHAPTER 5

Measurement of the Z-boson cross sections

5.1 Cross-section definition

The total cross section for Z-boson production times the branching ratio for decays into leptons, in both the electron and muon decay channels, can be calculated using the following equation

$$\sigma_Z^{\text{total}} = \sigma_Z \times BR(Z \to e^+e^-/\mu^+\mu^-) = \frac{N_Z - B}{\mathcal{L} \cdot C_Z \cdot A_Z}, \tag{5.1}$$

where

- N_Z is the number of Z-candidate events observed in data;
- B is the number of electroweak background events;
- $\mathcal{L}$ is the integrated luminosity, which corresponds to the dataset;
- C_Z is the correction factor, which corrects the cross section for the detector efficiency and is defined below;
- A_Z is the generator acceptance, defined below.

The correction factor, C_Z, includes as a primary component the efficiency of reconstruction and identification for Z-boson decays within fiducial volume. It is defined as the ratio of the total number of generated events which pass the final selection requirements after the reconstruction, $N_{\text{MC,rec}}$, and the total number of generated events within the fiducial acceptance, $N_{\text{MC,gen,fid}}$, using the equation

$$C_Z = \frac{N_{\text{MC,rec}}}{N_{\text{MC,gen,fid}}}. \tag{5.2}$$

The acceptance, A_Z, is estimated at generator level as the fraction of estimated events after the fiducial cuts, $N_{\text{MC,gen,fid}}$, to all generated events within the mass window $66 < m_{\text{ll}} < 116$ GeV, $N_{\text{MC,gen,mass}}$:

$$A_Z = \frac{N_{\text{MC,gen,fid}}}{N_{\text{MC,gen,mass}}}. \tag{5.3}$$

The fiducial cross section for Z-boson production times the branching ratio is defined in the fiducial volume of the detector (i.e. close to the detector volume) and is defined by several kinematic requirements

described in Section 2.5. The fiducial cross section does not require the knowledge of the A_Z factor and is connected to the total cross section in the following way:

$$\sigma_Z^{\text{fiducial}} = \sigma_Z^{\text{total}} \cdot A_Z = \frac{N_Z - B}{\mathcal{L} \cdot C_Z}. \tag{5.4}$$

Following the definition of the total and fiducial cross sections all components expressed in Equation 5.1 are evaluated. All sequential steps performed to obtain the cross-sections results are described in the next sections. The number of Z-candidate events decaying into leptonic final states with muons or electrons are estimated from the data samples, while the number of the background events (see Section 5.6), correction and acceptance factors are estimated from the Monte Carlo simulated samples, which are described in Section 5.2. The event and Z-boson selection criteria applied on the reconstructed objects are presented in Section 5.4. The calculation of corrections which enter the analysis through the correction factor, C_Z, is described in details in Section 5.5. The experimental systematic uncertainties in the measurements of the cross sections enter via the correction factor, the luminosity and through background subtracted events and are presented in Section 5.7. Finally, the evaluated cross sections are presented in Section 5.9.

5.2 Data and Monte Carlo simulations

5.2.1 Data sample

The dataset used for $Z \to \ell^+\ell^-$ (for $\ell^+\ell^- = e^+e^-$ and $\mu^+\mu^-$) measurements was recorded between August 16 and November 03 in 2015. At that time 6.5 TeV proton beams circulated at the LHC with 25 ns bunch spacing. The peak instantaneous luminosity was $L = 5.1 \times 10^{33}\,\text{cm}^{-1}\,\text{s}^{-1}$, and the average number of pile-up events was $\langle\mu\rangle = 13.5$. The runs corresponding to the full 25 ns dataset, collected during D–J data periods, are found in the range 276262–284484.

The analysed data that pass basic data-quality requirements, encoded in a Good Run List (GRL) (see Subsection 5.4.4), correspond to a total integrated luminosity of $3.16\,\text{fb}^{-1}$. The GRL specifies sets of good luminosity blocks, which are two minutes of data taking, with approximately constant instantaneous luminosity and a fully operational detector. It is formed by applying data-quality criteria to the list of all valid physics runs and luminosity blocks, since not all recorded data is good for physics analysis. The total integrated luminosity is calculated with the luminosity tag OflLumi-13TeV-004, available on May 23 in 2016. The comparison between total integrated luminosity delivered to ATLAS, recorded by ATLAS and luminosity after passing the GRL is shown in Figure 5.1. The uncertainty on the integrated luminosity is ±2.1%. It is derived, following a methodology similar to that detailed in Reference [118], from a preliminary calibration of the luminosity scale using $x - y$ beam-separation scans performed in August 2015. The values of integrated luminosity for each run are presented in Appendix A.2.

The data samples are available in new xAOD (Analysis Object Data) format, which is readable by both ROOT-based [116] and Athena frameworks (see Subsection 3.4.1) and is smaller size then the initial AOD format. The xAOD data format contains events, which are reconstructed from raw detector data. Reduced versions of the xAOD are produced from the xAOD samples by applying specific selection criteria required for a particular group of analyses and are referred to as derived xAOD (DxAOD). The DxAOD sample are designed to be not larger than 1% of the full xAOD.

Dedicated samples for the Drell–Yan processes, so-called STDM3, are produced by the Standard Model working group. They contain selected skim dilepton events with the data production tags (p-tag) p2425 and p2436 and are used for the selection of objects and calculation of cross sections. Skimming refers to a method of the reduction of events in which the events that do not pass selection criteria are

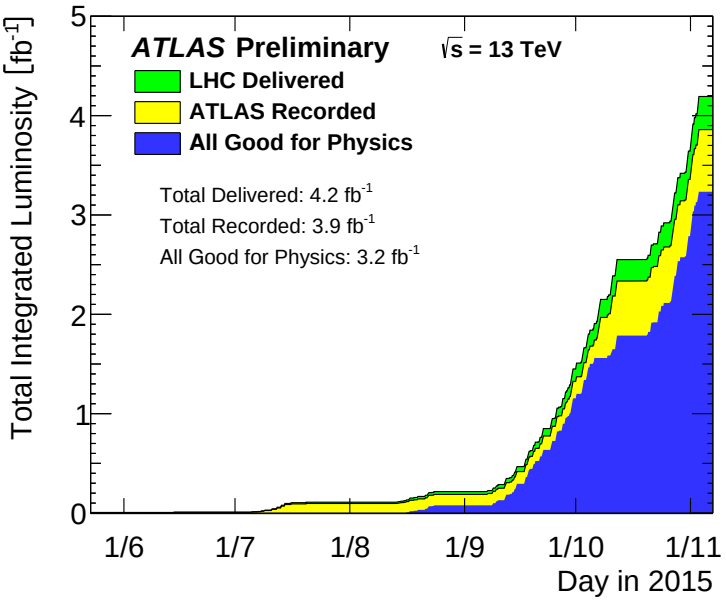

Figure 5.1: The luminosity measurement at the ATLAS interaction region for 2015 data taking. The total integrated luminosity delivered by LHC versus day, recorded by ATLAS and used for the analysis after passing basic data-quality requirements is presented. Taken from [119].

rejected. The p-tags correspond to the production features and configurations (ATLAS software releases and etc.). The selection which is applied for STDM3 derivation requires exactly two or more leptons or passing the dilepton triggers. The lepton selection criteria are shown in Table 5.1.

Selection criteria	**Electron channel**	**Muon channel**
p_{T}	$\geq$ 15 GeV	$\geq$ 15 GeV
$\lvert\eta\rvert$	< 2.6	< 2.6
Quality	IsEMLoose or LHLoose	GoodMuon (basic MCP track requirements)
Triggers	`HLT_2e12_loose_L12EM10VH` or `HLT_2e15_loose_L12EM13VH` or `HLT_2e17_loose` or `HLT_2e17_loose_L12EM15` or `HLT_2e12_lhloose_L12EM10VH` or `HLT_2e15_lhloose_L12EM13VH` or `HLT_2e17_lhloose` or `HLT_2e17_lhloose_L12EM15`	`HLT_2mu10` or `HLT_2mu14` or `HLT_mu24_mu8noL1`

Table 5.1: The electron and muon selection cuts applied for the STDM3 derivation. Based on information from [120].

The xAOD samples represent a new data file format which is employed for the Run 2 datasets and which had a requirement for a validation. The procedure of validation involved the testing of MC simulations at 8 TeV before the 2015 data taking period. Checks were made of access to the container information, the analysis framework was adjusted to read of electron and muon information and new performance tools, and kinematic distributions and detector level plots were produced. No problems or

deviations were observed, allowing fast and flexible analysis of the new data with the adjusted framework.

5.2.2 Monte Carlo samples

Monte Carlo (MC) simulation is used in the analysis to evaluate background contamination in the selected event sample, to calculate the acceptance and a selection efficiency and to compare the kinematics distributions with the real data.

Monte Carlo simulation is an important instrument for predicting the physical processes that occur in the pp collisions at the LHC. It is based on random sampling and aims to reproduce high-energy physics events from the collisions. The direct calculation of these processes is a challenging problem. They are simulated by event generators and put into the GEANT 4 (GEometry ANd Tracking) tool [121] to reproduce the detector response to particles that pass through the detector.

The factorization theorem allows this problem to be broken down into the following steps:

- hard process: an initial stage of proton collisions using PDFs and the calculation of matrix elements (ME) using perturbative QCD;
- parton showering process: quarks and gluons produced after the collision will emit QCD radiation in the form of gluons creating parton showers;
- hadronization process: formation of hadrons from partons emitted in the showers, which can decay further into particles;
- underlying events: secondary scattering between two partons that can occur in a single event.

The Monte Carlo generators which are used in the analysis are the following:

- POWHEG-Box (Positive Weight Hardest Emission Generator) [122–124]: is a general framework which produces events of hard hadron–hadron scatterings using the POWHEG method up to next-to-leading order (NLO) accuracy. The output can be interpreted to any shower Monte Carlo program for parton showering and hadronization. The POWHEG-Box is able to calculate Z pair, Drell–Yan vector boson, Z+1 jet, heavy-flavour, Higgs-boson and single-top productions.
- PYTHIA [125]: is a general-purpose parton shower based generator which can simulate lepton–lepton, lepton–hadron and hadron–hadron collisions. The hard processes are calculated at leading order (LO) and higher order corrections are calculated with the parton shower approach. For the hadronization, the PYTHIA uses the Lund string model.
- SHERPA (Simulation of High Energy Reactions of PArticles) [126]: is a multi-purpose event generator for the simulation of particle collisions. SHERPA can simulate the same types of events as PYTHIA but with additional photon induced processes. It has own parton shower and hadronization models. The hard processes are generated by tree-level matrix-element generators.

Samples of inclusive signals $Z \to e^+e^-$ and $Z \to \mu^+\mu^-$ and electroweak background events are generated with the POWHEG-Box Monte Carlo program [122–124], based on next-to-leading order (NLO) calculations, specifically for single boson production [127], interfaced with the leading-order (LO) PYTHIA v.8.1 parton shower program [125]. The programs use the CT10 parton distribution functions [128] and the AZNLO CTEQL1 tune for POWHEG+PYTHIA [129]. The EvtGen v1.2.0 program [130] is used for the bottom and charm hadron decays, and PHOTOS++ version 3.52 [131] is used for QED emissions from electroweak vertices and charged leptons.

The distributions of top quark production (both $t\bar{t}$ and single top) are generated with the POWHEG-BOX v2 generator [122–124] and PYTHIA v.6.4 [132] (Perugia 2012 tune), and the pair production is normalized to the cross section calculated at NNLO+NNLL with the Top++2.0 program [73]. For the $t\bar{t}$ sample, the POWHEG-BOX model parameter hdamp, which controls matrix element to parton shower matching in POWHEG and effectively regulates the high-p_{T} radiation, is set to the top-quark mass, 172.5 GeV, a setting which is found to give the best modelling of the $t\bar{t}$ system at 7 TeV [133].

Samples of simulated diboson events are generated with SHERPA v2.1.1 [126]. Matrix elements for the diboson samples are calculated for 0/1 partons at NLO and up to 3 partons at LO using the same generators and merged with the same parton shower.

Multiple overlaid proton–proton collisions, called pile-up, are simulated with the soft QCD processes of PYTHIA using the A2 tune [134] and the MSTW2008LO PDF [135].

All of the samples are processed with the GEANT 4-based simulation of the ATLAS detector [136].

Simulated event samples from the *MC15b* Monte Carlo production are used in the analysis [137]. The derivations are created with release 20.1.5.10.1 using the setup for 25 ns bunch spacing.

A complete list of all used simulation samples with values of their cross sections is given in Table 5.2 [138]. In addition, the table includes the values of applied filter and DAOD efficiencies, $\epsilon_{\mathrm{filter}}$ and ϵ_{DAOD}. $\epsilon_{\mathrm{filter}}$ takes into account whether all generated events are fully simulated or if some preselection is applied at generation level. ϵ_{DAOD} represents the fraction of events that pass from simulated AOD sample to final derived AOD (DAOD) sample.

Channel	Generator	Order	$\sigma \cdot Br$ [pb]	$\epsilon_{\mathrm{filter}}$	ϵ_{DAOD}	Number of events
Signal samples						
$Z \to ee$	POWHEG-BOX+PYTHIA 8.1	NLO+LO	1 892	1.0	1.0	19 920 600
$Z \to \mu\mu$	POWHEG-BOX+PYTHIA 8.1	NLO+LO	1 892	1.0	1.0	19 964 000
Background samples						
$W^+ \to e\nu$	POWHEG-BOX+PYTHIA 8.1	NLO+LO	11 501	1.0	0.015	699 023
$W^+ \to \mu\nu$	POWHEG-BOX+PYTHIA 8.1	NLO+LO	11 501	1.0	0.015	108 637
$W^- \to e\nu$	POWHEG-BOX+PYTHIA 8.1	NLO+LO	8 579	1.0	0.015	487 904
$W^- \to \mu\nu$	POWHEG-BOX+PYTHIA 8.1	NLO+LO	8 579	1.0	0.015	229 374
$Z \to \tau\tau$	POWHEG-BOX+PYTHIA 8.1	NLO+LO	1 892	1.0	0.025	108 637
$WZ \to qqll$	SHERPA 2.1.1	NLO	3.76	1.0	0.466	115 764
$ZZ \to qqll$	SHERPA 2.1.1	NLO	2.32	0.14	0.475	46 975
$WW \to lvlv$	POWHEG-BOX+PYTHIA 8.1	NLO+LO	10.63	1.0	0.32	319 444
$t\bar{t}$	POWHEG-BOX+PYTHIA 6.4	NNLO+NNLL	451	0.543	0.259	5 040 645

Table 5.2: Simulated event samples used in this measurement and their predicted cross sections times branching fraction, $\sigma \cdot Br$, with the corresponding filters and DAOD efficiencies, $\epsilon_{\mathrm{filter}}$ and ϵ_{DAOD}, and with total number of events for each MC sample as it is given in the AMI (ATLAS Metadata Interface) database in 2016.

5.2.3 MC corrections

Since not all effects are perfectly simulated in the MC samples, several corrections are applied to the MC samples to improve agreement between distributions in data and MC simulations. Scale factors are applied to the MC simulations to correct for any discrepancy in the trigger, identification, reconstruction, and isolation efficiencies for selected objects. Electron energy and muon momentum calibration corrections are applied as well. The differences in the pile-up distributions are corrected too.

p_T distribution reweighting

Comparing the Z-boson p_T and lepton p_T distributions predicted by Powheg+Pythia 8, obtained after the final event and Z-boson selection (see Subsection 5.4.4), a disagreement is noticed with the observed distribution in data in the high p_T regions. Therefore, a reweighting of the Z p_T is performed, using the same data and MC signal samples as for the nominal selection, to estimate effect of it on the C_Z. To take into account the discrepancies observed at high p_T in the Z p_T spectra in both muon and electron channels, the following procedure is done.

The ratio of the Z p_T distribution between data and MC simulations (including backgrounds) is fitted with a polynomial function of degree four: $f(x) = p_0 + p_1x + p_2x^2 + p_3x^3 + p_4x^4$. The fit is performed in the range of $0 < p_T < 250$ GeV and the results are shown in Figure 5.2.

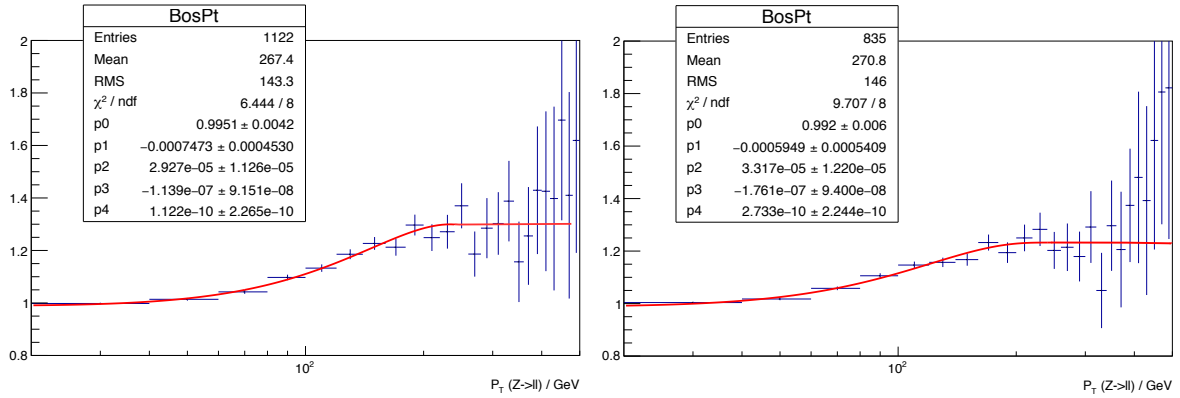

Figure 5.2: Ratio between data and MC simulation of the Z p_T distribution for the electron (left) and for the muon (right) channels. The red curve corresponds to the polynomial fit performed in the range of $0 < p_T < 250$ GeV.

Fit parameters	**Muon channel**	**Electron channel**
p_0	0.99 ± 0.01	0.10 ± 0.01
p_1	$(-5.95 \pm 5.41) \times 10^{-4}$	$(-7.47 \pm 4.53) \times 10^{-4}$
p_2	$(3.32 \pm 1.22) \times 10^{-5}$	$(2.93 \pm 1.13) \times 10^{-6}$
p_3	$(-1.76 \pm 0.94) \times 10^{-7}$	$(-1.14 \pm 0.92) \times 10^{-7}$
p_4	$(2.73 \pm 2.24) \times 10^{-10}$	$(1.12 \pm 2.27) \times 10^{-10}$

Table 5.3: Fit parameters obtained from polynomial fit in muon and electron channel.

A $\chi^2/\text{dof} = 9.7/8$ is obtained for the fit performed in the muon channel with the values for the fit parameters presented in Table 5.3. For the fit performed in the electron channel the values of parameters are found to be consistent with the ones from the muon channel.

The fit parameters obtained from the muon channel are used in the reweighting procedure for both channels in the range of $0 < p_T < 250$ GeV and a constant value determined at 250 GeV is used in the range above 250 GeV. The comparisons between data and MC simulation before the reweighting procedure for Z p_T and lepton p_T distributions for the electrons and muons are shown in Figure 5.3. The comparison between the data and MC simulation after the reweighting procedure for the lepton p_T distributions is shown in Figure 5.22 and for the boson p_T distributions in Figure 5.23.

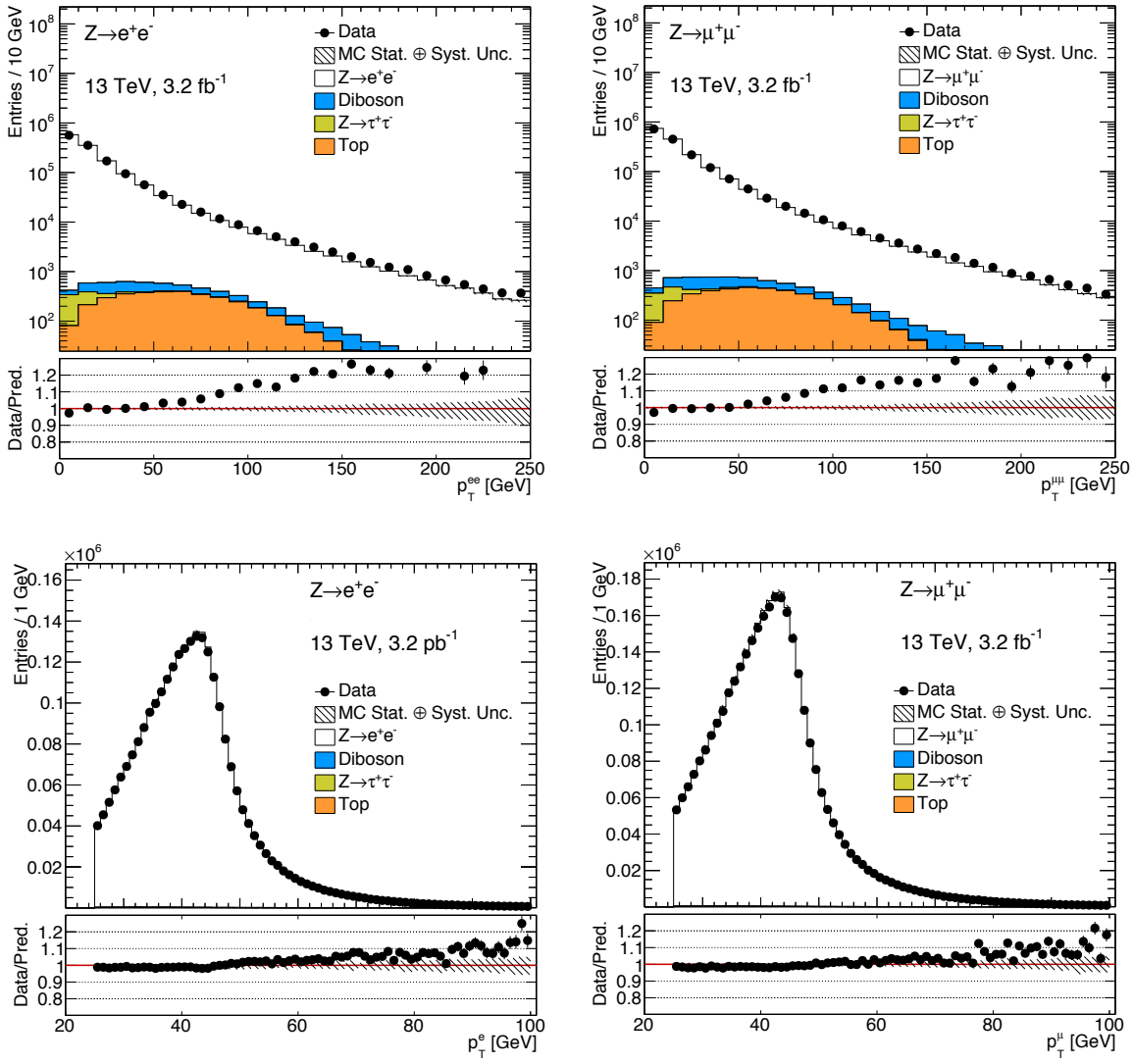

Figure 5.3: Comparison between data and MC simulation of the Z p_{T} and p_{T} distributions for the electrons (left) and for the muons (right) before reweighting of signal MC. Selection criteria applied to the samples and background estimation are described in Subsection 5.4.4 and section 5.6, respectively.

The effect of the impact on C_Z is found to be approximately 0.03% for the muon channel and 0.07% for the electron channel and is included as the systematic uncertainty.

Pile-up correction

Pile-up effect describes multiple proton–proton collisions occurring in the same bunch crossing due to high instantaneous luminosity. It includes interactions from the same bunch crossing (in-time) and from previous bunch crossings (out-of-time). Generally, MC samples are simulated with the pile-up data conditions which are not identical to those in data, because the true value is difficult to predict until data taking has finished. Pile-up can affect kinematic distributions, for instance, number of reconstructed vertices, or reconstruction and isolation efficiencies. Therefore, the MC simulation has to be corrected to match actual values in data by applying additional event weights to each MC event.

The ATLAS official general-purpose reweighting software package PileupReweighting-00-03-18 and the recommendations from the ATLAS Tracking CP group [139] are provided to perform the reweighting procedure. These were used with the recommended settings [140] and applied to the pile-up distribution in the signal Powheg+Pythia MC samples. The tool provides the correct weight for each event using the reference distribution of the mean number of interactions per bunch crossing, $\langle\mu\rangle$, from the MC (for particular run number of MC channel number) and from data (for the total integrated luminosity used in analysis). For that purpose, the pile-up reweighting configuration (PRW config) files are generated using unskimmed signal electron and muon MC samples separately and luminosity calculation file calculated by the iLumiCalc service using the GRL used in the analysis. The pileup weight for each event in the MC simulation is calculated by taking into account the total integrated luminosity delivered by the LHC, L, in the corresponding data periods (runs), A, in the bins, i, of μ distribution:

$$w = \frac{L_{Ai}/L}{N_{Ai}/N},$$

where N_{Ai} is the sum of weights of the events in the same i bins as for data distribution for particular MCRunNumber and N is total sum of weights of the events.

The distribution of $\langle\mu\rangle$ is correlated to the distribution of the number of vertices, which describes on average the contribution of in-time pile-up and which is sensitive for our analysis. Moreover, after $\langle\mu\rangle$ reweighting the distribution of the number of vertices shows a difference between data and MC simulation. Therefore, to improve the description of the number of vertices an additional pile-up scale factor of 1/1.16 is introduced. A comparison between data and MC ($Z \to \mu^+\mu^-$) sample distributions for average interactions per bunch crossing, $\langle\mu\rangle$, and a number of vertices before the correction and after including the additional scale factor is shown in Figure 5.4. It demonstrates that after applying the pile-up reweighting the distribution of number of vertices in MC simulation is not described by data. It is improved by applying the additional pile-up scale factor, while the $\langle\mu\rangle$ distribution is shifted. It is difficult to describe both distributions equally well in data and MC simulation, thus the reweighting is adjusted to fit better the distribution of number of vertices, which is relevant to this analysis.

Scale factors

The scale factor is defined as the ratio between the efficiency obtained on background subtracted data, ϵ^{data}, and the one obtained on $Z \to \ell^+\ell^-$ ($\ell^+\ell^- = e^+e^-$ and $\mu^+\mu^-$) simulated events, ϵ^{mc}, following the equation:

$$SF = \frac{\epsilon^{\text{data}}}{\epsilon^{\text{mc}}}. \tag{5.5}$$

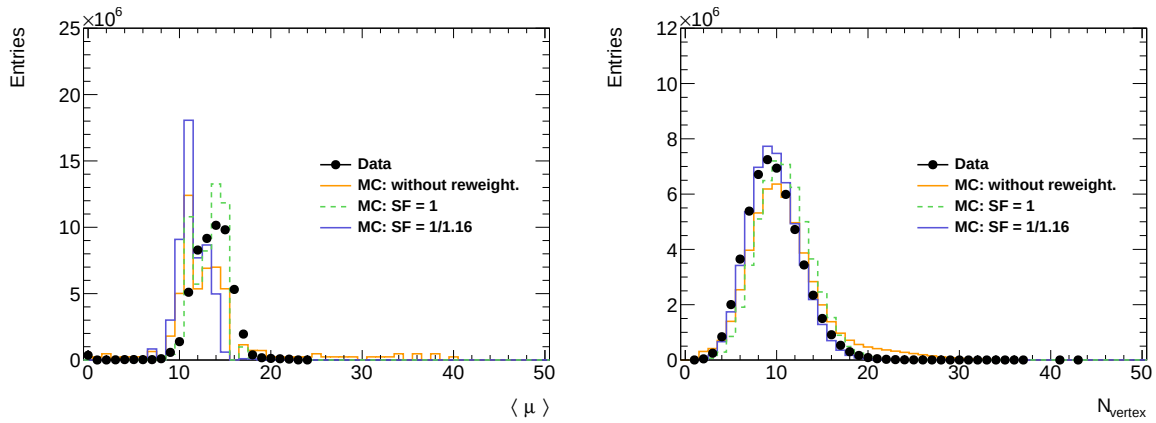

Figure 5.4: Left side: distribution of the average number of interactions per bunch-crossing compared between the data and Pythia MC before pile-up reweighting (orange line) and after (dash-green line) with applying scale factor (blue line). Right side: distribution of number of vertices compared between the data and Pythia MC before pile-up reweighting (orange line) and after (dash-green line) with applying scale factor (blue line).

The scale factors are estimated for trigger, identification, reconstruction, and isolation efficiencies (see Section 5.5) in both channels. They are employed to improve the agreement between data and MC efficiencies by correcting C_Z and therefore applied to each event in MC simulations as a weight in the following way:

$$w^{\mathrm{MC}} = w^{\mathrm{event}} \cdot SF^{\mathrm{reco}} \cdot SF^{\mathrm{id}} \cdot SF^{\mathrm{iso}} \cdot SF^{\mathrm{trig}}, \tag{5.6}$$

where w^{event} is the MC weight, SF^{reco}, SF^{id}, SF^{iso}, SF^{trig} are the reconstruction, identification, isolation and trigger scales factors applied for each lepton (l_1, l_2), accordingly. The event weight is factorized in a series of scale factors, that can be measured independently, since the efficiencies, used for the calculation of the scale factors, are determined for certain selection for leptons that passed previous selection. For instance, the identification efficiency is the efficiency of identification criteria for leptons that passed reconstruction requirements (see more details in Section 5.5).

Electron energy and muon momentum calibration

Corrections are applied to the data in order to correct for miscalibration of electron energy and muon momentum resolution. The official ATLAS tools are used in order to get the calibrations. To correct electron energy scale, the calibration is employed from the EgammaCalibrationAndSmearingTool [141]. To account for imperfect alignment of the muon spectrometer, the muon momentum calibration is performed using the MuonCalibrationAndSmearingTool [142] coupled with the recommendations from a Muon Combined Performance (MCP) group for EOYE (End of Year) 2015. The configuration of tools is summarized in Table 5.4. After, the corrections are applied, the invariant mass resolution is found to be in agreement between the data and simulation and the MC shapes describe the data under the peak within the systematic uncertainty (see Figure 5.25).

Tool name and tag	Tool configuration
ElectronPhotonFourMomentumCorrection-00-01-46	ESModel="es2015PRE" decorationModel="1NP_v1"
MuonMomentumCorrection-01-00-29	default

Table 5.4: Detailed information on the tools used to perform electron-energy and muon-momentum calibration.

5.3 Analysis framework

The measurement of cross sections in this thesis is performed using the ZeeD framework ($Z \to e^+e^-$ DESY) [143], which was initially developed for the selection of Z bosons, which decay into electrons, and evaluation of efficiencies, corrections, background contributions and systematic uncertainties. The ZeeD is a Athena based framework which was configured to read AOD-format information and to analyze data collected from Run 1. Therefore, the following mandatory adjustments are required in order to work with data collected from Run 2 and to analyze Z bosons decaying to muons:

- reading and assessing of all necessary input information from the containers in new xAOD data format;
- implementation of muon objects and all necessary elements into the ZeeD framework in order to analyze $Z \to \mu^+\mu^-$ decay;
- configurations and implementation of new combined performance tools in order to apply the necessary corrections and systematic uncertainties.

The main stages of analysis for the selection of the Z bosons in the ZeeD analysis framework are shown in Figure 5.5. According to the structure of the framework, all necessary information about objects related to the analysis (event, vertex, tracking, muon, electron data and etc.) can be read out and stored from the AOD containers as internal variables in the framework. Therefore, all variables related with the muons objects are added to the ZeeD. Then, the calculation of the four-vectors of muons, applying of various corrections and the evaluation of systematic shifts for each lepton in event, are performed in the corresponding ZeeD Calculator. The calculated lepton objects proceed to the boson Finder. The new Finder for the Z bosons decaying to the muons is added to select all possible Z-boson candidates from every possible pair of muon pairs. Afterwards, the best Z-boson candidate is selected in the next step by applying a final selection to the muon and boson candidates (see Subsection 5.4.4) through corresponding Cut Selectors. Multiple Cut Selectors can be used at the same time. The event, muon and electron selections require separate Cut Selectors in order to select the appropriate Z-bosons candidates and background events. Histograms of various variables, before and after selection including the systematics and generated information (MC) for the events, leptons and bosons, are filled in the Histogram Managers and stored in output files in the ROOT format. Different Histogram Managers represent different objects of the analysis and can be associated with any of the Cut Selectors.

The advantage of the corresponding structure in ZeeD is an opportunity to study efficiencies from tag-and-probe method, which is achieved due to a presence of the Finder, which selects Z-boson candidates using a minimal selection. This allows the selection of events in which leptons may fail some of the cuts as opposed to the standard selection, when the cuts are applied to the leptons first and the Z-boson candidate are built after.

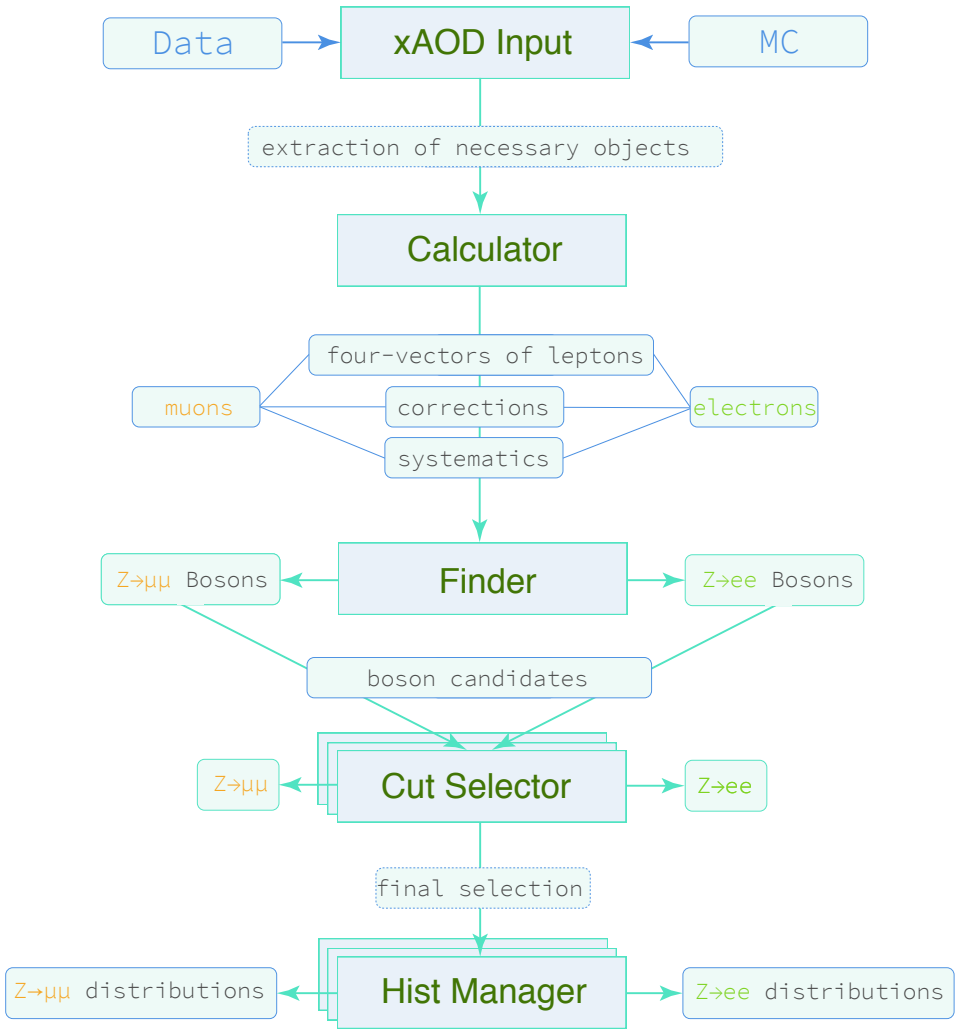

Figure 5.5: The scheme of main stages of analysis for the selection of Z boson in the ZEED framework.

5.4 Object reconstruction and selection

5.4.1 Lepton reconstruction

Reconstruction of electrons. Electrons from the central region of the ATLAS detector can be reconstructed using information about energy deposits from the electromagnetic (EM) calorimeter and tracking information of charged particles from the inner detector (ID). The standard procedure of reconstruction follows three main steps [144]:

1. *Cluster reconstruction.* The first step begins with cluster finding. A sliding window algorithm is used to find seed cluster with a certain amount of total transverse energy above 2.5 GeV in the window size of 3×5 towers in η/ϕ middle layer cell (0.025×0.025).

2. *Track association.* The electron is defined when at least one track can be matched to the seed cluster (central region $|\eta| < 2.5$). This is done by extrapolating tracks from the end of ID to the second layer of the calorimeter. If the distance between the track impact point

and cluster is $|\Delta\eta| < 0.05$ and $\Delta\phi < 0.1$ the track and cluster are matched. In the case, that more then one track matches the same seed cluster, the track with the smallest difference $\Delta R = \sqrt{(\Delta\eta)^2 + (\Delta\phi)^2}$ to the seed cluster is considered as the best match.

3. *Reconstructed electron candidate.* Next, the procedure mentioned above is repeated with tighter conditions, in order to reduce an number of fake electrons. The cluster size is changed (3×7 in the barrel part and 5×5 in the end-cap) to take into account the overall energy distributions in the different regions of the calorimeter. In this step more then one track can be associated to each seed cluster and the energy of the clusters is calibrated to the original electron energy. Then four-momentum of each electron is computed based on the final calibrated energy cluster and the best track matched to original seed cluster.

Reconstruction of muons. Muons are high-energy particles that can traverse through the whole detector reaching the outermost part of the ATLAS, muon spectrometer (MS) and are detected there. Most of the muons can be reconstructed using independent track reconstruction in both the inner detector (ID) and MS. The improved *Chain 3* algorithm from 8 TeV data is used for Run 2 measurements. Several methods are implemented to reconstruct muons depending on the available information from the ATLAS sub-detectors [145]:

1. *Stand-alone (SA) reconstruction.* The reconstruction is based entirely on the information from MS. The tracks are reconstructed there and extrapolated back through the rest of the detector to the beam line, taking into account the energy loss of the muon in the calorimeters. The steps of reconstruction are as follows: the pattern recognition, segment building and track finding and fitting.
2. *Combined (CB) reconstruction.* The reconstruction is based on matching and combining of tracks from ID and MS. Combined candidates have the highest muon purity.
3. *Segment-tagged (ST) muons.* The reconstruction is based on the extrapolation of ID track to the MS. If the ID track is associated with at least one local track segment in the monitored drift tubes or cathode strip chambers, the track is classified as a muon.
4. *Calorimeter-tagged (CT) muons.* The reconstruction is based on the association of ID tracks to an energy deposit in the calorimeter, which compatible with a minimum-ionizing particle.

After reconstruction, lepton objects have to pass more selection criteria to reject as much as possible fake contributions.

5.4.2 Lepton identification

Electron identification. Not all reconstructed electron candidates are signal-like objects and a large number of background candidates, electrons from photon conversions, non-isolated electrons from heavy-flavour decays or hadronic jets, must be identified and suppressed. The signal and background electrons can be identified by applying additional requirements on discriminating variables (electron cluster, shower shapes (calorimeter), tracking (ID detector), transition radiation tracker (TRT) information) and on combined track cluster. The discriminating variables are used for the determination of likelihood (LH) identification, which is summarised in Reference [146]. The LH identification algorithm employs multivariate analysis technique and uses the signal and background probability density functions (PDFs) of the discriminating variables. Three electron selection criteria are provided with applied different selections (*looseLH*, *mediumLH*, and

veryTightLH). These selections are designed to roughly match the electron efficiencies of the loose, medium and tight cut-based selections:

1. *Loose.* This criteria use shower-shape variables of middle layers of electromagnetic (EM) calorimeter. In addition, the hadronic leakage current variable is used, defined in Reference [146]
2. *Medium.* This criteria is based on the loose criteria, adding requirements on EM calorimeter strip layer, track quality with hit presence in the innermost layer of the pixel detector (to distinguish electrons from converted photons) and a looser selection of the transverse impact parameter, and requirements on track-cluster matching.
3. *Tight.* In addition to medium, track quality selection includes a presence of track extension in the TRT, ratio of the EM cluster energy to the track momentum, veto on reconstructed photon conversion vertices associated with the cluster and discrimination against photon conversions via a b-layer hit requirement.

Muon identification. Muons are selected using additional requirements to reject fake muons coming mainly from pion and kaon decays, while selecting prompt muons. Four muon identification selection requirements are provided [145]:

1. *Tight.* These criteria are used to optimize the purity of the sample. They are based only on the combined muon tracks satisfying the medium requirements. χ^2/dof of the global-muon track fit required to be less than eight and an η/p_{T} dependent cut on q/p significance is performed.
2. *Medium.* This is the default selection in ATLAS, which uses only combined and stand-alone muon tracks. The selection requires at least three hits in each of the three layers of monitored drift tubes (MDT) or cathode strip chambers in the pseudorapidity region of $-2.5 \leq |\eta| < 2.7$ and three or more hits on at least two layers of MDT, except the region of $|\eta| < 0.1$ (where tracks with at least three hits in one single MDT layer are allowed). The q/p significance is required to be less than seven.
3. *Loose.* These criteria are used to maximize the reconstruction efficiency while providing good quality muon tracks. Calorimeter-tagged and segment-tagged muons are restricted to the pseudorapidity region of $|\eta| < 0.1$.
4. *High-p_T.* These criteria maximize the momentum resolution for tracks with transverse momenta above 100 GeV. Combined muons passing the medium selection and having three or more hits in three different precision layers are selected.

The first three categories of selection are inclusive. Therefore, *tight* muons are included in *medium* muons, and both are included in *loose* muons.

5.4.3 Lepton isolation

In the addition to the identification requirement, a lepton isolation requirement is needed to reduce the number of fake leptons, the QCD background. The isolation measures the amount of energy near reconstructed lepton. Leptons from the signal are expected to be isolated and tend to have low values of energy, while leptons from weak decays within hadronic jets are non-isolated and lead to large values of energy. There are two approaches based on measuring energy in the calorimeter and the momentum of track in the inner detector:

1. *Tracking isolation.* This uses the information on transverse momenta of the tracks.

- $p_{\mathrm{T}}^{\mathrm{varcone30}}$ This variable is defined as the sum of the transverse momenta of the tracks in a cone $\Delta R = 10\ \mathrm{GeV}/p_{\mathrm{T}}^{\mu}$ around the muon. The maximum cone size is $\Delta R = 0.3$. The tracks considered in the sum must originate from the primary vertex associated with muon track, have $p_{\mathrm{T}} > 1$ GeV, $|\eta| < 2.5$, and at least seven silicon hits.
- $p_{\mathrm{T}}^{\mathrm{varcone20}}$ This variable is defined as the sum of the transverse momenta of the tracks in a cone $\Delta R = 10\ \mathrm{GeV}/E_{\mathrm{T}}$ around the electron, excluding the electron associated tracks. The maximum cone size is $\Delta R = 0.2$. The tracks considered in the sum must originate from the primary vertex associated to the electron track, have $E_{\mathrm{T}} > 1$ GeV, at least seven silicon hits, not more then two and one missing hits in the silicon and pixel detector respectively and one or no hits in the silicon detector assigned to more than one track.

2. *Calorimeter isolation.* It uses the energy measurement matched to a lepton candidate. $E_{\mathrm{T}}^{\mathrm{topocone20}}$ variable is defined as the sum of transverse energies of topological clusters within a cone of $\Delta R = 0.2$ around the candidate lepton cluster. The sum is corrected for the effect of pile-up. The pile-up contribution is estimated using the ambient energy-density technique [147].

Generally, the calorimeter-based isolation measures the energy of both neutral and charged particles, whereas track-based isolation only charged particles.

For the analysis the isolation working point is called *gradient* and uses the tracking and calorimeter variables listed above. Both use calorimeter-based variable $E_{\mathrm{T}}^{\mathrm{topocone20}}$ track-based electrons also use the $p_{\mathrm{T}}^{\mathrm{varcone20}}$ variable, while muons use $p_{\mathrm{T}}^{\mathrm{varcone30}}$.

5.4.4 Selection criteria

The selection of events and leptons for Z-boson production in both channels, $Z \to e^+e^-$ and $Z \to \mu^+\mu^-$, is fully consistent with the one in the $t\bar{t}$ analysis [22] and close to the selection used for the measurement of Z-boson cross sections with the 50 ns dataset [4]. The Z-boson analysis is performed using the Athena framework, a ATLAS software release 20, and AthAnalysisBase with tag 2.3.40.

5.4.4.1 Event selection

To select good events, the dataset used in the analysis must pass data quality requirements to ensure that only good runs are chosen for physics results. This selection is provided by the GRL (see Table 5.5). The selection of events requires at least one primary vertex with at least two associated tracks with $p_{\mathrm{T}} > 400$ MeV. The events affected by liquid argon calorimeter noise bursts and the events tagged with data integrity errors from the tile calorimeter are rejected. Additionally, incomplete events caused by trigger timing control (TTC) restarts and events affected by the recovery procedure in the semiconductor tracker are removed [148].

During the production process of derived xAOD samples from the xAOD some data acquisition issues can cause the same physics event to be written out more than once. For instance, an output file from a job that is cancelled can appear in the final merged file. Besides all event selections, the necessary cross-check is performed for duplicated events run by run. In two runs, 284285 and 283429, some duplicated events are found: 132 and 189 events, accordingly. These are very small fractions compared with the total number of events of these runs, 0.0048 and 0.0035, and these events do not enter the final selection performed in this analysis.

The selected events are then passed to single-lepton trigger chain recommended as the baseline in 2015. The following triggers are used to select the events for the analysis:

- HLT_e24_lhmedium_L1EM20VH or HLT_e24_lhmedium_L1EM18VH: They are combined Level-1 and higher-level triggers, which require at least one electron with a transverse energy E_T threshold of 24 GeV passing the medium likelihood-based identification criteria (taking as input the electromagnetic shower shape and tracking information). The Level-1, electromagnetic trigger (EM), requires one electron candidate to pass E_T threshold of 20 GeV or 18 GeV, with varying threshold versus η to correct for passive material before the EM calorimeter (V) and with a hadronic isolation requirement (H), which is E_T-dependent veto against energy deposited in the hadronic calorimeter.

- HLT_e60_lhmedium: High transverse momentum electron trigger, which requires at least one electron fired by the HLT with a electron p_T threshold of 60 GeV and likelihood-based medium identification. It is seeded from the L1 trigger, L1_EM22VHI, which requires an isolation criteria on the electron candidate in the ECAL (I) with E_T threshold above 22 GeV.

- HLT_e120_lhloose: High transverse momentum electron trigger, which requires one electron with E_T threshold of 120 GeV and a loose likelihood. It is used to improve the efficiency in the high transverse energy regime. It is seeded from the L1 trigger, L1_EM22VHI, as HLT_e60_lhmedium trigger.

- HLT_mu20_iloose_L1MU15: HLT trigger requiring at least one muon fired with transverse momentum, p_T, with a threshold of 20 GeV and at L1, a p_T threshold of 15 GeV with the loose track isolation requirement ($p_T^{\text{cone20}}/p_T^{\mu} < 0.12$ in cone $\Delta R = 0.2$) It is the lowest unprescaled single muon trigger.

- HLT_mu50: High level trigger requiring at least one muon fired by HLT with muon p_T threshold of 50 GeV without any isolation requirement. This trigger is used to recover any efficiency loss at high transverse momentum region. It is seeded by the L1_MU20 trigger which requires a muon with p_T above 20 GeV.

Event selection	
GRL	data15_13TeV.periodAllYear_DetStatus-v73-pro19-08_DQDefects-00-01-02_PHYS_StandardGRL_All_Good_25ns.xml
Vertex	xAOD::Vertex::vertexType() == xAOD::VxType::PriVtx
e trigger	Data: e24_lhmedium_L1EM20VH or e60_lhmedium or e120_lhloose MC: e24_lhmedium_L1EM18VH or e60_lhmedium or e120_lhloose
μ trigger	HLT_mu20_iloose_L1MU15 or HLT_mu50

Table 5.5: Overview of the event selection criteria.

5.4.4.2 Lepton selection

After good events are preselected, good quality electron and muon candidates should be selected. Both candidates, electrons and muons, are required to have transverse momentum $p_T > 25$ GeV. Then, the electron must be within the tracking region of the inner detector ($|\eta| < 2.47$) excluding the transition region between the barrel and end-cap electromagnetic calorimeters, $-1.37 \leq |\eta| < 1.52$, and muons within $|\eta| < 2.4$. Moreover, electrons and muons should pass the identification criteria defined above. In the case of electrons, the *mediumLH* working point is chosen, and for muons *medium* working point.

Both leptons must satisfy a *gradient* isolation requirement. The isolation requirements are tuned so that the lepton-isolation efficiency is at least 90% for $p_{\mathrm{T}} > 25$ GeV, increasing to 99% at 60 GeV. Also, at least one of the lepton candidates is required to match the lepton that triggered the event. Both electron and muon tracks are required to be associated with the primary vertex. For this, constraints are used on the transverse impact-parameter significance, $|d_0^{\mathrm{BL}}|/\delta d_0$, where $|d_0^{\mathrm{BL}}|$ is the transverse impact parameter with respect to the beamline (BL) and δd_0 is its uncertainty, and on the longitudinal impact parameter with respect to the beamline (BL), z_0^{BL}, corrected for the reconstructed position of the primary vertex. The transverse impact-parameter significance is required to be less than five for electrons and less then three for muons, while the absolute value of the corrected z_0^{BL} multiplied by the sine of the track polar angle is required to be less than 0.5 mm.

5.4.4.3 *Z*-candidate selection

Events containing a Z-boson candidate are selected by requiring two selected leptons of the same flavour which are oppositely charged. The dilepton invariant mass has to be within the range $66 < m_{\mathrm{ll}} < 116$ GeV.

Lepton selection		
Electrons	p_{T}	> 25 GeV
	η	$\lvert\eta\rvert < 2.47$ and $1.37 < \lvert\eta\rvert < 1.52$
	ID	*mediumLH*
	Isolation	*gradient* isolation
	d_0	$\lvert d_0^{\mathrm{BL}}\text{significance}\rvert < 5$
	z_0	$\lvert\Delta z_0^{\mathrm{BL}} \sin\theta\rvert < 0.5$ mm
Muons	p_{T}	> 25 GeV
	η	$\lvert\eta\rvert < 2.4$
	ID	*medium*
	Isolation	*gradient* isolation
	d_0	$\lvert d_0^{\mathrm{BL}}\text{significance}\rvert < 3$
	z_0	$\lvert\Delta z_0^{\mathrm{BL}} \sin\theta\rvert < 0.5$ mm
Boson selection		
$Z \to \ell^+\ell^-$	Leptons	exactly 2 same flavour oppositely charged
	Mass window	$66 < m_{ll} < 116$ GeV

Table 5.6: Overview of the lepton and boson selection criteria applied for both electron and muon channels.

Final numbers of $Z \to \ell^+\ell^-$ candidates in data for both analysis channels, numbers of candidates remaining in data after each major requirement that has been applied and the efficiencies of each cut are shown in Table 5.7. The efficiency of each cut is presented with respect to the previous cut.

The data yields (after all selection) and their ratio for selected data periods versus the run number are presented as the number of events from the $Z \to e^+e^-$ and $Z \to \mu^+\mu^-$ selection divided by the integrated luminosity for the corresponding run numbers in Figure 5.6. The absence of systematic trends shows a stability of selection versus the run number and indicates luminosity consistency. The data yields for each channel separately shows small luminosity inconsistencies since the luminosity is determined for full period and small trends can be observed. The ratio of yields for $Z \to e^+e^-$ to $Z \to \mu^+\mu^-$ events

	$Z \to e^+e^-$		$Z \to \mu^+\mu^-$	
Requirement	Number	Relative efficiency [%]	Number	Relative efficiency [%]
All	53 146 300		53 146 300	
GRL	51 349 300	96.62	51 349 300	96.62
Trigger	7 928 180	15.44	8 011 110	15.61
Two medium ID leptons	1 625 480	20.50	2 180 740	27.22
Isolation	1 464 160	90.08	1 832 100	84.01
Opposite charge pair	1 428 830	98.47	1 809 920	98.79
$66 < m_{\ell\ell} < 116$ GeV	1 367 026	95.67	1 735 197	95.79

Table 5.7: The number of $Z \to e^+e^-$ and $Z \to \mu^+\mu^-$ candidates in data, remaining after each major requirement and the relative efficiencies of each cut.

cancels some luminosity trends and demonstrates good compatibility between two channels showing an improved $\chi^2/ndf = 2.7$.

The same ratio of data yields between $t\bar{t}$ and Z-boson analyses is presented in Figure 5.7 and the corresponding numbers (using *OflLumi-13TeV-003*) are shown in Appendix A.3 as well.

In the ratios of data yields between Z and $t\bar{t}$ analyses (see Figure 5.7), three close-by runs seem to have lower yields. These runs are 280500, 280520 and 280614. The rate of these runs is approximately 20% lower than for the other runs and the number of events is much smaller then in the other cases. This effect is investigated from looking into selection efficiencies for these runs. The main difference comes from the requirement of having exactly one electron and one muon in $t\bar{t}$ analysis, but it has no significant impact on the results.

5.4.5 Selection cross-checks

Overlap removal

An overlap removal (OR) procedure is used to avoid double-counting of objects by the reconstruction algorithms, when an object is reconstracted as two different, but overlaping objects. The effect of OR is considered only for muon channel since the effect in the electron channel is observed to be much smaller [4]. The primary goal is to separate muons from Z-boson decays from those muons that originate from hadronic decays within jets. The overlapping of muons with jets can occur when pile-up produces muon and jet in the same area of detector; or muons from decays of long living light mesons ($\pi^\pm$ or K) or charm and beauty quarks appear in the region of the jet; or when muons are mis-reconstructed in the calorimeter as jets.

The OR selection is implemented between the muons and jets using a standard tool provided by Analysis Harmonisation Study Groups (ASG) [149]. The selected muons which passed the muon quality, p_T and η cuts, are given to the tool as input parameters together with the selected and calibrated jets with $|\eta| < 4.5$, $p_T > 20$ GeV. The tool performs the selection depending on a geometric distance (ΔR) of the objects in the following steps:

- Jets closer than $\Delta R < 0.4$ to a selected muon are removed (from the list of selected jets) if they have a number of tracks ≤ 2;
- Muons are removed if they are within $\Delta R < 0.4$ of a selected jet.

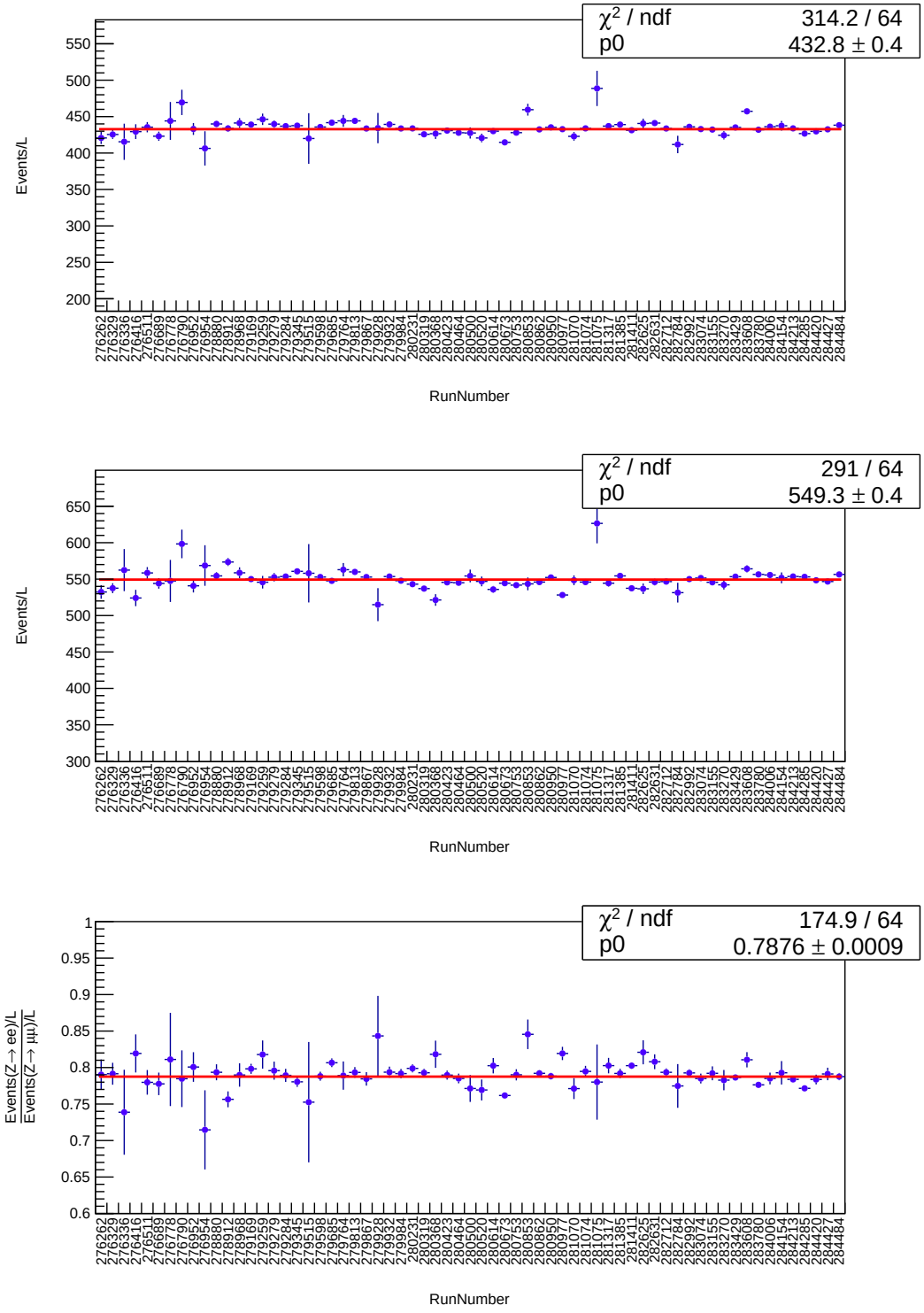

Figure 5.6: Data yield versus run number for the $Z \to \ell\ell$ selection. The upper plot shows the distribution for the $Z \to e^+e^-$ channel. The middle plot shows the distribution for the $Z \to \mu^+\mu^-$ channel. The bottom plot shows the ratio of $Z \to ee$ to $Z \to \mu\mu$ data yields versus run number. The error bars correspond to the statistical uncertainties.

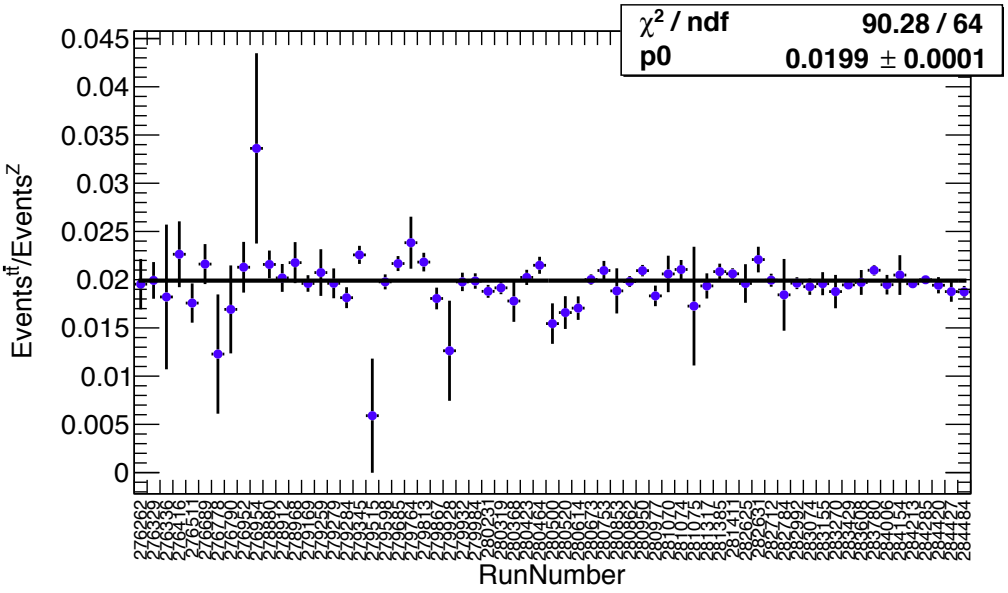

Figure 5.7: Ratio of the data yields versus run number between $t\bar{t}$ and $Z \to \ell\ell$ channels.

The effect of the OR selection on the final number of selected Z-boson candidates in the muon channel is found to be negligible, around 0.1% for data and 0.08% for MC simulation and did not considered in the analysis.

Cut flow comparison

The number of $Z \to e^+e^-$ and $Z \to \mu^+\mu^-$ candidates in data and the sum of the weights in Monte Carlo samples after each major requirement are compared between three independent groups, Z-boson analysis at DESY, Z + jets analysis [150] and Z-boson analysis at Institute for Research into the Fundamental laws of the Universe at CEA in Saclay (CEA/IRFU). The comparison is performed between all three analyses using the selection criteria that are shown in Table 5.6, except an implementation of the d_0 and z_0 cuts for which two analyses used a tool (DESY, CEA/IRFU). The common samples, tags and other important details are presented in Table 5.8. The comparison between final numbers of candidates and the sum of the weights is shown in Table 5.9. The discrepancy between the analyses is found in the MC simulations to be around 0.1% in both analysis channels, and for the data around 0.03% in the muon channel (which is negligible effect on full dataset) and 0.004% in the electron channel, which is negligible with the precision of the analysis. Small differences are expected as different selections and frameworks are employed by these analyses. Moreover, the correction factors, scale factors and event by event kinematics are compared showing good agreement.

5.5 Detector efficiencies

To evaluate differences between data and simulated events it is necessary to estimate efficiency of the selection. An identification efficiency, ϵ_{id}, accounts that reconstructed lepton passed the identification selection. An isolation efficiency, ϵ_{iso}, accounts that reconstructed and identified lepton passed the isolation requirement. A trigger efficiency, ϵ_{trig}, accounts that reconstructed and isolated lepton is

Release	
Electrons	2.3.36 + TrigEgammaMatchingTool-00-00-08
Muons	2.3.40
Data set	period D
MC samples	
Electrons	"mc15_13TeV.361106.PowhegPythia8EvtGen_AZNLOCTEQ6L1_Zee. merge.DAOD_STDM3.e3601_s2576_s2132_r7267_r6282_p2471" DAOD_STDM3.07333236._000001.pool.root.1
Muons	"mc15_13TeV.361107.PowhegPythia8EvtGen_AZNLOCTEQ6L1_Zmumu. merge.DAOD_STDM3.e3601_s2576_s2132_r7267_r6282_p2421" DAOD_STDM3.07001930._000001.pool.root.1
PRW files	
Electrons	my.prw_410000_mc15b.root
Muons	mc15_13TeV.361107.PowhegPythia8EvtGen_AZNLOCTEQ6L1_Zmumu. merge.AOD.e3601_s2576_s2132_r7267_r6282_PRWmc15b.root

Table 5.8: Common Monte Carlo and data samples used for the comparison between the analyses.

	Analysis 1 (DESY)	Analysis 2 (Z + jets)	Analysis 3 (CEA/IRFU)
Number of $\boldsymbol{Z \to e^+e^-}$ candidates			
Data	22 076	22 075	22 075
MC	4.086×10^7	–	4.08023×10^7
Number of $\boldsymbol{Z \to \mu^+\mu^-}$ candidates			
Data	28 017	28 026	28 026
MC	5.281×10^7	–	5.28527×10^7

Table 5.9: Final number of $Z \to ee$ and $Z \to \mu\mu$ candidates in the data and the sum of the weights in the MC in the three analyses.

triggered.

All efficiencies can be evaluated with the data and Monte Carlo simulations using a tag-and-probe method on $Z \to \mu^+\mu^-$ and $Z \to e^+e^-$ candidates. The tag-and-probe method measures how efficient is performance of some selection. It is based on the idea that one lepton from the pair is identified as a 'tag' and another one as a 'probe'. Two leptons originated from the Z boson can be clearly distinguished in the event as can be seen in the ATLAS event display in Figure 5.8. One of two final state leptons, tag, is required to pass set of selection criteria and used to tag and trigger the event and second one with no or relaxed selection is applied, serves as a probe and used to test the cuts. If first lepton in the selected event is the tag then the second is chosen as the probe, and if the second lepton is the tag then the first is saved as the probe. The fraction of probe muons that passes interested selection gives an evaluation of efficiency.

Following the tag-and-probe idea, the estimation of the efficiency requires the 'tag' with the common selection (including identification, isolation and trigger selection) described in Tables 5.5, 5.6 and the 'probe' appropriately to the selection of interest, requiring:

- ϵ_{id} probe: common selection + ID requirement

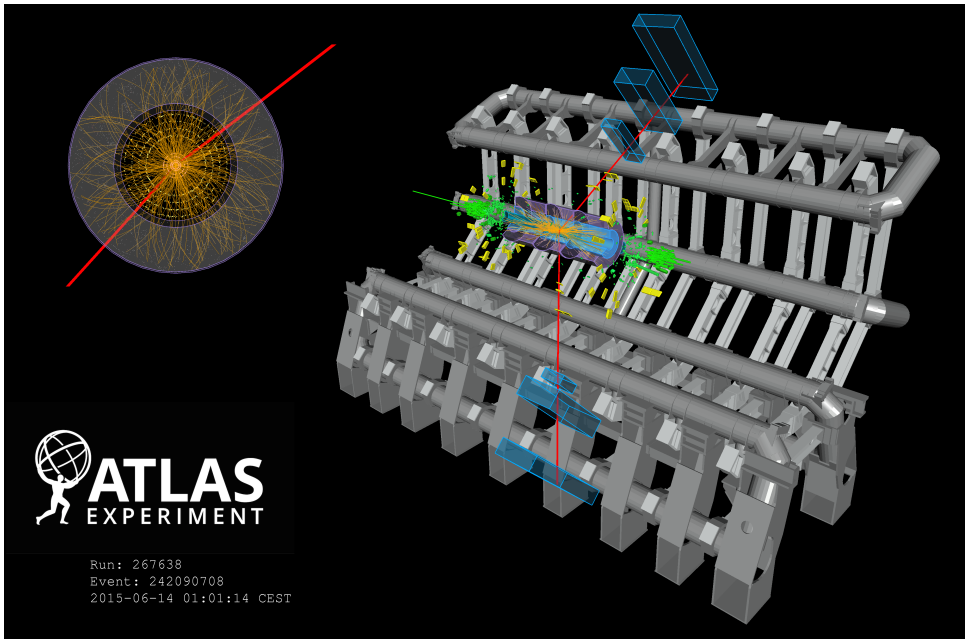

Figure 5.8: Event display of $Z \to \mu^+\mu^-$ candidate from proton–proton collisions recorded by ATLAS on 14 June 2015. Taken from [151].

- ϵ_{iso} probe: common selection + ID + isolation requirements
- ϵ_{trig} probe: common selection + ID + isolation + trigger matching requirements

After the efficiencies are obtained in both data and MC simulations, scale factors are calculated to correct the simulated data using Equation 5.5. Taking into account that the trigger scale factors are calculated for each lepton and the trigger selection requires any of the required triggers to be fired in event, the event scale factor is recalculated as:

$$SF^{\text{trig}} = \frac{\epsilon^{\text{data}}_{\text{trig}}(l_1) + (1 - \epsilon^{\text{data}}_{\text{trig}}(l_1)) \cdot \epsilon^{\text{data}}_{\text{trig}}(l_2)}{\epsilon^{\text{MC}}_{\text{trig}}(l_2) + (1 - \epsilon^{\text{MC}}_{\text{trig}}(l_1)) \cdot \epsilon^{\text{MC}}_{\text{trig}}(l_2)}.$$

The other scale factors are applied to the event weight as:

$$SF^i = SF^i_{l_2} \cdot SF^i_{l_2},$$

where i = id, iso, or reco.

The muon trigger, isolation, reconstruction, track-to-vertex association (TTVA) scale factors together with the statistical and systematics uncertainties are provided by the ATLAS MCP group in the MuonEfficiencyCorrections-03-02-03 package [152] with the MuonEfficiencyScaleFactors tool. The electron identification, reconstruction, trigger and isolation scale factors together with their statistical and systematics uncertainties are provided by Electron Egamma Group in the ElectronEfficiencyCorrection-00-01-36 package [153, 154]. The working points passed to the tools in the electron and muon channels are listed in Tables 5.10, 5.11.

The muon trigger efficiency is different for each data period. The efficiency maps in terms of η^μ and ϕ^μ are used to extract the efficiencies and scale factors. The binning in η and ϕ is determined by

Name of tool	Tool configuration			
	ForceDataType	*CorrelationModel*	*NumberOfToys*	*MCToySeeD*
Identification	1	"COMBMCTOYS"	100	10
CorrectionFileNameList	"efficiencySF.offline.MediumLLH_d0z0.2015.13TeV.rel20p0.25ns.v02.root"			
Reconstruction	1	"COMBMCTOYS"	100	13
CorrectionFileNameList	"efficiencySF.offline.RecoTrk.2015.13TeV.rel20p0.25ns.v02.root"			
Trigger	1	"COMBMCTOYS"	100	11
CorrectionFileNameList	"efficiencySF.e24_lhmedium_L1EM20VH_OR_e60_lhmedium_OR_e120 _lhloose.MediumLLH_d0z0_v8_isolGradient.2015.13TeV.rel20p0.25ns.v02.root"			
Isolation	1	"COMBMCTOYS"	100	12
CorrectionFileNameList	"efficiencySF.Isolation.MediumLLH_d0z0_v8_isolGradient.2015.13TeV.rel20"			

Table 5.10: Detailed information on the configuration of tools which are used for the Monte Carlo corrections in the electron channel.

Name of tool	Tool configuration	
	WorkingPoint	*CalibrationRelease*
Isolation	"GradientIso"	"Data15_allPeriods_260116"
Reconstruction	"Medium"	"Data15_allPeriods_260116"
TTVA	"TTVA"	"Data15_allPeriods_260116"
Trigger	WorkingQuality = "Medium", NReplicas = 100, ReplicaRandomSeed = 1234 RelicaTriggerList = "HLT_mu20_iloose_L1MU15_OR_HLT_mu50"	

Table 5.11: Detailed information on the configuration of tools which are applied for the Monte Carlo corrections in the muon channel.

the MS geometry. The efficiency for data and MC simulation is determined for the barrel and end-cap regions separately and is shown for the data period D in Figures 5.9, 5.10 and for all other periods in Appendix A.4. The maps in terms of pseudorapidity, η^e, and transverse momentum, p_{T}^e, are used for obtaining electron trigger efficiency and scale factors.

The efficiencies after the applied scale factors are cross-checked and obtained using the tag-and-probe method in the analysis framework. The corresponding trigger and isolation efficiencies as a function of the lepton pseudorapidity and lepton transverse momentum are compared between data and MC simulation after applied corrections for both electrons and muons candidates and shown in Figures 5.11, 5.12. Overall, data and MC efficiencies are in good agreement, demonstrating an average ratio between data and MC simulation at around 0.999. The trigger efficiency as a function of transverse momentum is around 97% at values of $p_{\mathrm{T}} > 40$ GeV and decreases at lowest values of p_{T} to 80% for electron channel, and for muon channel it is around 77% for all p_{T} bins. The trigger efficiency as a function of pseudorapidity is around 95% at central values and decreased up to 87% at the highest values of pseudorapidity in the electron channel, while for the muon channel it is around 65% and 90%, respectively. The low efficiency for muons in the region of $|\eta| < 1.0$ is due to the low efficiency of RPC in two sectors of ϕ. The isolation efficiency as a function of transverse momentum is at least 90% for $p_{\mathrm{T}} > 25$ GeV, increasing to 99% at p_{T} of 60 GeV in both channels. For the *gradient* working point, the cuts are derived per p_{T} bin, and the efficiency is expected to have some steps at bin boundaries. The isolation efficiency as the function of pseudorapidity is at least 94% in the central values of pseudorapidity and increases up to 95% for highest values of pseudorapidity in muon channel and 95% for all bins

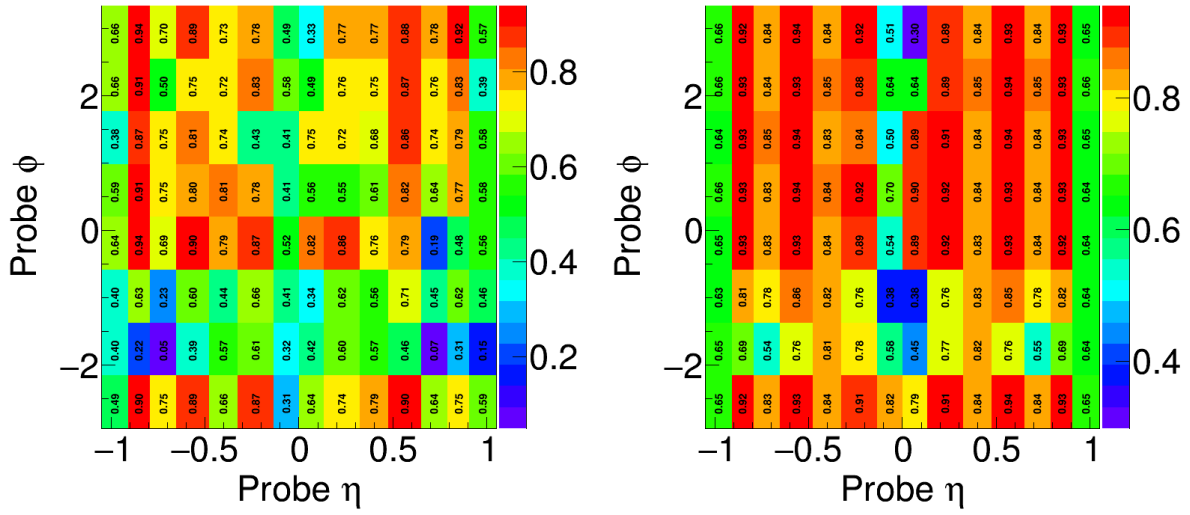

Figure 5.9: Trigger efficiency of HLT_mu20_iloose_L1MU15 or HLT_mu50 in the barrel regions in data (left) and in Monte Carlo simulations (right) in bins of the probe muon η and ϕ for the data taking period D. Taken from trigger efficiency tool [152].

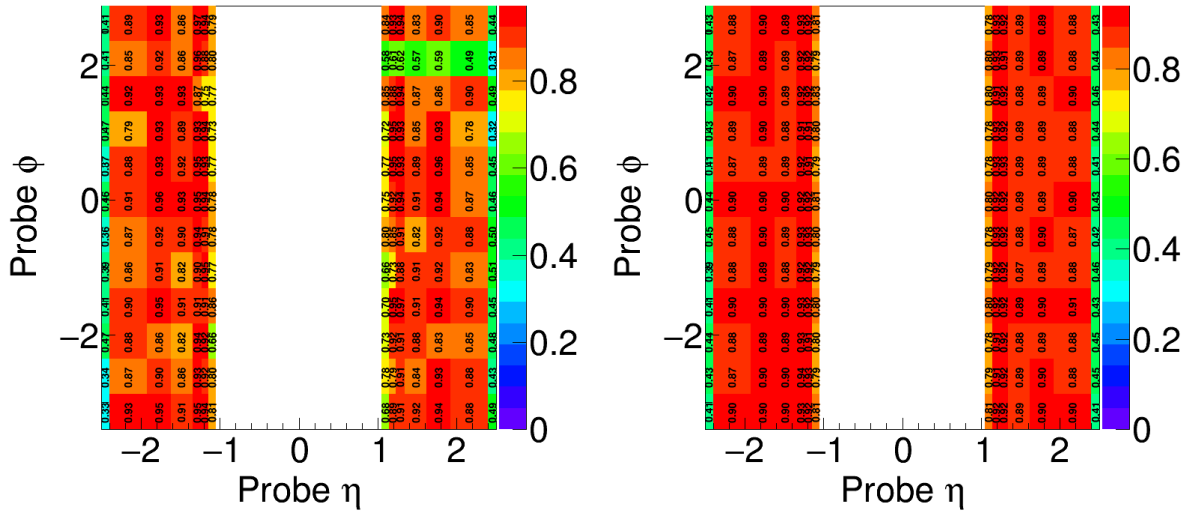

Figure 5.10: Trigger efficiency of HLT_mu20_iloose_L1MU15 or HLT_mu50 in the end-cap regions in data (left) and in Monte Carlo simulations (right) in bins of the probe muon η and ϕ for the data taking period D. Taken from trigger efficiency tool [152].

in electron channel. Small discrepancies between data and MC efficiencies are observed for isolation efficiency as the function of muon pseudorapidity, but in overall the ratio of data to MC simulation shows a value close to unity.

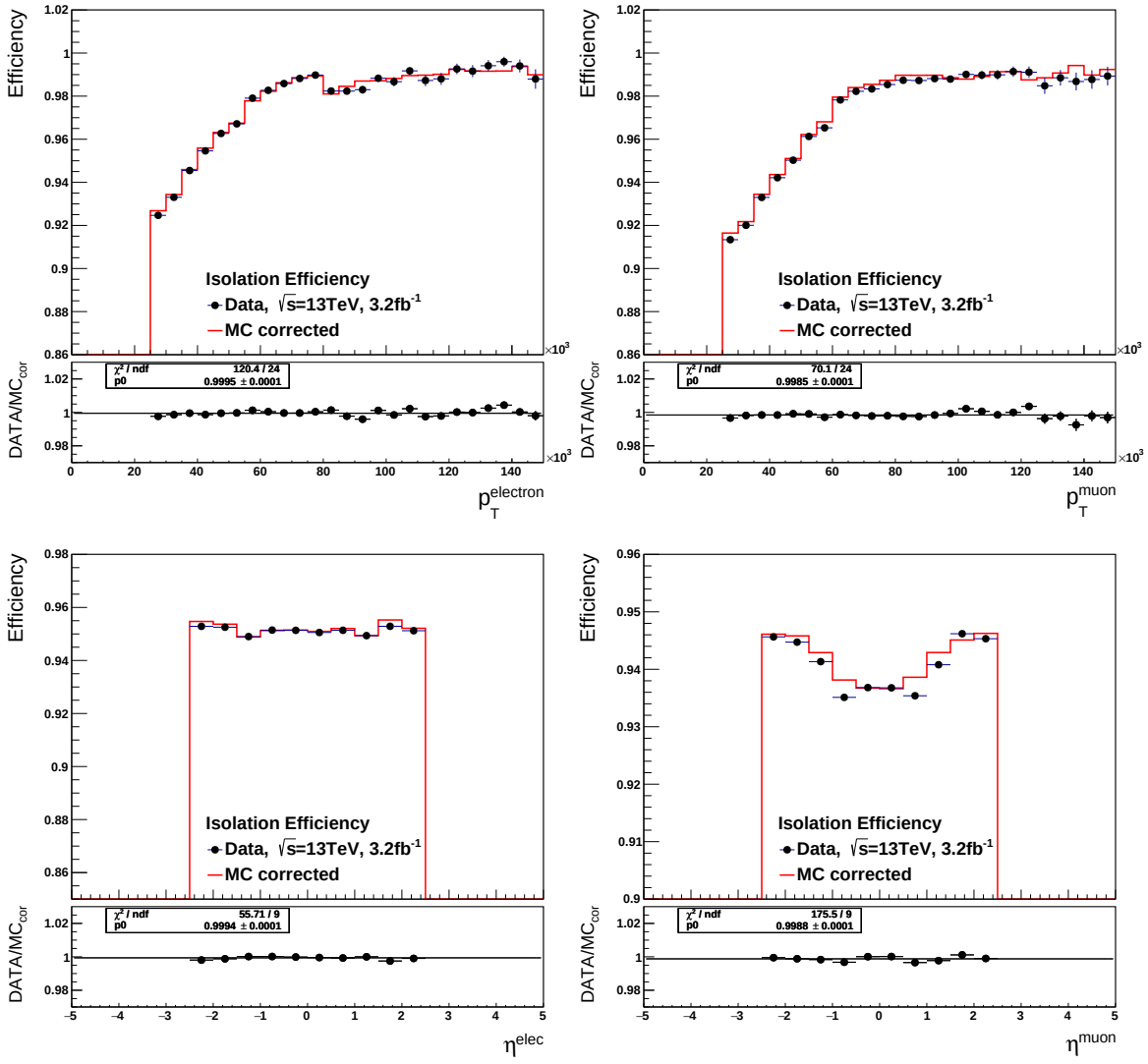

Figure 5.11: Isolation efficiency as a function of the lepton rapidity (top) and lepton transverse momentum (bottom) as determined using a tag-and-probe method for electron and muons in final states. The left plots show the efficiency for the electrons and right plots show the efficiency for the muons. The efficiencies are extracted from data (solid symbols) and from signal MC simulations after the correction is applied (red line) and their ratio between data and corrected MC simulations. The statistical errors are shown as black lines.

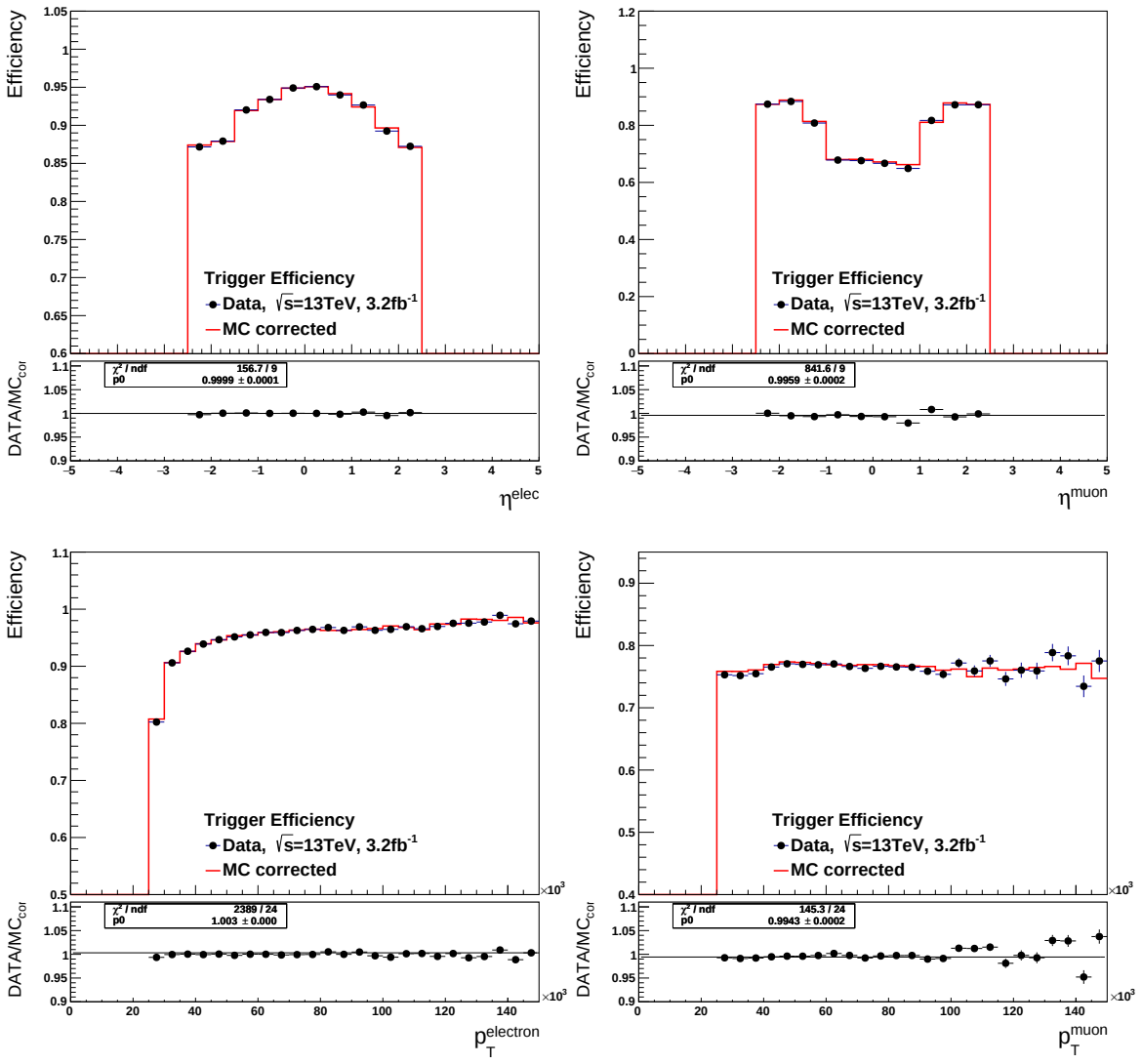

Figure 5.12: Trigger efficiency as a function of the lepton pseudorapidity (top) and lepton transverse momentum (bottom) as determined using a tag-and-probe method for electron and muons in final states. The left plots show the efficiency for the electrons and right plots show the efficiency for the muons. The efficiencies are extracted from data (solid symbols) and from signal MC simulations after the correction is applied (red line) and their ratio between data and corrected MC simulations. The statistical errors are shown as black lines.

	$Z \to e^+e^-$ [%]	$Z \to \mu^+\mu^-$ [%]
$W \to \tau\nu$	< 0.01	< 0.01
$Z \to \tau\tau$	0.04	0.04
Diboson	0.15 (0.18)	0.15 (0.18)
$t\bar{t}$	0.27	0.24
$W \to e\nu$	< 0.01	< 0.01
$W \to \mu\nu$	< 0.01	< 0.01

Table 5.12: Electroweak background contributions estimated from the MC simulations. The expectations are expressed as a percentage of the total number of simulated events coming from the sources listed in the table and passing the signal selection in each channel. The number in the parenthesis indicates the contribution using the list of diboson samples from $t\bar{t}$ analysis.

5.6 Background estimation

5.6.1 Top and electroweak backgrounds

Events which have two identified leptons in the final state can originate from different processes and form background events for the $Z \to \ell^+\ell^-$ measurement. This background, called electroweak (EW) background, is produced mostly by decays of W or Z bosons, top quark pairs and dibosons in the following way:

- $W \to \mu\nu$ and $W \to e\nu$ decays: produce one muon or electron in the final state, which can be combined with those from the jet. This background can be reduced by suppression of non-isolated muons.
- $Z \to \tau\tau$ and $W \to \tau\nu$ decays: produce τ leptons in the final state, which subsequently decay into muons (electrons) and neutrino (i.e. $Z \to \tau^+\tau^- \to \mu^+\mu^-(e^+e^-) + 4\nu$), which can be identified wrongly as primary muons (electrons). Those two muons (electrons) will give a smaller invariant mass compared to the nominal Z mass due to large missing energy. In general, the muons from τ decays have lower p_{T} than muons from the signal decay, therefore the background can be mainly reduced by kinematic constraints.
- $t\bar{t} \to W^+bW^-\bar{b}$ decay: each top quark pair decays to the W and two b-jets, and then each W boson decays to a lepton and a neutrino. The final state of this process can include two oppositely charged high-p_{T} and isolated leptons producing the signal channel, or one of the leptons can be combined with a jet giving $Z \to \mu^+\mu^-$ decay topology.
- dibosons: more than one electroweak gauge boson can be produced in the collision. WW, WZ, ZZ diboson processes are considered with their decay products containing leptons in the final state.

The background processes for $Z \to \mu\mu$ and $Z \to ee$ channels are evaluated from the MC simulations mentioned in Table 5.2.

The contribution from all sources is below 0.5%, with the largest contribution coming from $t\bar{t}$ events, and is summarized in Table 5.12.

Despite of the fact that both $t\bar{t}$ and Z-boson analyses are aiming to be fully consistent, different derivations of diboson background samples are used, TOPQ1 (p2454) and STDM3 (p2470/2471) respectively.

To confirm that the background from the dibosons is independent of the samples used, the cross-check is performed using the list of samples from the $t\bar{t}$ analysis. The contribution from dibosons which corresponds to the list of samples in $t\bar{t}$ analysis are given in parenthesis and presented in Table 5.12.

5.6.2 Multijet background

The multijet background, also referred to as QCD background, is related to leptons which are produced from heavy flavour hadrons in jets and from in-flight decays of light mesons (kaons or pions), providing non-isolated leptons which can be misidentified as leptons from the signal. It is one of the processes which is difficult to model correctly with event generators. Usually, the MC datasets with simulated QCD multijet events are limited due to the large cross section of these processes (compared to the electroweak processes) and the huge statistics needed to obtain proper distributions. Thus, the estimation of the contribution of QCD multijet background is based on a data-driven method.

In order to perform the estimation of multijet background using a data-driven method it is necessary to get a control sample which is enriched with background events containing small amount of signal events. This can be achieved by loosening or inverting some criteria from the original signal selection. Mainly, the suppression of multijet events is reached by lepton isolation and impact transverse parameter criteria, where the later suppresses leptons coming from heavy meson decays and in-flight decays of light mesons, since they are characterized by large impact parameter, d_0. The signal leptons have small d_0, however electrons may be reconstructed at large d_0 due to a Bremsstrahlung effect. The Bremsstrahlung photons are collinear to the electron direction and yield an underestimation of track curvature. This leads to a bias of d_0 corresponding to the charge of the electron. Therefore, the $d_0 \cdot Q$ distribution can be used as a discriminative variable between the signal and background events, where d_0 is the impact parameter in the transverse plane, which characterize the distance between the primary vertex and the track of lepton, and Q is the charge of lepton. For the muons, both side-bands of the $d_0 \cdot Q$ distribution can be used, while only the positive side-band can be used for the electrons.

$Z \rightarrow \mu^+\mu^-$ channel

The background template sample for $Z \rightarrow \mu^+\mu^-$ channel is obtained from the data by inverting the isolation selection and requiring transverse impact-parameter $|d_0| > 0.1$ mm on one of the muons. One of the isolation variables from which the *gradient* isolation working point is based, the calorimeter ($E_{\mathrm{T}}^{\mathrm{topocone20}}/p_{\mathrm{T}}$) or track relative ($p_{\mathrm{T}}^{\mathrm{varcone30}}/p_{\mathrm{T}}$), is inverted. The region where events pass the *gradient* isolation working point (see Figure 5.13) determines the following cuts applied for both isolation variables:

$$p_{\mathrm{T}}^{\mathrm{varcone30}}/p_{\mathrm{T}} < 0.1$$
$$E_{\mathrm{T}}^{\mathrm{topocone20}}/p_{\mathrm{T}} < 0.08.$$

To create a template with the largest possible statistics, the $p_{\mathrm{T}}^{\mathrm{varcone30}}/p_{\mathrm{T}}$ isolation cut is chosen. Trigger issues are taken into account for the template selection. The `HLT_mu20_iloose_L1MU15` trigger has an isolation requirement at trigger level thus the template is selected for the events failing offline isolation but passing online isolation. The `HLT_mu50` trigger does not have the isolation requirement and thus when it is included into the template selection the extra events around $p_T = 50$ GeV are observed. Those events fail the isolation requirement of `HLT_mu20_iloose_L1MU15` but collected by non-isolated `HLT_mu50`. The effect is shown in Figure 5.14. In order to avoid bias in p_{T} distribution, the `HLT_mu50` trigger is

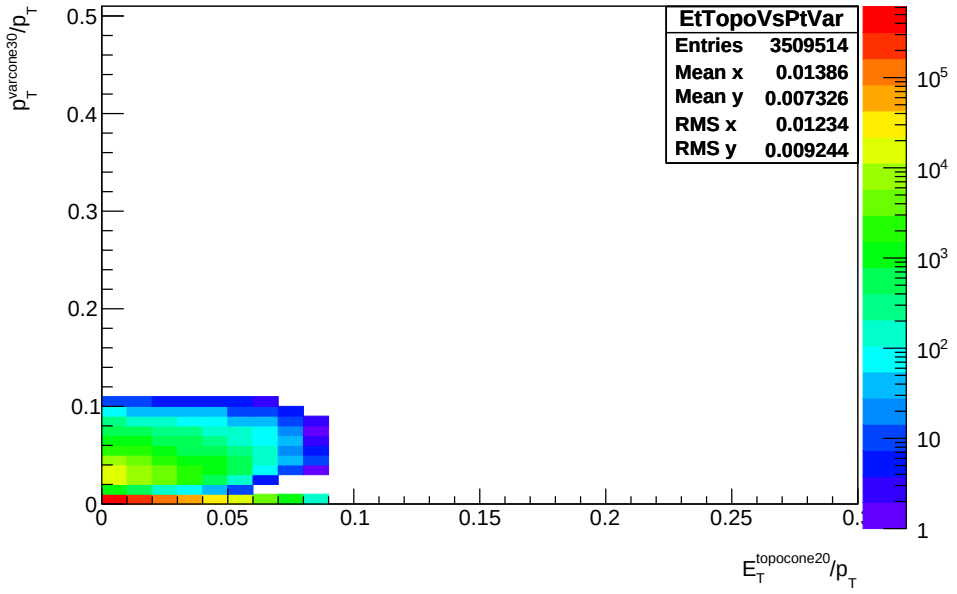

Figure 5.13: Distribution of $E_T^{\text{topocone20}}/p_{\text{T}}$ versus $p_T^{\text{varcone30}}/p_{\text{T}}$ for events containing muons which pass the *gradient* isolation selection in the data.

excluded from the template selection. The track to vertex association requirement is not applied and the rest of the selection is kept as for the nominal signal selection.

The comparison between data and MC for the $d_0 \cdot Q$ distribution for the muon, for which the $|d_0| > 0.1$ mm cut is not applied, shows a discrepancy around the peak region due to some deficiency in the resolution description of the signal MC in Figure 5.15. To remove this discrepancy, the $d_0 \cdot Q$ resolution is corrected to match the one found in data by applying additional Gaussian smearing. The distribution is randomly smeared using the following equation:

$$d_0 \cdot Q \quad = \quad d_0 \cdot Q \cdot \left(1 + \left(\frac{1}{\sqrt{2\pi}\,0.033} e^{-\frac{(d_0 \cdot Q)^2}{2 \cdot 0.033^2}}\right)^2\right), \tag{5.7}$$

where $0.033 = \delta_{\text{smear}}$ and is found by using the equation:

$$\delta_{\text{smear}} \quad = \quad \frac{\sqrt{(\sigma^2_{\text{data}} - \sigma^2_{\text{MC}})}}{\sigma_{\text{MC}}}. \tag{5.8}$$

The smearing procedure improves the agreement between the data and MC as shown in Figure 5.16. The additional smearing has a negligible effect on the background fit.

The tag-and-probe method is used to obtain the $d_0 \cdot Q$ distribution for the multijet background by applying a $|d_0| > 0.1$ mm cut on tag lepton while the second lepton is used as the probe. The invariant mass distribution of the two muon candidates shows no peak around the Z-boson mass for the template, indicating a high background purity of the template (see Figure 5.17).

The multijet background estimation is performed by fitting the $d_0 \cdot Q$ distribution in data. The TFractionFitter method [155] from the ROOT data analysis software framework [156] is used to fit

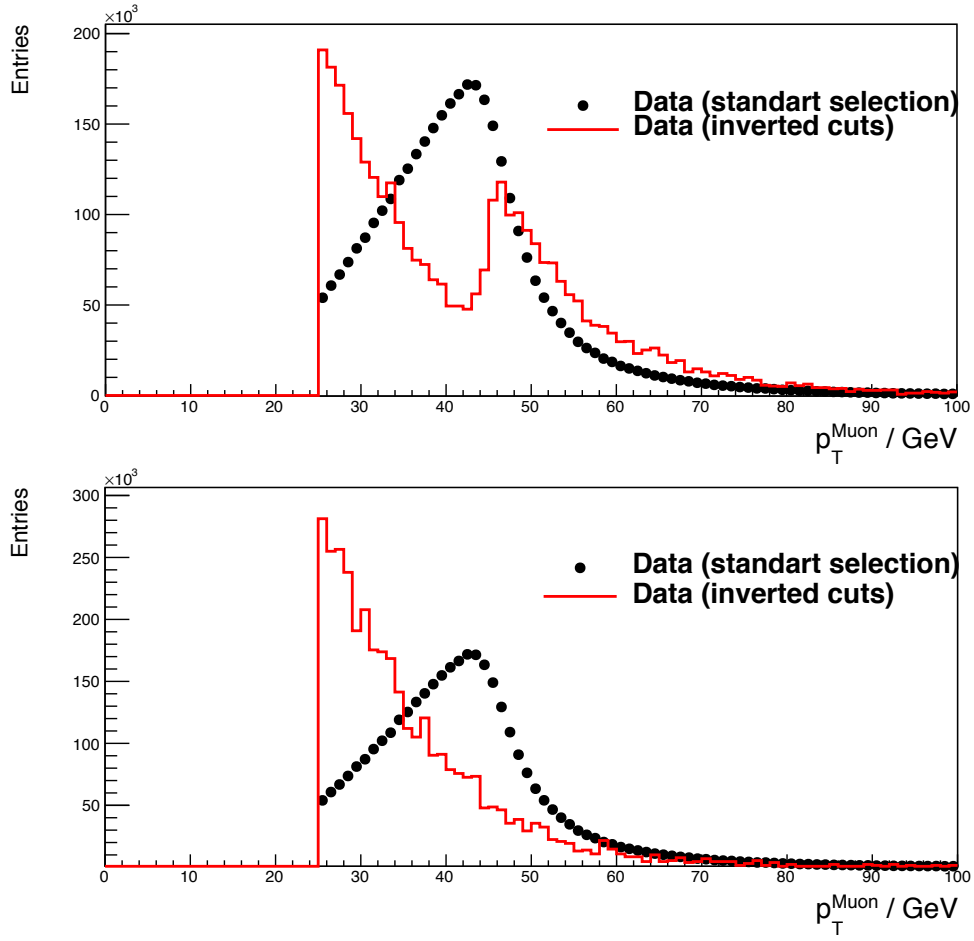

Figure 5.14: Transverse momentum distribution of the muon in the template selection with (upper) and without (bottom) the `HLT_mu50` trigger requirement for the selection. The distributions are normalized to the area.

the data-driven template (multijet background) and the signal MC template to the data distribution. It evaluates the fraction of the data contained in each template for a given distribution and normalizes both templates by the corresponding fraction. The normalization factors are the only free parameters of the fit. The fit is performed in the range of $-0.5 < d_0 \cdot Q < 0.5$. The fit estimates the background of $(0.02 \pm 0.01)\%$, consistent with being below 0.1%. The result of the fit is reported in Figure 5.18.

$Z \to e^+e^-$ channel

The multijet contribution to the $Z \to e^+e^-$ channel is estimated with a data-driven method using the same discriminating variable, $d_0 \cdot Q$, to take into account the direction of photon radiation. The template is selected by inverting the isolation and offline identification requirements for both electrons. Figure 5.19 shows asymmetric shape of the $d_0 \cdot Q$ distribution with more events at large negative values. The simulation describes the radiative tail well and the multijet background has a significant contribution for large positive values, which are used for its normalization. The details on method applied and procedure of estimation of the multijet background can be found in Reference [157].

The contribution of multijet events to the event selection in both channels is found to be $< 0.1\%$ and therefore is neglected in the calculation of the central value of the cross section. In order to properly

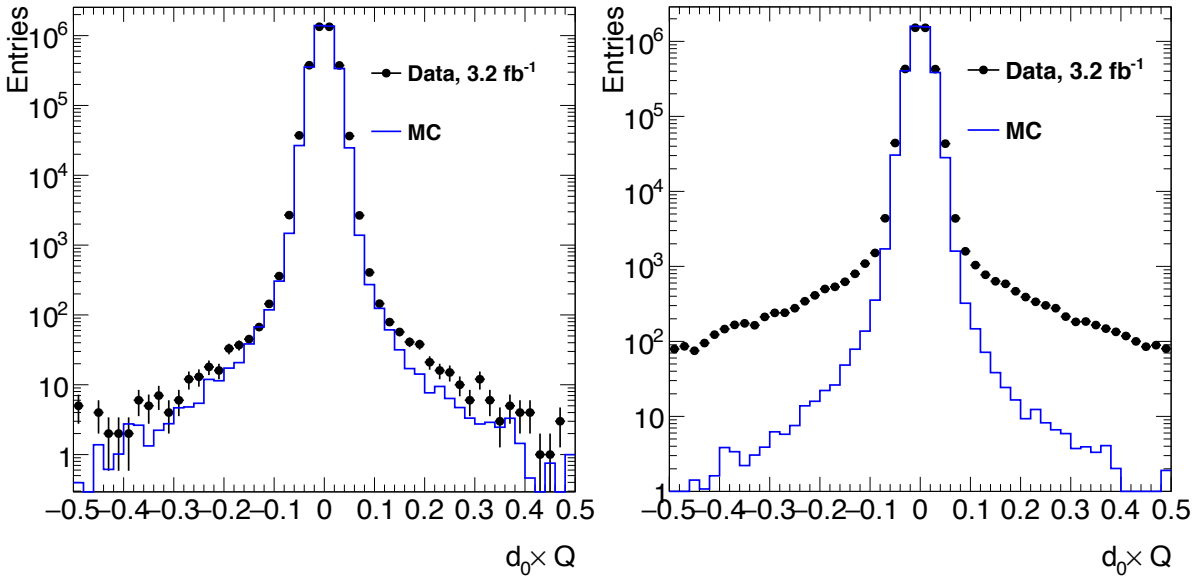

Figure 5.15: Comparison of the data with the signal MC simulation for $d_0 \cdot Q$ distribution after applying (left) or not applying (right) the isolation requirement for the nominal selection. Blue line indicates the MC and black points are data.

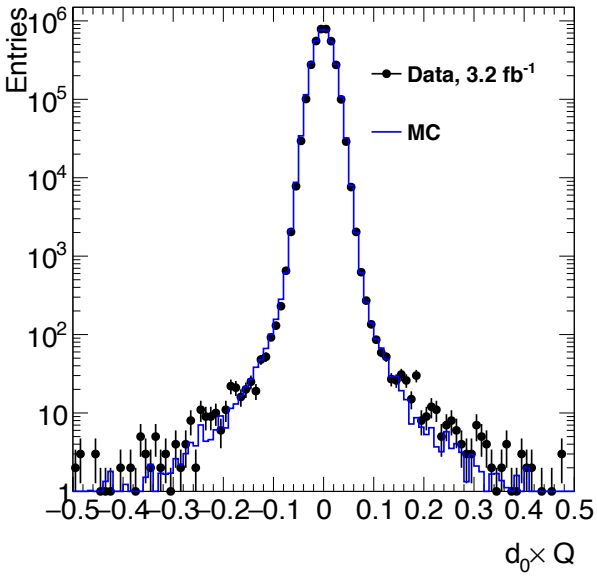

Figure 5.16: Comparison of the data with the signal MC simulation for $d_0 \cdot Q$ distribution for the nominal selection after applying the Gaussian smearing. Blue line indicate the MC and black points are data.

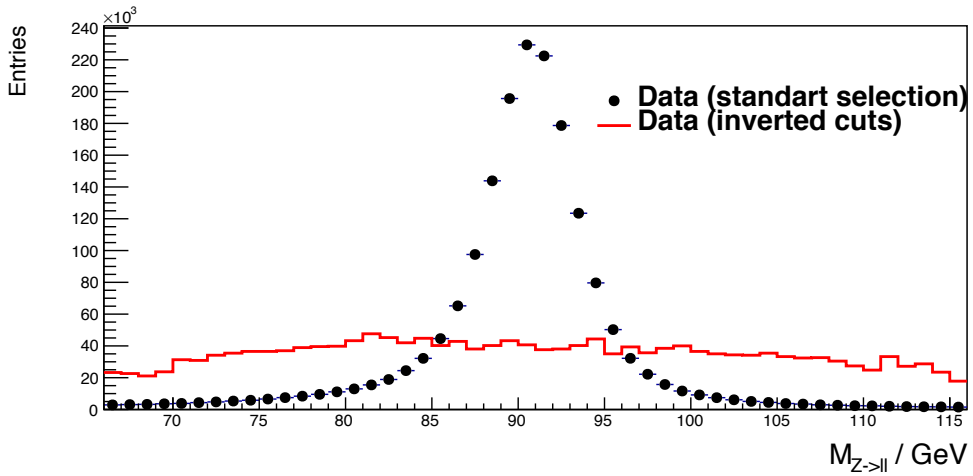

Figure 5.17: The invariant mass distributions of the two muon candidates using inversion of the isolation cut and requiring $|d_0| > 0.1$ mm for one of the muons (red line) and standard selection (black points).

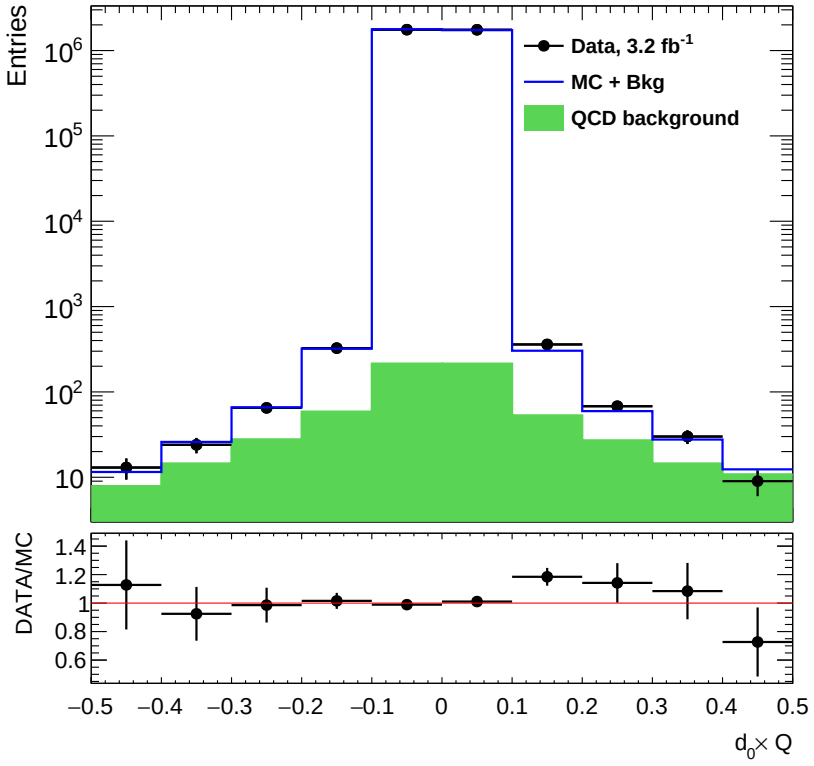

Figure 5.18: Fit of the $d_0 \cdot Q$ distribution for $Z \to \mu\mu$ events used to derive the multijet contribution. The template is determined using the 'probe' muon ('tag' cuts on $|d_0| > 0.1$). The fit is done to the $d_0 \cdot Q$ distribution of selected events, for both muons.

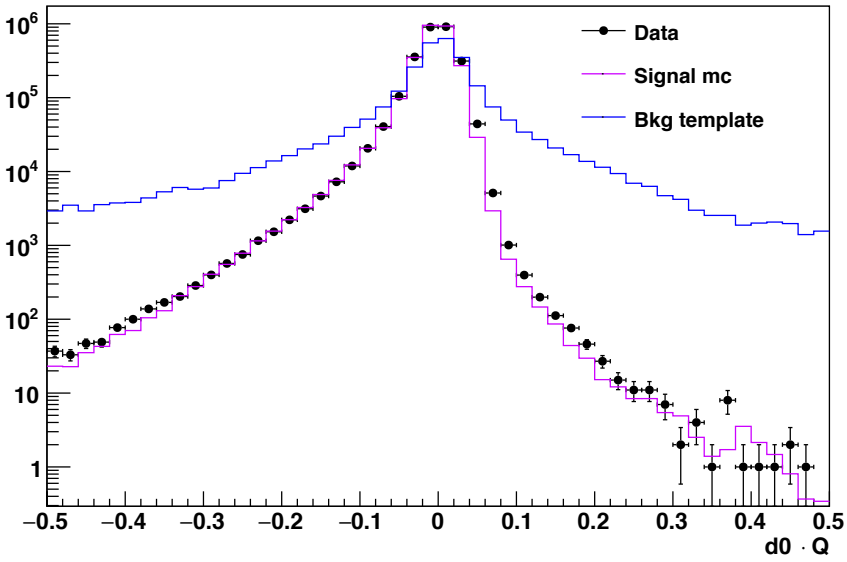

Figure 5.19: Comparison of the data with the signal MC simulation and multijet template for $d_0 \cdot Q$ distribution.

cover all possible mismodelings of this number which is challenging to measure due to its smallness, the systematic uncertainty on the multijet background is assigned to be 0.05%.

5.7 Systematic uncertainties on the cross-section measurement

Many sources of systematic uncertainty affect the cross-section measurements. When the measurement is not limited by statistics the systematic component plays the main role and define the precision of the measurement. The systematic uncertainty reflects the incomplete model assumptions in the measurement or poorly understood features of the detector or analysis techniques.

Systematic uncertainties can be subdivided into experimental uncertainties, arising from the efficiencies of lepton selection, luminosity and backgrounds evaluations, and uncertainties arising from the theoretical predictions. The size of the uncertainty for a particular systematic source can be estimated by varying it up and down and comparing it to the nominal value. Then, the difference between the nominal and the varied systematic values is taken as the uncertainty. To take into account proper correlation of uncertainty, toy MC or combined toy MC methods are used for the propagation of non-correlated uncertainties on the efficiency scale factors (which have the largest uncertainties).

5.7.1 Toy Monte Carlo method

The toy MC method is used for the propagation of uncorrelated uncertainties, while the combined toy MC method propagates correlated and uncorrelated uncertainties at the same time. Usually, the value of the scale factors are determined in N i, j bins of corresponding kinematic variables with the statistical and systematic components of the uncertainty

$$SF_{i,j} + \Delta_{i,j}^{stat} + \Delta_{i,j}^{syst}.$$

The statistical component is considered as uncorrelated for particular bins of maps, while the systematic

component can consist of correlated and uncorrelated uncertainties

$$\Delta_{i,j}^{syst} = \Delta_{i,j}^{cor} + \Delta_{i,j}^{uncor}.$$

To take into account the proper correlation between the bins, the defined numbers of toy efficiency maps, *N*toy maps, are generated using a random Gaussian function with a mean of zero and a standard deviation of one:

$$SF_{i,j}^{Ntoy} = SF_{i,j} + \Delta_{i,j}^{stat} Rndm.Gauss(0,1) + \sum_{k} \Delta_{i,j,k}^{cor} Rndm.Gauss(0,1),$$

where k is number of correlated systematic sources.

To determine the uncertainty coming from the scale factors, the RMS of the distribution of the N maps can be employed:

$$\bar{C_z} = \frac{1}{N\text{toy}} \sum_{i=1}^{N\text{toy}} C_{zi}$$

$$\sigma = \frac{1}{N\text{toy} - 1} \sqrt{\sum_{i=1}^{N\text{toy}} (C_{zi} - \bar{C_z})^2}.$$

5.7.2 Experimental systematic uncertainties

Electrons and muons have uncertainties associated with the scale factors correcting the Monte Carlo description of the trigger, reconstruction, identification, isolation efficiencies and with associated uncertainties on the momentum and energy scale. The systematic uncertainties are propagated into the final measurement through the corresponding C_Z uncertainty, and the effect of uncertainties on the total cross-section measurement is estimated thought C_Z factor, respectively. The correction factor, C_Z, is determined using simulation and data-driven corrections and includes the efficiencies for the trigger, reconstruction, and identification for the Z decays falling within the fiducial acceptance. Those are derived according to the prescription of the tools which are used for the MC corrections, described in Section 5.5. Moreover, additional uncertainties which enter into the cross-section measurement are luminosity, beam and background estimation uncertainties.

For some of sources of systematics, the toy MC method is used to reduce the uncertainty of the correlated sources of uncertainty in the different p_{T} and η bins.

Evaluated uncertainties for muon and electron channels are presented in Tables 5.13 and 5.14, respectively, and details on their determination are given below.

5.7.2.1 Common uncertainties

Pile-up uncertainty. The systematic uncertainty is defined as the difference between reweighting to $\langle\mu\rangle$ with the nominal scale factor and scale factor varied according to the tracking combined performance group recommendations, corrected for changes in the lepton identification and isolation efficiencies. The variation is done for the scale factors 1.00, 1.09 and 1.23. The variation of the pileup scaling factor demonstrated the significant influence on the isolation efficiency for both channels. The change in C_Z due to change in the efficiencies is subtracted, to avoid double counting of the uncertainties. The size of uncertainty is found be small. More details on the method of estimation are in Reference [157].

Z p_{T} mismodeling. The systematic uncertainty estimated from the Z p_{T} reweighting procedure by evaluating the difference between nominal C_Z and C_Z after Z p_{T} distributions are reweighted in both channels. The procedure is described in Subsection 5.2.3.

PDF uncertainty. The uncertainty is evaluated using PDF reweighing. It is based on the NNPDF3.0 set, where eigenvectors consist of a central value of PDF and 100 Monte Carlo replicas. The event weight for the PDF reweighting is calculated as:

$$w = \frac{f_{\mathrm{PDF_{var}}}(x_1, q_1, Q^2) \cdot f_{\mathrm{PDF_{var}}}(x_2, q_2, Q^2)}{f_{\mathrm{PDF_{nom}}}(x_1, q_1, Q^2) \cdot f_{\mathrm{PDF_{nom}}}(x_2, q_2, Q^2)},$$

where $f_{\mathrm{PDF}}(x_i, q_i, Q^2)$ is probability function characterized by flavours q_i and momentum fractions x_i of the initial partons, and by Q^2, the event scale. $\mathrm{PDF_{nom}}$ corresponds to the nominal prediction, used to generate the MC sample, and $\mathrm{PDF_{var}}$ with the modified input parameter.

The uncertainty is evaluated as the RMS of the replicas and chosen as the baseline in order to have compatibility with $t\bar{t}$ analysis. The evaluated uncertainties, NNPDF30_nlo_as_0118, for the muon and electron channel are presented in Tables 5.13 and 5.14, respectively.

The difference between the electron and muon channels is a consequence of the difference in selection efficiency as a function of rapidity Y_{Z}. This is confirmed by reweighting the $Y_{\mu\mu}$ reconstructed distribution to Y_{ee}. The $Y_{\mu\mu}$ distribution is reweighted with a polynomial function of degree five with parameters extracted from the fit of ratio of Y_{ee} to $Y_{\mu\mu}$. Reweighting of $Y_{\mu\mu}$ to Y_{ee} makes the PDF uncertainty consistent between the two channels. The details on the Y_{Z} reweighting are given in Appendix A.7.

Additionally, the systematics uncertainty is estimated with the 26 eigenvector variations of CT10NLO (as the Z signal MC is simulated using CT10NLO PDFs) and demonstrated similar size of the uncertainty. The details can be fond in Appendix A.8.

Luminosity uncertainty. The LUCID luminosity measurement is one of the sources of systematic uncertainty. The total uncertainty for the 2015 data set is estimated to be ±2.1%. The main contributions to this uncertainty are calibration (a determination of visible cross section), run to run stability and background uncertainties [95]. The biggest contribution comes from the calibration.

LHC beam energy. Relative uncertainty is estimated to be 0.66% of beam-energy value which is determined from the comparison of the revolution frequency of protons and ions [158] and propagated to the cross section with the VRAP 0.9 program [159]. A new value of the relative uncertainty on the beam energy was released after the results were published and this value is 0.1% [160].

Background estimation. Electroweak and top backgrounds are estimated from the MC simulation. Their uncertainties are based on the corresponding uncertainties on the cross sections to which the top and diboson samples are normalized. Those uncertainties contribute to the measurement negligibly. The uncertainty from multijet background estimation are assigned to be 0.05% in order to properly cover all possible mismodelings (see Subsection 5.6.2).

Underlying event and parton shower. An uncertainty contribution from the modeling of the parton showering (PS) process depends on the choice of parton shower program. Powheg-Box+Pythia 8.1 is used in this analysis, which has NLO+PS approximation. Different PS and NLO+PS merging schemes can be used, thus potentially relusting in an uncertainty, especially if UE and

PS change the hadronic environment and affect the particle ID (PID) and isolation efficiency. The uncertainty can be probed by using alternative Monte Carlo samples: Powheg-Box+Herwig for PS and aMCNLO [161]+Pythia for different model of NLO+PS merging. However, PID and isolation are determined in a data driven way, thus they should be compensated for, similar to pileup effect (see section about pileup). This is studied in 7 TeV analysis [2] and an uncertainty $< 0.2\%$ is found, dominated by the statistical uncertainty of the Powheg-Box+Herwig and aMCNLO+Pythia samples. Given that the error is below PID and isolations systematics, we do not include it.

5.7.2.2 Electron uncertainties

Each scale factor, which is applied to MC, is obtained in η and p_{T} bins and has statistical and systematic uncertainties. Systematic uncertainties can be either correlated or uncorrelated between the different bins. Those uncertainties are estimated and provided by the ElectronEfficiencyCorrection package [153, 154].

Electron energy resolution and scale. The systematic uncertainty on the energy resolution and scale, EG_RESOLUTION_ALL and EG_SCALE_ALL, is derived following a methodology from Run 1 taking into account added IBL detector and some simplified correlation model where all the systematics are summed in quadrature. The primally sources of uncertainty come from the in-situ corrections (event selection, procedures and statistics used for data-driven corrections) and beam conditions, detector descriptions, calibration procedures [162]. The tool provides two systematic variations. EG_RESOLUTION_ALL uncertainty has a small impact on the result.

Electron identification, isolation, reconstruction. The systematic uncertainty on the scale factors $\mathrm{SF_{id}}$, $\mathrm{SF_{iso}}$, $\mathrm{SF_{reco}}$: EL_EFF_ID_COMBMCTOY, EL_EFF_Iso_COMBMCTOY, EL_EFF_Reco_TotalCorrUncertainty. The systematics for identification come from two methods used for background estimation and variations of the selection on each method (invariant mass window variation, modification of the tag-and-probe selection, background template variation). The systematics for the isolation and reconstruction comes in a similar way as for the identification uncertainty. Details on the method and selection variation are given in Reference [144]. They are evaluated using the combined toy MC method. The dominant source is EL_EFF_ID_COMBMCTOY uncertainty.

Trigger efficiency. The systematic uncertainty on the scale factor, EL_EFF_Trigger_COMBMCTOY is evaluated using the combined toy MC method and is found to be small.

Opposite-charge requirement. The charge of one of the electrons can be mis-reconstructed for a fraction of $Z \to e^+e^-$ events, causing the event to be rejected by the opposite charge requirement. The estimation of this uncertainty is performed for 50 ns results and is described in Reference [163].

The total systematic uncertainty on the C_Z is then the sum in quadrature of the all electron related contributions which are listed in Table 5.13. The main source of uncertainty is electron identification uncertainty. Compared to the 50 ns analysis, the total systematic uncertainty is reduced from 1.0% to 0.5%, mainly due to improvements in the statistical component of the scale factor uncertainties and employing the toy MC method for the electron reconstruction source of uncertainty, which is the dominant source of systematic uncertainty in the 50 ns measurement.

Parameter	Up [%]	Down [%]
Pileup	0.01	−0.01
Z p_T mismodeling	−0.07	0.07
PDFNNPDF30_nlo_as_0118	0.10	−0.10
EG_RESOLUTION_ALL__1	−0.04	0.01
EG_SCALE_ALL__1	0.24	−0.25
EL_EFF_ID_COMBMCTOY__1	0.38	−0.38
EL_EFF_Iso_COMBMCTOY__1	0.14	−0.14
EL_EFF_Reco_COMBMCTOY__1	0.05	−0.05
EL_EFF_Trig_COMBMCTOY__1	0.01	−0.01
Opposite charge requirement	−0.15	0.15
Total	0.51	0.52

Table 5.13: Summary of the different terms contributing to the systematic uncertainty on C_Z for electron final states.

5.7.2.3 Muon uncertainties

The systematic uncertainty on correction factor, C_Z, comes in part from the uncertainties on the reconstruction and trigger efficiencies. Other effects are due to inefficiencies for selecting collisions with a reconstructed primary vertex, as well as the muon momentum scale and resolution.

Energy scale and resolution. The following variations are assigned to C_Z: variations in the smearing of the inner detector track (MUONS_ID), variations in the smearing of the muon spectrometer track (MUONS_MS) and variations in the scale of the momentum (MUONS_SCALE) with $\pm 1\sigma$ (Gaussian standard deviation), provided by the ATLAS MCP group. The main contribution to the uncertainty comes from mass window varying, background parametrization, scale parameter for the inner detector corrections, alignment studies [145]. The impact of these variations on C_Z is small.

Muon reconstruction. The following variations are assigned to C_Z: statistical uncertainty on the scale factor (MUON_EFF_STAT), and systematic uncertainty on the scale factor (MUON_EFF_SYS). The main contributions to the uncertainty are from the background estimation, varying the cone size, comparing the efficiency measured with the tag-and-probe method with the 'true' efficiency given by the fraction of generator-level muons [145]. Both components are estimated by a variation of one standard deviation. The MUON_EFF_SYS source is one of dominant sources of uncertainty in the muon channel. The size of this uncertainty is close to the one found in the $t\bar{t}$ analysis and in the ratio this source is almost cancelled (see Subsection 6.2.1).

Trigger efficiency. The following variations are assigned to C_Z: statistical uncertainty on the scale factor (MUON_EFF_STAT), estimated using the toy MC method as described above, and systematic uncertainty on the scale factor (MUON_EFF_SYS).

Isolation scale factor. The following variations are assigned to C_Z: statistical uncertainty and systematic uncertainty on the scale factor. Both components are estimated by variation of one standard deviation and provided within the standard ASG systematics framework. The contributions to the systematics are background and some variation of selection: invariant mass selection window, the

Parameter	Up [%]	Down [%]
Pileup	−0.01	−0.03
Z p_T mismodeling	−0.03	0.03
PDFNNPDF30_nlo_as_0118_eigenset	0.02	−0.02
MUONS_ID__1	−0.01	0.00
MUONS_MS__1	−0.01	0.00
MUONS_SCALE__1	−0.07	0.04
MUON_EFF_STAT__1	0.33	−0.33
MUON_EFF_SYS__1	0.59	−0.59
MUON_EFF_TrigSystUncertainty__1	0.12	−0.12
MUON_EFF_TrigStatTOYUncertainty__1	0.03	−0.03
MUON_ISO_STAT__1	0.07	−0.07
MUON_ISO_SYS__1	0.40	−0.40
MUON_TTVA_STAT__1	0.00	0.00
MUON_TTVA_SYS__1	0.00	0.00
Opposite charge requirement	0.00	0.00
Total	0.80	0.81

Table 5.14: Summary of the different terms contributing to the systematics uncertainty on C_Z for muon final states.

isolation of the tag muon, the minimum quality of the probe muon, the opening angle between the two muons, the ΔR between the probe muon and the closest jet [145]. The MUON_EFF_SYS source is one of the dominant sources of systematic uncertainty in the muon channel and does not cancel in the ratio with $t\bar{t}$.

Muon track-to-vertex-association (TTVA). The following variations are assigned to C_Z: statistical uncertainty on the scale factor (MUON_TTVA_STAT), and systematic uncertainty on the scale factor (MUON_TTVA_SYS). Both components are estimated by variation of one standard deviation and provided within the standard ASG systematics framework. The effect of those errors is found to be negligible.

Opposite-charge requirement. The effect is estimated by checking at the efficiency of the opposite-charge requirement at the end of cut-flow. It is found to be negligibly small.

The total systematic uncertainty on C_Z is then the sum in quadrature of the all muon related contributions which are listed in Table 5.14. Compared to the 50 ns analysis, the total systematic uncertainty is reduced from 1.1% to 0.8%, mainly due to improvements in the statistical component of the scale factor uncertainties. The dominant sources of uncertainty are the muon reconstruction and isolation uncertainties.

5.7.3 Theoretical systematic uncertainties for predictions

The theoretical systematic uncertainties assigned to the calculated Z-boson cross sections are described in Section 2.5.1. The systematics uncertainty of the theoretical predictions are comprised of PDF, scale, strong coupling constant variations and some intrinsic theory uncertainties. The dominant source of the uncertainty is uncertainty on the proton PDFs.

5.8 Kinematic distributions

The comparison of important kinematic distributions between data and the signal Monte Carlo simulations in the electron and muon channels including expected contributions from all backgrounds sources after all selection criteria and corrections applied are presented in Figures 5.20–5.25. Figures 5.20, and 5.22 show the distributions of the lepton pseudorapidity and the lepton transverse momentum. Figures 5.21, and 5.23–5.25 show the dilepton transverse momentum, rapidity and the invariant mass of Z-boson candidates (in linear and logarithmic scales), respectively. All kinematic distributions are in a good agreement between data and Monte Carlo simulation in general. The lepton and boson transverse momentum distributions are in a good agreement as well, after applying the reweighting procedure for the MC as is described in Subsection 5.2.3. The invariant mass distribution of the lepton pair is in reasonable agreement, with some deviations at low masses.

The signal MC samples are normalized to the measured combined total cross section of the electron and muon channels, while background samples are normalized to the their MC cross sections. All MC samples are normalized to the luminosity, taking into account the sum of weights from the MC samples as well:

$$scale = N_{MC} \cdot L \cdot \sigma \cdot \epsilon_{MC_{filter}} \cdot \epsilon_{DAOD},$$
$$\epsilon_{DAOD} = \frac{\sum w_{DAOD}}{\sum w_{AOD}} = \frac{\cancel{\sum w_{DAOD}}}{\cancel{\sum w_{DAOD}}} \cdot \frac{N_{DAOD}}{N_{AOD}}$$

where

- σ is cross-section value used by generator in the MC simulation (see Table 5.2);
- $\epsilon_{MC_{filter}}$ is filter efficiency at the generator level, indicate the ratio between events passing the filter and the total number of generated events;
- $\sum w_{AOD}$ is the initial sum of weights which corresponds to the total generated event in the AOD samples;
- $\sum w_{DAOD}$ is the sum of weights which corresponds to the total generated event in the derived DAOD samples.

Only systematics related to the applied correction factors in the MC are considered on the control distributions, since they are evaluated in each bin of distributions. The electron resolution and energy scale corrections are the dominant sources of uncertainties on the invariant mass of electron pair distribution up to 0.15% under mass peak. The muon scale and resolution sources of uncertainties have biggest impact on invariant mass of the muon pair, up to 0.04% in the invariant mass range $85 < m_{ll} < 100$ GeV. The boson and lepton transverse momentum distributions have biggest impact from isolation efficiency and resolution, up to 0.05%, and from muon efficiency systematic, up to 0.03%, for the electron and muon channels, respectively. The systematic uncertainties on electron and muon pseudorapidity and boson rapidity distributions are tiny sources of uncertainties with the main contribution from identification efficiency and muon efficiency, respectively.

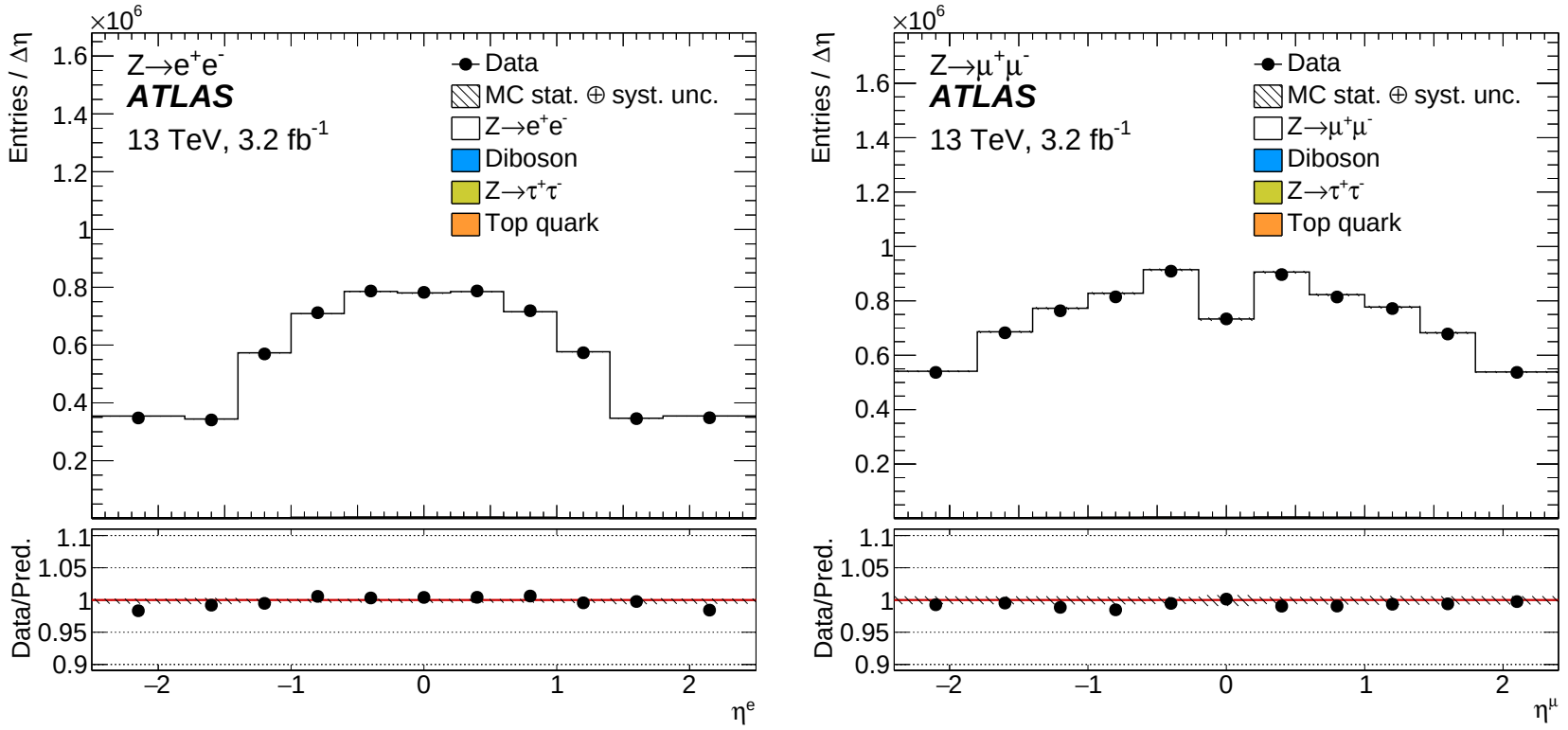

Figure 5.20: Lepton pseudorapidity distribution from the $Z \to e^+e^-$ selection (left) and the $Z \to \mu^+\mu^-$ selection (right). The bins in the distributions are divided by the bin width due to unequal bin widths. The expected contributions from all backgrounds are estimated with Monte Carlo simulations. The background processes are heavily suppressed and not visible on the linear scale. The systematic uncertainties for the signal are combined in the shaded band, and the statistical uncertainties are shown on the data points. The luminosity uncertainty is not included. The systematic error bands and statistical uncertainties are often hidden by the symbols and lines.

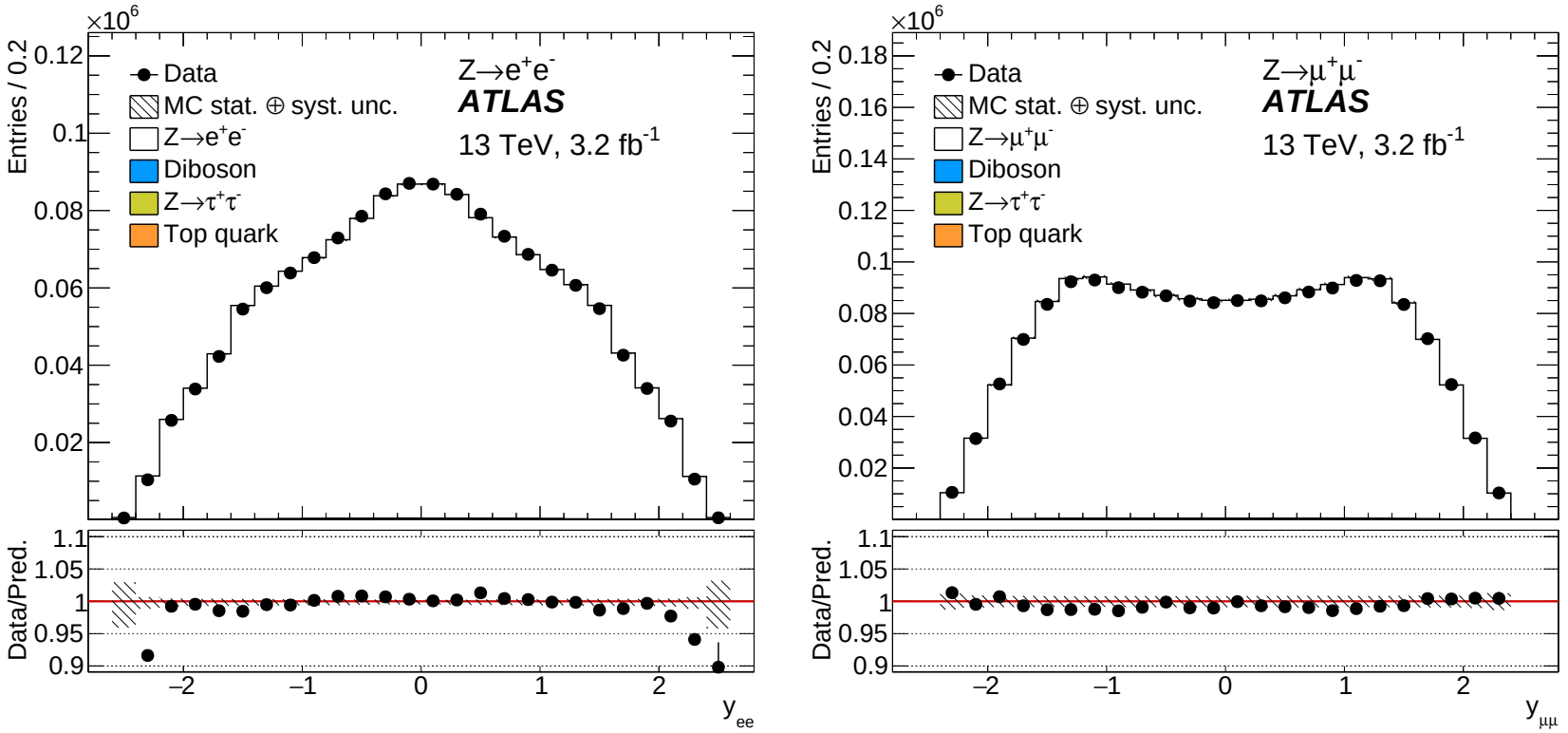

Figure 5.21: Z-boson rapidity distribution after the $Z \to e^+e^-$ selection (left) and the $Z \to \mu^+\mu^-$ selection (right). The expected contributions from all backgrounds are estimated with Monte Carlo simulations. The background processes are heavily suppressed and not visible on the linear scale. The systematic uncertainties for the signal are combined in the shaded band, and the statistical uncertainties are shown on the data points. The luminosity uncertainties are not included. The systematic error bands and statistical uncertainties are often hidden by the symbols and lines. The discrepancies observed at high $|y_{ee}|$ are due to mismatch of the plot and scale-factor binning in $|\eta_e|$.

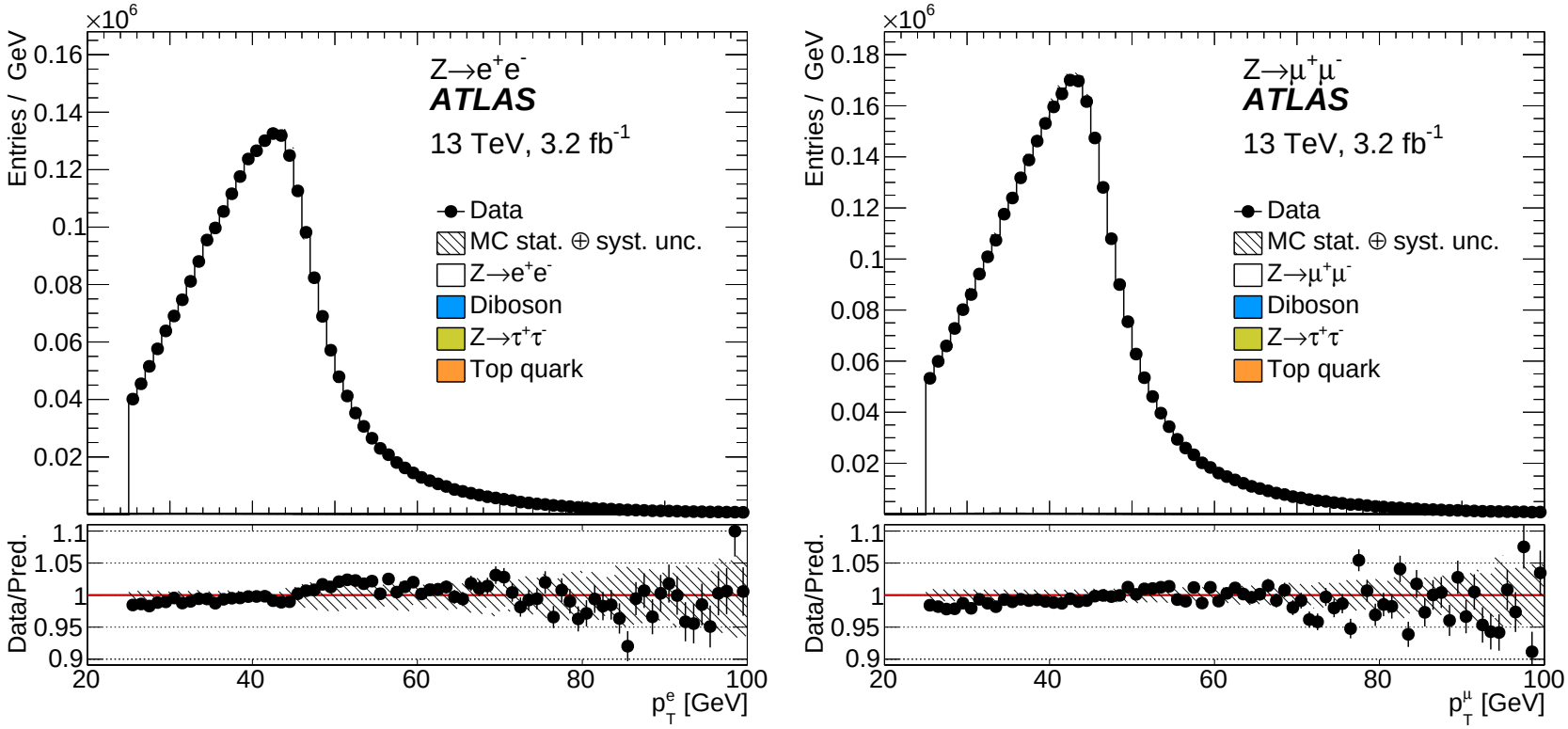

Figure 5.22: Lepton transverse momentum distributions from the $Z \to e^+e^-$ selection (left) and the $Z \to \mu^+\mu^-$ selection (right). The expected contributions from all backgrounds are estimated with Monte Carlo simulations. The background processes are heavily suppressed and not visible on the linear scale. The systematic uncertainties for the signal are combined in the shaded band, and the statistical uncertainties are shown on the data points. The luminosity uncertainties are not included. The systematic error bands and statistical uncertainties are often hidden by the symbols and lines.

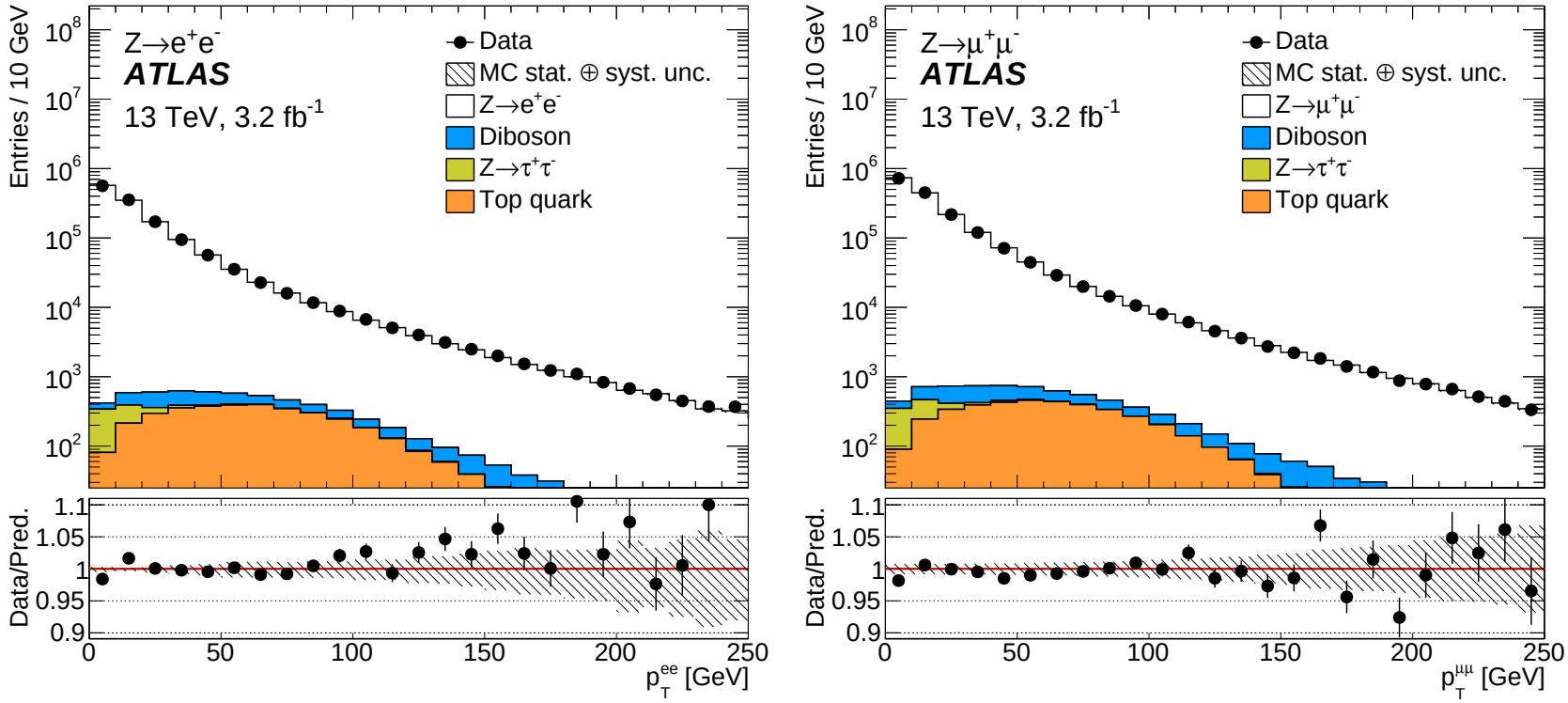

Figure 5.23: Z-boson transverse momentum distribution after the $Z \to e^+e^-$ selection (left) and the $Z \to \mu^+\mu^-$ selection (right). The expected contributions from all backgrounds are estimated with Monte Carlo simulations. The systematic uncertainties for the signal are combined in the shaded band, and the statistical uncertainties are shown on the data points. The luminosity uncertainties are not included. There are ten entries in the histogram for each candidate event. The systematic error bands and statistical uncertainties are often hidden by the symbols and lines.

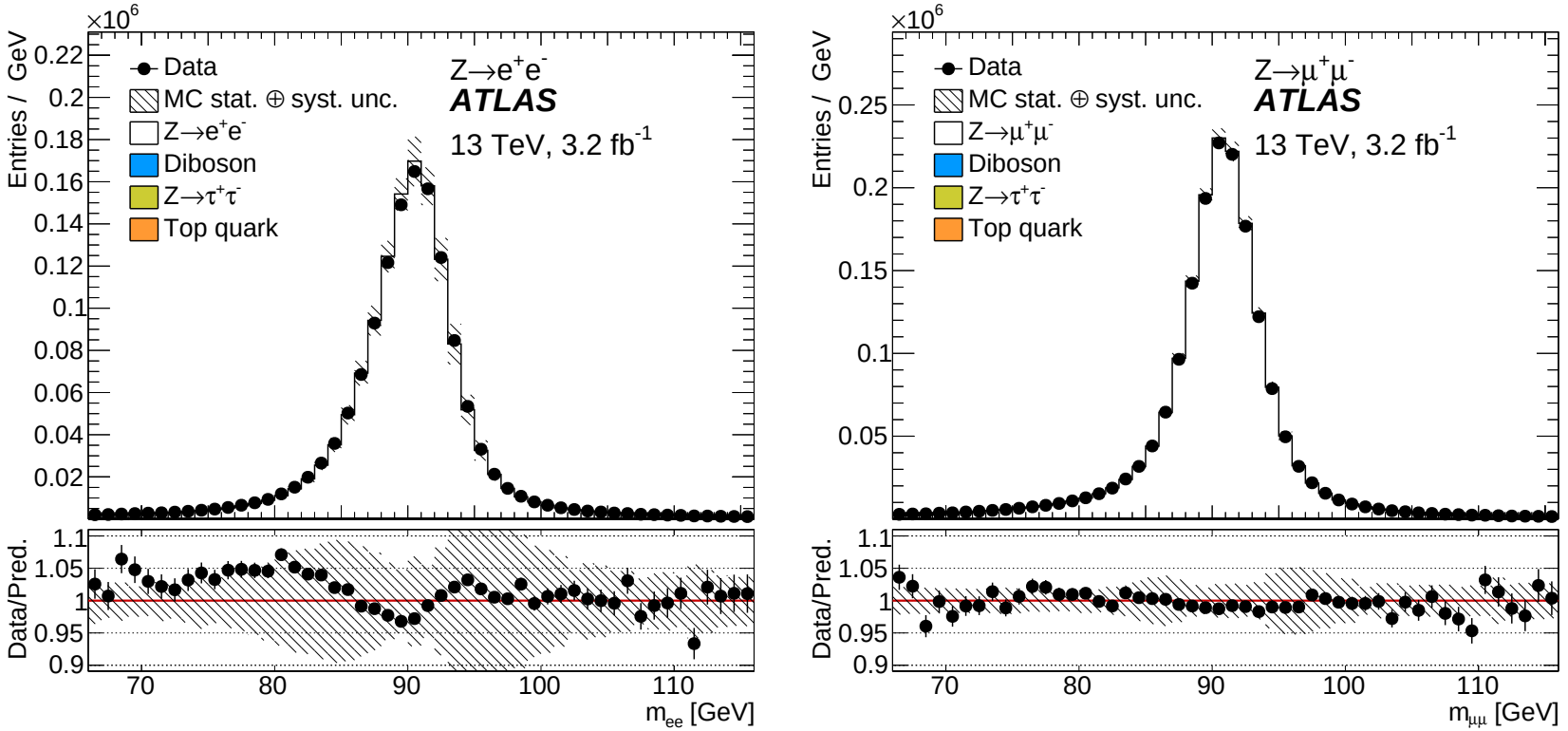

Figure 5.24: Dilepton mass distribution after the $Z \to e^+e^-$ selection (left) and the $Z \to \mu^+\mu^-$ selection (right) in linear scale. The expected contributions from all backgrounds are estimated with Monte Carlo simulations. The background processes are heavily suppressed and not visible on the linear scale. Systematic uncertainties for the signal are combined in the shaded band, and the statistical uncertainties are shown on the data points. The luminosity uncertainties are not included. The systematic error bands and statistical uncertainties are often hidden by the symbols and lines.

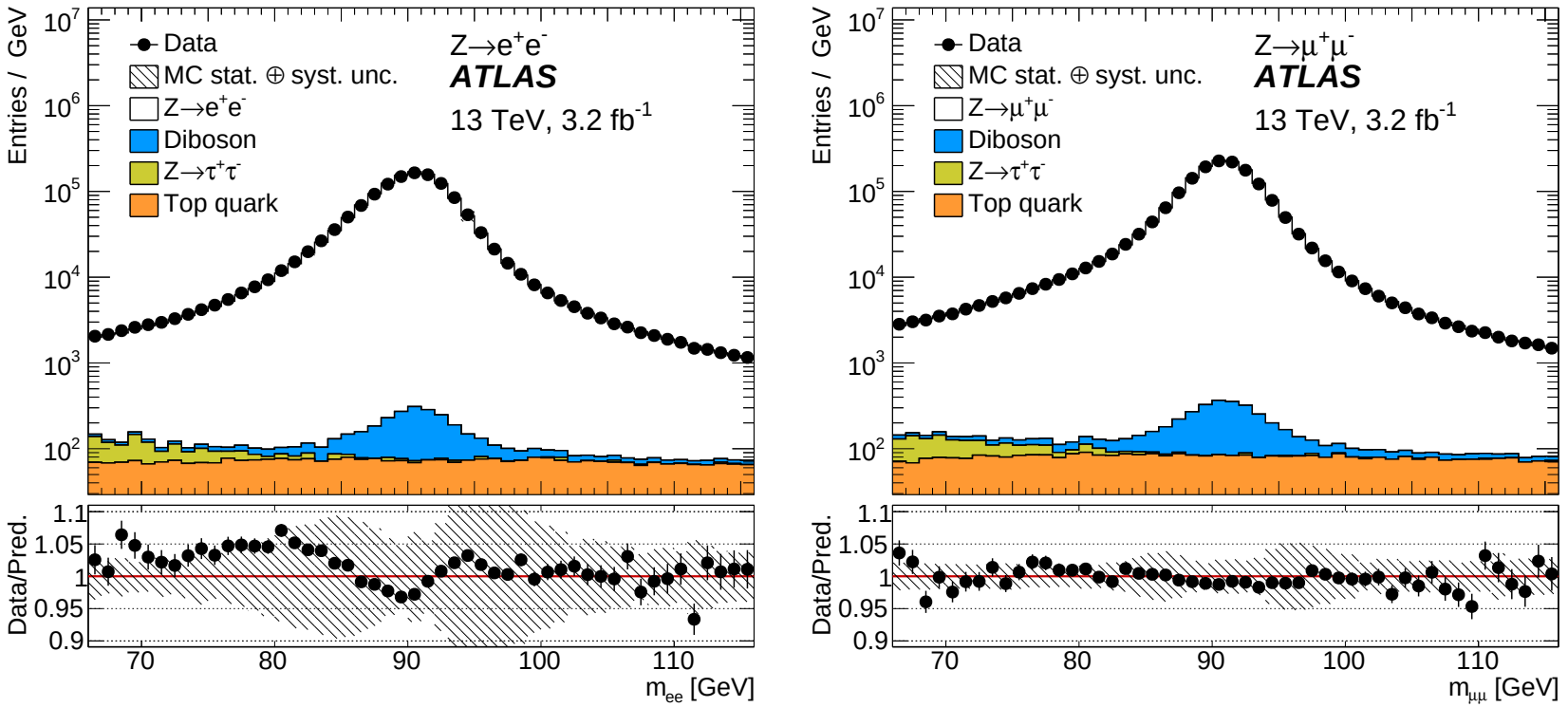

Figure 5.25: Dilepton mass distribution after the $Z \to e^+e^-$ selection (left) and the $Z \to \mu^+\mu^-$ selection (right) in logarithmic scale. The expected contributions from all backgrounds are estimated with Monte Carlo simulations. The systematic uncertainties for the signal are combined in the shaded band, and the statistical uncertainties are shown on the data points. The luminosity uncertainties are not included. The systematic error bands and statistical uncertainties are often hidden by the symbols and lines.

5.9 Cross-section results

All of the elements necessary to calculate the fiducial cross section for Z-boson production in the electron and muon decay channels are summarized in Table 5.15. The A_Z factor (see definition in 5.1) is calculated with the DYNNLO 1.5 program using the CT14 PDF set for the central value and FEWZ 3.1 for the variations accounting for systematic uncertainties. The statistical uncertainties resulting from these evaluations are negligible. The systematic uncertainties on the acceptance are dominated by the limited knowledge of the parton distribution functions. A detailed description of the extraction of the A_Z factor can be found in Reference [20]. The fiducial cross sections are calculated using the equation 5.4 and are presented along with their statistical, systematic, beam and luminosity uncertainties.

	Electron channel	**Muon channel**
Background-subtracted signal	1 360 681.9 ± 1 169.2(stat) ± 761.7(syst) ± 133.2(lumi)	1 727 697.5 ± 1 317.3(stat) ± 953.3(syst) ± 157.5(lumi)
Correction factor, C_Z	$0.5536 \pm 0.0002(\text{stat})\,^{+0.0028}_{-0.0029}$ (syst)	$0.7064 \pm 0.0003(\text{stat})\,^{+0.0057}_{-0.0057}$ (syst)
Fiducial cross section [pb]	778.3 ± 0.7(stat) ± 4.0(syst) ± 5.4(beam) ± 16.3(lumi)	774.4 ± 0.6(stat) ± 6.2(syst) ± 5.3(beam) ± 16.3(lumi)
Acceptance factor, A_Z	0.395 ± 0.007(syst)	0.395 ± 0.007(syst)
Total cross section [pb]	1 970.3 ± 1.7(stat) ± 36.5(syst) ± 13.8(beam) ± 41.4(lumi)	1 960.6 ± 1.5(stat) ± 38.3(syst) ± 13.7(beam) ± 41.2(lumi)

Table 5.15: Results for the fiducial cross sections, σ^{fid}, for the Z-boson in the electron and muon decay channels. The observed numbers of signal events after background subtraction are shown for each channel, along with the correction factors, C_Z, the fiducial cross sections with their statistical, systematic, beam and luminosity uncertainties quoted in that order. The systematic uncertainty of the luminosity is 2.1%.

The measured cross sections in the electron and muon decay channels can be used to examine of lepton universality ($\Gamma_{Z\to ee} = \Gamma_{Z\to\mu\mu}$). The ratio of the fiducial cross sections is calculated as:

$$R_Z = \frac{\sigma^{\text{fid}}_{Z\to ee}}{\sigma^{\text{fid}}_{Z\to\mu\mu}} = 1.0050 \pm 0.001(\text{stat}) \pm 0.009(\text{syst}) = 1.005 \pm 0.009.$$

This result agrees with the Standard Model expectation (unity) and confirms that muons and electrons are produced equally in Z decays. In addition, the result agrees with previous published ATLAS results using 7 TeV [2] and 13 TeV (50 ns) data [4] and with the latest Particle Data Group (PDG) world average value [27] (see Table 5.16).

Source	R_Z
7 TeV	1.0026 ± 0.0050
13 TeV (50 ns)	1.0050 ± 0.0162
PDG	0.9991 ± 0.0028

Table 5.16: Ratios of Z-boson production cross sections in the electron and muon decay channels.

5.9.1 Comparison between 25 ns and 50 ns results

The fiducial and total cross sections using 50 ns data set along with their statistical, systematic and luminosity uncertainties are presented in Table 5.17. The 50 ns data set corresponds to the integrated luminosity of 80.9 pb^{-1}. The comparison between measurements using the 25 ns and 50 ns data sets for the electron and muon channels is shown in Figure 5.26. The two measurements for both analysis channels agree within the systematic uncertainties and within the statistical uncertainties between the same flavour of channels, showing good consistency with one another.

	50 ns	
	Electron channel	**Muon channel**
	value ± stat ± syst ± lumi	value ± stat ± syst ± lumi
Correction C_Z	$0.5520 \pm 0.0002\,^{+0.0055}_{-0.0054}$	$0.7111 \pm 0.0003\,^{+0.0075}_{-0.0075}$
Fiducial cross section [pb]	780.8 ± 4.2 ± 7.7 ± 16.4	777.0 ± 3.7 ± 8.2 ± 16.3
Total cross section [pb]	1 986.9 ± 10.7 ± 40.5 ± 41.7	1 977.1 ± 9.4 ± 40.9 ± 41.5

Table 5.17: Measured fiducial, σ^{fid}, and total cross sections, σ^{tot}, for Z bosons in the electron and muon decay channels using 50 ns datasets. The correction factors, C_Z, the fiducial cross sections with their statistical, systematic, beam and luminosity uncertainties quoted in that order. The systematic uncertainty of the luminosity is 2.1%.

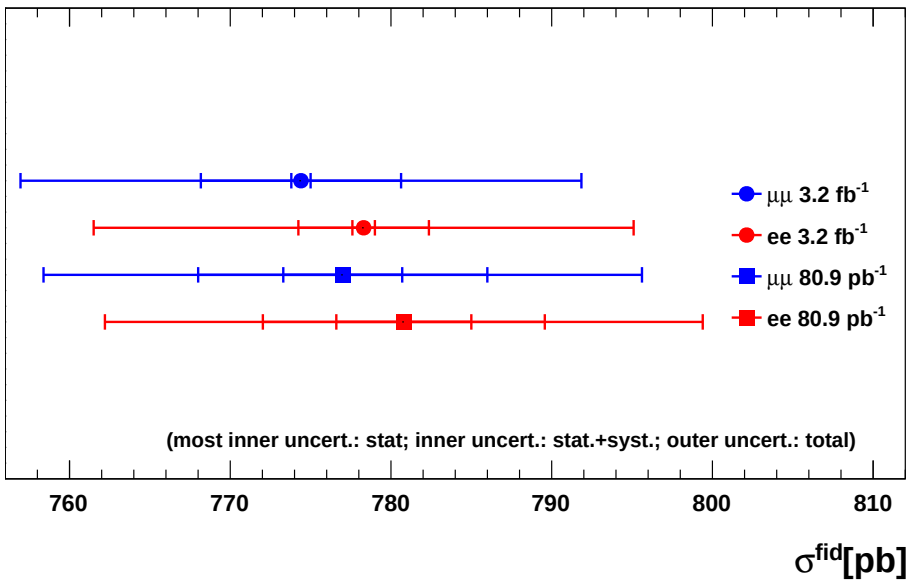

Figure 5.26: Comparison of fiducial cross sections between electron and muon decay channels and between 25 ns and 50 ns data sets (which corresponds to the integrated luminosity of 3.2 fb^{-1} and 80.9 pb^{-1}). The figure shows the central values in blue color for muon channel and red color for electron channel and their statistical, statistical with systematics and total uncertainties as well.

Figure 5.26 demonstrates that both measurements are dominated by the luminosity uncertainty of

2.1% and the 50 ns measurement has a bigger statistical uncertainty than the 25 ns measurement. The systematic uncertainties for the 25 ns results are significantly reduced, mainly due to the reduced statistical uncertainty and with employing the toy MC method for some of the systematics, which is not the case for 50 ns.

5.10 Combination of the cross sections

The combination of the total and fiducial cross sections measured in the $Z \to e^+e^-$ and $Z \to \mu^+\mu^-$ channels is done using the HERAverager tool [164], which was developed for the combination of results from the experiments at HERA. The tool performs the combination of the cross sections by taking into account all sources of correlated and uncorrelated uncertainties. The combination procedure is based on the χ^2 method in which the combined χ^2 function is defined as:

$$\chi^2(m,b) = \sum_l \frac{(m - \mu_l - \sum_j^{N_s} \Gamma_l^j b_j)^2}{\Delta_l^2} + \sum_j^{N_s} b_j^2, \tag{5.9}$$

where

- μ_l is the measured value of the cross section with an uncertainty Δ_l
- b_j are the nuisance parameters corresponding to each source of systematic uncertainty
- Γ_l^j is the absolute correlated systematics uncertainty
- l corresponds to the summation over statistically uncorrelated measurements and j to the summation over all sources of systematics uncertainty N_s.

The averaging procedure is performed by minimizing χ^2 function:

$$\frac{d\chi^2}{dm} = 0.$$

For this combination, the systematic uncertainties are symmetrized as $\Delta_{sym} = 0.5 \cdot (\Delta_+ - \Delta_-)$ and are shown in Table 5.18. Sources corresponding to lepton reconstruction and identification are considered as uncorrelated between electron and muon channel. The systematic uncertainties from electroweak background sources and luminosity are treated as correlated.

The resulting combined fiducial Z-boson cross section and extrapolated to the total cross section by applying acceptance factor A_Z are following:

- $\sigma_Z^{\text{fid}} = 777 \pm 1(\text{stat}) \pm 3(\text{syst}) \pm 5(\text{beam}) \pm 16(\text{lumi})$ [pb]
- $\sigma_Z^{\text{tot}} = 1969 \pm 1(\text{stat}) \pm 36(\text{syst}) \pm 14(\text{beam}) \pm 41(\text{lumi})$ [pb]

There is a sizeable reduction of uncertainty compared to the individual electron and muon channel measurements since most of the systematic error sources are correlated.

5.11 Comparison with the theoretical predictions

The predictions for Z-boson production are calculated using the following PDF sets: CT14, NNPDF3.0, MMHT14, ATLAS-epWZ12, HERAPDF2.0, and ABM12. The details on the calculation are described in

Source of uncertainty	$\delta C/C$ [%] $Z \to e^+e^-$	$Z \to \mu^+\mu^-$
Lepton trigger	< 0.1	0.1
Lepton reconstruction, identification	0.4	0.7
Lepton isolation	0.1	0.4
Lepton scale and resolution	0.2	0.1
Charge identification	0.1	–
Pile-up modelling	< 0.1	< 0.1
PDF	0.1	< 0.1
$p_{\mathrm{T}}^{\ell\ell}$ mismodelling	0.1	< 0.1
Total	0.5	0.8

Table 5.18: Relative symmetrized systematic uncertainties, in %, in the correction factors C_Z in the electron and muon channels.

Subsection 2.5.1. The comparison between measured fiducial cross section and predictions using different PDF sets is shown in Figure 5.27. All predictions agreed with the measurement within uncertainties except NNPDF3.0 PDF set. Especially, HERAPDF2.0 prediction at NNLO describes the measurement best.

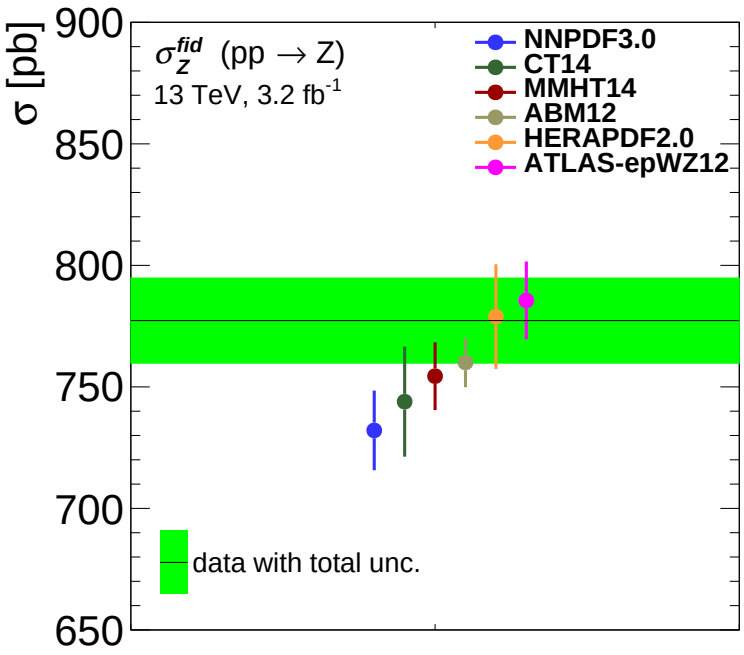

Figure 5.27: Theoretical predictions for the fiducial cross section using different PDF sets: CT14, NNPDF3.0, MMHT14, ATLAS-epWZ12, HERAPDF2.0, and ABM12 (includes only the symmetrised PDF uncertainty) and compared to the measured combined cross section.

CHAPTER 6

Results on ratios

The measured combined $Z \to e^+e^-$ and $Z \to \mu^+\mu^-$ production cross sections are used to evaluvate the various ratios using new accurate measurements of the $t\bar{t}$-pair production cross section [22] at the centre-of-mass energy of $\sqrt{s} = 13$ TeV, previous measurements of the $t\bar{t}$ and Z-boson production cross section at the centre-of-mass energy of $\sqrt{s} = 7$ TeV and 8 TeV [2, 3, 21] the results are reported in Reference [20]. The measurements probe different Bjorken-x regions at various $\sqrt{s}$ values with decreased an x value with the $\sqrt{s}$. Gluon–gluon processes, gg, dominate in the $t\bar{t}$-pair production and quark–antiquark annihilation, $q\bar{q}$, prevail in the Z-boson production. The ratio of the $t\bar{t}$-pair to the Z-boson cross section at a given centre-of-mass energy is sensitive to gluon density [23]. An advantage to build the ratio between cross sections at a given $\sqrt{s}$ using identical data samples is that the experimental uncertainty on a LHC luminosity and some experimental and theoretical uncertainties can be eliminated in the ratio. Hence, ratio results will become more accurate. The same thing happens when a double ratio of $t\bar{t}$ to Z at two different $\sqrt{s}$ is calculated. The luminosity, which is correlated for the different $\sqrt{s}$, disappears already from the single ratio and does not affect the results. In this section, the focus will be on the single ratios of $t\bar{t}$ to Z-boson cross sections at $\sqrt{s} = 13$ TeV and double ratios at the different centre-of-mass energies.

6.1 Input to the ratios

6.1.1 $t\bar{t}$ at $\sqrt{s} = 13$ TeV

Inclusive total and fiducial $t\bar{t}$ production cross sections are measured in a decay channel where the top (antitop) quark decays into a positively (negatively) charged W boson (W^+, W^-) and b-quark jet, and afterwards the W decays to a charged lepton ($l^+ = e^+, \mu^+, l^- = e^-, \mu^-$) and an antineutrino ($\nu^+, \nu^-$). The measurement is based on the data collected in 2015 with 25 ns bunch spacing and corresponds to a total integrated luminosity of $3.2\,\text{pb}^{-1}$. As it was previously mentioned (see Section 5.4.4), the event and lepton selection are entirely consistent with Z-boson selection at $\sqrt{s} = 13$ TeV. The measured total cross section is reported to be:

$$\sigma^{\text{tot}}_{t\bar{t}} = 818 \pm 8(\text{stat}) \pm 27(\text{syst}) \pm 19(\text{lumi}) \pm 12(\text{beam})\,[\text{pb}]$$

where four uncertainties arise from data statistics, experimental and theoretical systematic effects, the integrated luminosity and the LHC beam energy. The total relative uncertainty is 4.4% and an internal systematic uncertainty without the luminosity is 3.3%. The fiducial inclusive cross section measured in

$\sqrt{s}$ [TeV]	13	8	7
$p_{\mathrm{T}}^{\ell} >$	25 GeV	20 GeV	20 GeV
$\lvert\eta_{\ell}\rvert <$	2.5	2.4	2.5
$\lvert y_{\ell\ell}\rvert <$	–	2.4	–
$m_{\ell\ell}$	66–116 GeV	66–116 GeV	66–116 GeV
Extrapolation E	–	0.941 ± 0.001 (PDF)	0.898 ± 0.001 (PDF)

Table 6.1: Definition fiducial regions at $\sqrt{s} = 13, 8, 7$ TeV used in the Z-boson measurements. A factor E is used to extrapolate the 7 and 8 TeV results to the common phase space defined by the 13 TeV results. A PDF uncertainty is obtained from the CT14 eigenvector set.

the fiducial phase space under conditions that $p_{\mathrm{T}} > 25$ GeV and $|\eta| < 2.5$ is:

$$\sigma_{t\bar{t}}^{\mathrm{fid}} = 11.32 \pm 0.10(\mathrm{stat}) \pm 0.29(\mathrm{syst}) \pm 0.26(\mathrm{lumi}) \pm 0.17(\mathrm{beam})\,[\mathrm{pb}]$$

which corresponds to the total relative uncertainty of 3.9% and the internal systematic uncertainty excluding the luminosity and the LHC beam energy of 2.5%.

The values and procedure of estimation of the theoretical predictions for the total $t\bar{t}$ cross sections are described in Section 2.5.

6.1.2 $t\bar{t}$ and Z-boson cross sections at $\sqrt{s}$ = 7 TeV and 8 TeV

The measurements of the Z-boson and $t\bar{t}$ production cross sections at $\sqrt{s} = 7$ TeV and 8 TeV are performed using the data that correspond to the total integrated luminosity of 4.6 fb^{-1} and 20.2 fb^{-1} (20.3 fb^{-1} in the case of $t\bar{t}$), appropriately. They are measured in a slightly different fiducial phase space in the comparison to one used for the results at $\sqrt{s} = 13$ TeV. Therefore, to use them in the ratios, their original cross sections are corrected to a common fiducial phase space, which is defined by the measurement of the total cross section at $\sqrt{s} = 13$ TeV by applying extrapolation factors, E. Those factors are calculated from eigenvector-by-eigenvector for the CT14 PDF uncertainties using DYNNLO 1.5. The fiducial phase space employed in the measurements at $\sqrt{s} = 7$ TeV, 8 TeV, and 13 TeV and corresponding extrapolation factors, E, are presented in Table 6.1. The $t\bar{t}$ fiducial phase space remained unchanged for all three centre-of-mass energies.

Z at 7 TeV: Extrapolated to the common fiducial volume, the fiducial cross sections for the electron and muon channels [2]:

$$\sigma_Z^{\mathrm{com.fid}}(ee,\ \sqrt{s} = 7\ \mathrm{TeV}) = 451.17 \pm 0.45(\mathrm{stat}) \pm 8.71(\mathrm{syst})\ [\mathrm{pb}]\,,$$
$$\sigma_Z^{\mathrm{com.fid}}(\mu\mu,\ \sqrt{s} = 7\ \mathrm{TeV}) = 450.02 \pm 0.34(\mathrm{stat}) \pm 8.76(\mathrm{syst})\ [\mathrm{pb}]\,.$$

Z at 8 TeV: Extrapolated to the common fiducial volume, the fiducial cross sections for the electron and muon channels [3]:

$$\sigma_Z^{\mathrm{com.fid}}(ee,\ \sqrt{s} = 8\ \mathrm{TeV}) = 506.99 \pm 0.20(\mathrm{stat}) \pm 11.03(\mathrm{syst})\ [\mathrm{pb}]\,,$$
$$\sigma_Z^{\mathrm{com.fid}}(\mu\mu,\ \sqrt{s} = 8\ \mathrm{TeV}) = 504.74 \pm 0.15(\mathrm{stat}) \pm 10.82(\mathrm{syst})\ [\mathrm{pb}]\,.$$

$t\bar{t}$ at 7 and 8 TeV: the $t\bar{t}$ total cross sections are [21]:

$$\sigma^{\text{tot}}_{t\bar{t}}(\sqrt{s} = 7\text{ TeV}) = 182.9 \pm 3.1(\text{stat}) \pm 4.2(\text{exp + theo}) \pm 3.6(\text{lumi}) \pm 3.3(\text{beam})\text{ [pb]},$$
$$\sigma^{\text{tot}}_{t\bar{t}}(\sqrt{s} = 8\text{ TeV}) = 242.9 \pm 1.7(\text{stat}) \pm 5.5(\text{exp + theo}) \pm 5.1(\text{lumi}) \pm 4.2(\text{beam})\text{ [pb]}.$$

6.2 Ratios

6.2.1 Correlation model at 13 TeV

The correlation model is estimated for the systematic uncertainties related to the Z-boson and $t\bar{t}$ production measurements prior to calculation of uncertainties of ratios. A detailed list of the uncertainties on the ratio of $t\bar{t}$ to Z-boson cross sections at $\sqrt{s} = 13$ TeV is presented in Table 6.2, and the description of names for systematics uncertainties mentioned in this table is explained in Appendix A.5. The details on the correlation of systematic uncertainties for other centre-of-mass energies can be found in Reference [157]. Dominant sources of the systematic uncertainties in the extracted $t\bar{t}$ cross section are the luminosity determination and $t\bar{t}$ modelling (the choice of $t\bar{t}$ generator), in particular, from the $t\bar{t}$ shower and hadronization uncertainty.

The sources of systematics for the $t\bar{t}$ and Z-boson cross-section measurements related to the luminosity, beam energy, lepton identification and trigger requirements, and momentum scales and resolutions are considered to be correlated, since all selection criteria are synchronized between two analyses by applying the same electron and muon identification, isolation and trigger requirements within the same lepton kinematic phase space. The systematic uncertainties, employed by toy MC method, used identical toy MC configurations as well. Some lepton-related uncertainties do not cancel completely as they depend on the transverse momentum and pseudorapidity of the lepton. The uncertainties related to the lepton isolation requirements are regarded to be uncorrelated between both analyses because for the $t\bar{t}$ measurement they are determined in situ to account different hadronic environments. The background uncertainties are considered to be uncorrelated between two analysis, as the leading background sources are different for each measurement.

Indeed, the uncertainty on the ratio is reduced in the comparison to the uncertainty on the $t\bar{t}$ cross section from 4.42 to 3.94, which is 11 % difference, mainly due to the almost entirely cancellation of luminosity uncertainty (see Table 6.2). The systematic uncertainty on the ratio is dominated by the $t\bar{t}$ modelling uncertainty.

6.2.2 Single ratios

The ratio of the $t\bar{t}$ to Z-boson production cross sections, $R_{t\bar{t}/Z}$, is defined as:

$$R_{t\bar{t}/Z} = \frac{\sigma_{t\bar{t}}}{0.5(\sigma_{Z\to e^+e^-} + \sigma_{Z\to\mu^+\mu^-})}, \tag{6.1}$$

where $\sigma_{Z\to ee}$ and $\sigma_{Z\to\mu\mu}$ are the inclusive Z-boson production cross sections measured in dielectron and dimuon channel multiplied by the corresponding $Z \to e^+e^-$ and $Z \to \mu^+\mu^-$ branching fractions. The factor of 0.5 in the denominator is employed in order to have the same weight in the ratio and to maximize the cancellation of lepton-related systematic uncertainties concerning the numerator, where only one electron and one muon are in the final state.

The evaluated ratio between the $\sigma_{t\bar{t}}$ to σ_Z, as defined in Equation (6.1) is measured to be:

Uncertainty	$\sigma^{\text{tot}}_{Z\to\mu\mu}$,[%]	$\sigma^{\text{tot}}_{Z\to ee}$,[%]	$\sigma^{\text{tot}}_{t\bar{t}}$,[%]	$R_{t\bar{t}(\text{tot})/Z(\text{tot})}$
BTAG1			−0.29	−0.29
BTAG2			0.07	0.07
BTAG3			0.1	0.10
BTAG4			−0.01	−0.01
BTAG5			0	0.00
BTAG6			0	0.00
CTAG1			0.04	0.04
CTAG2			−0.02	−0.02
CTAG3			0	0.00
CTAG4			0	0.00
ChargeIDZ	0	−0.15		0.08
DLUMI_13TeV	2.1	2.1	2.31	0.21
EBEAM	0.69	0.69	1.5	0.81
EG_RESOLUTION_ALL__1		−0.025	−0.01	0.00
EG_SCALE_ALL__1		0.245	0.2	0.08
EL_EFF_ID_COMBMCTOY__1_nui_0		−0.363	−0.32	−0.14
EL_EFF_ID_COMBMCTOY__1_nui_1		0.112	−0.115	−0.17
EL_EFF_Iso_COMBMCTOY__1		0.14		−0.07
EL_EFF_Isott13TeV			0.39	0.39
EL_EFF_Reco_COMBMCTOY__1_nui_0		−0.047	−0.034	−0.01
EL_EFF_Reco_COMBMCTOY__1_nui_1		0.017	−0.021	−0.03
EL_EFF_Trig_COMBMCTOY__1		0.01	0.14	0.13
FLOSR			0.52	0.52
FLSTAT1			0.16	0.16
FLSTAT2			0.03	0.03
GENIFSR			−0.4	−0.40
GENTT			0.84	0.84
GENVV			−0.09	−0.09
GENWIFSR			−0.21	−0.21
GENWT			−0.14	−0.14
HADRTT			−2.8	−2.80
JET_19NP_JET_BJES_Response			−0.02	−0.02
JET_19NP_JET_EffectiveNP_1			−0.22	−0.22
JET_19NP_JET_EffectiveNP_2			0.02	0.02
JET_19NP_JET_EffectiveNP_3			−0.01	−0.01
JET_19NP_JET_EffectiveNP_4			−0.01	−0.01
JET_19NP_JET_EffectiveNP_5			0.01	0.01
JET_19NP_JET_EffectiveNP_6restTerm			−0.01	−0.01
JET_19NP_JET_EtaIntercalibration_Modelling			−0.04	−0.04
JET_19NP_JET_EtaIntercalibration_TotalStat			−0.03	−0.03
JET_19NP_JET_Flavor_Composition			−0.17	−0.17
JET_19NP_JET_Flavor_Response			0.1	0.10
JET_19NP_JET_GroupedNP_1			−0.08	−0.08
JET_19NP_JET_Pileup_OffsetMu			0.08	0.08
JET_19NP_JET_Pileup_OffsetNPV			0.08	0.08
JET_19NP_JET_Pileup_PtTerm			0	0.00
JET_19NP_JET_Pileup_RhoTopology			−0.07	−0.07
JET_19NP_JET_PunchThrough_MC15			0	0.00
JET_19NP_JET_SingleParticle_HighPt			0	0.00
JET_JER_SINGLE_NP__1			−0.16	−0.16
MISTAG1			0.05	0.05
MISTAG10			0	0.00
MISTAG11			0	0.00
MISTAG12			0	0.00
MISTAG2			0	0.00
MISTAG3			0	0.00
MISTAG4			0	0.00
MISTAG5			0	0.00
MISTAG6			0	0.00
MISTAG7			0	0.00
MISTAG8			0	0.00
MISTAG9			0	0.00
MUONS_ID__1	−0.005		−0.01	−0.01
MUONS_MS__1	−0.005		0	0.00
MUONS_SCALE__1	−0.055		−0.04	−0.01
MUON_EFF_ISOtt13TeV			0.27	0.27
MUON_EFF_STAT__1	0.33		0.19	0.03
MUON_EFF_SYS__1	0.59		0.4	0.11
MUON_EFF_TrigStatTOYUncertainty__1	0.03		0.05	0.04
MUON_EFF_TrigSystUncertainty__1	0.12		0.02	−0.04
MUON_ISO_STAT__1	0.07			−0.03
MUON_ISO_SYS__1	0.4			−0.20
MUON_TTVA_STAT__1	0			0.00
MUON_TTVA_SYS__1	0			0.00
NSTTSYS			−0.3	−0.30
PDFNNPDF30_nlo_as_0118_eigenset	0.02	0.1		−0.06
PDFtt			0.48	0.48
PILEUP_W__1	0.01	0.01		−0.01
R32			−0.39	−0.39
RZMSYS			0.15	0.15
WTDRS			−0.62	−0.62
XSVV			0.02	0.02
XSWT			0.52	0.52
ZPTMismodel	−0.03	−0.07		0.05
AZ	1.77	1.77		1.77
BgEWKLumi	0.01	0.01		−0.01
DiBosZ	0.01	0.01		−0.01
MJBkg	0.05	0.05		−0.05
TopZ	0.02	0.02		−0.02
WBosZ	0	0		0.00
ZTauZ	0	0		0.00
Total Systematics	2.95	2.88	4.32	3.83
Stat	0.08	0.09	0.92	0.92
Total	2.95	2.88	4.42	3.94

Table 6.2: Summary of the statistical, systematic and total uncertainties on the $Z \to e^+e^-$, $Z \to \mu^+\mu^-$ and $t\bar{t}$ total cross-section measurements, along with the corresponding uncertainties on the ratio for the data at $\sqrt{s}$ =13 TeV. The values presented in a single (different) row are considered to be 100% (0%) correlated. The values that are smaller than 0.05% shown as equal to zero.

- total to fiducial:

$$R_{t\bar{t}/Z}(\text{tot/fid}) = 1.053 \ \pm 0.010(\text{stat}) \pm 0.036(\text{syst}) \pm 0.002(\text{lumi}),$$

- total to total:

$$R_{t\bar{t}/Z}(\text{tot/tot}) = 0.416 \pm 0.004(\text{stat}) \pm 0.016(\text{syst}) \pm 0.001(\text{lumi})$$

- fiducial to fiducial:

$$R_{t\bar{t}/Z}(\text{fid/fid}) = 0.01280 \pm 0.00012(\text{stat}) \pm 0.00033(\text{syst}) \pm 0.00003(\text{lumi})$$

The total to total cross-sections ratio has a larger systematics uncertainty (3.8%), apart from the luminosity uncertainty in comparison with the total to fiducial cross-sections ratio (3.4%) and fiducial to fiducial cross-sections ratio (2.6%) due to the uncertainty on an acceptance factor which comes from Z-boson total cross section.

The extracted ratio of the total cross sections can be compared with the preliminary result that is based on the data sample with 50 ns bunch spacing [165]

$$R_{t\bar{t}/Z}(\text{tot/tot, 50 ns}) = 0.445 \pm 0.027(\text{stat}) \pm 0.028(\text{syst + lumi})$$

The new result shows significantly reduced uncertainty, mainly because of increased statistics and the improved lepton-related systematic uncertainties owing to use of the toy MC method that allowed reducing the statistical components of the uncertainties. The central values are consistent with each other within 1.1 stat. sigma.

The evaluated single ratios of the total to fiducial and the total to total cross sections at $\sqrt{s} = 13$ TeV are compared to the theoretical predictions based on different PDF sets: CT14, NNPDF3.0, MMHT14, ATLAS-epWZ12, HERAPDF2.0, and ABM12 (see Subsection 2.5.3.) and shown in Figures 6.1 and 6.2. The predictions of top-quark-pair fiducial cross sections not yet available at NNLO. The trend of the predictions for both ratios is similar. The ABM12 set has the lowest value with the smallest uncertainty, while the CT14, NNPDF3.0 and MMHT14 sets predict the largest value with the uncertainties similar in size. The HERAPDF2.0 and ATLAS-epWZ12 PDF sets are in the middle with the biggest uncertainty in the HERAPDF2.0 set. The variation in predictions between the different sets can be explained by the lower value of α_s used in the ABM12 set ($\alpha_s = 0.1132$) and differences in the gluon density distributions. Indeed, the HERAPDF2.0, ATLAS-epWZ12 and ABM12 sets do not include collider jet data and hence have the different gluon distributions as a function of x leading to the lower gluon density at the x values where $t\bar{t}$ data are sensitive.

The comparison of measured single ratios with the theoretical prediction indicates that the ATLAS data are more accurate than most of the theoretical predictions, showing strong constraining power.

6.2.3 Double ratios

The double ratios are highly precise ratios that provide a stringent test of the Standard Model and are defined in this analysis as:

$$R_{t\bar{t}/Z}(\text{tot/fid}, i/j) = \frac{R_{t\bar{t}/Z}(i)}{R_{t\bar{t}/Z}(j)} = \left[\sigma^{\text{tot}}_{t\bar{t}(i)}/\sigma^{\text{fid}}_{Z(i)}\right]/\left[\sigma^{\text{tot}}_{t\bar{t}(j)}/\sigma^{\text{fid}}_{Z(j)}\right],$$

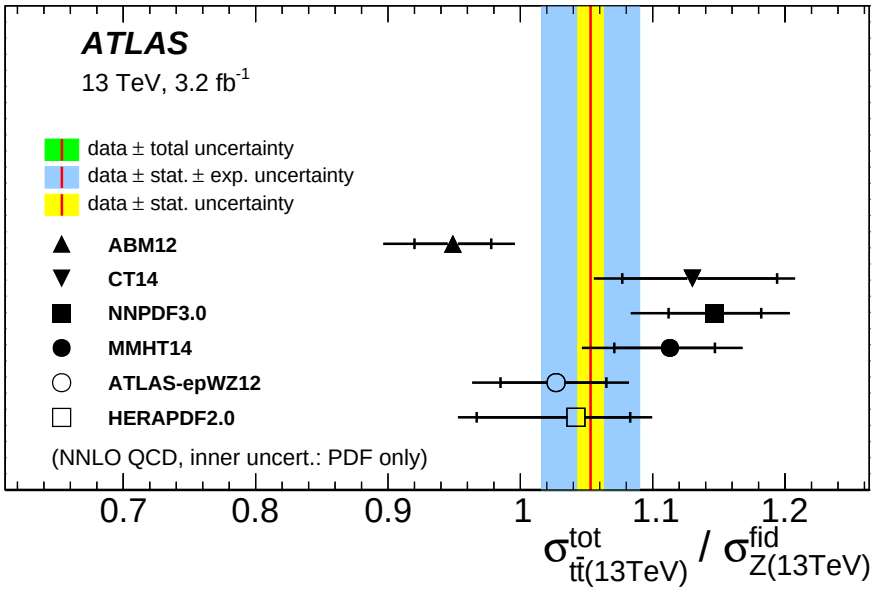

Figure 6.1: Ratios of the total $t\bar{t}$ to fiducial Z-boson production cross sections compared to predictions based on different PDF sets. The inner shaded band corresponds to statistical uncertainty while the outer band shows statistical and systematic uncertainties added in quadrature. The theory predictions are given with the corresponding PDF uncertainties shown as inner error bars. The outer error bars include the scale and α_s uncertainties added in quadrature.

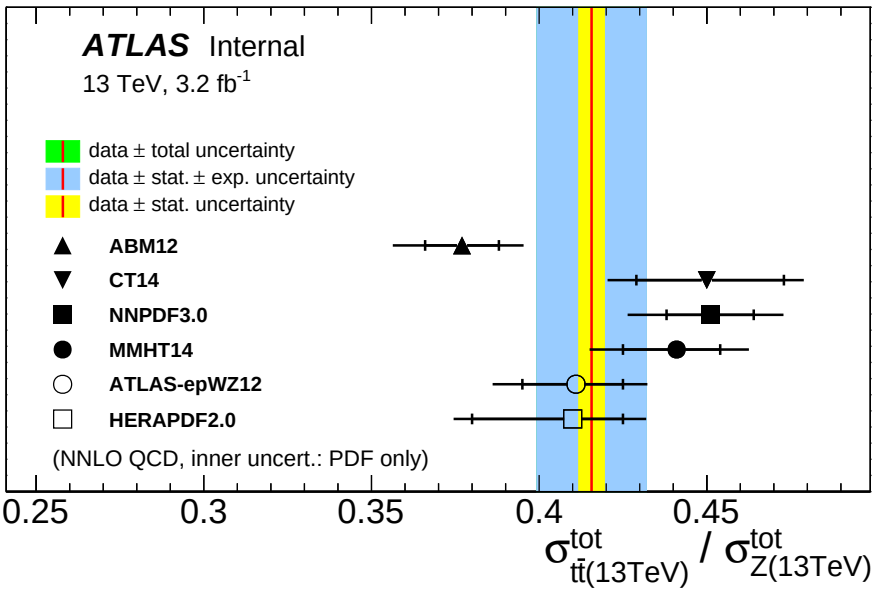

Figure 6.2: Ratios of the total $t\bar{t}$ to total Z-boson production cross sections compared to predictions based on different PDF sets. The inner shaded band corresponds to statistical uncertainty while the outer band shows statistical and systematic uncertainties added in quadrature. The theory predictions are given with the corresponding PDF uncertainties shown as inner error bars. The outer error bars include the scale and α_s uncertainties added in quadrature.

where i and j indicates different centre-of-mass energies, 13 TeV, 8 TeV, 7 TeV, and $i \neq j$. The Z-boson measurements in both decay channels, electron and muon, are combined to quantify double ratios. The double ratios of the total $t\bar{t}$ to fiducial Z-boson cross sections at the different centre-of-mass energies, $\sqrt{s}$ = 13 TeV, 8 TeV and 7 TeV, are compared to the different set of the theoretical predictions in Figures 6.3 and 6.4. The values of the measured double cross-section ratios are shown in Table 6.3. The predictions show the same trend as it is found for the single ratios at the various centre-of-mass energies (see Reference [20]).

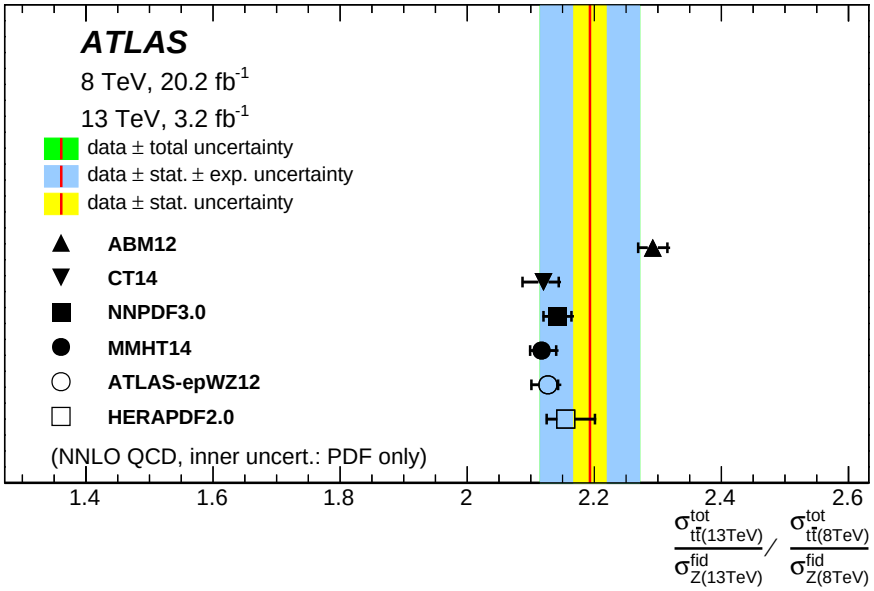

Figure 6.3: The double ratios of production cross sections at $\sqrt{s}$ = 13 TeV and 8 TeV compared to the theoretical predictions based on the different PDF sets. The inner shaded band corresponds to statistical uncertainty while the outer band shows the statistical and systematic uncertainties added in quadrature. The theory predictions are given with the corresponding PDF uncertainties shown as inner error bars. The outer error bars include the scale and α_s uncertainties added in quadrature.

$t\bar{t}/Z$	$[\sigma^{\text{tot}}/\sigma^{\text{tot}}]/[\sigma^{\text{fid}}/\sigma^{\text{fid}}]$ Value ± stat ± syst ± lumi
13/8	2.193 ± 0.026(1.2%) ± 0.074(3.4%) ± 0.008(0.4%)
13/7	2.594 ± 0.050(1.9%) ± 0.086(3.3%) ± 0.008(0.3%)
8/7	1.184 ± 0.022(1.8%) ± 0.015(1.3%) ± 0.003(0.3%)

Table 6.3: Double ratios of the Z-boson and $t\bar{t}$ production cross section at different centre-of-mass energies.

The benefit from the double ratio is that most of the experimental and theoretical uncertainties are canceled, providing the high precision ratios. The dominant source of experimental uncertainty, luminosity uncertainty, is almost completely removed in this ratios as well. The highest predicted ratio arises from the ABM12 PDF set and predictions from the other one have lower values. The double ratios of results at $\sqrt{s}$ = 13 TeV to $\sqrt{s}$ = 8 TeV are consistent with all predictions within one standard deviation. The ratio of cross sections between 13 TeV to 8 TeV agrees with all predictions within experimental

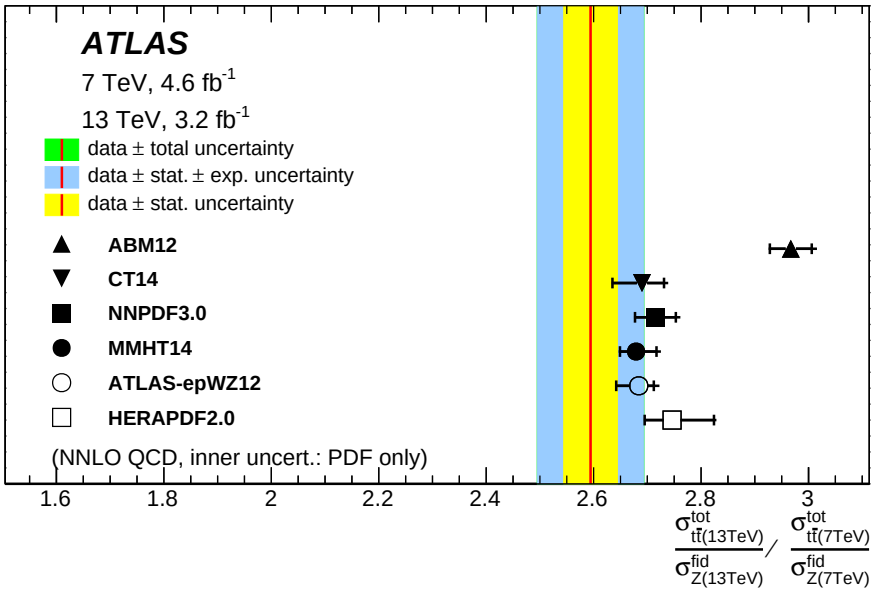

Figure 6.4: The double ratios of production cross sections at $\sqrt{s}$ = 13 TeV and 7 TeV compared to the theoretical predictions based on the different PDF sets. The inner shaded band corresponds to statistical uncertainty while the outer band shows the statistical and systematic uncertainties added in quadrature. The theory predictions are given with the corresponding PDF uncertainties shown as inner error bars. The outer error bars include the scale and α_s uncertainties added in quadrature.

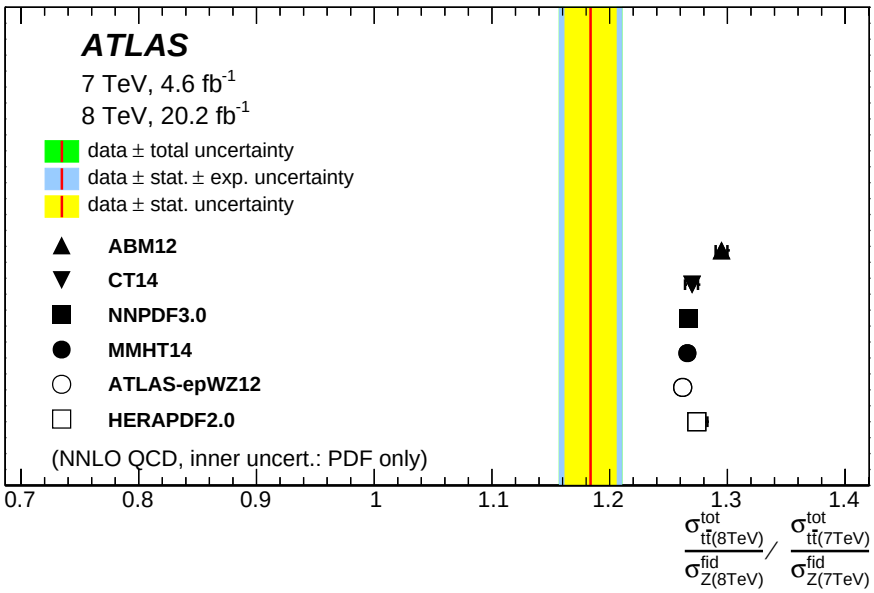

Figure 6.5: The double ratios of production cross sections at $\sqrt{s}$ = 8 TeV and 7 TeV compared to the theoretical predictions based on the different PDF sets. The inner shaded band corresponds to statistical uncertainty while the outer band shows statistical and the systematic uncertainties added in quadrature. The theory predictions are given with the corresponding PDF uncertainties shown as inner error bars. The outer error bars include the scale and α_s uncertainties added in quadrature.

uncertainties and has the relative experimental uncertainty of 3.4%. The best agreement of central values is with the prediction using the HERAPDF2.0 PDF set. The ratios between 13 TeV and 7 TeV, 8 TeV and 7 TeV have the lower central values for data. The biggest deviation from the predictions is for ratio 8 TeV to 7 TeV. This deviation is observed in the previous results from the ATLAS [21]. In this ratio, the statistical uncertainty coming from the data at 7 TeV is dominated by the relative uncertainty 1.8%, while the relative systematic uncertainty is 1.3%. The ABM12 has deviation at the four sigma level when all the other predictions only at the three sigma. This behaviour is difficult to ascribe to the x dependence of the gluon distribution versus $\sqrt{s}$, since the average change in the x values is bigger from 13 TeV to 8 TeV data than for 8 TeV to 7 TeV.

The comparison of the single ratios of the $t\bar{t}$ cross sections at 8 TeV and 7 TeV between measured values and the baseline CT14 PDF prediction shows that difference between them is 3.5 sigma, excluding the luminosity uncertainty. By adding the Z-boson cross sections, which agree within the experimental uncertainties, to the double ratio, the difference between the measured and theoretical values become within three sigma. Taking the baseline CT14 predictions for double ratio, the ratio between experimental double ratio (see Figure 6.5) and theoretical calculated can be estimated and is equal

$$R_{\text{data/CT14}}(\text{tot/fid}, 8/7\ \text{TeV}) = 0.934 \pm 0.017(\text{stat}) \pm 0.012(\text{syst}) \pm 0.005(\text{theo}).$$

It indicate that the experimental statistical uncertainty is a significant component for this ratio of the double ratios.

CHAPTER 7

Interpretation of the results

The previously measured inclusive Z-boson and $t\bar{t}$ production cross sections at the centre-of-mass energy $\sqrt{s} = 7$ TeV and 8 TeV and the new measurements of the same processes at $\sqrt{s} = 13$ TeV, which were used to calculate the ratios (see Chapter 6), are studied to test several different scenarios. Primarily, these data are used to estimate the impact on existing PDF sets and to determine the pole mass of the top quark, m_t^{pole}. For this purpose, quantitative estimation is performed by using dedicated PDF profiling method. This chapter is organized as follows: a short description of the profiling procedure is outlined in Section 7.1. The impact of the data on the existing ATLAS-epWZ12 PDF set is discussed in Section 7.2. Finally, the interpretation of the results of the top-quark mass scan using CT14 and ATLAS-epWZ12 PDF sets is presented in Section 7.3.

7.1 PDF profiling method

The PDF profiling method, which is implemented in the xFitter framework [166], is used to estimate the impact of the LHC data from Run 1 and Run 2 using the inclusive Z-boson and $t\bar{t}$ production measurements at the centre-of-mass energy of 7 TeV, 8 TeV and 13 TeV. This method uses a χ^2 function, which includes both the experimental and theoretical uncertainties. The theoretical uncertainties include uncertainty on PDF, scale and strong coupling constant α_s. The χ^2 function is similar to one used in the combination procedure (see Equation 5.9) and is defined as [23]:

$$\chi^2(\vec{\beta}_{\text{exp}}, \vec{\beta}_{\text{theo}}) = \sum_i^{N_{\text{data}}} \frac{(\sigma_i^{\text{exp}} + \sum_j \Gamma_{ji}^{\text{exp}} \beta_{j,\text{exp}} - \sigma_i^{\text{theo}} - \sum_k \Gamma_{ik}^{\text{theo}} \beta_{k,\text{theo}})^2}{\Delta_i^2} + \sum_j \beta_{j,\text{exp}}^2 + \sum_k \beta_{k,\text{theo}}^2 , \quad (7.1)$$

where

- $\vec{\beta_{\text{exp}}}, \vec{\beta_{\text{theo}}}$ are vectors of correlated experimental and theoretical uncertainties, respectively
- Γ_{ji}^{exp}, $\Gamma_{ik}^{\text{theo}}$ are matrices describing an influence of uncertainties on data and theory, respectively
- σ_i^{exp}, σ_i^{theo} are experimental measurements and theoretical predictions, respectively
- Δ_i represents uncorrelated experimental uncertainty
- index i runs over all data points, N_{data}, and index j (k) over all experimental (theoretical) sources of uncertainties.

	ATLAS-epWZ12	CT14	MMHT14	NNPDF3.0	HERAPDF2.0	ABM12
χ^2/NDF	8.3 / 6	15 / 6	13 / 6	17 / 6	10 / 6	25 / 6
p-value	0.22	0.02	0.05	0.01	0.11	< 0.001

Table 7.1: The χ^2 values for the comparison of the ATLAS data to the predictions based on the ATLAS-epWZ12, CT14, MMHT14, NNPDF3.0, HERAPDF2.0 and ABM12 PDF sets, along with the probability of finding the observed value or higher.

The value of the χ^2 function at the minimum, χ^2_{min}, provides the compatibility of the data and theory. Asymmetric theoretical uncertainties are taken into account in the profiling procedure as:

$$\Gamma_{ik}^{\text{theo}} = 0.5((\Gamma_{ik}^{\text{up}} + \Gamma_{ik}^{\text{down}}) + (\Gamma_{ik}^{\text{up}} - \Gamma_{ik}^{\text{down}})\beta_{k,\text{theo}}),$$

where Γ_{ik}^{up} and $\Gamma_{ik}^{\text{down}}$ are the prediction variations corresponding to the up and down PDF eigenvector variations. The theoretical predictions can be altered by the shifts of the theory nuisance parameters, $\beta_{k,\text{theo}}$. The values at the minimum of the nuisance parameters, $\beta_{k,\text{theo}}^{min}$, can be interpreted as an optimization ('profiling') of PDFs in order to better describe the data. The profiled central PDF set f' is given by:

$$f' = f^0 + 0.5 \sum_k (f_k^{\text{up}} - f_k^{\text{down}})\beta_{k,\text{theo}}^{\text{min}} + (f_k^{\text{up}} + f_k^{\text{down}})(\beta_{k,\text{theo}}^{\text{min}})^2,$$

where $f^0 = f(x, Q^2)$ is the initial central PDF set and f_k^{up} and f_k^{down} are the eigenvector sets corresponding to up and down variations. After the profiling, the shifted PDFs have reduced uncertainties because of the introduction of the additional data. The shifted nuisance parameters are no longer orthogonal to each other and can be diaginalized using a dedicated procedure [167].

7.2 Comparison with theory predictions

Profiling method is used to perform the quantitative comparison between the data and theoretical predictions for the Z-boson and $t\bar{t}$ cross sections at the centre-of-mass energy of 7 TeV, 8 TeV and 13 TeV. The visual comparison is done using different PDF sets: CT14 [37], NNPDF3.0 [38], MMHT14 [39], ATLAS-epWZ12 [40], HERAPDF2.0 [41], and ABM12 [42] and is shown in Figure 7.1. The corresponding χ^2 values for the various PDFs are summarized in Table 7.1. The top-quark pole mass used in the predictions is fixed to $m_t^{\text{pole}} = 172.5$ GeV and corresponding α_s and scale values are set as described in Section 2.5.

The predicted cross sections based on the HERAPDF2.0 and ATLAS-epWZ12 PDF sets have the best compatibility with the ATLAS data, while other PDF sets provide lower values of the cross sections for the Z-boson production and higher values for the $t\bar{t}$ production, except the ABM12 PDF set which which predicts the lowest cross sections the $t\bar{t}$ data. Both PDF sets, HERAPDF2.0 and ATLAS-epWZ12, do not include the cross-sections from this analysis. The ATLAS-epWZ12 PDF set has the smallest uncertainties comparing to the HERAPDF2.0, and for that reason it is chosen to study the impact of the measurements on this PDF set. This impact is quantified using the ATLAS-epWZ12-EIG set, which consist of up and down PDF variations for each of 15 eigenvectors.

The profiling is performed using six Z-boson and $t\bar{t}$ cross-section measurements altogether, or only $t\bar{t}$ data in order to see an individual and total impact of each process. The Z-boson data have potential influence on the sea-quark ($\Sigma = \bar{u} + \bar{d} + \bar{s}$) distribution and $t\bar{t}$ measurements on the gluon (g) distribution.

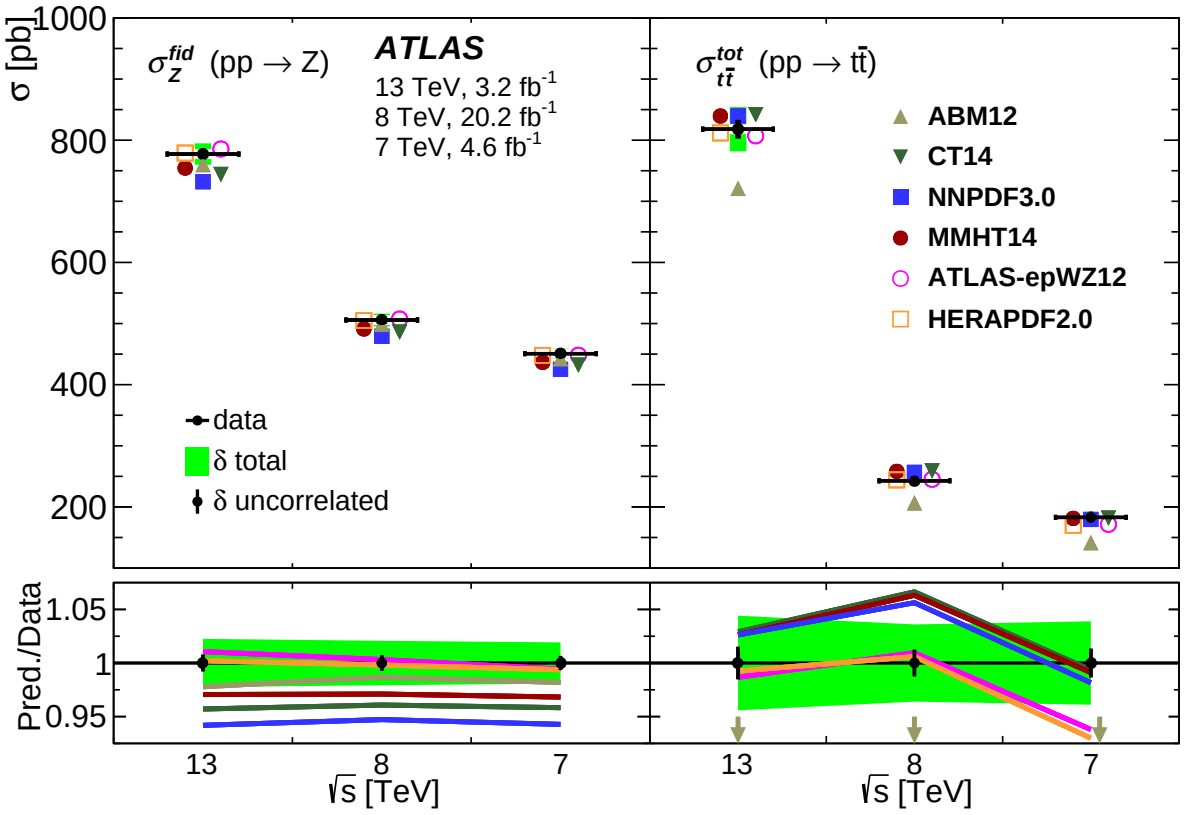

Figure 7.1: Comparison of the fiducial and total cross sections with theory predictions based on different PDF sets. Left plot corresponds to Z-boson data and right plot to $t\bar{t}$ data at different centre-of-mass energies.

The light-sea and gluon distributions divided by the central value and the relative uncertainty of the ATLAS-epWZ12 PDF set at fixed scale of $Q^2 = m_Z^2$ or $Q^2 = m_t^2$ are shown in Figure 7.2 and 7.3. It indicates that ATLAS data have a significant constraining power for reducing the uncertainties on the light-sea distribution at $x < 0.02$ and for the gluon distribution at $x \sim 0.1$. Moreover, it can be noticed that the $t\bar{t}$ and Z-boson data together provide a significant reduction of the uncertainties for the gluon density compared to the $t\bar{t}$ data only. The PDF profiling is also performed excluding $t\bar{t}$ cross section at $\sqrt{s} = 7$ TeV, which shows improved agreement between the data and predictions with no significant changes on the gluon distribution of profiled ATLAS-epWZ12 set (see Appendix B.1).

7.3 Scan of the top-quark mass

In addition to the direct measurement of the top-quark mass (see Figure 2.10), the value of mass can also be extracted from $t\bar{t}$ cross sections by comparing a dependence of theoretical predictions for it on the top-quark mass with the measurements. The analysis from ATLAS [21] followed this approach, using data at $\sqrt{s} = 7$ TeV and 8 TeV, and showed that extracted values of the top-quark mass[1] have sizeable

[1] The top-quark mass extracted in the indirect method is referred to the pole top-quark mass in this study.

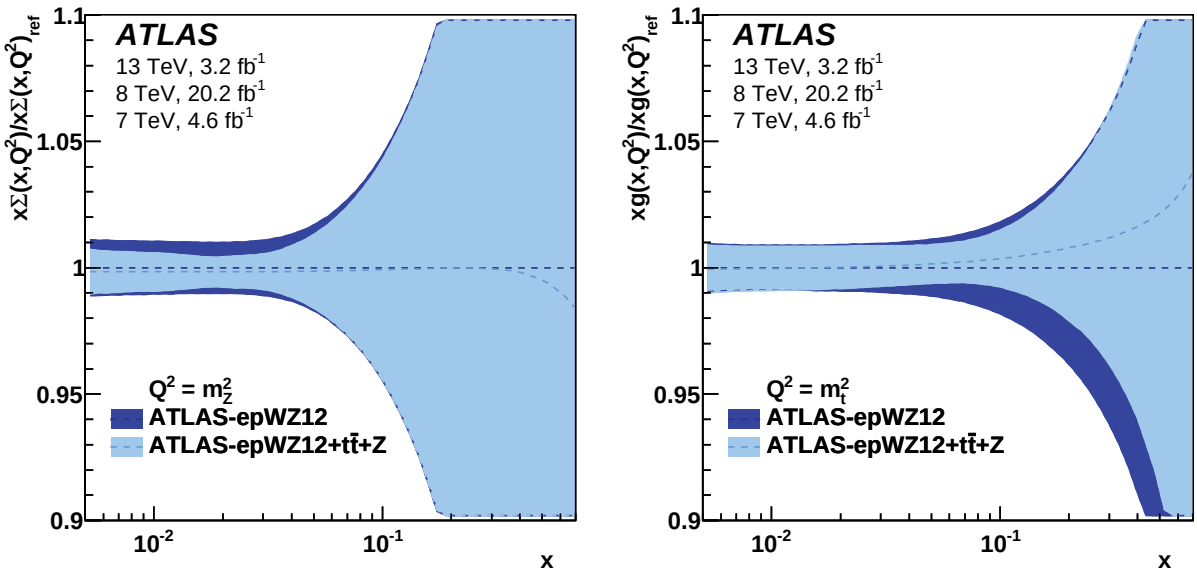

Figure 7.2: Impact of the ATLAS Z-boson and $t\bar{t}$ production cross-section data on the PDFs. The bands represent the uncertainties for the ATLAS-epWZ12 PDF set and the uncertainty of the profiled ATLAS-epWZ12 PDF set, including $t\bar{t}$ and Z-boson data only. The profiled PDF is divided by central value of ATLAS-epWZ12 PDF set and represented as solid blue line. The left plot demonstrate the total light-quark-sea distribution as a function of Bjorken-x at $Q^2 = m_Z^2$ and the right plot shows the gluon density at $Q^2 = m_t^2$.

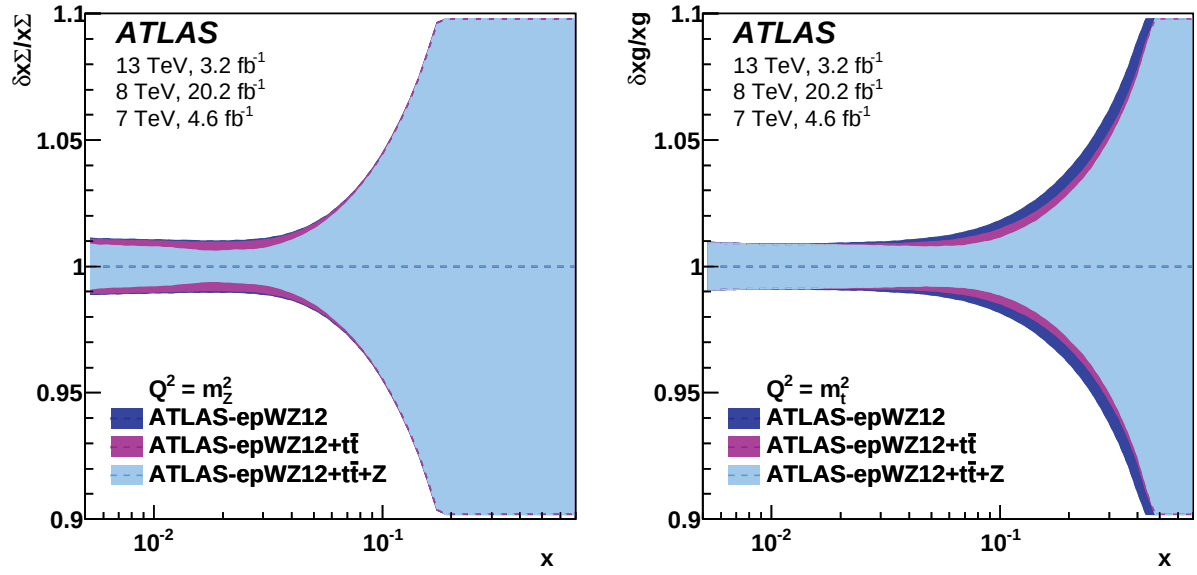

Figure 7.3: Impact of the ATLAS Z-boson and $t\bar{t}$ production cross-section data on the relative uncertainty of PDFs. The bands represent the relative uncertainties on PDFs for the ATLAS-epWZ12 PDF set and the profiled ATLAS-epWZ12 PDF set, including $t\bar{t}$ cross sections only, and the profiled ATLAS-epWZ12 PDF set including both Z and $t\bar{t}$ cross-section data as a function of Bjorken-x for a total light sea-quark distribution at $Q^2 = m_Z^2$ (left) and for the gluon density at $Q^2 = m_t^2$ (right). The solid blue line represents the ratio of the central value of the profiled to original ATLAS-epWZ12 PDF set.

uncertainties compared to those obtained from the direct reconstruction (see Figure 2.10). An imperfect knowledge of the PDFs used in the theoretical predictions as well as the experimental uncertainties from data such as luminosity uncertainty impact the precision of the extracted value of the top-quark mass.

The profiling method can be used to estimate quantitatively the impact of the Z-boson measurements at $\sqrt{s}$ = 7 TeV, 8 TeV and 13 TeV and the new $t\bar{t}$ measurement at $\sqrt{s}$ = 13 TeV on a given PDF set and the top-quark mass value. The normalization added by the Z-boson data allows the large luminosity uncertainty of the $t\bar{t}$ data to be reduced. The top-quark mass scan is based on minimizing the χ^2 function of Equation 7.1 as a function of m_t^{pole}.

The xFitter program takes as inputs the cross sections from the following experimental and theoretical calculations:

Theoretical predictions: the calculation of theoretical predictions for the total $t\bar{t}$ production cross sections at $\sqrt{s}$ = 7 TeV, 8 TeV and 13 TeV is done following the same prescription as described in Subsection 2.5.2). The Top++v2.0 program [73] is used for the calculation of the central values and theory uncertainties at NNLO+NNLL using CT14 [37] and ATLAS-epWZ12 [40] PDF sets. The central value of the cross sections and the systematic uncertainties are calculated as a function of the top-quark mass value in the mass range of $135 \leq m_t^{\text{pole}} \leq 210$ GeV with 0.5 GeV steps for central range and with the step of 5 GeV on edges. The statistical uncertainties resulting from the calculations are small and, therefore, negligible.

The following sources of uncertainties are assigned to the predicted cross sections:

- *PDF*: the uncertainty is evaluated from the variations of eigenvectors for a given PDF set. The CT14 set includes 28 up and down PDF eigenvector variations and the ATLAS-epWZ12 set 15 up and down eigenvector variations, respectively. The calculated PDF variations for the CT14 PDF sets for all three centre-of-mass energies are shown in Tables 7.2–7.4 and for the ATLAS-epWZ12 PDF set in Table 7.5. The CT14 uncertainties are rescaled from 90% to 68% confidence level.
- *Scale*: the uncertainty is only calculated for the CT14 PDF set as it is described in Section 2.5.2 for each centre-of-mass energy and each value of the top-quark mass and is presented in Tables 7.2–7.4.
- α_S: the central value of the α_S used in the calculation of the cross sections is $\alpha_s(M_Z) = 0.118$. The systematic uncertainties are obtained following prescription from Section 2.5.2. This uncertainty is calculated only for CT14 PDF set, for each centre-of-mass energy and each value of the top-quark mass, and is shown in Tables 7.2–7.4 .

Data same set of measurements as in the ratio calculations (see Section 6.1) is used.

The calculated cross sections with corresponding uncertainties for the CT14 and ATLAS-epWZ12 PDF sets are shown in Tables 7.2–7.5.

The dependence of the predictions of the $t\bar{t}$ cross section at $\sqrt{s}$ = 7 TeV, 8 TeV and 13 TeV on $m_{\text{t}}^{\text{pole}}$ including only PDF uncertainty is shown in Figure 7.4. The dependence of the predictions on $m_{\text{t}}^{\text{pole}}$ including only α_S uncertainty is shown in Appendix B.2. As expected, the theoretical predictions have a strong dependence on the top-quark mass. The measured cross sections have minimal dependence on the top-quark mass, as observed in Reference [21]. Therefore, the current measurements offer good possibility to determine m_t^{pole}. Furthermore, the experimental measurements of $t\bar{t}$ production cross sections have better precision accuracy comparing to the theoretical predictions, which can be used to estimate the impact on the PDF uncertainty and the uncertainty on extracted value of m_t^{pole}.

7 TeV CT14 PDF set							
m_t^{pole}	central value [pb]	CT14 up [*pb*]	CT14 dn [pb]	scale up [pb]	scale down [pb]	α_S up [pb]	α_S down [pb]
135.0	632.14	−33.73	36.48	−24.34	17.53	−13.26	13.52
140.0	527.18	−28.69	31.47	−19.99	14.47	−11.08	11.32
145.0	441.97	−24.52	27.25	−16.50	12.03	−9.31	9.52
150.0	372.38	−21.05	23.69	−13.70	10.08	−7.86	8.05
155.0	315.18	−18.12	20.66	−11.43	8.46	−6.67	6.83
160.0	267.94	−15.68	18.09	−9.59	7.14	−5.68	5.82
165.0	228.71	−13.60	15.89	−8.08	6.05	−4.85	4.99
167.5	211.62	−12.69	14.88	−7.43	5.59	−4.49	4.61
170.0	195.99	−11.85	13.95	−6.84	5.17	−4.17	4.29
171.0	190.11	−11.52	13.63	−6.62	5.01	−4.04	4.16
171.5	187.25	−11.36	13.46	−6.51	4.93	−3.98	4.10
172.0	184.44	−11.21	13.29	−6.40	4.86	−3.92	4.04
172.5	181.67	−11.07	13.13	−6.30	4.78	−3.86	3.98
173.0	178.96	−10.92	12.96	−6.20	4.70	−3.80	3.92
173.5	176.29	−10.78	12.81	−6.10	4.63	−3.74	3.87
174.0	173.66	−10.64	12.65	−6.00	4.56	−3.69	3.81
174.5	171.08	−10.50	12.50	−5.90	4.49	−3.63	3.76
175.0	168.55	−10.37	12.34	−5.81	4.42	−3.58	3.70
177.5	156.51	−9.72	11.61	−5.36	4.08	−3.33	3.44
180.0	145.45	−9.12	10.92	−4.95	3.78	−3.10	3.20
185.0	125.94	−8.04	9.67	−4.24	3.26	−2.69	2.77
190.0	109.38	−7.11	8.60	−3.64	2.83	−2.33	2.42
195.0	95.28	−6.30	7.66	−3.13	2.45	−2.04	2.11
200.0	83.23	−5.59	6.84	−2.71	2.13	−1.78	1.85
205.0	72.90	−4.98	6.11	−2.34	1.85	−1.56	1.62
210.0	64.02	−4.44	5.48	−2.04	1.63	−1.37	1.42

Table 7.2: Predictions for the $t\bar{t}$ production cross section at $\sqrt{s}$ = 7 TeV using the CT14 PDF set for the different top-quark mass values together with the corresponding variations of the PDF eigenvectors. The CT14 PDF uncertainties are given at 90% confidence level.

8 TeV CT14 PDF set							
m_t^{pole}	central value [pb]	CT14 up [pb]	CT14 down [pb]	scale up [pb]	scale down [pb]	α_S up [pb]	α_S down [pb]
135.0	875.94	−43.41	45.06	−34.00	23.83	−17.79	18.08
140.0	733.45	−37.10	38.95	−28.03	19.86	−14.93	15.18
145.0	617.27	−31.83	33.87	−23.24	16.51	−12.59	12.81
150.0	522.06	−27.42	29.52	−19.38	13.88	−10.67	10.87
155.0	443.55	−23.71	25.88	−16.23	11.71	−9.08	9.26
160.0	378.45	−20.58	22.74	−13.67	9.91	−7.76	7.93
165.0	324.21	−17.93	20.04	−11.56	8.42	−6.66	6.81
167.5	300.52	−16.75	18.84	−10.65	7.80	−6.18	6.33
170.0	278.82	−15.67	17.71	−9.82	7.22	−5.74	5.88
171.0	270.65	−15.26	17.28	−9.51	7.00	−5.57	5.72
171.5	266.67	−15.06	17.07	−9.36	6.89	−5.48	5.63
172.0	262.76	−14.86	16.87	−9.21	6.78	−5.40	5.55
172.5	258.91	−14.66	16.67	−9.06	6.68	−5.32	5.48
173.0	255.13	−14.47	16.47	−8.92	6.58	−5.24	5.40
173.5	251.42	−14.28	16.27	−8.78	6.48	−5.17	5.32
174.0	247.76	−14.09	16.08	−8.64	6.38	−5.09	5.25
174.5	244.17	−13.91	15.88	−8.51	6.28	−5.02	5.17
175.0	240.64	−13.73	15.69	−8.37	6.19	−4.95	5.10
177.5	223.85	−12.87	14.79	−7.74	5.73	−4.62	4.73
180.0	208.40	−12.07	13.95	−7.17	5.32	−4.30	4.41
185.0	181.06	−10.64	12.42	−6.16	4.60	−3.74	3.85
190.0	157.79	−9.40	11.08	−5.30	3.98	−3.27	3.36
195.0	137.92	−8.34	9.91	−4.58	3.47	−2.86	2.95
200.0	120.88	−7.44	8.89	−3.97	3.03	−2.51	2.58
205.0	106.22	−6.64	7.98	−3.45	2.64	−2.21	2.28
210.0	93.59	−5.95	7.17	−3.01	2.32	−1.95	2.01

Table 7.3: Predictions for the $t\bar{t}$ production cross section at $\sqrt{s}$ = 8 TeV using the CT14 PDF set for the different top-quark mass values together with the corresponding variations of the PDF eigenvectors. The CT14 PDF uncertainties are given at 90% confidence level.

13 TeV CT14 PDF set							
m_t^{pole}	central value [pb]	CT14 up [pb]	CT14 down [pb]	scale up	scale down [pb]	α_S up [pb]	α_S down [pb]
135.0	2 610.08	−100.16	94.43	−103.97	68.37	−47.53	47.63
140.0	2 212.47	−86.40	81.63	−86.84	57.55	−40.34	40.44
145.0	1 884.69	−74.88	71.04	−72.91	47.89	−34.41	34.64
150.0	1 612.95	−65.30	62.16	−61.55	41.51	−29.48	29.60
155.0	1 386.42	−56.82	54.89	−52.21	34.81	−25.39	25.71
160.0	1 196.65	−50.19	48.15	−44.50	29.80	−21.99	22.06
165.0	1 036.73	−44.12	42.78	−38.09	25.56	−19.06	19.16
167.5	966.32	−41.44	40.34	−35.29	23.73	−17.76	17.90
170.0	901.52	−38.99	38.04	−32.73	22.05	−16.59	16.70
171.0	877.04	−38.04	37.18	−31.77	21.43	−16.10	16.19
171.5	865.09	−37.59	36.75	−31.30	21.13	−15.87	15.96
172.0	853.34	−37.14	36.33	−30.84	20.83	−15.66	15.89
172.5	841.78	−36.69	35.93	−30.39	20.54	−15.46	15.69
173.0	830.40	−36.26	35.52	−29.94	20.25	−15.27	15.48
173.5	819.20	−35.83	35.13	−29.50	19.96	−15.08	15.22
174.0	808.17	−35.37	34.77	−29.07	19.70	−14.88	15.02
174.5	797.32	−34.95	34.38	−28.65	19.41	−14.67	14.84
175.0	786.64	−34.54	33.99	−28.23	19.14	−14.47	14.64
177.5	735.72	−32.56	32.15	−26.26	17.83	−13.57	13.68
180.0	688.63	−30.71	30.44	−24.44	16.63	−12.71	12.82
185.0	604.67	−27.37	27.36	−21.22	14.48	−11.18	11.28
190.0	532.52	−24.44	24.66	−18.48	12.67	−9.85	9.95
195.0	470.29	−21.88	22.28	−16.16	11.14	−8.71	8.82
200.0	416.43	−19.66	20.16	−14.16	9.79	−7.73	7.82
205.0	369.66	−17.66	18.31	−12.44	8.64	−6.87	6.96
210.0	328.95	−15.92	16.63	−10.96	7.66	−6.12	6.20

Table 7.4: Predictions for the $t\bar{t}$ cross section at $\sqrt{s}$ = 13 TeV using the CT14 PDF set for the different top-quark mass values together with the corresponding variations of the PDF eigenvectors. The CT14 PDF uncertainties are given at 90% confidence level.

ATLAS-epWZ12 PDF set									
	7 TeV			8 TeV			13 TeV		
m_t^{pole}	central value [pb]	PDF up [pb]	PDF down [pb]	central value [pb]	PDF up [pb]	PDF down [pb]	central value [pb]	PDF up [pb]	PDF down [pb]
135.0	599.41	−13.73	14.41	833.66	−16.99	19.82	2 518.17	−32.41	59.06
140.0	499.55	−11.84	12.00	697.45	−14.74	31.25	2 132.62	−28.61	78.42
145.0	418.53	−10.25	10.04	586.58	−12.82	26.68	1 815.18	−25.32	67.36
150.0	352.42	−8.90	8.45	495.78	−11.19	22.88	1 552.23	−22.46	58.40
155.0	298.14	−7.75	7.15	420.94	−9.80	19.71	1 333.21	−19.99	50.59
160.0	253.34	−6.77	6.08	358.96	−8.61	17.06	1 149.81	−17.85	44.10
165.0	216.12	−5.93	5.18	307.31	−7.58	14.80	995.37	−15.95	38.59
167.5	199.89	−5.55	4.81	284.74	−7.12	13.80	927.36	−15.10	36.14
170.0	185.06	−5.20	4.46	264.07	−6.69	12.89	864.76	−14.31	33.88
171.0	179.48	−5.07	4.32	256.29	−6.52	12.54	841.12	−14.00	33.02
171.5	176.77	−5.01	4.25	252.50	−6.44	12.37	829.58	−13.84	32.60
172.0	174.10	−4.95	4.18	248.78	−6.36	12.21	818.23	−13.70	32.20
172.5	171.49	−4.88	4.12	245.12	−6.29	12.04	807.07	−13.55	31.79
173.0	168.91	−4.82	4.06	241.53	−6.21	11.88	796.08	−13.41	31.39
173.5	166.38	−4.76	4.00	237.99	−6.14	11.72	785.28	−13.26	30.99
174.0	163.90	−4.70	3.94	234.52	−6.06	11.56	774.64	−13.12	30.60
174.5	161.46	−4.64	3.88	231.10	−5.99	11.41	764.18	−12.98	30.22
175.0	159.06	−4.58	3.82	227.75	−5.92	11.26	753.88	−12.85	29.85
177.5	147.67	−4.30	3.55	211.78	−5.57	10.55	704.75	−12.20	28.05
180.0	137.20	−4.04	3.30	197.10	−5.25	9.88	659.35	−11.57	26.38
185.0	118.74	−3.58	2.86	171.14	−4.66	8.67	578.48	−10.44	23.38
190.0	103.09	−3.17	2.49	149.07	−4.15	7.66	509.08	−9.44	20.78
195.0	89.79	−2.82	2.17	130.26	−3.71	6.78	449.34	−8.54	18.53
200.0	78.45	−2.51	1.90	114.17	−3.31	6.00	397.75	−7.76	16.58
205.0	68.74	−2.24	1.67	100.35	−2.97	5.34	353.02	−7.06	14.86
210.0	60.39	−2.00	1.47	88.43	−2.67	4.76	314.10	−6.43	13.35

Table 7.5: Predictions for the $t\bar{t}$ production cross section at $\sqrt{s}$ = 7 TeV, 8 TeV and 13 TeV using the ATLAS-epWZ12 PDF sets for the different top-quark mass values together with the corresponding variations of the PDF eigenvectors. The CT14 PDF uncertainties are given at 90% confidence level.

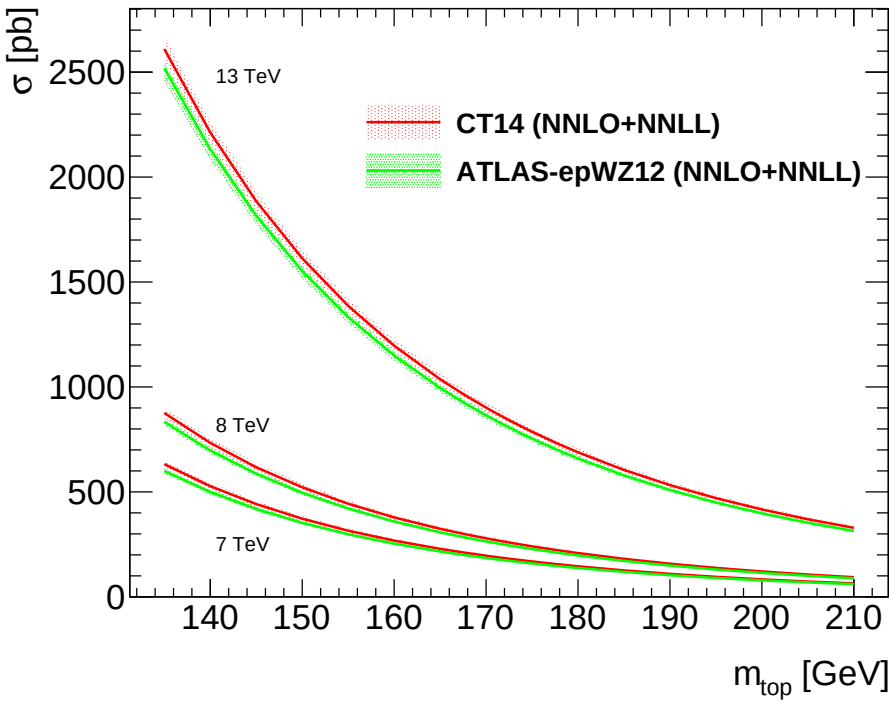

Figure 7.4: The theoretical calculation (NNLO+NNLL) of the top quark pair production cross sections, $\sigma_{t\bar{t}}$, as a function of the top-quark pole mass m_t^{pole} showing the central values (solid lines) and PDF uncertainties (dashed lines) using two PDF sets.

7.3.1 Impact of PDF uncertainty

The χ^2 scans are performed using the $t\bar{t}$ data only, or $t\bar{t}$ and Z-boson data together with excluding or including PDF uncertainties.

Figures 7.5 and 7.6 show the χ^2_{min} values as a function of m_t^{pole}, which have nearly parabolic shapes in a vicinity of the minimum. The plots are obtained without any theoretical uncertainties assigned to the cross sections for the CT14 and ATLAS-epWZ12 PDF sets. One parabola (green color) includes only $t\bar{t}$ cross sections and another (orange color) $t\bar{t}$ and Z-boson cross sections. For both PDF sets an inclusion of Z-boson data shows a constraining power for low and high values of m_t^{pole}. For the CT14 set, the minimum value of the parabola is shifted to the higher values of m_t^{pole}, which can be explained by the fact that the CT14 set does not describe the Z-boson data accurately (see Figure 7.1). When the Z-boson data is included in the scan procedure, the total experimental uncertainty decreases due to the luminosity error cancellation, thus, generating sizeable deviation from the prediction. Generally, the ATLAS-epWZ12 PDF set describes the data better than CT14 set as can be seen from the p-values in Tables 7.6 and 7.7; hence no shifts in the minimum value of a parabola are observed.

Figures 7.7 and 7.8 show the χ^2_{min} values obtained with included PDF uncertainties for the CT14 and ATLAS-epWZ12 PDF sets. If the scan is performed using the CT14 PDF set, the inclusion of Z-boson data has smaller constraint power for the low values of m_t^{pole}, with minimal shifts for the minimum value of the parabola. The PDF uncertainties allow to compensate this difference without the shift of the minimum value, When the scan is performed using ATLAS-epWZ12 PDF set, an inclusion of the Z-boson data contributes to the constraints in a similar way as for the CT14 set.

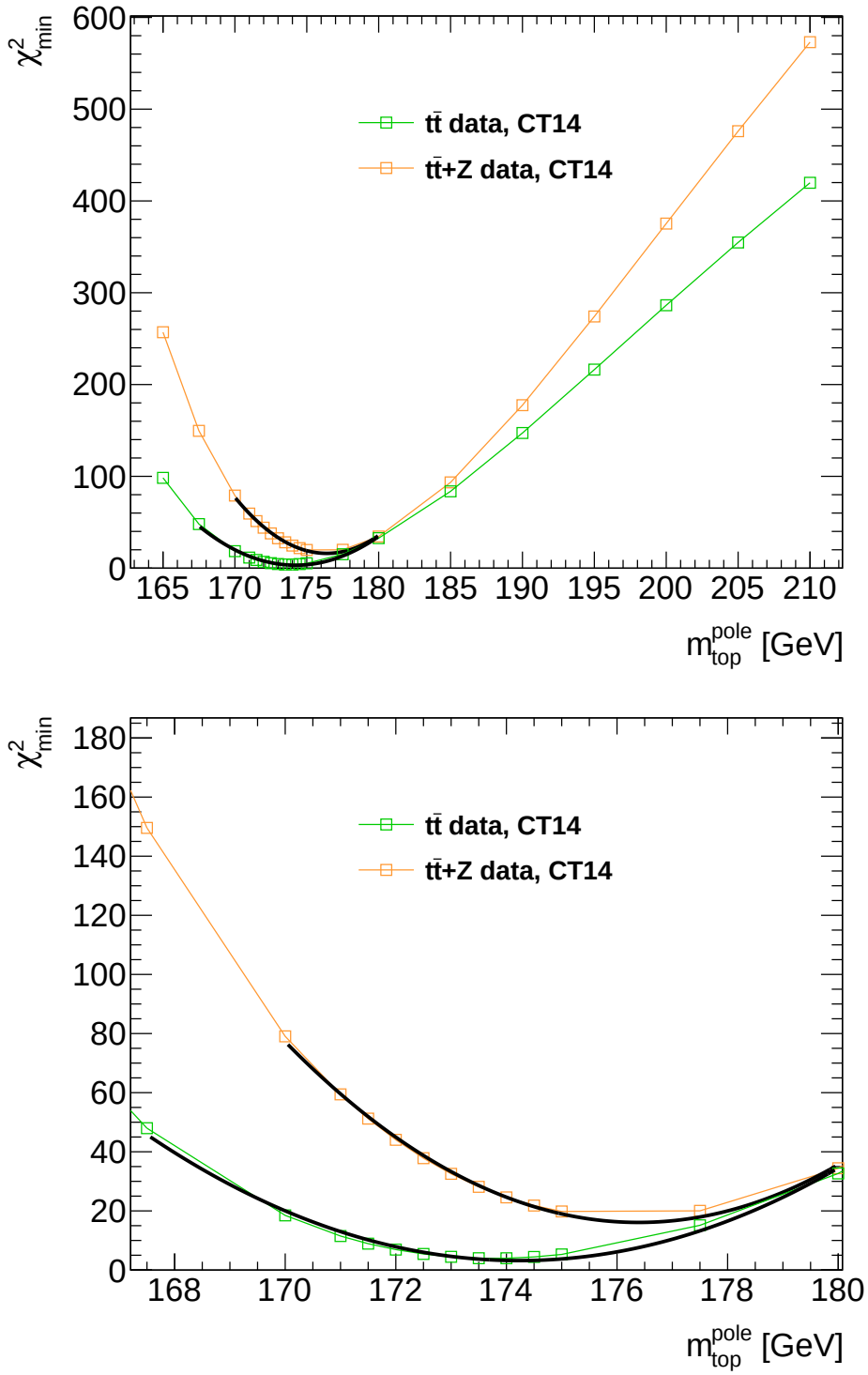

Figure 7.5: The indirect measurement of the top-quark mass: χ^2 scan based on the CT14 PDF predictions as a function of the top-quark pole mass, m_t^{pole}, including the $t\bar{t}$ production measurements (green color) or $t\bar{t}$ and Z-boson measurements (orange color) at $\sqrt{s}$ = 7 TeV, 8 TeV and 13 TeV. The χ^2 scan procedure does not include PDF uncertainties. The curves are fitted with a parabolic function (black curve). The bottom plot shows zoomed region where the fit is performed.

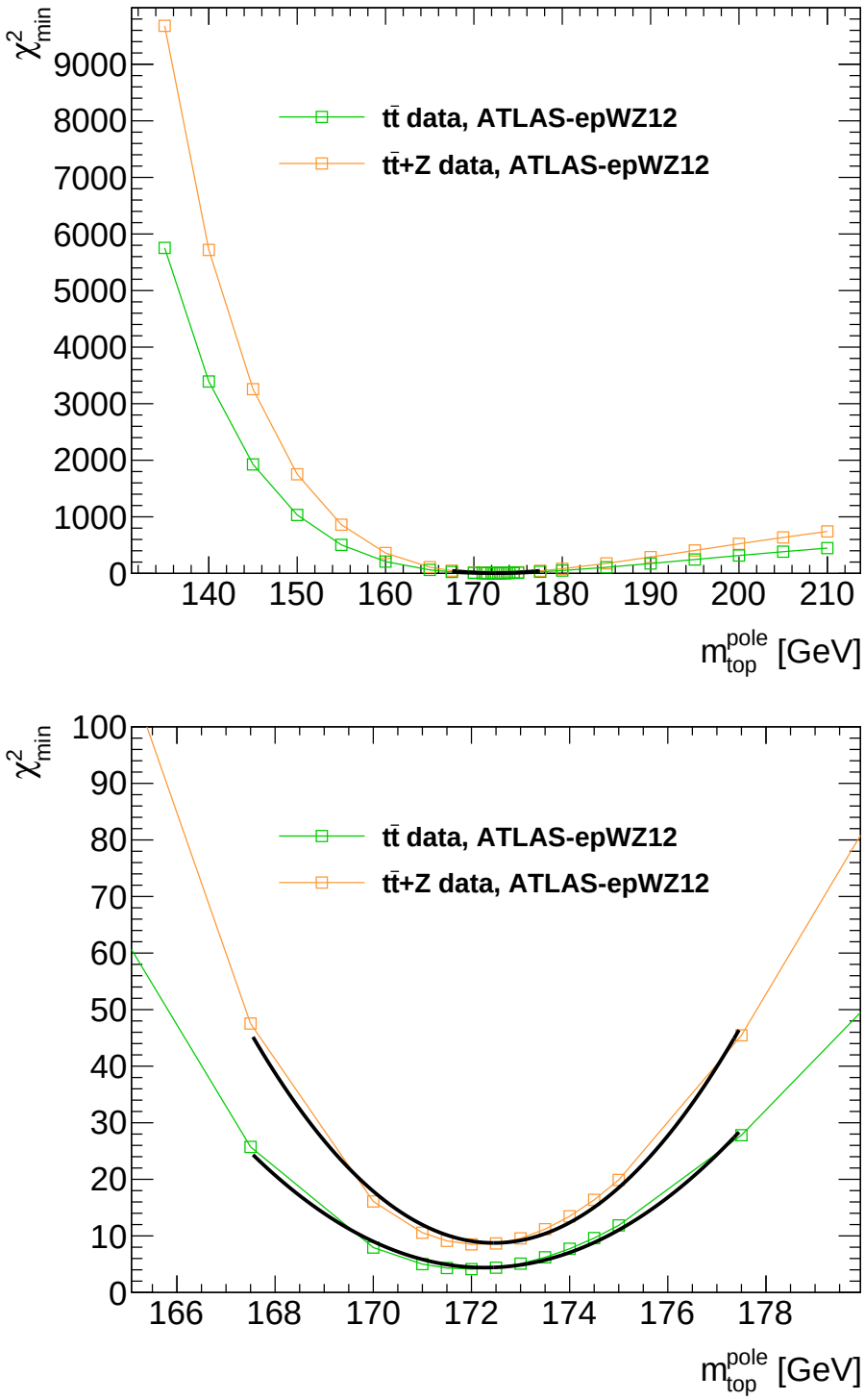

Figure 7.6: The indirect measurement of the top-quark mass: χ^2 scan based on the ATLAS-epWZ12 PDF predictions as a function of the top-quark pole mass, m_t^{pole}, including the $t\bar{t}$ measurements (green color) and $t\bar{t}$ with Z-boson measurements (orange color) at $\sqrt{s}$ = 7 TeV, 8 TeV and 13 TeV. The χ^2 scan procedure does not include PDF uncertainties. The curves are fitted with a parabolic function (black curve). The bottom plot shows zoomed region where the fit is performed.

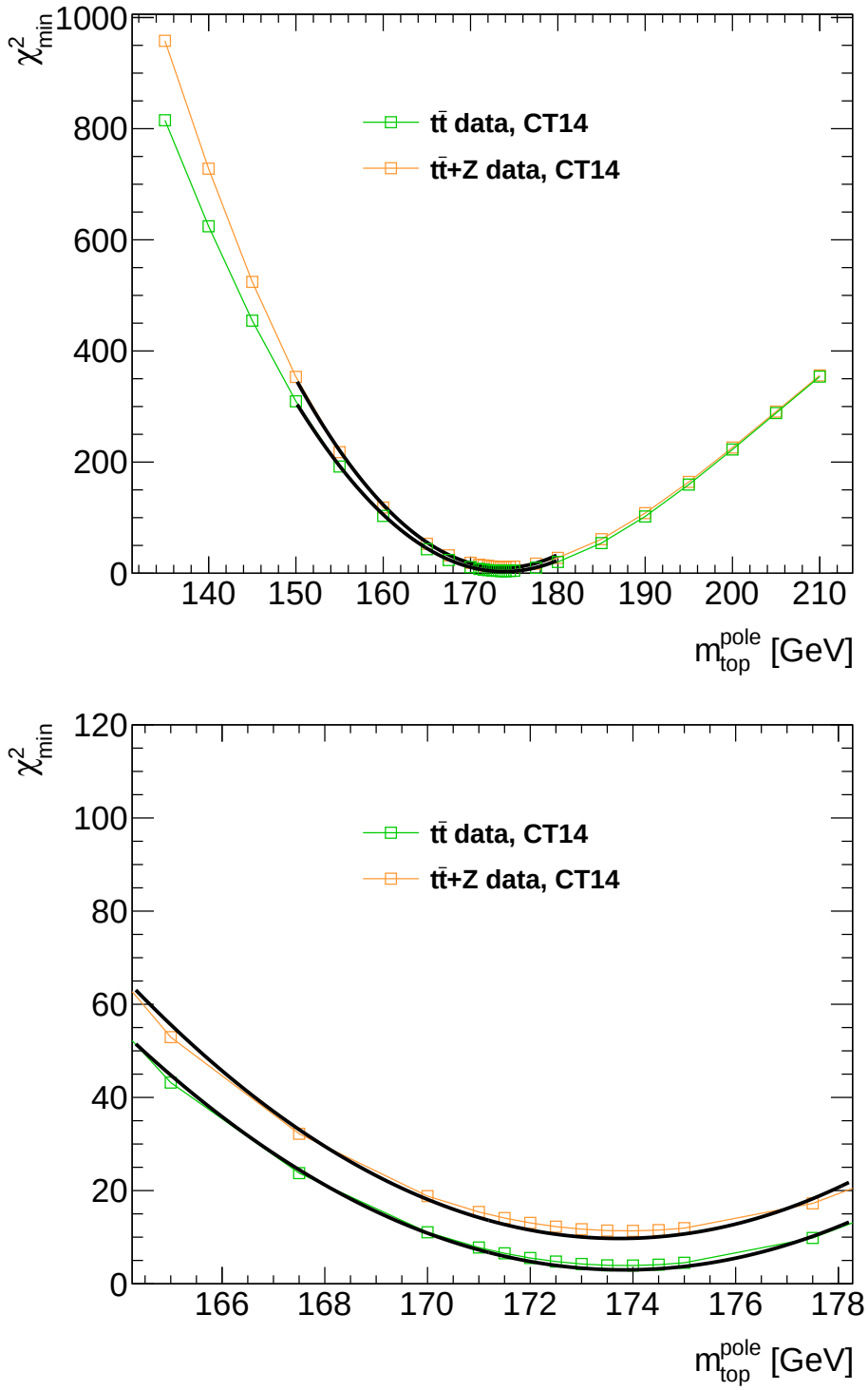

Figure 7.7: The indirect measurement of the top-quark mass: χ^2 scan based on the CT14 PDF predictions as a function of the top-quark pole mass, m_t^{pole}, including the $t\bar{t}$ measurements (green color) and $t\bar{t}$ with Z-boson measurements (orange color) at $\sqrt{s} = 7$ TeV, 8 TeV and 13 TeV. The χ^2 scan procedure includes PDF uncertainties. The curves are fitted with a parabolic function (black curve). The bottom plot shows zoomed region where the fit is performed.

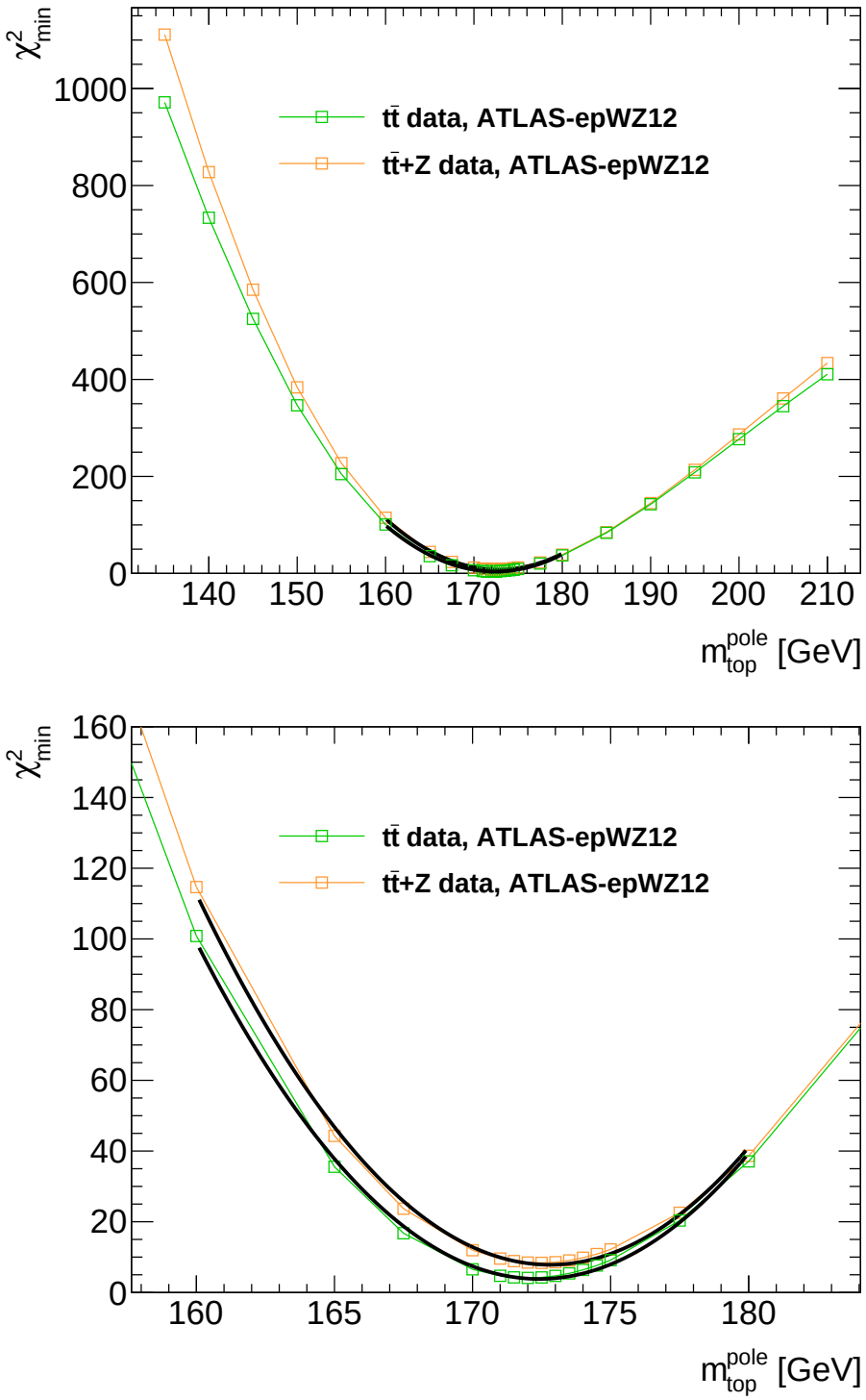

Figure 7.8: The indirect measurement of the top-quark mass: χ^2 scan based on the ATLAS-epWZ12 PDF predictions as a function of the top-quark pole mass, m_t^{pole}, including the $t\bar{t}$ measurements (green color) and $t\bar{t}$ with Z-boson measurements (orange color) at $\sqrt{s}$ = 7 TeV, 8 TeV and 13 TeV. The χ^2 scan procedure includes PDF uncertainties. The curves are fitted with a parabolic function (black curve). The bottom plot shows zoomed region where the fit is performed..

To obtain the values of m_t^{pole}, all χ^2_{min} values are fitted with a parabolic function around the minimum in different ranges. The value of m_t^{pole} at a minimum of the function corresponds to the result of the m_t^{pole} extraction, and the associated uncertainty corresponds to the width of the parabola. The derived values of m_t^{pole} for both PDF sets with and without PDFs uncertainties are presented in Tables 7.6 and 7.7. When the Z-boson cross-section measurements are added to the profiling, the impact on the error of m_t^{pole} is moderate. However this gets more significant when the PDF errors are excluded. The reduction of the uncertainty is mostly due to the luminosity error cancellation. Both central values, with included $t\bar{t}$ and Z-boson data agree within the uncertainty. If the PDF uncertainties are included to the scan, the difference between the relative uncertainties is 0.05% and 0.01% for the CT14 and ATLAS-epWZ12 sets. If the PDF uncertainties are excluded, the difference is 0.13% for the CT14 PDF set and 0.15% for the ATLAS-epWZ12 set. In general, the results illustrate an influence of the PDF uncertainty on the precision of the measurements of m_t^{pole}. The values extracted for both PDF sets are more consistent between each other when the Z-boson data are added and when the PDF uncertainty is considered in the χ^2 scan.

	CT14					
	without PDF uncertainty			with PDF uncertainty		
Data	m_t^{pole} [GeV]	χ^2/dof	p-value	m_t^{pole} [GeV]	χ^2/dof	p-value
$t\bar{t}$	174.23 ± 1.03	3.2/2	0.20	173.83 ± 1.37	3/2	0.22
$t\bar{t}$ + Z	176.38 ± 0.82	16.1/5	0.01	173.73 ± 1.29	9.7/5	0.08

Table 7.6: Summary of the m_t^{pole} extraction from the measured $t\bar{t}$ and Z-boson production cross sections at $\sqrt{s}$ = 7 TeV, 8 TeV and 13 TeV with the CT14 PDF set, considering only PDF uncertainties. The results are presented with and without including PDF uncertainties.

	ATLAS-epWZ12					
	without PDF uncertainty			with PDF uncertainty		
Data	m_t^{pole} [GeV]	χ^2/dof	p-value	m_t^{pole} [GeV]	χ^2/dof	p-value
$t\bar{t}$	172.27 ± 1.06	4.4/2	0.11	172.41 ± 1.27	3.8/2	0.15
$t\bar{t}$ + Z	172.46 ± 0.81	8.8/5	0.12	172.80 ± 1.25	7.8/5	0.17

Table 7.7: Summary of the m_t^{pole} extraction from the measured $t\bar{t}$ and Z-boson production cross sections at $\sqrt{s}$ = 7 TeV, 8 TeV and 13 TeV with the ATLAS-epWZ12 PDF set, considering only PDF uncertainties. The results are presented with and without including PDF uncertainties.

An impact of the data on the gluon distribution from the ATLAS-epWZ12 PDF set for the top-quark mass values, m_t^{pole} = 171.5 GeV and 173 GeV, below and above the minimum, is shown in Figure 7.9. In both cases, the reduced PDF uncertainty is observed for the gluon distribution around $x \sim 0.1$. The central values of the gluon distribution are shifted with the respect to the mass value, suggesting some level of anti-correlation.

7.3.2 Impact of scale and α_S uncertainties

In addition to the PDF uncertainties, the α_S and scale uncertainties should be taken into account in the top-quark mass extraction procedure. Therefore, the scan of the top-quark mass is performed including these uncertainties for the CT14 PDF set, for each m_t^{pole} value for the $t\bar{t}$ and Z-boson cross-section

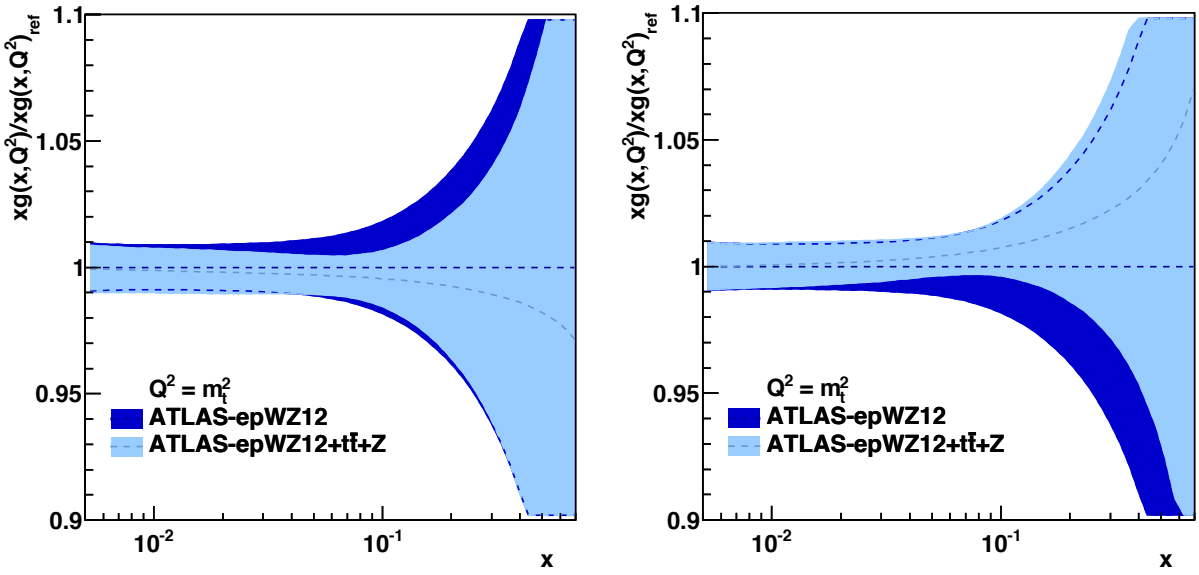

Figure 7.9: An effect of the ATLAS Z-boson and $t\bar{t}$ production cross section data on the PDFs. The bands represent the uncertainties for the ATLAS-epWZ12 PDF set and the uncertainty of the profiled ATLAS-epWZ12 PDF set profiled including $t\bar{t}$ and Z-boson data. Profiled PDF is divided by central value of ATLAS-epWZ12 PDF set and represented as solid blue line. The left plot demonstrate the gluon density at $Q^2 = m_t^2$ as a function of Bjorken-x for the $m_t^{\text{pole}} = 171.5$ GeV and the right plot for the $m_t^{\text{pole}} = 173$ GeV.

predictions. The uncertainty on α_S is considered as correlated between the $t\bar{t}$ and Z-boson predictions, and the uncertainties from the scale variations are considered as uncorrelated.

The χ^2 scan results including scale, α_S and PDF uncertainties is shown in Figure 7.10. The derived values of the m_t^{pole} for the CT14 PDF set, including all theoretical uncertainties, are presented in Table 7.8.

The results show that the uncertainties of the extracted m_t^{pole} values are increased, as expected. The relative uncertainty increased from 0.7% to 1.1%, but is smaller in the comparison with the previous result from the ATLAS (see Equation 2.33). The inclusion of the Z-boson data has smaller sensitivity to the m_t^{pole} due to increased theoretical uncertainty. Thus, better constrain on the PDF sets in future should allow for an improved top-quark pole mass determination with the indirect method.

	CT14		
	with PDF + Scale + α_S uncertainties		
Data	m_t^{pole} [GeV]	χ^2/dof	p-value
$t\bar{t}$	173.51 ± 2.00	4.14/2	0.13
$t\bar{t} + Z$	173.51 ± 1.99	11.5/5	0.04

Table 7.8: Summary of the m_t^{pole} extraction from the measured $t\bar{t}$ and Z-boson production cross sections at $\sqrt{s}$ = 7 TeV, 8 TeV and 13 TeV with the CT14 PDF set, considering PDF, scale and α_S uncertainties.

The shift of the α_S nuisance parameters in the profiling procedure has a Gaussian prior condition, which means that a shift of $\Delta\alpha_s = 0.001$ introduces the χ^2 penalty of $\Delta\chi^2 = 1$. This prior can be removed to allow for free variations. The values of α_S, which are estimated from the shifts of the nuisance

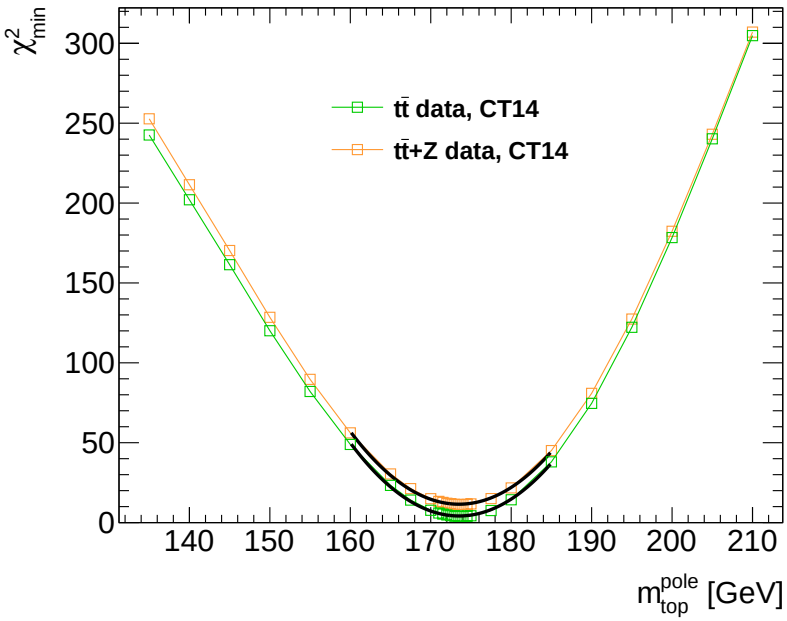

Figure 7.10: The indirect measurement of the top-quark mass: χ^2 scan based on the ATLAS-epWZ12 PDF predictions as a function of the top-quark pole mass m_t^{pole} including the $t\bar{t}$ measurements (green color) and $t\bar{t}$ with Z-boson measurements (orange color) at $\sqrt{s}$ = 7 TeV, 8 TeV and 13 TeV. Both curves includes the uncertainties from the PDF, scale and α_S variations and are fitted with a parabolic function (black curve).

parameters after the profiling when the prior condition is included or not, are evaluated as:

$$\alpha_S = 0.118 - \text{shift} \times 0.001,$$

and are shown as the function of the top-quark mass in Figure 7.11.

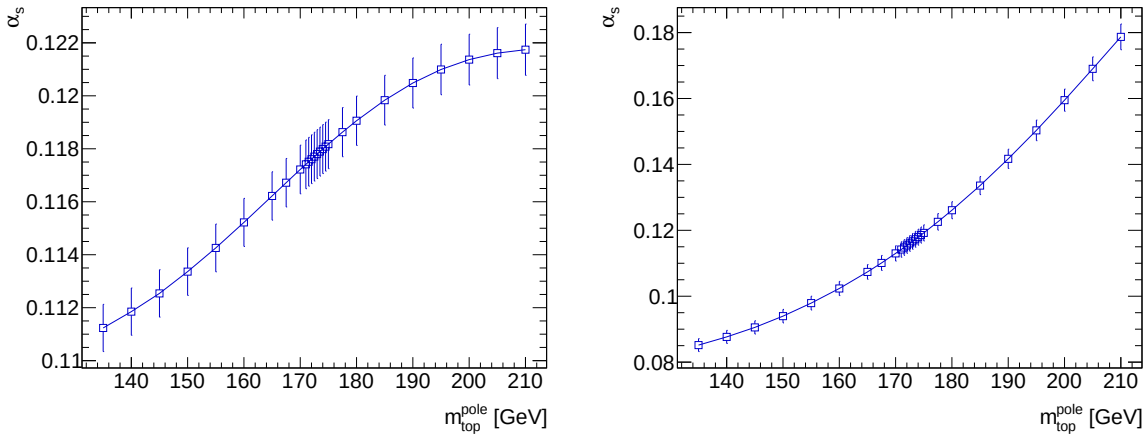

Figure 7.11: Dependence of α_S on the the top-quark mass. Left: α_S values as the function of the m_t^{pole} which correspond to the shift of the α_S nuisance parameters with the prior condition. Right: α_S values as the function of the m_t^{pole} corresponding to the shift of the α_S nuisance parameters without the prior condition.

The estimated value of α_S for the best-fit value of the top-quark mass, $m_t^{\text{pole}} = 173.5$ GeV, is:

$$\alpha_S = 0.117 \pm 0.002.$$

7.4 Discussion

The measured $t\bar{t}$ and Z-boson cross sections at the different centre-of-mass energies demonstrate a significant power to constrain the gluon distribution at Bjorken-x around 0.1 and can be used for the determination of the top-quark mass with well-controlled theoretical uncertainties. The values of the top-quark mass are extracted using indirect method, comparing the dependence of theoretical predictions with the measurements on the top-quark mass. The obtained values are similar to previously published ATLAS results (see Equation 2.33) and show improved precision. The relative uncertainty on the top-quark mass value is reduced from 1.4% to 1.1% mostly due to improved luminosity and beam-energy uncertainties and reduced PDF uncertainties in CT14 PDF set with respect to older CT10 PDF set. However, recent results from direct measurements (see Figure 2.10) are quite accurate in contract to the indirect results. The precision of the top-quark mass measurement evaluated in the indirect method depends on the knowledge of the PDFs, which are essential component of theoretical calculations. The PDF and α_S uncertainties are the dominant theoretical uncertainties, and translate this uncertainty to the mass measurement. Therefore, better understanding and new constrains on gluon distributions and α_S will improve the indirect top-quark mass determination procedure.

CHAPTER 8

Summary

The Large Hadron Collider (LHC) began successfully new data-taking period in 2015, Run 2, with an increased centre-of-mass energy of 13 TeV, providing a potential to collect huge amount of events for physics analyses in order to explore new kinematic phase-space. New precision measurement of Z-boson cross sections is obtained in a kinematic region never reached before. The Z-bosons decaying into two leptons provide a clean signature, with small background contributions. This measurement can serve as a standard candle for the calibration and understanding of the ATLAS detector, and is important to test Standard Model predictions. Moreover, these Run 2 measurement is essential to check if there no deviation in new LHC regime. The Run 2 is planned to be completed by the end of 2018 for a preparation for new data-taking periods with increased collision energy and an instantaneous luminosity in order to improve discovery potential and reach highest precision measurements. The future technical stop will involve an entire replacement of the ATLAS Inner Detector with a new silicon tracker for the High-Luminosity Large Hadron Collider project. This dissertation describes the contributions related to a future upgrade of the ATLAS detector and studies of Z-boson production at the centre-of-mass energy of 13 TeV.

The first contribution to this dissertation is the assembly and testing of small-scale petal prototypes, so-called petalets, which consist of silicon sensor modules and electronic readout components. They are small version of the basic mechanical constituents, petals, for the new ATLAS Inner Tracker (ITk) in the forward region. Single- and double-sided prototypes, with different sensor designs (standard and embedded) and with two different readout and powering electronics layouts (split and common), are assembled with a goal to study an electrical performance of both options and to understand the issues, benefits and suitability of the two different designs. Three petalets with the split readout scheme and different sensor designs are evaluated at DESY. Before each petalet assembly, the silicon sensors were shipped to DESY and required dedicated tests to ensure their functionality. A measurement of current-voltage characteristics at three different temperatures, and with low voltage powered on and off, is performed and provides information on the amount of the leakage current and the depletion voltage. Next, a set of tests for all petalets and silicon modules (before being mounted onto the petalet support core) is executed using SCTDAQ software package and binary High-Speed-Input/Output board. The essential characteristics, an input noise and gain, are measured for a binary readout chip (ABCN-25) using threshold scans. The main results are obtained from the three point gain tests (after correct settings of the strobe delay, idelay and trimming) for different sensor bias voltages. Comparison of averaged input noise between two single-sided petalets presents slightly lower noise for the petalet, which has better quality sensors and improved grounding and shielding. Moreover, the comparison of the input noise between two running modes for double-sided petalet, where both sides are read out simultaneously and independently,

demonstrates almost negligible increase in noise concerning each side tested simultaneously. This is related to the increased temperature due to higher power dissipation.

The outcome from the production of all six petalets, including the cores, module on core assembly and the electrical characterization, is summarized and considered to support a decision towards the electronics layout of the petals for the end-cap of the ATLAS ITk strip detector. All modules are run simultaneously and all values of the input noise are obtained for fully depleted sensors at the lowest temperature of the operation. The best layout is chosen after internal ATLAS ITk review as the baseline for the future production of the petal. The layout, which has data and power lines on separate sides of the petalet, demonstrates the lower input noise and the advantages for electrical performance and mechanical assembly. The standard high-quality sensors maintain the lower noise performance versus the sensors with an additional metal layer. In general, the chosen version allows the production and development of primary components more directly with the barrel modules, while another layout version will require additional solutions.

The main contribution of this dissertation is expressed by measurements of fiducial and total Z-boson production cross sections at a centre-of-mass energy of the proton–proton collisions of 13 TeV. Data used for the analysis corresponds to an integrated luminosity of $3.16\,\text{fb}^{-1}$ recorded with the ATLAS detector in 2015, when the LHC was operating with the 25 ns bunch-spacing configuration. The cross sections obtained in both $Z \to e^+e^-$ and $Z \to \mu^+\mu^-$ channels are published for the first time at this centre-of-mass energy, and this thesis describes the results which went to the publication [20] and which are close to previously published results [4], where my contribution was dedicated to measurements of fiducial and total Z-boson production cross sections in the muon channel. The combined cross section is used in a calculation of several types of ratio, an estimation of its impact on the parton distribution function (PDF) set and an extraction of top-quark pole mass using an indirect method.

The event selection criteria are tuned to be consistent with the $t\bar{t}$ analysis [22] to ensure a cancellation of the uncertainties in the ratios. Approximately 1.3 and 1.7 million of Z-boson candidates were observed in the electron and muon channels, respectively.

An expected amount of background processes is determined from the Monte Carlo simulations with a contribution to the Z-boson event yield approximately 0.5% in both analysis channels. The main contribution is dominated by $t\bar{t}$ production, while the electroweak contribution was 0.2%. The contribution of multijet events is estimated using a data-driven method and is found to be less than 0.1% in both analysis channels.

The Monte Carlo simulation is corrected for any discrepancy in the trigger, identification, reconstruction, and isolation efficiencies for selected leptons, by applying scale factors which are extracted from official performance tolls. The tag-and-probe method is introduced to cross-check the efficiencies after using corresponding scale factors. The correction factors which correct the cross sections for the detector efficiency, are estimated from the Monte Carlo simulation. Moreover, the selected events, the correction factors, scale factors and event-by-event kinematics are compared with different analyses showing good agreement.

The comparison of important kinematic distributions between the data and simulated signal including expected contributions from all backgrounds sources shows a good agreement, except small miss-modellings in the high-p_{T} regions. This effect is examined by reweighting of the simulated p_{T} distribution to a polynomial derived from a fit to the corresponding data distribution, and shows a small impact on the measured fiducial cross sections.

The measured cross section in electron and muon channels are used to check the lepton universality. The result agrees with previous published ATLAS results using $\sqrt{s} = 7$ TeV [2] and $\sqrt{s} = 13$ TeV (50 ns) data [4] and with the latest Particle Data Group (PDG) world average value [27]. The cross sections from both channels are combined, reaching precision below 1%, and are compared with corresponding

values using the 50 ns dataset. The comparison indicates that measurements have good consistency between each other, better statistical and reduced systematic uncertainty for 25 ns cross sections. The systematic uncertainties for the 25 ns results is significantly reduced, mainly due to the reduced statistical components of systematics and with employing toy MC method for some of the systematics, which was not the case for 50 ns results. Experimental systematic uncertainties on fiducial and total cross sections are estimated and dominated by luminosity uncertainty (2.1%) in both analysis channels. Apart from the luminosity uncertainty, the main contribution to the systematic uncertainties arises from the lepton reconstruction and identification sources and muon isolation. Next, the cross sections are compared to QCD predictions based on different PDF sets: CT14 [37], NNPDF3.0 [38], MMHT14 [39], ATLAS-epWZ12 [40], HERAPDF2.0 [41], and ABM12 [42] and show a good agreement. Especially, HERAPDF2.0 and ATLAS-epWZ12 predictions at NNLO describe the measurement better than other PDF sets.

The Z-boson production measurements are used for an evaluation of single and double cross-section ratios with top quark pair production at the same and three different centre-of-mass energy. The concept of ratio allows the elimination of luminosity uncertainty and partial cancellation of lepton reconstruction, identification, trigger and beam energy uncertainties. The comparison of measured single ratios with the theoretical prediction indicates that the ATLAS data are more accurate than most of the theoretical predictions, demonstrating strong constraining power. The single ratio between $t\bar{t}$ and Z-boson cross sections shows improved result in the comparison with the preliminary result that was based on the data sample with 50 ns bunch spacing, mainly because of increased statistics and the improved lepton-related systematic uncertainties. The relative uncertainty was reduced approximately in 2 times.

Quantitative comparison is performed between measured combined cross section obtained in this dissertation and new $t\bar{t}$ measurement [22] and previous measurements of the $t\bar{t}$ and Z-boson production cross section at the centre-of-mass energy of $\sqrt{s}$ = 7 TeV and 8 TeV [2, 3, 21] with the theoretical predictions for different PDF sets. The best agreement is observed with the HERAPDF2.0 and ATLAS-epWZ12 PDF sets. The other three PDF sets, CT14, NNPDF3.0, MMHT14, have lower predictions for Z-boson production and higher for $t\bar{t}$ production, while the ABM12 PDF set is in better agreement with the Z-boson production cross sections and predicts much lower cross sections for $t\bar{t}$ production. In addition, the measured cross sections are used to estimate the impact on existing ATLAS-epWZ12 PDF set using the profiling method from the xFitter framework. The results present the reduction of the uncertainties for the light-sea distribution at $x < 0.02$ and for the gluon distribution at $x \sim 0.1$.

The same dataset is used to estimate the top-quark mass by comparing measured and predicted cross sections as a function of the top-quark mass. The top-quark mass values are obtained for both, CT14 and ATLAS-epWZ12 PDF sets. The results suggest that the inclusion of the Z-boson data has higher sensitivity when the PDF uncertainties were excluded from the top-quark mass scan. Also, the results demonstrates reduced uncertainty on the value of the top-quark mass using CT14 PDF set in contract to the previous published results from the ATLAS and dependence of the gluon distribution from the choice of the value of the top-quark mass. The precision of the top-quark mass extraction with the indirect method can be improved by reducing PDF and α_S uncertainties which are the dominant sources of the theoretical uncertainties in the method.

APPENDIX A

Details on the Z-boson cross-section measurements

A.1 Theoretical predictions for Z-boson cross sections

Table A.1 shows the predictions for the total and fiducial cross sections for Z-boson production at centre-of-mass energy $\sqrt{s}$ = 13 TeV, 8 TeV and 7 TeV for the CT14 [37] PDF set and the overall uncertainties in the α_S, scale variations and intrinsic uncertainty are given as well as the PDF uncertainties for the PDF variations of CT14, NNPDF3.0 [38], MMHT14 [39], ATLAS-epWZ12 [40], HERAPDF2.0 [41], and ABM12 [42].

A.2 Integrated luminosity per run number

The integrated luminosity is calculated for each run of data periods D–J and presented in Table A.2. The values are obtained using the GRL, which is described in subsection 5.4.4, and the luminosity tag *OflLumi-13TeV-004*.

A.3 Data yield versus run number for the $Z \to ll$

The ratio of data yields between $t\bar{t}$ and Z-boson analyses using *OflLumi-13TeV-003* are shown in Table A.3.

	7 TeV				8 TeV				13 TeV			
σ [pb]	tot.	stat.	fid.	stat.	tot.	stat.	fid.	stat.	tot.	stat.	fid.	stat.
CT14												
central	956.34	0.71	433.35	0.37	1112.47	0.67	487.70	0.30	1890.98	0.47	746.37	0.60
α_s dn	948.04	0.60	430.45	0.26	1103.47	0.55	483.80	0.34	1873.38	1.11	738.37	0.64
α_s up	964.24	0.57	437.85	0.28	1120.77	0.80	492.39	0.32	1909.78	1.40	753.37	0.67
μ_f dn	947.94	0.52	432.55	0.31	1102.17	0.63	485.30	0.34	1869.78	0.86	740.57	0.50
μ_f up	958.44	0.55	434.55	0.30	1117.07	0.56	487.90	0.32	1896.08	2.04	745.77	0.80
μ_r dn	955.64	0.81	431.95	0.46	1111.17	0.76	486.20	0.38	1883.98	1.60	743.67	0.67
μ_r up	954.44	0.63	433.75	0.28	1110.27	0.58	488.20	0.26	1891.00	1.12	747.27	0.44
μ_f, μ_r dn	952.44	0.69	434.05	0.34	1107.67	0.80	487.10	0.37	1881.38	1.12	744.57	0.60
μ_f, μ_r up	960.84	0.54	436.55	0.25	1119.57	0.54	490.20	0.26	1903.78	1.18	749.77	0.84
Uncertainties [pb]												
α_s dn	8.30		2.90		9.00		3.90		17.60		8.00	
α_s up	7.90		4.50		8.30		4.69		18.80		7.00	
scale dn	8.40		1.40		10.30		2.40		21.20		5.80	
scale up	4.50		3.20		7.10		2.50		12.80		3.40	
Intrinsic dn			3.00				3.40				5.21	
Intrinsic up			3.00				3.40				5.21	
CT14 up	20.75		10.64		24.40		12.10		45.10		20.30	
CT14 dn	23.88		13.11		28.00		15.10		50.30		24.97	
MMHT14												
central	966.43	1.27	437.83	0.51	1123.41	1.34	492.90	0.74	1908.33	3.10	756.89	1.39
MMHT14 up	14.50		6.80		16.60		7.80		31.20		15.00	
MMHT14 dn	13.10		6.40		15.00		7.30		27.02		12.90	
NNPDF3.0												
central	943.63	1.00	426.31	0.65	1096.23	1.35	480.81	0.67	1867.92	2.43	734.50	1.46
NNPDF3.0 up	18.68		8.60		21.87		9.83		39.59		16.39	
NNPDF3.0 dn	18.68		8.60		21.87		9.83		39.59		16.39	
ATLAS-epWZ12												
central	990.03	1.14	449.62	0.50	1153.63	1.88	509.21	0.71	1970.30	2.44	788.16	1.39
ATLAS-epWZ12 up	16.98		8.36		19.58		9.55		34.63		15.73	
ATLAS-epWZ12 dn	14.95		8.37		17.59		9.69		31.69		16.28	
HERAPDF2.0												
central	994.07	1.12	449.37	0.67	1158.90	1.34	506.66	0.70	1982.30	2.85	781.13	1.91
HERAPDF2.0 up	31.93		15.32		35.80		16.97		58.26		25.85	
HERAPDF2.0 dn	17.96		8.73		20.63		9.76		34.67		17.18	
ABM12												
central	969.26	1.04	443.99	0.60	1123.89	1.39	500.93	0.59	1915.68	2.33	762.56	1.29
ABM12 up	10.94		5.25		12.82		6.05		23.08		10.17	
ABM12 dn	10.94		5.25		12.82		6.05		23.08		10.17	

Table A.1: Z predictions of the total (tot.) and fiducial (fid.) cross-sections at centre-of-mass energy $\sqrt{s}$ = 13 TeV, 8 TeV and 7 TeV for the CT14 PDF set, where the fiducial region is given in the 13 TeV fiducial phase space. The central values for the α_S and scale variations up and down (dn) are included. In the bottom half of the table, the overall uncertainties in the α_S, scale variations and intrinsic uncertainty are given as well as the PDF uncertainties for the PDF variations of CT14, MMHT14, NNPDF3.0, ATLAS-epWZ12, HERAPDF2.0 and ABM12. The EW corrections have not been applied to these numbers.

Period	Run Number	Integrated luminosity, [pb^{-1}]
D	276262	6.15
	276329	11.71
	276336	0.67
	276416	4.18
	276511	8.73
	276689	10.65
	276778	0.66
	276790	1.55
	276952	6.48
	276954	0.73
E	278880	21.42
	278912	19.63
	278968	9.86
	279169	55.00
	279259	7.31
	279279	16.90
	279284	31.82
	279345	52.68
	279515	0.35
	279598	67.61
	279685	74.45
	279764	6.69
	279813	47.62
	279867	29.51
	279928	1.00
F	279932	44.52
	279984	64.83
	280231	88.28
	280319	93.64
	280368	8.21
G	280423	68.42
	280464	58.22
	280500	7.27
G	280520	12.12
	280614	24.24
	280673	148.50
	280753	44.61
	280853	7.01
	280862	130.10
	280950	124.00
	280977	34.20
	281070	12.13
	281074	45.22
	281075	0.83
H	281317	23.65
	281385	62.88
	281411	134.00
J	282625	10.26
	282631	25.94
	282712	91.31
	282784	2.88
	282992	106.60
	283074	55.80
	283155	28.69
	283270	13.27
	283429	232.70
	283608	23.81
	283780	145.10
	284006	38.92
	284154	10.00
	284213	199.60
	284285	247.20
	284420	57.09
	284427	35.26
	284484	103.40

Table A.2: Integrated luminosity per run number of 25 ns dataset.

Run Number	$N_{(Z_{ee}+Z_{\mu\mu})/2}$	$N_{t\bar{t}}$	$R_{t\bar{t}/Z}$
276262	2 917.5±54.014	57.0±7.55	0.01954±0.0026
276329	5 621.0±74.973	112.0±10.58	0.01993±0.0019
276336	329.5±18.152	6.0±2.449	0.01821±0.0075
276416	1 988.0±44.587	45.0±6.708	0.02264±0.0034
276511	4 324.0±65.757	76.0±8.718	0.01758±0.002
276689	5 135.0±71.659	111.0±10.54	0.02162±0.0021
276778	325.5±18.042	4.0±2	0.01229±0.0062
276790	827.5±28.766	14.0±3.742	0.01692±0.0046
276952	3 147.0±56.098	67.0±8.185	0.02129±0.0026
276954	357.0±18.894	12.0±3.464	0.03361±0.0099
278880	10 612.0±103.01	229.0±15.13	0.02158±0.0014
278912	9 860.0±99.298	199.0±14.11	0.02018±0.0014
278968	4 915.5±70.111	107.0±10.34	0.02177±0.0021
279169	27 133.5±164.72	532.0±23.07	0.01961±0.00086
279259	3 616.5±60.137	75.0±8.66	0.02074±0.0024
279279	8 358.5±91.425	164.0±12.81	0.01962±0.0015
279284	15 716.5±125.37	285.0±16.88	0.01813±0.0011
279345	26 227.0±161.95	592.0±24.33	0.02257±0.00094
279515	169.5±13.019	1.0±1	0.00590±0.0059
279598	33 329.5±182.56	659.0±25.67	0.01977±0.00078
279685	36 728.0±191.65	796.0±28.21	0.02167±0.00078
279764	3 356.5±57.935	80.0±8.944	0.02383±0.0027
279813	23 828.0±154.36	520.0±22.8	0.02182±0.00097
279867	14 514.5±120.48	262.0±16.19	0.01805±0.0011
279928	475.0±21.794	6.0±2.449	0.01263±0.0052
279932	22 053.5±148.5	436.0±20.88	0.01977±0.00096
279984	31 721.5±178.11	630.0±25.1	0.01986±0.0008
280231	42 997.0±207.36	808.0±28.43	0.01879±0.00067
280319	44 950.0±212.01	861.0±29.34	0.01915±0.00066
280368	3 878.5±62.278	69.0±8.307	0.01779±0.0022
280423	33 304.5±182.5	674.0±25.96	0.02024±0.00079
280464	28 241.5±168.05	607.0±24.64	0.02149±0.00088
280500	3 560.5±59.67	55.0±7.416	0.01545±0.0021
280520	5 846.5±76.462	97.0±9.849	0.01659±0.0017
280614	11 670.5±108.03	199.0±14.11	0.01705±0.0012
280673	71 001.5±266.46	1 421.0±37.7	0.02001±0.00054
280753	21 574.0±146.88	452.0±21.26	0.02095±0.001
280853	3 503.5±59.19	66.0±8.124	0.01884±0.0023
280862	63 475.5±251.94	1 257.0±35.45	0.01980±0.00056
280950	61 086.0±247.16	1 279.0±35.76	0.02094±0.00059
280977	16 375.5±127.97	300.0±17.32	0.01832±0.0011
281070	5 875.0±76.649	121.0±11	0.02060±0.0019
281074	22 085.0±148.61	465.0±21.56	0.02106±0.00099
281075	463.5±21.529	8.0±2.828	0.01726±0.0062
281317	11 575.0±107.59	224.0±14.97	0.01935±0.0013
281385	31 147.0±176.49	649.0±25.48	0.02084±0.00083
281411	64 720.0±254.4	1 334.0±36.52	0.02061±0.00057
282625	4 998.5±70.7	98.0±9.899	0.01961±0.002
282631	12 768.5±113	282.0±16.79	0.02209±0.0013
282712	44 624.0±211.24	890.0±29.83	0.01994±0.00068
282784	1 356.5±36.831	25.0±5	0.01843±0.0037
282992	52 398.5±228.91	1 029.0±32.08	0.01964±0.00062
283074	27 394.5±165.51	528.0±22.98	0.01927±0.00085
283155	13 990.0±118.28	274.0±16.55	0.01959±0.0012
283270	6 394.5±79.966	120.0±10.95	0.01877±0.0017
283429	114 710.0±338.69	2 232.0±47.24	0.01946±0.00042
283608	12 123.5±110.11	239.0±15.46	0.01971±0.0013
283780	71 507.0±267.41	1 500.0±38.73	0.02098±0.00055
284006	19 250.5±138.75	375.0±19.36	0.01948±0.001
284154	4 931.5±70.225	101.0±10.05	0.02048±0.0021
284213	98 280.5±313.5	1 924.0±43.86	0.01958±0.00045
284285	120 760.0±347.5	2 414.0±49.13	0.01999±0.00041
284420	27 853.0±166.89	541.0±23.26	0.01942±0.00084
284427	17 213.5±131.2	323.0±17.97	0.01876±0.0011
284484	51 281.5±226.45	961.0±31	0.01874±0.00061

Table A.3: Data yields per run number for the $Z \to ll$ and $t\bar{t}$ selections and their ratios.

A.4 Muon trigger efficiency

The efficiency of the muon trigger has been evaluated on both data and Monte Carlo with a tag-and-probe method using $Z \to \mu\mu$ events. The efficiency was obtained for muons, passing the trigger combination of HLT_mu20_iloose_L1MU15 or HLT_mu50. From these efficiencies the scale factor were applied to MC, in bins of η and ϕ. FiguresA.1–A.5 show the efficiency in data and in MC in the barrel and in the end-caps respectively for each period of data.

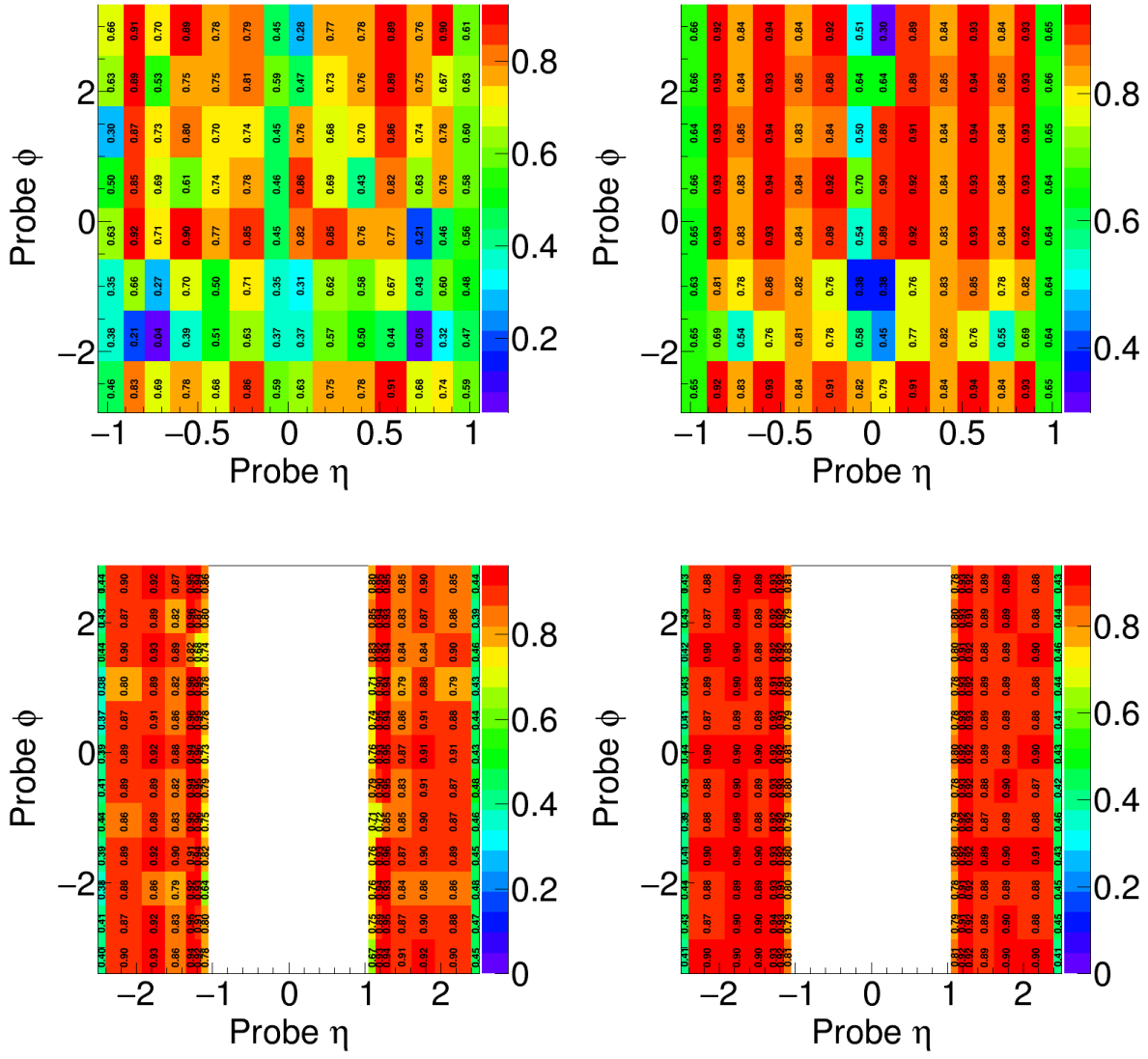

Figure A.1: Trigger efficiency of HLT_mu20_iloose_L1MU15 or HLT_mu50 in the barrel regions (top) and end-cap regions (bottom) in data (left) and in MC (right) for muons for data taking period E.

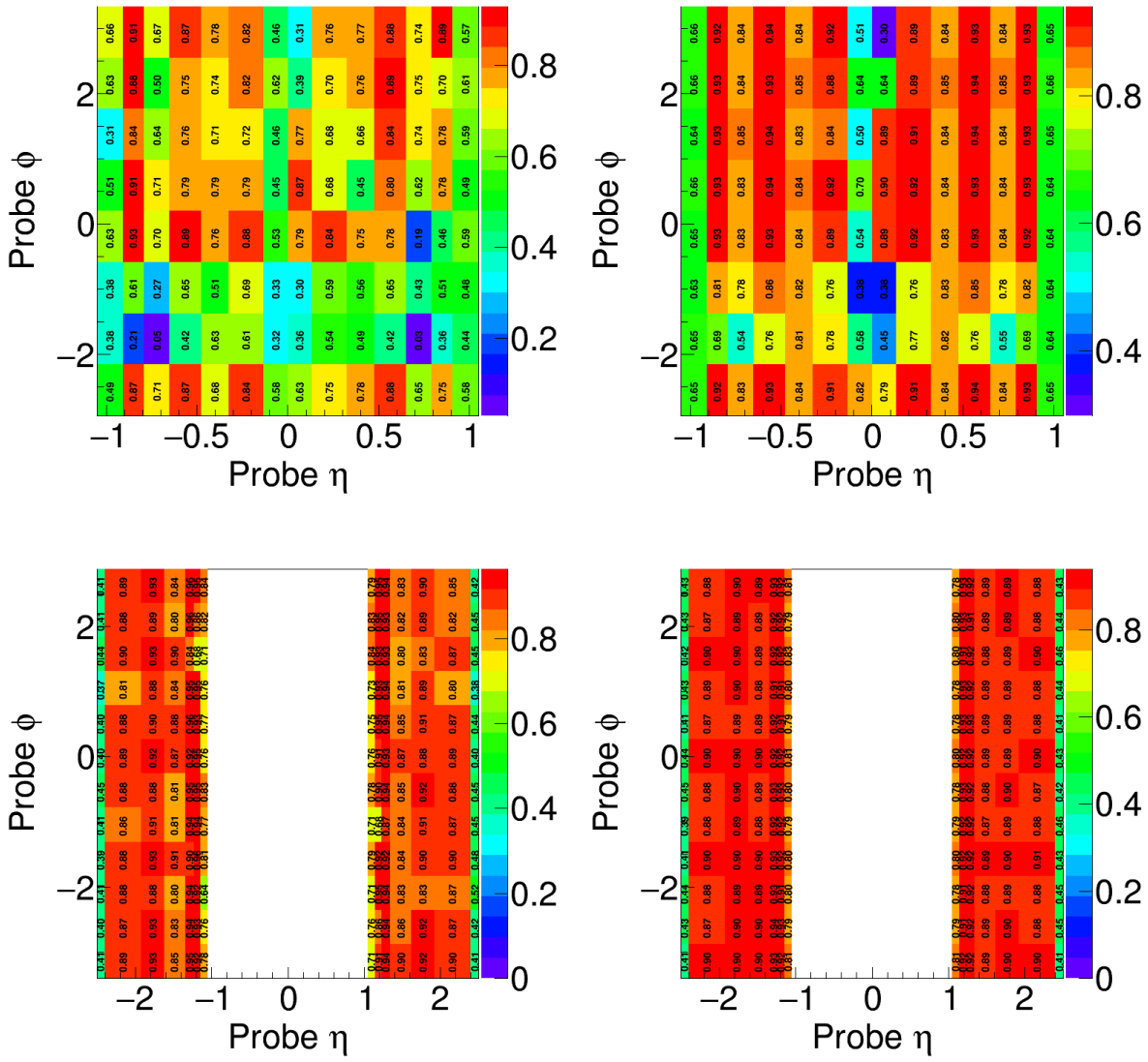

Figure A.2: Trigger efficiency of HLT_mu20_iloose_L1MU15 or HLT_mu50 in the barrel regions (top) and end-cap regions (bottom) in data (left) and in MC (right) for muons for data taking period F.

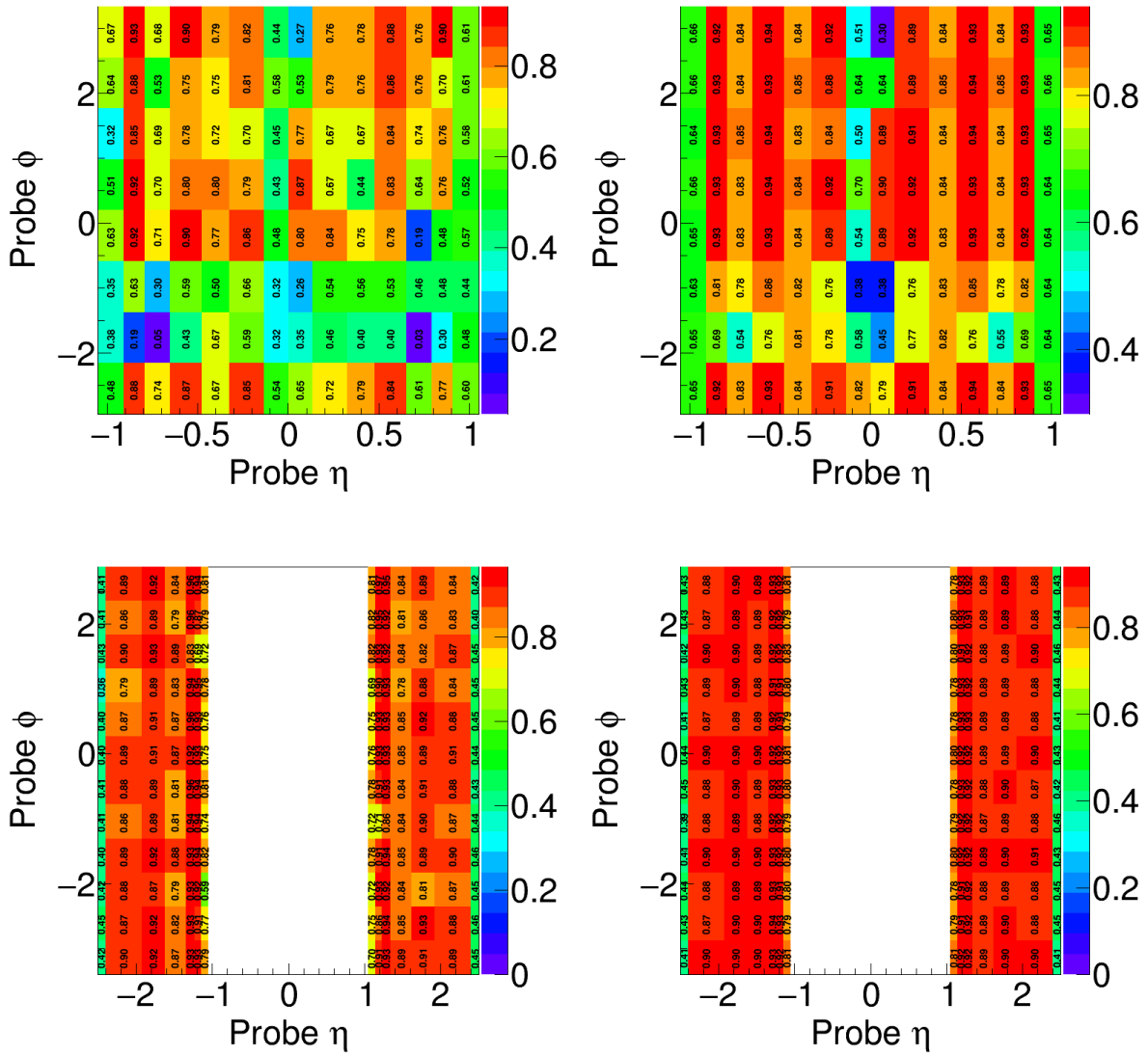

Figure A.3: Trigger efficiency of HLT_mu20_iloose_L1MU15 or HLT_mu50 in the barrel regions (top) and end-cap regions (bottom) in data (left) and in MC (right) for muons for data taking period G.

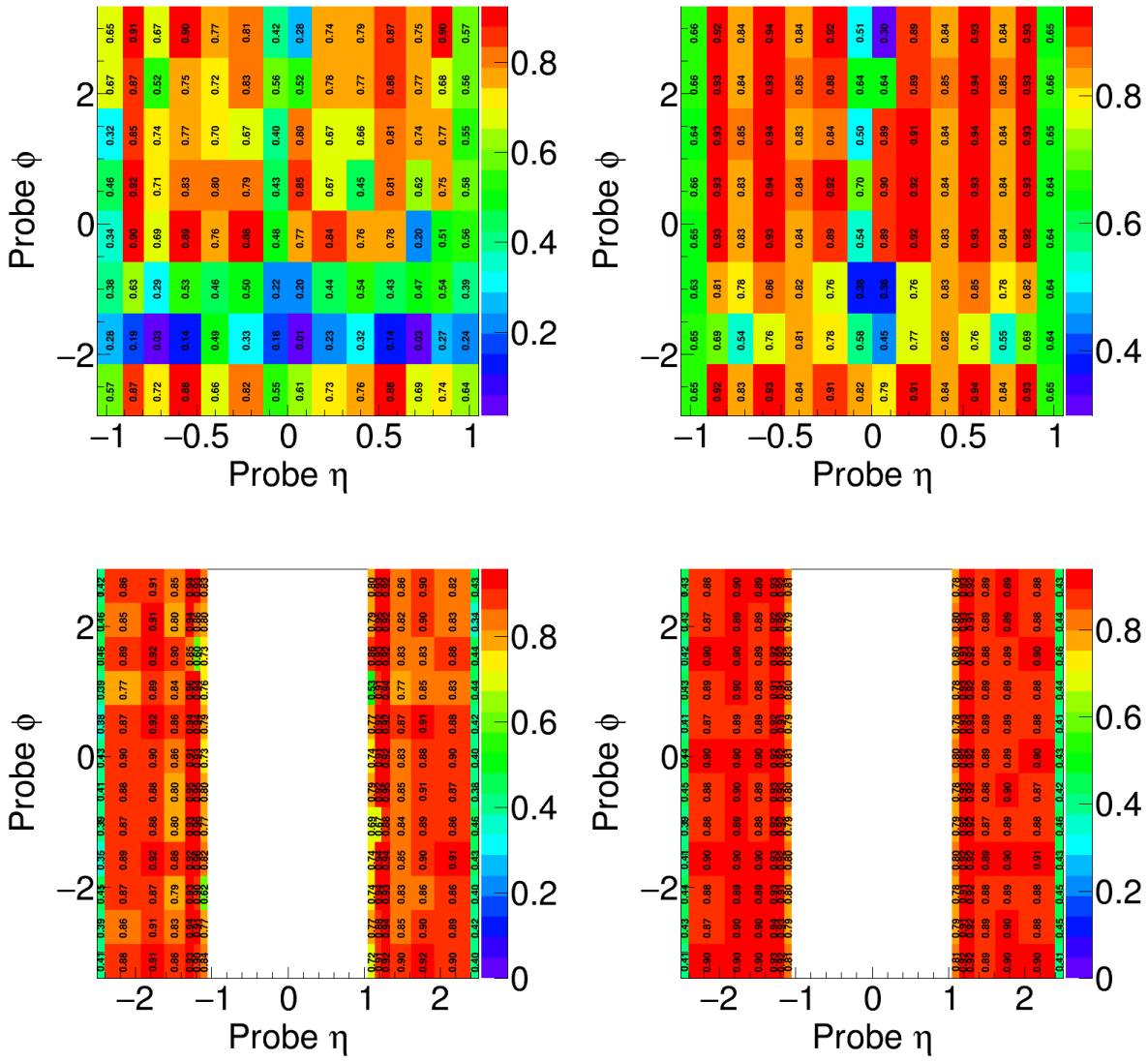

Figure A.4: Trigger efficiency of HLT_mu20_iloose_L1MU15 or HLT_mu50 in the barrel regions (top) and end-cap regions (bottom) in data (left) and in MC (right) for muons for data taking period H.

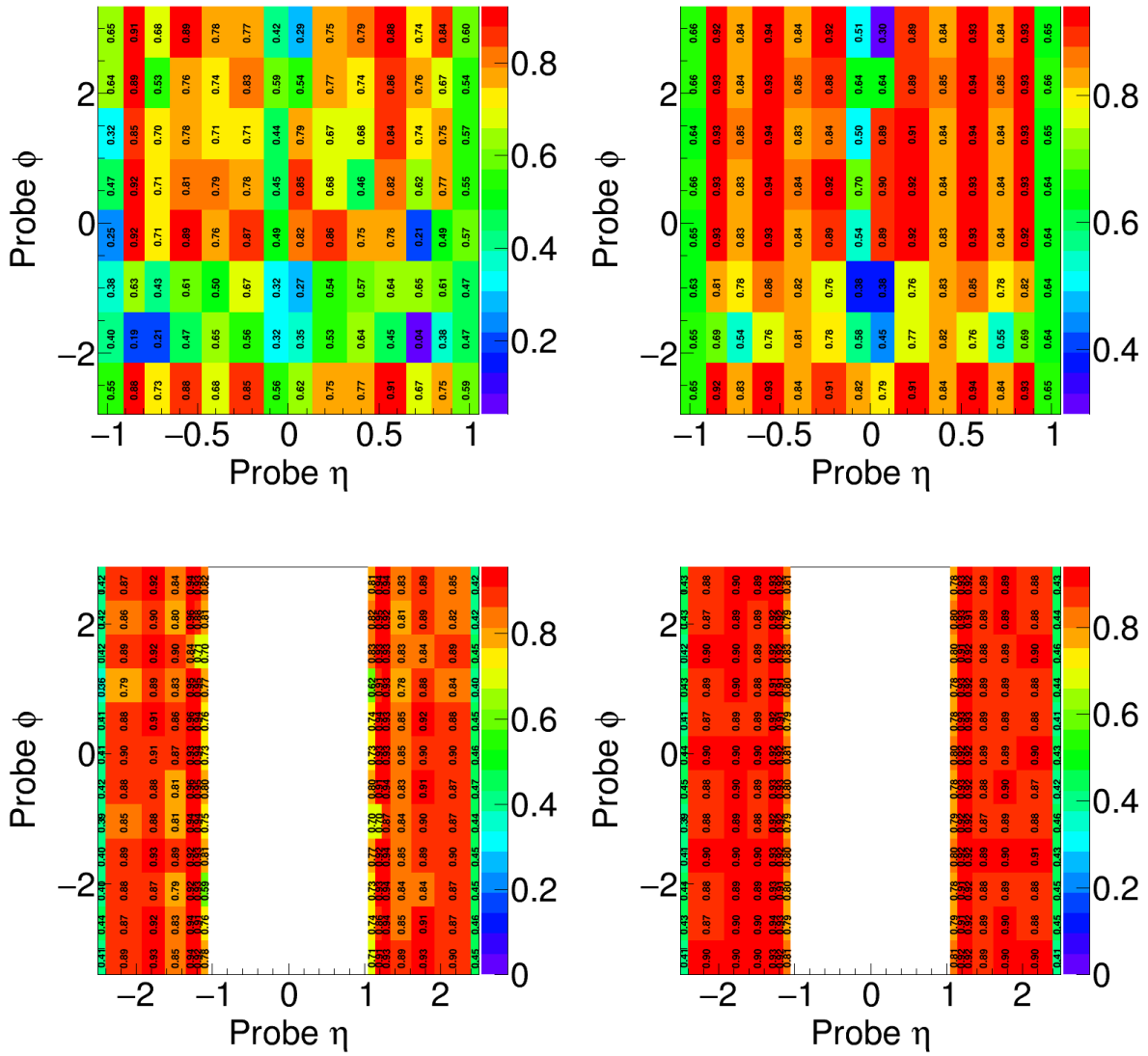

Figure A.5: Trigger efficiency of HLT_mu20_iloose_L1MU15 or HLT_mu50 in the barrel regions (top) and end-cap regions (bottom) in data (left) and in MC (right) for muons for data taking period J.

A.5 Descriptions of systematic uncertainties

Full list of systematic uncertainty sources with the description for $t\bar{t}$ and Z-boson cross-section measurements at 13 TeV center-of-mass energy is given in Table A.4.

A.6 Toy Monte Carlo replicas

A.7 PDF systematic uncertainty verification

The PDF systematics uncertainties for $Z \to ee$ and $Z \to \mu\mu$ channels are estimated from the 100 Monte Carlo replicas using NNPDF3.0 set and were found to be different for both channels, as described in subsection 5.7.2. The difference between electron and muon channels is a consequence of the difference in selection efficiency as a function of rapidity Y. Z-boson rapidity distributions for the electron and muons channel are shown in Figure A.6. To confirm that, the reweighting procedure of $Y_{\mu\mu}$ reconstructed

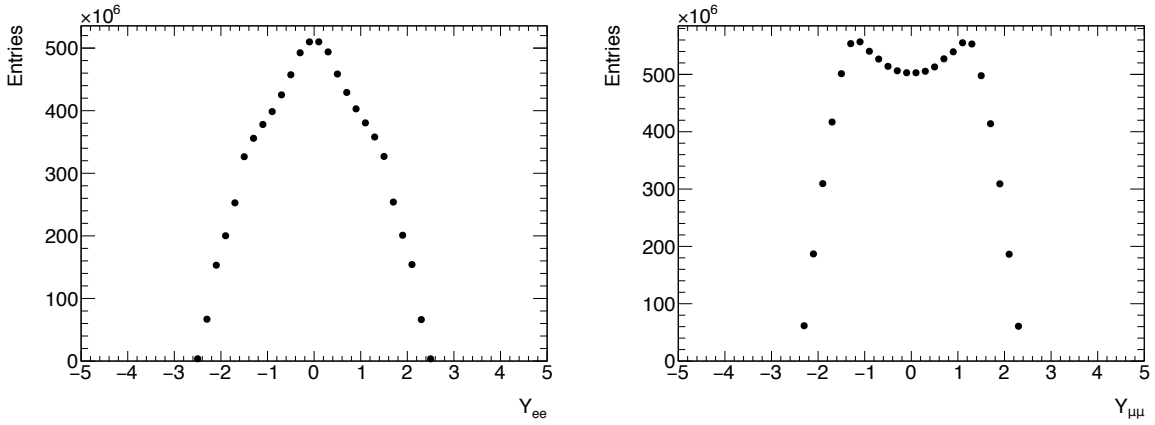

Figure A.6: Z-boson rapidity distribution for $Z \to ee$ (left) and $Z \to \mu\mu$ (right) channels for signal MC.

distribution to Y_{ee} was performed. $Y_{\mu\mu}$ was reweighted with a polynomial function of degree five with parameters extracted from the fit of the ratio between Y_{ee} and $Y_{\mu\mu}$ distributions, shown in Figure A.7. The fit was performed in range $|Y| < 2.5$ and in range $|Y| >= 2.5$ with a constant value of $|Y| = 2.5$. The following parameters were applied to:

$$\begin{aligned} p_0 &= 0.992 \pm 0.004 \\ p_1 &= 0.460 \pm 0.035 \\ p_2 &= -2.410 \pm 0.094 \\ p_3 &= 2.819 \pm 0.103 \\ p_4 &= -1.419 \pm 0.050 \\ p_5 &= 0.268 \pm 0.009 \end{aligned} \tag{A.1}$$

After this procedure, the estimation of the PDF systematic uncertainty was repeated and shown that

Systematic uncertainty name	Description
DLumi13TeV	Uncertainty on the integrated luminosity at 13 TeV
A_Z	Uncertainty for the extrapolation factor from fiducial to total phase space (PDF eigenvectors used)
EBEAM	LHC beam energy uncertainty
BTAG	Efficiency for tagging b-jets (single parameter, not eigenvectors)
BTAG1, 2, 3, 4, 5, 6	Efficiency for tagging b-jets (six independent eigenvectors)
CTAG	Efficiency for tagging c-jets (single parameter, not eigenvectors)
CTAG1, 2, 3, 4	Efficiency for tagging b-jets (four independent eigenvectors)
MISTAG	b-tagging uncertainty for light jets (single parameter, not eigenvectors)
MISTAG(1-12)	b-tagging uncertainty for light jets (twelve independent eigenvectors)
FLSTAT1	Same sign lepton statistical uncertainty (1-btag sample) for 13 TeV $t\bar{t}$ analysis
FLSTAT2	Same sign lepton statistical uncertainty (2-btag sample) for 13 TeV $t\bar{t}$ analysis
R32	The number of events with at least three b-tagged jets divided by the number with at least two b-tagged jets (ratio is sensitive to the number of extra b-tagged jets coming from additional heavy quarks or mis-tagged light jets
JET_19NP_JET_BJES_Response	
JET_19NP_JET_EffectiveNP_1	
JET_19NP_JET_EffectiveNP_2	
JET_19NP_JET_EffectiveNP_3	
JET_19NP_JET_EffectiveNP_4	
JET_19NP_JET_EffectiveNP_5	
JET_19NP_JET_EffectiveNP_6restTerm	
JET_19NP_JET_EtaIntercalibration_Modelling	
JET_19NP_JET_EtaIntercalibration_TotalStat	Nuisance parameters for jet energy scale
JET_19NP_JET_Flavor_Composition	
JET_19NP_JET_Flavor_Response	
JET_19NP_JET_GroupedNP_1	
JET_19NP_JET_Pileup_OffsetMu	
JET_19NP_JET_Pileup_OffsetNPV	
JET_19NP_JET_Pileup_PtTerm	
JET_19NP_JET_Pileup_RhoTopology	
JET_19NP_JET_PunchThrough_MC15	
JET_19NP_JET_SingleParticle_HighPt	
JET_JER_SINGLE_NP__1	Nuisance parameter for jet energy resolution
FLOSR	Fake lepton opposite to same sign ratio uncertainty
GENIFSR	ISR/FSR uncertainty on Wt background (AcerMC+Pythia samples)
GENTT	$t\bar{t}$ generator uncertainty (Powheg+PY vs MC@NLO+Herwig)
GENVV	WW/WZ/ZZ generator uncertainty (Alpgen+Herwig vs Sherpa)
GENWIFSR	Uncertainty on Wt single-top initial/final state radiation ($t\bar{t}$ at 13 TeV analysis)
GENWT	Wt generator uncertainty (Powheg+Pythia vs MC@NLO+Herwig)
HADRTT	$t\bar{t}$ hadronisation efficiency uncertainty
RZMSYS	Z+jets background for $t\bar{t}$ ($Z \to \mu\mu$ and $Z \to ee$ plus one and two b-tagged jets ratios were used)
ChargeIDZ	Efficiency for opposite-charge requirement
NSTTSYS	Uncertainty on prompt same-sign lepton components
EG_RESOLUTION_ALL__1	Electron energy resolution uncertainty
EG_SCALE_ALL__1	Uncertainty on the electron energy scale
EL_EFF_ID_COMBMCTOY__1_nui_0	Uncertainty on the electron identification scale factor (first nuisance parameter for $t\bar{t}/Z$ ratio at 13 TeV, toy MC method used)
EL_EFF_ID_COMBMCTOY__1_nui_1	Uncertainty on the electron identification scale factor (second nuisance parameter for $t\bar{t}/Z$ ratio at 13 TeV, toy MC method used)
EL_EFF_ID_ttbar	Uncertainty on the electron identification scale factor for $t\bar{t}$ measurements at 13 TeV
EL_EFF_Iso_COMBMCTOY__1	Uncertainty on the electron isolation efficiency for $Z \to ee$ measurements at 13 TeV
EL_EFF_Isott13TeV	Uncertainty on the electron isolation efficiency for $t\bar{t}$ measurements at 13 TeV
EL_EFF_Reco_COMBMCTOY__1_nui_0	Uncertainty on the electron reconstruction scale factor (first nuisance parameter for $t\bar{t}/Z$ ratio at 13 TeV, toy MC method used)
EL_EFF_Reco_COMBMCTOY__1_nui_1	Uncertainty on the electron reconstruction scale factor (second nuisance parameter for $t\bar{t}/Z$ ratio at 13 TeV, toy MC method used)
EL_EFF_Reco_ttbar	Uncertainty on the electron reconstruction efficiency for $t\bar{t}$ measurements at 13 TeV
EL_EFF_Trig_COMBMCTOY__1	Uncertainty on the single lepton trigger efficiency for $Z \to ee$ measurements at 13 TeV
MUONS_ID__1	Muon identification uncertainty (variations in the smearing of the ID track)
MUONS_MS__1	Muon energy resolution uncertainty (variations in the smearing of the MS track)
MUONS_SCALE__1	Muon energy scale uncertainty (variations in the scale of the momentum)
MUON_EFF_ISO__1	Muon isolation efficiency uncertainty for Z-boson analysis at 13 TeV (statistical and systematic parts added in quadrature)
MUON_EFF_ISOtt13TeV	Muon isolation efficiency uncertainty for Z-boson analysis at 13 TeV (statistical and systematic parts added in quadrature)
MUON_EFF_Rec__1	Muon reconstruction efficiency uncertainty for Z-boson analysis at 13 TeV (statistical and systematic parts added in quadrature)
MUON_EFF_Reco_ttbar	Muon reconstruction efficiency uncertainty for $t\bar{t}$ analysis
MUON_EFF_SingleTrig__1	Uncertainty on the single lepton trigger efficiency for muon channel (statistical and systematic parts added in quadrature)
MUON_TTVA__1	Muon track-to-vertex-association (statistical and systematic parts added in quadrature)
PDFNNPDF30_nlo_as_0118_eigenset	PDF uncertainty for Z signal (using NNPDF3.0 set)
PDFtt	PDF uncertainty for $t\bar{t}t$ signal (PDF4LHC recipe with CT10, MSTW, NNPDF)
WTDRS	Wt background diagram removal versus diagram subtraction
XSVV	Diboson cross-section (theoretical prediction uncertainty)
XSWT	Wt cross-section (theoretical prediction uncertainty)
ZPTMismodel	Uncertainty due to Z_{p_T} reweighting
Zvtx	Uncertainty due to reweighting of z position of primary vertex
PILEUP_W__1	Uncertainty according to pileup reweighting
BgEWKLumi	Electroweak background uncertainty (systematic part)
BkgEWStat	Electroweak background uncertainty (statistical part)
BkgEWSystgg	Background of gluon-induced process with two gluons coupling to the top quark current
DiBosZ	Diboson (ZZ, WW, WZ) background uncertainty
MJBkg	Multi-jet background uncertainty
SingleTopZ	Single top background uncertainty
TopZ	$t\bar{t}$ background uncertainty
WBosZ	W background for Z-boson analysis
ZTauZ	$Z \to \tau\tau$ background for $Z \to ee$ and $Z \to \mu\mu$ channels
tWt	$t \to Wt$ background uncertainty

Table A.4: Description of systematic names for $t\bar{t}$ and Z-boson analysis at 13 TeV.

	$Z \to ee$ ID	$Z \to ee$ Reco	$Z \to ee$ Iso	$Z \to ee$ Trig	$Z \to \mu\mu$ Trig
Seed	10	13	12	11	1234
Toy MC replica 1	0.5548	0.5536	0.5528	0.5536	0.7064
Toy MC replica 2	0.5557	0.5536	0.5536	0.5536	0.7061
Toy MC replica 3	0.555	0.5539	0.5533	0.5536	0.7063
Toy MC replica 4	0.5545	0.5538	0.5539	0.5536	0.7065
Toy MC replica 5	0.5528	0.554	0.5534	0.5536	0.7064
Toy MC replica 6	0.5528	0.5536	0.5532	0.5536	0.7063
Toy MC replica 7	0.5531	0.5535	0.553	0.5536	0.7064
Toy MC replica 8	0.5567	0.5533	0.5542	0.5536	0.7064
Toy MC replica 9	0.5516	0.5539	0.5531	0.5536	0.7063
Toy MC replica 10	0.5512	0.5537	0.5529	0.5536	0.7064
Toy MC replica 11	0.556	0.5541	0.554	0.5537	0.7065
Toy MC replica 12	0.553	0.554	0.555	0.5535	0.7066
Toy MC replica 13	0.5564	0.5538	0.553	0.5536	0.7064
Toy MC replica 14	0.5515	0.5542	0.553	0.5536	0.7062
Toy MC replica 15	0.5572	0.5538	0.5536	0.5537	0.7066
Toy MC replica 16	0.5479	0.5539	0.5538	0.5536	0.7067
Toy MC replica 17	0.5495	0.5535	0.5542	0.5536	0.7065
Toy MC replica 18	0.5534	0.5539	0.5547	0.5536	0.7063
Toy MC replica 19	0.552	0.5539	0.5547	0.5536	0.7068
Toy MC replica 20	0.5511	0.5536	0.5537	0.5536	0.7067
Toy MC replica 21	0.5523	0.5535	0.5541	0.5537	0.7063
Toy MC replica 22	0.5542	0.5541	0.5532	0.5536	0.7065
Toy MC replica 23	0.5531	0.5534	0.5541	0.5536	0.7066
Toy MC replica 24	0.5563	0.5542	0.5535	0.5536	0.7067
Toy MC replica 25	0.5559	0.5537	0.5539	0.5536	0.7062
Toy MC replica 26	0.5509	0.5537	0.5534	0.5536	0.7062
Toy MC replica 27	0.5523	0.5539	0.5542	0.5536	0.7064
Toy MC replica 28	0.5534	0.5536	0.5528	0.5537	0.7064
Toy MC replica 29	0.5537	0.5535	0.5537	0.5536	0.7062
Toy MC replica 30	0.5532	0.5535	0.5533	0.5536	0.706
Toy MC replica 31	0.5571	0.554	0.5524	0.5536	0.7062
Toy MC replica 32	0.5482	0.5537	0.5539	0.5536	0.7062
Toy MC replica 33	0.5531	0.5537	0.5528	0.5536	0.7066
Toy MC replica 34	0.5523	0.5536	0.5546	0.5536	0.7063
Toy MC replica 35	0.5515	0.5533	0.5531	0.5536	0.7063
Toy MC replica 36	0.5515	0.5541	0.5547	0.5536	0.7064
Toy MC replica 37	0.5557	0.5532	0.5552	0.5536	0.7062
Toy MC replica 38	0.5545	0.554	0.5543	0.5536	0.7064
Toy MC replica 39	0.5549	0.5534	0.5531	0.5536	0.7063
Toy MC replica 40	0.553	0.5537	0.5537	0.5536	0.706
Toy MC replica 41	0.5564	0.5533	0.5537	0.5536	0.7064
Toy MC replica 42	0.5531	0.5533	0.5532	0.5536	0.7065
Toy MC replica 43	0.555	0.5538	0.5539	0.5536	0.7062
Toy MC replica 44	0.558	0.5537	0.5524	0.5536	0.7062
Toy MC replica 45	0.5534	0.5535	0.5542	0.5536	0.7066
Toy MC replica 46	0.5539	0.5542	0.5536	0.5536	0.7065
Toy MC replica 47	0.5569	0.5533	0.5544	0.5536	0.706
Toy MC replica 48	0.5516	0.5536	0.5534	0.5536	0.7062
Toy MC replica 49	0.5544	0.554	0.5532	0.5536	0.7066
Toy MC replica 50	0.5529	0.5537	0.552	0.5536	0.7063

Table A.5: All toy MC replicas and corresponding seeds for lepton identification, reconstruction, isolation, trigger efficiency sources for $t\bar{t}$ and Z channels at 13 TeV.

	$Z \to ee$ ID	$Z \to ee$ Reco	$Z \to ee$ Iso	$Z \to ee$ Trig	$Z \to \mu\mu$ Trig
Toy MC replica 51	0.5577	0.5538	0.5537	0.5536	0.7064
Toy MC replica 52	0.5528	0.5528	0.5527	0.5536	0.7065
Toy MC replica 53	0.5544	0.5533	0.5537	0.5536	0.7062
Toy MC replica 54	0.5514	0.5538	0.5534	0.5536	0.7061
Toy MC replica 55	0.5529	0.5536	0.5539	0.5537	0.7063
Toy MC replica 56	0.5541	0.5536	0.5538	0.5536	0.7065
Toy MC replica 57	0.5556	0.5536	0.5556	0.5536	0.7066
Toy MC replica 58	0.5504	0.5535	0.5539	0.5536	0.7062
Toy MC replica 59	0.5543	0.5533	0.5545	0.5536	0.7065
Toy MC replica 60	0.5518	0.5536	0.553	0.5536	0.7064
Toy MC replica 61	0.5508	0.5536	0.5561	0.5536	0.706
Toy MC replica 62	0.5537	0.5533	0.5542	0.5536	0.7064
Toy MC replica 63	0.5548	0.5536	0.554	0.5536	0.7064
Toy MC replica 64	0.5527	0.5536	0.5534	0.5536	0.7063
Toy MC replica 65	0.5514	0.5539	0.5534	0.5536	0.7064
Toy MC replica 66	0.5525	0.5536	0.5545	0.5536	0.7065
Toy MC replica 67	0.5511	0.553	0.5537	0.5536	0.7064
Toy MC replica 68	0.5508	0.5537	0.5544	0.5536	0.7066
Toy MC replica 69	0.5547	0.5538	0.5524	0.5536	0.7067
Toy MC replica 70	0.556	0.5537	0.5539	0.5536	0.7062
Toy MC replica 71	0.553	0.5537	0.5542	0.5536	0.7063
Toy MC replica 72	0.5545	0.5533	0.5543	0.5537	0.7063
Toy MC replica 73	0.5504	0.5537	0.554	0.5536	0.7065
Toy MC replica 74	0.5517	0.5533	0.5528	0.5536	0.7065
Toy MC replica 75	0.5555	0.5535	0.5535	0.5536	0.7063
Toy MC replica 76	0.5535	0.5537	0.5532	0.5536	0.7064
Toy MC replica 77	0.5559	0.5537	0.5541	0.5536	0.7063
Toy MC replica 78	0.5553	0.5536	0.554	0.5535	0.7065
Toy MC replica 79	0.5575	0.5535	0.5518	0.5536	0.7066
Toy MC replica 80	0.5552	0.5536	0.5533	0.5536	0.7063
Toy MC replica 81	0.5541	0.5539	0.5539	0.5536	0.7063
Toy MC replica 82	0.5514	0.5538	0.555	0.5535	0.7064
Toy MC replica 83	0.5526	0.5533	0.5539	0.5536	0.7063
Toy MC replica 84	0.5525	0.5533	0.555	0.5536	0.7067
Toy MC replica 85	0.5549	0.5535	0.5532	0.5536	0.7063
Toy MC replica 86	0.5521	0.5538	0.5542	0.5536	0.7067
Toy MC replica 87	0.5543	0.5534	0.5545	0.5536	0.7066
Toy MC replica 88	0.5537	0.5535	0.5533	0.5536	0.7071
Toy MC replica 89	0.5516	0.5533	0.553	0.5536	0.7066
Toy MC replica 90	0.5534	0.5534	0.553	0.5536	0.7064
Toy MC replica 91	0.5512	0.5537	0.5534	0.5536	0.7065
Toy MC replica 92	0.5527	0.5541	0.5536	0.5536	0.7063
Toy MC replica 93	0.5549	0.5538	0.5536	0.5536	0.7065
Toy MC replica 94	0.5535	0.5533	0.5518	0.5536	0.7064
Toy MC replica 95	0.5513	0.554	0.5535	0.5536	0.7068
Toy MC replica 96	0.5509	0.5541	0.5545	0.5536	0.7063
Toy MC replica 97	0.5521	0.5536	0.5543	0.5536	0.7063
Toy MC replica 98	0.5482	0.5536	0.5552	0.5536	0.7065
Toy MC replica 99	0.5527	0.5539	0.5538	0.5536	0.7065
Toy MC replica 100	0.554	0.5537	0.5541	0.5536	0.7064

Table A.6: All toy MC replicas and corresponding seeds for lepton identification, reconstruction, isolation, trigger efficiency sources for $t\bar{t}$ and Z channels at 13 TeV.

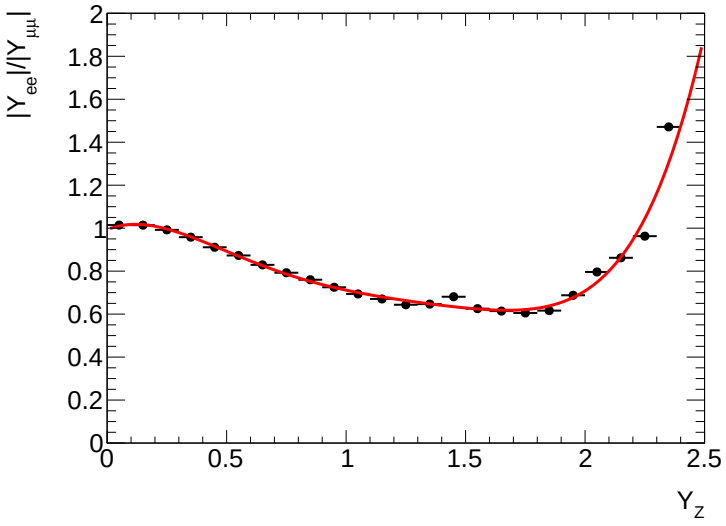

Figure A.7: The ratio between Z-boson rapidity distributions in the $Z \to ee$ and $Z \to \mu\mu$ channels fitted with the polynomial function.

the PDF uncertainty consistent between the two channels. The PDF systematics for the muon channel become the same as for electron channel (0.11, -0.11).

A.8 CT10NLO PDF reweighting

The systematics uncertainty was estimated with 26 eigenvectors variations of CT10NLO (as the Z signal MC is simulated using CT10NLO PDFs). Each eigenvector pair corresponds to up and down variations of uncertainty in one of the input parameters. The CT10NLO has 26 free parameters and therefore a total of 52 error PDFs are assigned.

The difference between the predictions of each eigenvector pair and the central (nominal) prediction is taken as a source of systematic uncertainty. The resulting shifts and uncertainties on C_Z and A_Z are presented in Tables A.8,A.7 for muon and electron channel, respectively.

Eigenvector	C_Z Up [%]	C_Z Down [%]	A_Z Up [%]	A_Z Down [%]
1	−0.002	0.002	−0.218	0.200
2	−0.001	0.001	0.105	−0.115
3	0.014	−0.012	−0.001	−0.008
4	0.018	−0.025	0.234	−0.327
5	−0.003	0.005	−0.096	0.127
6	−0.007	0.004	−0.174	0.104
7	−0.045	0.082	−0.449	0.720
8	0.002	−0.001	−0.081	0.067
9	0.001	0.005	0.226	−0.057
10	0.042	−0.015	0.535	−0.186
11	0.055	−0.030	0.314	−0.157
12	0.014	0.016	0.240	0.005
13	0.003	−0.004	−0.008	0.008
14	−0.018	0.014	−0.259	0.142
15	−0.013	0.011	−0.078	0.070
16	0.013	−0.004	0.080	0.023
17	−0.005	0.004	−0.005	−0.023
18	0.047	0.020	0.415	0.185
19	0.010	−0.010	0.146	−0.090
20	0.010	0.032	0.223	0.259
21	−0.044	0.041	−0.452	0.369
22	−0.012	0.013	−0.147	0.174
23	0.029	−0.036	0.310	−0.311
24	0.047	−0.010	0.324	−0.120
25	0.023	−0.020	0.205	−0.277
26	0.051	−0.005	0.547	−0.476
Total uncertainty	0.156	−0.092	1.466	−1.096

Table A.7: Summary of the different variations of PDF contributing to the uncertainty on C_Z and A_Z for electron final states.

Eigenvector	C_Z Up [%]	C_Z Down [%]	A_Z Up [%]	A_Z Down [%]
1	−0.003	0.002	−0.218	0.200
2	0.001	−0.001	0.105	−0.115
3	−0.002	0.002	−0.001	−0.008
4	0.004	−0.005	0.235	−0.327
5	−0.002	0.003	−0.096	0.127
6	−0.003	0.002	−0.175	0.104
7	−0.003	0.004	−0.449	0.720
8	−0.001	0.001	−0.081	0.067
9	0.009	−0.004	0.228	−0.058
10	0.008	−0.003	0.538	−0.187
11	−0.001	0.002	0.315	−0.157
12	0.006	−0.004	0.240	0.005
13	0.000	0.001	−0.008	0.008
14	−0.004	0.002	−0.259	0.142
15	0.001	−0.001	−0.078	0.070
16	−0.002	0.003	0.080	0.023
17	−0.002	0.000	−0.006	−0.023
18	−0.002	0.004	0.416	0.185
19	0.002	−0.001	0.146	−0.091
20	0.002	0.002	0.223	0.259
21	−0.006	0.004	−0.454	0.370
22	−0.003	0.004	−0.147	0.175
23	0.004	−0.004	0.311	−0.313
24	0.003	−0.001	0.324	−0.120
25	0.000	−0.003	0.205	−0.279
26	0.005	−0.002	0.547	−0.477
Total uncertainty	0.019	−0.014	1.469	−1.098

Table A.8: Summary of the different variations of PDF contributing to the uncertainty on C_Z and A_Z for muon final states.

APPENDIX B

Details on the interpretations of results

B.1 Quantitative comparison with theory predictions

Figure B.1 show the light-sea and gluon distributions divided by the central value of the ATLAS-epWZ12 PDF set at the scales of $Q^2 = m_Z^2$ and $Q^2 = m_t^2$, respectively, for profiling excluding the measurement of $t\bar{t}$ at $\sqrt{s} = 7$ TeV.

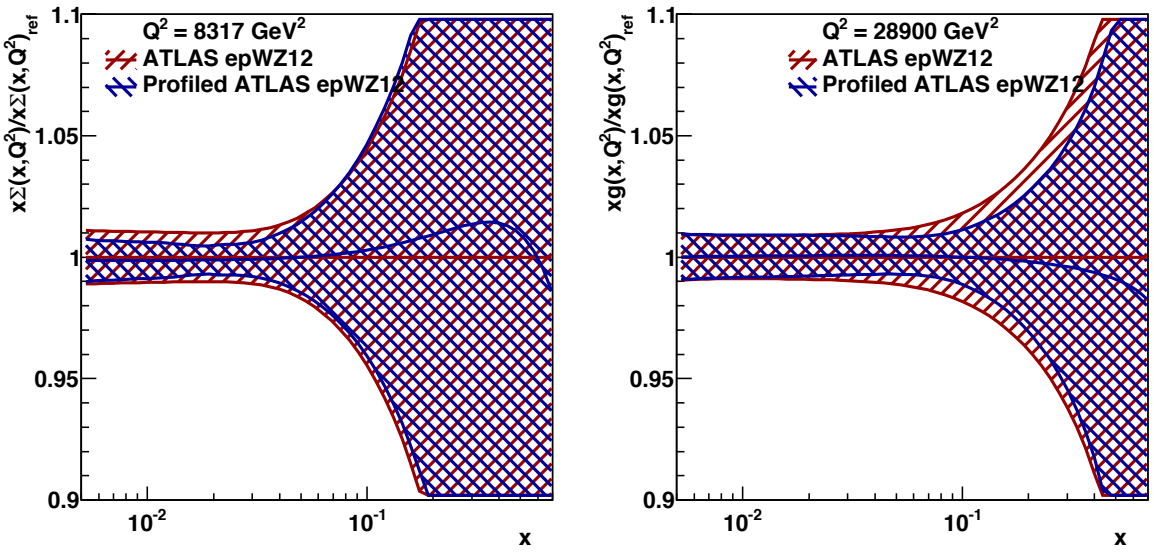

Figure B.1: Effect of the ATLAS Z-boson and $t\bar{t}$ production cross-section data on PDFs based on profiling excluding measurement of $t\bar{t}$ at $\sqrt{s} = 7$ TeV. The bands represent relative uncertainty on PDFs for the ATLASepWZ12-EIG PDF set and uncertainty of profiled ATLASepWZ12-EIG PDF set divided by the central value of ATLASepWZ12-EIG PDF set as a function of Bjorken-x for the total light sea-quark distribution at $Q^2 = m_Z^2$ (left) and for the gluon density at $Q^2 = m_t^2$ (right). The solid blue line represents the ratio of the central value of the profiled to ATLASepWZ12-EIG PDF set.

B.2 Variation of the α_s for $t\bar{t}$ predictions

The variation of the α_s uncertainty for the predicted $t\bar{t}$ cross sections as the function of the top-quark mass is shown in Figures B.2–B.4.

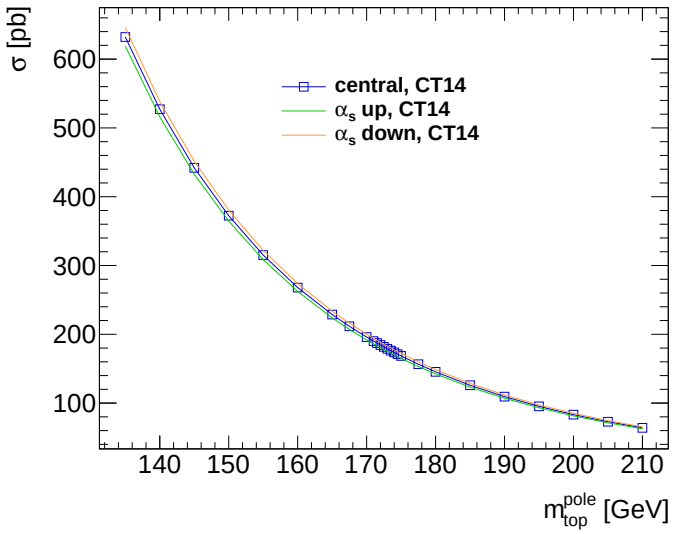

Figure B.2: The theoretical calculation (NNLO+NNLL) of the top quark pair production cross-sections, $\sigma_{t\bar{t}}$, as a function of the top-quark pole mass m_t^{pole} showing the central values (blue markets) and α_s uncertainties (orange and green lines) using CT14 PDF sets at the centre-of-mass energy $\sqrt{s} = 7$ TeV.

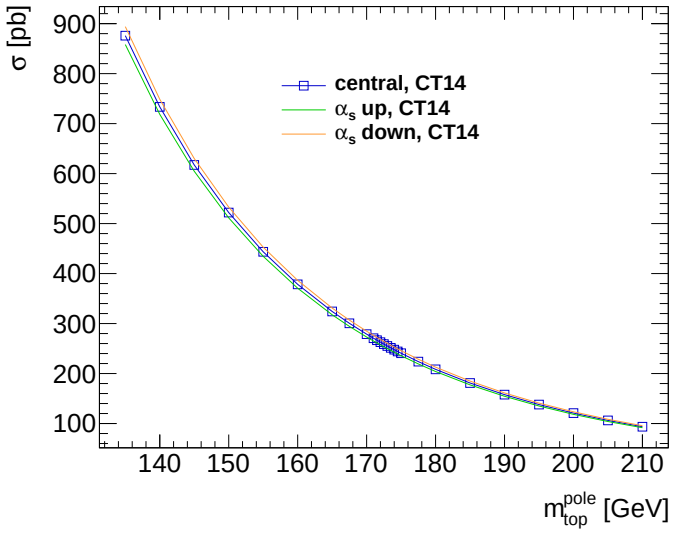

Figure B.3: The theoretical calculation (NNLO+NNLL) of the top quark pair production cross-sections, $\sigma_{t\bar{t}}$, as a function of the top-quark pole mass m_t^{pole} showing the central values (blue markets) and α_s uncertainties (orange and green lines) using CT14 PDF sets at the centre-of-mass energy $\sqrt{s} = 8$ TeV.

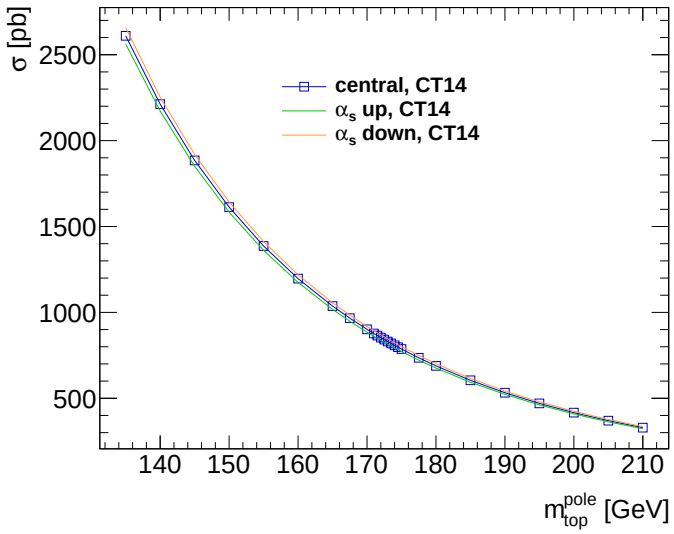

Figure B.4: The theoretical calculation (NNLO+NNLL) of the top quark pair production cross-sections, $\sigma_{t\bar{t}}$, as a function of the top-quark pole mass m_t^{pole} showing the central values (blue markets) and α_s uncertainties (orange and green lines) using CT14 PDF sets at the centre-of-mass energy $\sqrt{s}$ = 13 TeV.

References

[1] ATLAS Collaboration, *Measurement of the inclusive $W^{\pm}$ and Z/gamma cross sections in the electron and muon decay channels in pp collisions at $\sqrt{s}$ = 7 TeV with the ATLAS detector*, Phys. Rev. **D85** (2012) p. 072004, arXiv: 1109.5141 [hep-ex].

[2] ATLAS Collaboration, *Precision measurement and interpretation of inclusive W^+, W^- and Z/γ^* production cross sections with the ATLAS detector* (2016), arXiv: 1612.03016 [hep-ex].

[3] ATLAS Collaboration, *Measurement of the transverse momentum and ϕ^*_η distributions of Drell–Yan lepton pairs in proton–proton collisions at $\sqrt{s}$ = 8 TeV with the ATLAS detector*, Eur. Phys. J. **C76**.5 (2016) p. 291, arXiv: 1512.02192 [hep-ex].

[4] ATLAS Collaboration, *Measurement of $W^{\pm}$ and Z-boson production cross sections in pp collisions at $\sqrt{s}$ = 13 TeV with the ATLAS detector*, Phys. Lett. **B759** (2016) p. 601, arXiv: 1603.09222 [hep-ex].

[5] CMS Collaboration, *Measurement of the Inclusive W and Z Production Cross Sections in pp Collisions at $\sqrt{s}$ = 7 TeV*, JHEP **10** (2011) p. 132, arXiv: 1107.4789 [hep-ex].

[6] CMS Collaboration, *Measurement of inclusive W and Z boson production cross sections in pp collisions at $\sqrt{s}$ = 8 TeV*, Phys. Rev. Lett. **112** (2014) p. 191802, arXiv: 1402.0923 [hep-ex].

[7] CMS Collaboration, *Measurement of the differential and double-differential Drell-Yan cross sections in proton-proton collisions at $\sqrt{s}$ = 7 TeV*, JHEP **12** (2013) p. 030, arXiv: 1310.7291 [hep-ex].

[8] CMS Collaboration, *Measurements of differential and double-differential Drell-Yan cross sections in proton-proton collisions at 8 TeV*, Eur. Phys. J. **C75**.4 (2015) p. 147, arXiv: 1412.1115 [hep-ex].

[9] CMS Collaboration, *The CMS Experiment at the CERN LHC*, JINST **3** (2008) S08004.

[10] ATLAS Collaboration, *The ATLAS Experiment at the CERN Large Hadron Collider*, JINST **3** (2008) S08003.

[11] S. Catani and M. Grazzini, *An NNLO subtraction formalism in hadron collisions and its application to Higgs boson production at the LHC*, Phys. Rev. Lett. **98** (2007) p. 222002, arXiv: hep-ph/0703012 [hep-ph].

[12] S. Catani et al., *Vector boson production at hadron colliders: a fully exclusive QCD calculation at NNLO*, Phys. Rev. Lett. **103** (2009) p. 082001, arXiv: 0903.2120 [hep-ph].

[13] C. Anastasiou et al., *High precision QCD at hadron colliders: Electroweak gauge boson rapidity distributions at NNLO*, Phys. Rev. D **69** (2004) p. 094008, arXiv: hep-ph/0312266 [hep-ph].

[14] R. Gavin et al., *FEWZ 2.0: A code for hadronic Z production at next-to-next-to-leading order*, Comput. Phys. Commun. **182** (2011) p. 2388, arXiv: 1011.3540 [hep-ph].

[15] R. Gavin et al., *W Physics at the LHC with FEWZ 2.1*, Comput. Phys. Commun. **184** (2013) p. 208, arXiv: 1201.5896 [hep-ph].

[16] Y. Li and F. Petriello, *Combining QCD and electroweak corrections to dilepton production in FEWZ*, Phys. Rev. **D86** (2012) p. 094034, arXiv: 1208.5967 [hep-ph].

[17] D. Bardin et al., *SANC integrator in the progress: QCD and EW contributions*, JETP Lett. **96** (2012) p. 285, arXiv: 1207.4400 [hep-ph].

[18] A. B. Arbuzov, R. R. Sadykov, and Z. Was, *QED Bremsstrahlung in decays of electroweak bosons*, Eur. Phys. J. **C73**.11 (2013) p. 2625, arXiv: 1212.6783 [hep-ph].

[19] M. L. Mangano and J. Rojo, *Cross Section Ratios between different CM energies at the LHC: opportunities for precision measurements and BSM sensitivity*, JHEP **08** (2012) p. 010, arXiv: 1206.3557 [hep-ph].

[20] ATLAS Collaboration, *Measurements of top-quark pair to Z-boson cross-section ratios at* $\sqrt{s} = 13, 8, 7$ *TeV with the ATLAS detector*, JHEP **02** (2017) p. 117, arXiv: 1612.03636 [hep-ex].

[21] ATLAS Collaboration, *Measurement of the* $t\bar{t}$ *production cross-section using* $e\mu$ *events with b-tagged jets in pp collisions at* $\sqrt{s} = 7$ *and 8* TeV *with the ATLAS detector*, Eur. Phys. J. **C74**.10 (2014) p. 3109, [Addendum: Eur. Phys. J.C76,no.11,642(2016)], arXiv: 1406.5375 [hep-ex].

[22] ATLAS Collaboration, *Measurement of the* $t\bar{t}$ *production cross-section using* $e\mu$ *events with b-tagged jets in pp collisions at* $\sqrt{s}$*=13 TeV with the ATLAS detector*, Phys. Lett. **B761** (2016) p. 136, arXiv: 1606.02699 [hep-ex].

[23] J. Rojo et al., *The PDF4LHC report on PDFs and LHC data: Results from Run I and preparation for Run II*, J. Phys. **G42** (2015) p. 103103, arXiv: 1507.00556 [hep-ph].

[24] F. Halzen and A. D. Martin, *QUARKS AND LEPTONS: AN INTRODUCTORY COURSE IN MODERN PARTICLE PHYSICS*, 1984, ISBN: 0471887412, 9780471887416.

[25] M. Gell-Mann, *A Schematic Model of Baryons and Mesons*, Phys. Lett. **8** (1964) p. 214.

[26] G. Zweig, "An SU(3) model for strong interaction symmetry and its breaking. Version 2", *DEVELOPMENTS IN THE QUARK THEORY OF HADRONS. VOL. 1. 1964 - 1978*, ed. by D. Lichtenberg and S. P. Rosen, 1964 p. 22, URL: http://inspirehep.net/record/4674/files/cern-th-412.pdf.

[27] C. Patrignani et al., *Review of Particle Physics*, Chin. Phys. **C40**.10 (2016) p. 100001.

[28] P. W. Higgs, *Broken Symmetries and the Masses of Gauge Bosons*, Phys. Rev. Lett. **13** (1964) p. 508.

[29] F. Englert and R. Brout, *Broken Symmetry and the Mass of Gauge Vector Mesons*, Phys. Rev. Lett. **13** (9 1964) p. 321, URL: https://link.aps.org/doi/10.1103/PhysRevLett.13.321.

[30] A. Pich, "The Standard model of electroweak interactions", *2004 European School of High-Energy Physics, Sant Feliu de Guixols, Spain, 30 May - 12 June 2004*, 2005 p. 1, arXiv: hep-ph/0502010 [hep-ph], URL: http://doc.cern.ch/yellowrep/2006/2006-003/p1.pdf.

[31] Y. L. Dokshitzer, *Calculation of the Structure Functions for Deep Inelastic Scattering and e+ e- Annihilation by Perturbation Theory in Quantum Chromodynamics.*, Sov. Phys. JETP **46** (1977) p. 641, [Zh. Eksp. Teor. Fiz.73,1216(1977)].

[32] V. N. Gribov and L. N. Lipatov, *Deep inelastic e p scattering in perturbation theory*, Sov. J. Nucl. Phys. **15** (1972) p. 438, [Yad. Fiz.15,781(1972)].

[33] G. Altarelli and G. Parisi, *Asymptotic Freedom in Parton Language*, Nucl. Phys. **B126** (1977) p. 298.

[34] W. Furmanski and R. Petronzio, *Singlet parton densities beyond leading order*, Physics Letters B **97**.3 (1980) p. 437, ISSN: 0370-2693, URL: http://www.sciencedirect.com/science/article/pii/037026938090636X.

[35] S. Moch, J. A. M. Vermaseren, and A. Vogt, *The Three loop splitting functions in QCD: The Nonsinglet case*, Nucl. Phys. **B688** (2004) p. 101, arXiv: hep-ph/0403192 [hep-ph].

[36] A. Vogt, S. Moch, and J. A. M. Vermaseren, *The Three-loop splitting functions in QCD: The Singlet case*, Nucl. Phys. **B691** (2004) p. 129, arXiv: hep-ph/0404111 [hep-ph].

[37] S. Dulat et al., *New parton distribution functions from a global analysis of quantum chromodynamics*, Phys. Rev. D **93**.3 (2016) p. 033006, arXiv: 1506.07443 [hep-ph].

[38] R. D. Ball et al., *Parton distributions for the LHC Run II*, JHEP **04** (2015) p. 040, arXiv: 1410.8849 [hep-ph].

[39] L. A. Harland-Lang et al., *Parton distributions in the LHC era: MMHT 2014 PDFs*, Eur. Phys. J. **C75**.5 (2015) p. 204, arXiv: 1412.3989 [hep-ph].

[40] ATLAS Collaboration, *Determination of the strange quark density of the proton from ATLAS measurements of the $W \to \ell\nu$ and $Z \to \ell\ell$ cross sections*, Phys. Rev. Lett. **109** (2012) p. 012001, arXiv: 1203.4051 [hep-ex].

[41] H1 and ZEUS Collaborations, *Combination of measurements of inclusive deep inelastic $e^{\pm}p$ scattering cross sections and QCD analysis of HERA data*, Eur. Phys. J. **C75**.12 (2015) p. 580, arXiv: 1506.06042 [hep-ex].

[42] S. Alekhin, J. Bluemlein, and S. Moch, *The ABM parton distributions tuned to LHC data*, Phys. Rev. **D89**.5 (2014) p. 054028, arXiv: 1310.3059 [hep-ph].

[43] J. C. Collins, D. E. Soper, and G. F. Sterman, *Factorization of Hard Processes in QCD*, Adv. Ser. Direct. High Energy Phys. **5** (1989) p. 1, arXiv: hep-ph/0409313 [hep-ph].

[44] G. Arnison et al., *Experimental Observation of Lepton Pairs of Invariant Mass Around 95-GeV/c**2 at the CERN SPS Collider*, Phys. Lett. **126B** (1983) p. 398.

[45] P. Bagnaia et al., *Evidence for Z0 —> e+ e- at the CERN anti-p p Collider*, Phys. Lett. **129B** (1983) p. 130.

[46] W.J. Stirling, private communication.

[47] K. Melnikov and F. Petriello, *Electroweak gauge boson production at hadron colliders through $O(\alpha_s^2)$*, Phys. Rev. D **74** (2006) p. 114017, arXiv: hep-ph/0609070 [hep-ph].

[48] R. Gavin et al., *FEWZ 2.0: A code for hadronic Z production at next-to-next-to-leading order*, Comput. Phys. Commun. **182** (2011) p. 2388, arXiv: 1011.3540 [hep-ph].

[49] R. Gavin et al., *W Physics at the LHC with FEWZ 2.1*, Comput. Phys. Commun. **184** (2013) p. 209, arXiv: 1201.5896 [hep-ph].

[50] Y. Li and F. Petriello,
Combining QCD and electroweak corrections to dilepton production in FEWZ,
Phys. Rev. D **86** (2012) p. 094034, arXiv: 1208.5967 [hep-ph].

[51] CDF Collaboration, *Observation of top quark production in $\bar{p}p$ collisions*,
Phys. Rev. Lett. **74** (1995) p. 2626, arXiv: hep-ex/9503002 [hep-ex].

[52] D0 Collaboration, *Observation of the top quark*, Phys. Rev. Lett. **74** (1995) p. 2632,
arXiv: hep-ex/9503003 [hep-ex].

[53] ATLAS, CDF, CMS and D0 Collaborations,
First combination of Tevatron and LHC measurements of the top-quark mass (2014),
arXiv: 1403.4427 [hep-ex].

[54] Visual diagrams of different concepts and objects used in high-energy physics,
http://bartosik.pp.ua/hep_sketches/tt_decay_channels.

[55] Summary plots from the ATLAS Top physics group,
http://atlas.web.cern.ch/Atlas/GROUPS/PHYSICS/CombinedSummaryPlots/TOP/.

[56] U. Husemann, *Top-Quark Physics: Status and Prospects*, Prog. Part. Nucl. Phys. **95** (2017) p. 48,
arXiv: 1704.01356 [hep-ex].

[57] M. Baak et al., *The global electroweak fit at NNLO and prospects for the LHC and ILC*,
Eur. Phys. J. **C74** (2014) p. 3046, arXiv: 1407.3792 [hep-ph].

[58] ATLAS Collaboration, *Measurement of the top quark mass in the $t\bar{t} \to$ lepton+jets and $t\bar{t} \to$ dilepton channels using $\sqrt{s} = 7$ TeV ATLAS data*, Eur. Phys. J. **C75**.7 (2015) p. 330,
arXiv: 1503.05427 [hep-ex].

[59] ATLAS Collaboration,
Measurement of the top quark mass in the $t\bar{t} \to$ dilepton channel from $\sqrt{s} = 8$ TeV ATLAS data,
Phys. Lett. **B761** (2016) p. 350, arXiv: 1606.02179 [hep-ex].

[60] D. Wicke and P. Z. Skands, *Non-perturbative QCD Effects and the Top Mass at the Tevatron*,
Nuovo Cim. **B123** (2008) S1, arXiv: 0807.3248 [hep-ph].

[61] A. H. Hoang and I. W. Stewart,
Top Mass Measurements from Jets and the Tevatron Top-Quark Mass,
Nucl. Phys. Proc. Suppl. **185** (2008) p. 220, arXiv: 0808.0222 [hep-ph].

[62] M. C. Smith and S. S. Willenbrock, *Top quark pole mass*, Phys. Rev. Lett. **79** (1997) p. 3825,
arXiv: hep-ph/9612329 [hep-ph].

[63] G. 't Hooft, *Dimensional regularization and the renormalization group*,
Nucl. Phys. **B61** (1973) p. 455.

[64] S. Weinberg, *New approach to the renormalization group*, Phys. Rev. **D8** (1973) p. 3497.

[65] U. Langenfeld, S. Moch, and P. Uwer, *Measuring the running top-quark mass*,
Phys. Rev. **D80** (2009) p. 054009, arXiv: 0906.5273 [hep-ph].

[66] P. Marquard et al., *Quark Mass Relations to Four-Loop Order in Perturbative QCD*, English,
Physical Review Letters **114**.14 (2015) p. 142002, ISSN: 0031-9007; 1079-7114.

[67] A. Yagil,
"Observation of top quark production in $\bar{p}p$ collisions with the Collider Detector at Fermilab",
'95 QCD and high-energy hadronic interactions. Proceedings, 30th Rencontres de Moriond, Moriond Particle Physics Meetings, Hadronic Session, Le Arcs, France, March 19-25, 1995, 1995 p. 13,
URL: http://inspirehep.net/record/410560/files/C95-03-19_13-22.pdf.

[68] Tevatron Electroweak Working Group, *Combination of CDF and D0 results on the mass of the top quark using up to 9.7 fb^{-1} at the Tevatron* (2014), arXiv: 1407.2682 [hep-ex].

[69] Tevatron Electroweak Working Group, *Combination of CDF and D0 results on the mass of the top quark using up* 9.7 fb^{-1} *at the Tevatron* (2016), arXiv: 1608.01881 [hep-ex].

[70] Hollik, Wolfgang F. L., *Radiative Corrections in the Standard Model and their Role for Precision Tests of the Electroweak Theory*, Fortsch. Phys. **38** (1990) p. 165.

[71] K. A. Olive et al., *Review of Particle Physics*, Chin. Phys. **C38** (2014) p. 090001.

[72] S. Dittmaier and M. Huber, *Radiative corrections to the neutral-current Drell-Yan process in the Standard Model and its minimal supersymmetric extension*, JHEP **01** (2010) p. 060,
arXiv: 0911.2329 [hep-ph].

[73] M. Czakon and A. Mitov,
Top++: A Program for the Calculation of the Top-Pair Cross-Section at Hadron Colliders,
Comput. Phys. Commun. **185** (2014) p. 2930, arXiv: 1112.5675 [hep-ph].

[74] M. Aliev et al., *HATHOR: HAdronic Top and Heavy quarks crOss section calculatoR*,
Comput. Phys. Commun. **182** (2011) p. 1034, arXiv: 1007.1327 [hep-ph].

[75] P. Nason, S. Dawson, and R. K. Ellis, *The One Particle Inclusive Differential Cross-Section for Heavy Quark Production in Hadronic Collisions*,
Nucl. Phys. **B327** (1989) p. 49, [Erratum: Nucl. Phys.B335,260(1990)].

[76] W. Beenakker et al., *QCD corrections to heavy quark production in hadron hadron collisions*,
Nucl. Phys. **B351** (1991) p. 507.

[77] W. Bernreuther et al., *Top quark pair production and decay at hadron colliders*,
Nucl. Phys. **B690** (2004) p. 81, arXiv: hep-ph/0403035 [hep-ph].

[78] M. Czakon and A. Mitov,
Inclusive Heavy Flavor Hadroproduction in NLO QCD: The Exact Analytic Result,
Nucl. Phys. **B824** (2010) p. 111, arXiv: 0811.4119 [hep-ph].

[79] N. Kidonakis and G. F. Sterman, *Resummation for QCD hard scattering*,
Nucl. Phys. **B505** (1997) p. 321, arXiv: hep-ph/9705234 [hep-ph].

[80] S. Moch and P. Uwer,
Theoretical status and prospects for top-quark pair production at hadron colliders,
Phys. Rev. **D78** (2008) p. 034003, arXiv: 0804.1476 [hep-ph].

[81] M. Beneke, P. Falgari, and C. Schwinn, *Soft radiation in heavy-particle pair production: All-order colour structure and two-loop anomalous dimension*, Nucl. Phys. **B828** (2010) p. 69,
arXiv: 0907.1443 [hep-ph].

[82] J. Ferrando and D. Wendland, *Reference $t\bar{t}$ production cross sections for use in ATLAS analyses*,
tech. rep. ATL-COM-PHYS-2014-112, CERN, 2014,
URL: https://cds.cern.ch/record/1662536.

[83] L. Evans and P. Bryant, *LHC Machine*, JINST **3** (2008) S08001.

[84] E. Mobs, *The CERN accelerator complex. Complexe des accélérateurs du CERN* (2017), General Photo, URL: https://cds.cern.ch/record/2244406.

[85] J. Pequenao, "Computer generated image of the whole ATLAS detector", 2008, URL: https://cds.cern.ch/record/1095924.

[86] ATLAS Collaboration, *ATLAS inner detector: Technical design report. Vol. 1* (1997).

[87] J. Pequenao, "Computer generated image of the ATLAS inner detector", 2008, URL: https://cds.cern.ch/record/1095926.

[88] T. G. Cornelissen et al., *Updates of the ATLAS Tracking Event Data Model (Release 13)*, tech. rep. ATL-SOFT-PUB-2007-003. ATL-COM-SOFT-2007-008, CERN, 2007, URL: https://cds.cern.ch/record/1038095.

[89] M. Capeans et al., *ATLAS Insertable B-Layer Technical Design Report*, tech. rep. CERN-LHCC-2010-013. ATLAS-TDR-19, 2010, URL: https://cds.cern.ch/record/1291633.

[90] ATLAS TRT Collaboration, *The ATLAS Transition Radiation Tracker (TRT) proportional drift tube: Design and performance*, JINST **3** (2008) P02013.

[91] J. Pequenao, "Computer Generated image of the ATLAS calorimeter", 2008, URL: https://cds.cern.ch/record/1095927.

[92] ATLAS Collaboration, *Electron and photon energy calibration with the ATLAS detector using LHC Run 1 data*, Eur. Phys. J. **C74**.10 (2014) p. 3071, arXiv: 1407.5063 [hep-ex].

[93] ATLAS Collaboration, *ATLAS muon spectrometer: Technical design report* (1997).

[94] ATLAS Collaboration, *Performance of the ATLAS Trigger System in 2015*, Eur. Phys. J. **C77**.5 (2017) p. 317, arXiv: 1611.09661 [hep-ex].

[95] ATLAS Collaboration, *Luminosity determination in pp collisions at $\sqrt{s}$ = 8 TeV using the ATLAS detector at the LHC*, Eur. Phys. J. **C76**.12 (2016) p. 653, arXiv: 1608.03953 [hep-ex].

[96] S. van der Meer, *Calibration of the effective beam height in the ISR*, tech. rep. CERN-ISR-PO-68-31. ISR-PO-68-31, CERN, 1968, URL: https://cds.cern.ch/record/296752.

[97] ATLAS Collaboration, *ATLAS Computing: technical design report*, Technical Design Report ATLAS, Geneva: CERN, 2005, URL: https://cds.cern.ch/record/837738.

[98] G. Barrand et al., *GAUDI - A software architecture and framework for building HEP data processing applications*, Comput. Phys. Commun. **140** (2001) p. 45.

[99] *HL-LHC High Luminosity Large Hadron Collider: The HL-LHC project*, URL: https://hilumilhc.web.cern.ch/about/hl-lhc-project.

[100] ATLAS Collaboration, *Letter of Intent for the Phase-I Upgrade of the ATLAS Experiment*, tech. rep. CERN-LHCC-2011-012. LHCC-I-020, CERN, 2011, URL: https://cds.cern.ch/record/1402470.

[101] ATLAS Collaboration, *Letter of Intent for the Phase-II Upgrade for the ATLAS Experiment*, tech. rep. CERN-LHCC-2012-022. LHCC-I-023, CERN, 2012, URL: https://cds.cern.ch/record/1502664.

[102] ATLAS Collaboration, *New Small Wheel Technical Design Report*, tech. rep. CERN-LHCC-2013-006. ATLAS-TDR-020, 2013, URL: https://cds.cern.ch/record/1552862.

[103] ATLAS Collaboration, *ATLAS Liquid Argon Calorimeter Phase-I Upgrade Technical Design Report*, tech. rep. CERN-LHCC-2013-017. ATLAS-TDR-022, 2013, URL: https://cds.cern.ch/record/1602230.

[104] ATLAS Collaboration, *ATLAS Phase-II Upgrade Scoping Document*, tech. rep. CERN-LHCC-2015-020. LHCC-G-166, CERN, 2015, URL: https://cds.cern.ch/record/2055248.

[105] ATLAS Collaboration, *Technical Design Report for the ATLAS Inner Tracker Strip Detector*, tech. rep. CERN-LHCC-2017-005. ATLAS-TDR-025, CERN, 2017, URL: https://cds.cern.ch/record/2257755.

[106] S. Díez et al., *A double-sided, shield-less stave prototype for the ATLAS Upgrade strip tracker for the High Luminosity LHC*, JINST **9** (2014) P03012.

[107] I. Bloch, *Strip Upgrade Petal*, URL: http://twiki.cern.ch/twiki/bin/view/Atlas/StripUpgradePetal.

[108] Allcomp Inc., http://www.allcomp.net/.

[109] Elgoline D.o.o.., http://en.elgoline.si.

[110] V. Benítez et al., *Sensors for the End-cap prototype of the Inner Tracker in the ATLAS Detector Upgrade*, Nucl. Instrum. Meth. **A833** (2016) p. 226.

[111] F. Anghinolfi et al., *Performance of the ABCN-25 readout chip for the ATLAS Inner Detector Upgrade* (2009), URL: http://cds.cern.ch/record/1234868.

[112] S. Kuehn et al., *Prototyping of hybrids and modules for the forward silicon strip tracking detector for the ATLAS Phase-II upgrade*, JINST **12**.05 (2017) P05015.

[113] Dow Corning Inc., http://www.dowcorning.com.

[114] H. Spieler, *Semiconductor Detector Systems*, vol. v.12, Semiconductor Science and Technology, Oxford: Oxford University Press, 2005, ISBN: 9780198527848, URL: http://www.oup.co.uk/isbn/0-19-852784-5.

[115] G. M. L. Eklund J. Hill and P. Phillips, *Atlas SCT Test DAQ Online Documentation*, URL: http://sct-testdaq.home.cern.ch/sct-testdaq/sctdaq/sctdaq.html.

[116] R. Brun and F. Rademakers, *ROOT: An object oriented data analysis framework*, Nucl. Instrum. Meth. **A389** (1997) p. 81.

[117] B. G. P. Phillips, *Strips Upgrade DAQ GUI Docs*, URL: http://twiki.cern.ch/twiki/bin/view/Atlas/StripsUpgradeDAQGUIDocs.

[118] ATLAS Collaboration, *Improved luminosity determination in pp collisions at $\sqrt{s} = 7$ TeV using the ATLAS detector at the LHC*, Eur. Phys. J. C **73** (2013) p. 2518, arXiv: 1302.4393 [hep-ex].

[119] ATLAS Collaboration, *Luminosity Public Results Run 2*, URL: http://twiki.cern.ch/twiki/bin/view/AtlasPublic/LuminosityPublicResultsRun2#2015_pp_Collisions.

[120] Standard Model ASG, http://twiki.cern.ch/twiki/bin/view/AtlasProtected/StandardModelASG.

[121] S. Agostinelli et al., *GEANT4: A Simulation toolkit*, Nucl. Instrum. Meth. **A506** (2003) p. 250.

[122] P. Nason, *A New method for combining NLO QCD with shower Monte Carlo algorithms*, JHEP **11** (2004) p. 040, arXiv: hep-ph/0409146 [hep-ph].

[123] S. Frixione, P. Nason, and C. Oleari, *Matching NLO QCD computations with Parton Shower simulations: the POWHEG method*, JHEP **11** (2007) p. 070, arXiv: 0709.2092 [hep-ph].

[124] S. Alioli et al., *A general framework for implementing NLO calculations in shower Monte Carlo programs: the POWHEG BOX*, JHEP **06** (2010) p. 043, arXiv: 1002.2581 [hep-ph].

[125] T. Sjöstrand, S. Mrenna, and P. Z. Skands, *A Brief Introduction to PYTHIA 8.1*, Comput. Phys. Commun. **178** (2008) p. 852, arXiv: 0710.3820 [hep-ph].

[126] T. Gleisberg et al., *Event generation with SHERPA 1.1*, JHEP **02** (2009) p. 007, arXiv: 0811.4622 [hep-ph].

[127] S. Alioli et al., *NLO vector-boson production matched with shower in POWHEG*, JHEP **07** (2008) p. 060, arXiv: 0805.4802 [hep-ph].

[128] H.-L. Lai et al., *New parton distributions for collider physics*, Phys. Rev. D **82** (2010) p. 074024, arXiv: 1007.2241 [hep-ph].

[129] ATLAS Collaboration, *Measurement of the Z/γ^* boson transverse momentum distribution in pp collisions at $\sqrt{s} = 7$ TeV with the ATLAS detector*, JHEP **1409** (2014) p. 145, arXiv: 1406.3660 [hep-ex].

[130] D. J. Lange, *The EvtGen particle decay simulation package*, Nucl. Instrum. Meth. A **462** (2001) p. 152.

[131] N. Davidson, T. Przedzinski, and Z. Was, *PHOTOS Interface in C++: Technical and Physics Documentation*, Comput. Phys. Commun. **199** (2016) p. 86, arXiv: 1011.0937 [hep-ph].

[132] T. Sjöstrand, S. Mrenna, and P. Z. Skands, *PYTHIA 6.4 Physics and Manual*, JHEP **05** (2006) p. 026, arXiv: hep-ph/0603175 [hep-ph].

[133] ATLAS Collaboration, *Comparison of Monte Carlo generator predictions to ATLAS measurements of top pair production at 7 TeV*, ATL-PHYS-PUB-2015-02, 2015, URL: https://cds.cern.ch/record/1981319.

[134] ATLAS Collaboration, *Summary of ATLAS Pythia 8 tunes*, ATLAS-PHYS-PUB-2012-003, 2012, URL: http://cdsweb.cern.ch/record/1474107.

[135] A. D. Martin et al., *Parton distributions for the LHC*, Eur. Phys. J. **C63** (2009) p. 189, arXiv: 0901.0002 [hep-ph].

[136] ATLAS Collaboration, *The ATLAS Simulation Infrastructure*, Eur. Phys. J. C **70** (2010) p. 823, arXiv: 1005.4568 [hep-ex].

[137] ATLAS MC production, http://twiki.cern.ch/twiki/bin/view/AtlasProtected/AtlasProductionGroup.

[138] Single boson cross section predictions: https://twiki.cern.ch/twiki/bin/view/AtlasProtected/CrossSectionHighOrder, diboson predictions: https://twiki.cern.ch/twiki/bin/view/AtlasProtected/SMDC14xsecs, and top-quark-pair predictions: https://twiki.cern.ch/twiki/bin/view/LHCPhysics/TtbarNNLO.

[139] Proposal for pileup reweighting, http://indico.cern.ch/event/437993/contribution/1/attachments/1138739/1630981/spagan_MuRescaling.pdf.

[140] Extended Pileup Reweighting, http://twiki.cern.ch/twiki/bin/viewauth/AtlasProtected/ExtendedPileupReweighting.

[141] Electron Photon four momentum correction, http://twiki.cern.ch/twiki/bin/viewauth/AtlasProtected/ElectronPhotonFourMomentumCorrection.

[142] Muon momentum scale and resolution corrections, http://twiki.cern.ch/twiki/bin/view/AtlasProtected/MCPAnalysisGuidelinesMC15.

[143] Analysis framework ZeeD, http://wiki-zeuthen.desy.de/ATLAS/Projects/ZeeD.

[144] ATLAS Collaboration, *Electron efficiency measurements with the ATLAS detector using the 2015 LHC proton-proton collision data*, tech. rep. ATLAS-CONF-2016-024, CERN, 2016, URL: https://cds.cern.ch/record/2157687.

[145] ATLAS Collaboration, *Muon reconstruction performance of the ATLAS detector in proton–proton collision data at* $\sqrt{s}$ *=13 TeV*, Eur. Phys. J. **C76**.5 (2016) p. 292, arXiv: 1603.05598 [hep-ex].

[146] ATLAS Collaboration, *Electron identification measurements in ATLAS using* $\sqrt{s}$ *= 13 TeV data with 50 ns bunch spacing*, tech. rep. ATL-PHYS-PUB-2015-041, CERN, 2015, URL: https://cds.cern.ch/record/2048202.

[147] M. Cacciari and G. P. Salam, *Pileup subtraction using jet areas*, Phys. Lett. **B659** (2008) p. 119, arXiv: 0707.1378 [hep-ph].

[148] Combined Performance Tools for Physics Analysis, http://twiki.cern.ch/twiki/bin/view/AtlasProtected/PhysicsAnalysisWorkBookRel20CPRec.

[149] ATLAS Collaboration, *Recommendations of the Physics Objects and Analysis Harmonisation Study Groups 2014*, ATL-PHYS-INT-2014-018, 2014, URL: https://cds.cern.ch/record/1743654.

[150] ATLAS Collaboration, *Measurements of the production cross section of a Z boson in association with jets in pp collisions at* $\sqrt{s}$ = 13 *TeV with the ATLAS detector* (2017), arXiv: 1702.05725 [hep-ex].

[151] Event Displays from Collision Data, http://twiki.cern.ch/twiki/bin/view/AtlasPublic/EventDisplayRun2Collisions.

[152] MCP Analysis Guidelines MC15, http://twiki.cern.ch/twiki/bin/view/AtlasProtected/MCPAnalysisGuidelinesMC15.

[153] Electron Efficiencies Recommendations, http://twiki.cern.ch/twiki/bin/view/AtlasProtected/EfficiencyMeasurements2015MC15b.

[154] Electron Efficiency Correlation Model, http://twiki.cern.ch/twiki/bin/view/AtlasProtected/ElectronEfficiencyCorrelationModel.

[155] R. J. Barlow and C. Beeston, *Fitting using finite Monte Carlo samples*, Comput. Phys. Commun. **77** (1993) p. 219.

[156] R. Brun, F. Rademakers, and S. Panacek, *ROOT, an object oriented data analysis framework*, Conf. Proc. **C000917** (2000) p. 11.

[157] A. Trofymov, *Measurements of $W^{\pm}$ and top-quark pair to Z-boson cross-section ratios at $\sqrt{s} = 13, 8, 7$ TeV with the ATLAS detector*, PhD thesis: University of Hamburg, 2017, unpublished thesis.

[158] J. Wenninger, *Energy Calibration of the LHC Beams at 4 TeV*, tech. rep. CERN-ATS-2013-040, CERN, 2013, URL: https://cds.cern.ch/record/1546734.

[159] The source code of VRAP 0.9 may be found at, http://www.slac.stanford.edu/~lance/Vrap/.

[160] J. Wenninger and E. Todesco, *Large Hadron Collider momentum calibration and accuracy*, tech. rep. CERN-ACC-2017-0007, CERN, 2017, URL: https://cds.cern.ch/record/2254678.

[161] S. Frixione and B. R. Webber, *Matching NLO QCD computations and parton shower simulations*, JHEP **06** (2002) p. 029, arXiv: hep-ph/0204244 [hep-ph].

[162] ATLAS Collaboration, *Electron and photon energy calibration with the ATLAS detector using data collected in 2015 at $\sqrt{s} = 13$ TeV*, tech. rep. ATL-PHYS-PUB-2016-015, CERN, 2016, URL: https://cds.cern.ch/record/2203514.

[163] ATLAS Collaboration, *Support note of the measurement of the W and Z cross section at 13 TeV*, ATL-COM-PHYS-2015-767, 2015, URL: https://cds.cern.ch/record/2037669.

[164] HERAverager package, http://wiki-zeuthen.desy.de/HERAverager.

[165] ATLAS Collaboration, *Measurements of the $t\bar{t}$ production cross-section in the dilepton and lepton-plus-jets channels and of the ratio of the $t\bar{t}$ and Z boson cross-sections in pp collisions at $\sqrt{s} = 13$ TeV with the ATLAS detector*, tech. rep. ATLAS-CONF-2015-049, CERN, 2015, URL: https://cds.cern.ch/record/2052605.

[166] S. Alekhin et al., *HERAFitter*, Eur. Phys. J. **C75**.7 (2015) p. 304, arXiv: 1410.4412 [hep-ph].

[167] H1 Collaboration, *Measurement of the Inclusive ep Scattering Cross Section at Low Q^2 and x at HERA*, Eur. Phys. J. **C63** (2009) p. 625, arXiv: 0904.0929 [hep-ex].

List of Figures

List of Tables

Hiermit erkläre ich an Eides statt, dass ich die vorliegende Dissertationsschrift selbst verfasst und keine anderen als die angegebenen Quellen und Hilfsmittel benutzt habe.

I hereby declare, on oath, that I have written the present dissertation by my own and have not used other than the acknowledged resources and aids.

Hamburg, 05 October 2017

Acknowledgements

I am pleased to express my thanks to all those people who helped me with various aspects and contributed in different ways to make this dissertation real.

First of all, I would like to thank my doctoral supervisor, Alexander Glazov. The analysis studies would not be possible without his valuable guidance during all years, constant support and encouragement. Thank you for spending your time on all discussions, explanations and answering my questions (especially during first year). It was a great pleasure to work with you and to gain new experience.

I warmly thank Prof. Manuella Vincter for being as an inofficial supervisor during the analysis work. Thank you for your assist, advises and inspiration. Without you the publications would not appear so instant, your guidance and support in the way of approving and publishing our results made it possible.

Also I would like to thank all the people in the W/Z Standard Model group, in particular for informative discussions on my analysis, constructive comments and suggestions. I would like to thank Ulla Blumenschein for a cooperation in the cut-flows for the analysis. I am really grateful to Fabrice Balli and Stefano Camarda for providing theoretical predictions for Z-boson production. Thanks to Chiara, Federico and Ludovica for many important recommendations, help, sharing knowledge and friendly meetings during my visits to CERN.

I am very thankful to James Ferrando for providing huge input, theoretical predictions for the $t\bar{t}$ production for different range of top-quark mass, used in the top-quark mass scan. Many thanks to Barbara Alvarez Gonzalez and Richard Hawkings for their collaboration for getting consistent analyses in order to calculate ratios and work on the publication. Also I would like to thank Alexander Law and Hayk Pirumov for providing and adjusting plotting tool, which allowed to produce nice control plots for main kinematic distributions in this dissertation.

I am very grateful to people who introduced me to the detector upgrade activities. I thank Ingrid-Maria Gregor for suggesting an interesting subject for my qualification task and her guidance and support during this project. I am particularly grateful for the assistance given by John Stakely Keller and Sergio Diez Cornell. They always supported, encouraged and helped me with different issues and difficulties. Also, I would like to thank Dario Ariza, who contributed to the petalet assembly and supported me all time. I have enjoyed the intensive work with you all. I am indebted also to many people, who contributed to the petalet project in many ways.

Thanks to Sergio Diez Cornell, Mateusz Dyndal, James Ferrando, Ingrid-Maria Gregor, Oleg Kuprash and James Robinson for patient reading of dissertation and their suggestions and comments.

I would like to thank Artur Trofymov, who accompanied me since first university years, for work together, for contribution to the analysis results, for all interesting discussions. I am very thankful to all my friends who supported me all the time, making my life interesting, exciting and inspiring. Thanks for various unforgettable memories.

Finally, I am truly grateful to my family and my husband, Oleksandr, who always believe in me, support and encourage me in all situations.